Numerical Simulation of Proppant Transport in Hydraulic Fractures

by

Morteza Roostaei

A thesis submitted in partial fulfillment of the requirements for the degree of

Doctor of Philosophy

in

PETROLEUM ENGINEERING

Department of Civil and Environmental Engineering
University of Alberta

Abstract

This research focuses on the study of mechanisms of proppant transport in reservoirs during frac-packing operation. As an attempt to improve current numerical modeling of proppant transport, a multi-module, numerical proppant, reservoir and Geomechanics simulator was developed, linked and tailored for capturing the processes and mechanisms that are believed to be of significance in frac-pack operations.

Extensive laboratory experiments have shown that several factors affect the final distribution of proppants in the fracture. Most often these factors are accounted for through an empirical correlation coming from a wide range of experiments. Although it is extremely hard, or impossible, to include all of these interacting phenomena of proppant transport in a numerical model, we have investigated most of them and involved them in our numerical model.

The complicating phenomena that are addressed in the literature and has been captured by our developed tool are: hindered settling velocity (terminal velocity of proppants in the injection fluid), effect of fracture walls, proppant concentration and inertia on settling (due to extra drag exerted on particles, compared to single particle motion in Stokes regime in unbounded medium), possible propped fracture porosity and also mobility change due to the presence of proppants and fracture closure or extension during proppant injection.

Most of the current (published) numerical models for simulating proppant transport require an analytical hydraulic fracture model. Most of the time the fracture width, if not assumed to be constant, is calculated based on PKN, KGD, P3D or PL3D models. Even in most recent works, an adaptive re-meshing technique is employed to couple a fully 3D fracture model with a proppant transport model, yet the fracture model is fully elastic. These models neglect plastic deformations of the medium, assuming plasticity has minor effects during the operation. In

addition, unlike our model, conventional simulators do not include deformation resulting from the interaction between stress and fluid flow response in a porous medium.

The main objective of this research is to link a numerical hydraulic fracture model to a proppant transport model to study the fracturing response and proppant distribution and to investigate the effect of proppant injection on fracture propagation and fracture dimensions. The results have provided valuable information in the field for frac-packing operations and optimization. An investigation of different design parameters in proppant transport operation was performed. This investigation not only is useful in testing the robustness of the developed numerical tool, it provides practical recommendations and trends in a better design of the treatment operation. Moreover, the errors in the model were distinguished through this sensitivity analysis when an unexpected relationship between inputs and outputs was observed.

From a numerical point of view, we have utilized different techniques to reduce the expected long computational time of the model. Local mesh refinement, dimensional splitting and sparse method of solving matrix equations were employed to optimize the running time of the model. Geomechanics and fluid mechanics equations were solved by finite difference method, while the hyperbolic proppant transport PDE were solved by WENO scheme of finite volume through the application of flux limiters. The reason of using this method is that the solution of hyperbolic PDEs may encounter smooth transition or there can be large gradients of the field variables. The numerical challenge posed in a shock situation is that high-order finite difference schemes lead to significant oscillations in the vicinity of shocks despite that such schemes result in higher accuracy in smooth regions. On the other hand, first-order methods provide monotonic solution convergences near the shocks, while giving poorer accuracy in the smooth regions. Accurate

numerical simulation of such systems is a challenging task using conventional numerical methods.

As of now, there is a significant uncertainty in the effect of proppant properties and fluid parameters on the final proppant distribution. Therefore, our tool will increase the understanding of the relationship between fluid and proppant properties and the final distribution of these particles, which in turn determines the conductivity of the propped fracture, leading to reduction of the mentioned uncertainty and more realistic production forecast especially for reservoirs under improved or enhanced oil recovery scheme as found in heavy oil and oil sands projects.

Preface

The research conducted for this thesis was a part of a research program funded by NSERC through a Collaborative Research Development program supported by BP.

A slightly different version of Chapter 5 (excluding the sensitivity analysis) was published as Taghipoor S., Roostaei M., Nouri A. and Chan D., 2014, "Numerical Investigation of the Hydraulic Fracturing Mechanism in Oilsands," *SPE Heavy Oil Conference*, Calgary, Alberta, June 10-12 2014, SPE-170132-MS.

Dedication

To Liana and Amir

Acknowledgements

I wish to express my sincere appreciations from the bottom of my heart to all those who supported me to complete this thesis and in one way or another, contributed and extended their valuable assistance towards the completion of this study.

Firstly, my strong appreciation goes to my supervisor, Dr. Alireza Nouri for his continuous support, patient encouragement and insightful guidance throughout whole the study and research. I definitely enjoyed the years of studies and research under his guidance. His teachings will be with me through my whole career

I would also like to thank my co-supervisor Dr. Dave Chan for his ongoing guidance, support and encouragement throughout the research. I am very grateful for his supervision and patience in improving the numerous revisions of numerical simulations. This thesis would not have been possible without his support and guidance.

I would like to express my sincere gratitude to Dr. Vahiddodin Fattahpour who always granted me his time without hesitation and gave me a lot of help and valuable ideas.

I also would like to thank Dr. Hassan Dehghanpour and Dr. Nobuo Maeda for being the members of the supervisory and examination committee of PhD. program and to Dr. John Chen for being the external examiner of the examination committee. This dissertation could not have been completed without their help.

Finally, I would like to express my gratitude to my wife, Sarah, my parents and parents-in-law for their endless understanding, support, encouragement and love during the past and future tough or easy times.

Table of Contents

List of Tables

List of Figures

Nomenclature

A	Cross Section of the Container
A	Information Propagation Velocity
B	Formation Volume Factor
c	Volumetric Concentration of Proppants
c^*	Saturation Concentration
c_b	Bulk Compressibility
C_D	Dimensionless Drag Coefficient
C_{Dt}	Drag Coefficient at Terminal Conditions
$C_{Dt\infty}$	Drag Coefficient at Terminal Conditions in Infinite Medium
c_{gr}	Grain Compressibility
C_L	Coefficient
c^{new}	Concentration after Adjustment due to Width Change
c^{old}	Concentration before Adjustment due to Width Change
c_r	Rock Compressibility
c_{rj}	Constant Coefficients of the Interpolating Polynomial
c_{sat}	Saturation Concentration
D	Diffusivity Coefficient
D_c, D	Container Diameter
d_p, d	Proppant Diameter
D_{pf}	Diffusivity Coefficient
D_{pf}^{mo}	Diffusivity Coefficient due to Molecular Movement
D_{pf}^{te}	Diffusivity Coefficient due to Temperature Gradient

D_{pf}^{tu}	Diffusivity Coefficient due to Turbulent Flow
dx, dy	Fracture Grid Cell Dimensions
f	Flux Vector
F	Numerical Flux Function
f	Drag Coefficient
f(c)	Voidage Function or Concentration Function
F_D	Drag Force
F_{Ds}	Terminal Drag Force in a Single Particle System
F_{Dt}	Terminal Drag Force in a Multi-Particle System
f_F	Wall Factor in Terms of Drag Force
F_H	Higher Order Flux
F_h	Horizontal Force on a Fluid Section per Unit Length
F_L	Lower Order Flux
$F^n_{i\pm1/2}$	Average Flux along Cell Boundary
f_u	Wall Factor in Terms of Terminal Velocity
F_v	Vertical Force on a Fluid Section per Unit Length
f_μ, f_w, f	Wall Factor in Terms of Viscosity
g	Flux Vector
g =	Acceleration due to Gravity
G’	Suspension Modulus
Ga	Galileo Number
h	Fracture or Slot Height
k	Permeability

K	Intrinsic Viscosity
k_1, k_2, k_3	Runge-Kutta Coefficients
k_{avg}	Average Permeability
k_f	Fracture Permeability
k_m	Matrix Permeability
l	Length of the Slot
L_f	Fracture Length
L_{grids}	Total Length of Subgrids
$L_{pen.}$	Fracture Penetration Length
m_p	Proppant Mass
N_{Bu}	Buoyancy Number
$N_{new\ Elements}$	Number of New Elements Added due to Fracture Propagation
p	Pressure
p_0	Initial Pore Pressure
p_D	Dimensionless Pressure
$p_i(x)$	k^{th} order Interpolating Polynomial
p_{DW}	Dimensionless Wellbore Pressure
p_{init}	Initial Reservoir Pressure
p_{wf}	Wellbore Pressure
q	Conserved Quantity
$q_0(x)$	Initial Value of Conserved Quantity
q_f	Fracture Flow Rate
Q_h	Horizontal Flow

Q_i^n	Average Value of Conserved Quantity
q_{inj}	Injection Rate
q_m	Matrix Flow Rate
$\hat{Q}$	Flux Approximation
qt	Total Flow Rate through Matrix and Fracture
Re	Reynolds Number
Re_t	Reynolds number at Terminal Velocity
R_{ret}	Retardation Factor
S(i)	Stencil
T	Rock Tensile Strength
t	Time
t_{DA}	Dimensionless Time
t_{Df}	Dimensionless Time
TV	Total Variation
u	Horizontal Velocity
u_∞	Settling Velocity without the Presence of the Walls
u_f	Fluid Horizontal Velocity
u_p	Proppant Horizontal Velocity
u_{sl}	Slurry Horizontal Velocity
u_{Stokes}	observed Stokes velocity
u_t	Terminal Velocity
ut	Terminal Velocity
$u_{t\infty}$	Terminal Velocity in Infinite Fluid

u_w	Settling Velocity with the Presence of the Walls
u_x	Velocity in the x Direction
u_y	Velocity in the y Direction
u_y	Vertical Displacement
u_z	Velocity in the z Direction
V	Grid Cell Volume
v	Vertical Velocity
V_b	Bulk Volume
V_f	Fracture Volume
v_f	Fluid Vertical Velocity
V_g	Grain Volume
$V^{old}_{subgrids}$	Previous Time Step Fracture Grids Volume
V_p	Proppant Volume
v_p	Proppant Vertical Velocity
V_{p1}	Proppant Volume Before Closure
V_{p2}	Proppant Volume After Closure
V_{pore}	Pore Volume
v_{set}	Settling Velocity
v_{sl}	Slurry Vertical Velocity
$V_{subgrids}$	Fracture Grids Volume
V_t	Total Volume
w	Fracture or Slot Width
w_{avg}	Average Width

w_{centre}	Maximum Width of elliptic slot
w^{new}	Current Time Step Width
w^{old}	Previous Time Step Width
$w_{propped}$	Fracture Propped Width
x	Horizontal Coordinate
x_e, y_e	Half Length of Reservoir Drainage Area
x_f	Fracture Half Length
$x_{i\pm1/2}$	Cell Centre Coordinates
x_w, y_w	Fracture Axis Coordinates
y	Vertical Coordinate
α	Ratio of Proppant to Fluid Horizontal Velocities
β_r	Smooth Indicator
γ	Euler's constant equal to 0.5772157
Δp	Pressure Difference
Δp_t	Total Pressure Drop
Δt	Time Step
Δx, Δy	Grid Cell Dimensions
ΔX, ΔY	Reservoir Grid Dimensions
$\Delta \rho$	Density Difference
ε_v	Volumetric Strain
ε_x, ε_y, ε_z	Strain Components
λ	Ratio of the Diameters of the Spheres and Container
μ	Viscosity

μ_0	Initial Viscosity
μ_0	Initial Viscosity
μ_{rel}	Relative Viscosity
μ_{sl}	Slurry Viscosity
ρ	Density
ρ_f	Fluid Density
ρ_p	Proppant Density
ρ_{sl}	Slurry Density
σ'_y	Vertical Effective Stress
σ_h	Minimum Horizontal Stress
σ_{Tip}	Stress at the Fracture Tip
τ_{ij}	Stress Components
ϕ	Porosity
ϕ^0	Initial Porosity
ϕ_f	Fracture Porosity
$\phi^n_{i\pm1/2}$	Flux Limiter
$\psi(x)$	Source Term
ω_p	Mass Fraction of the Proppant
ω_r, d_r	Weights
Φ	Flux Limiter

Abbreviations

2D	Two Dimensional
3D	Three Dimensional
FDM	Finite Difference Method
FEM	Finite Element Method
FVM	Finite Volume Method
HF	Hydraulic Fracturing
KGD	Khristianovic-Geertsma-de Klerk
MC	Mohr-Coulomb
MS	Micro Seismic
PKN	Perkins-Kern-Nordgren
Sec	Seconds
TVD	Total Variation Diminishing

Chapter 1: General introduction

1.1 Introduction

The technique of hydraulic fracturing consists of injecting a fluid into a medium to initiate and propagate (a) fracture(s) inside that medium. Hydraulic fracturing was first introduced in the Houston gas field in western Kansas in 1947 (Howard & Fast, 1970) and it has been successfully used for stimulation purposes and improving oil recovery. In 1950, Shell Oil Company in Germany used the term "frac-pack" for sand control completions that were hydraulically fractured before being gravel packed (Ellis, 1998). The second successful treatment in which viscous crude oil and sand were pumped dates back to 1963 in a Venezuelan field (Roodhart et al., 1994). However, it was more than 20 years before the technique was widely applied. After 1985, the improvement in production of frac-packs compared to other completion methods and the development of deep-water fields in the Gulf of Mexico, suddenly increased the impetus for frac-packing (Bale et al., 1994; Hannah et al., 1994).

Proppant injection also helps to increase the productivity of the stimulated well. Proppants, which are granular materials like sand, prevent the fracture closure and provide a conductive path to facilitate flow from the reservoir through the fracture and to the well. However, premature bridging of the fracture by proppant particles, which is called screen-out, should be avoided. After pumps are shut down, proppants need to withstand in-situ stresses and they should remain in place at flowback.

An important part of hydraulic fracturing modelling is proppant transport and deposition, since the proppant placement and the properties of the proppant bed strongly affect the eventual productivity of the well. Injection of low viscosity fluids makes the proppant transport and deposition even more important as the faster settling of the proppants may reduce propped fracture length and the expected productivity.

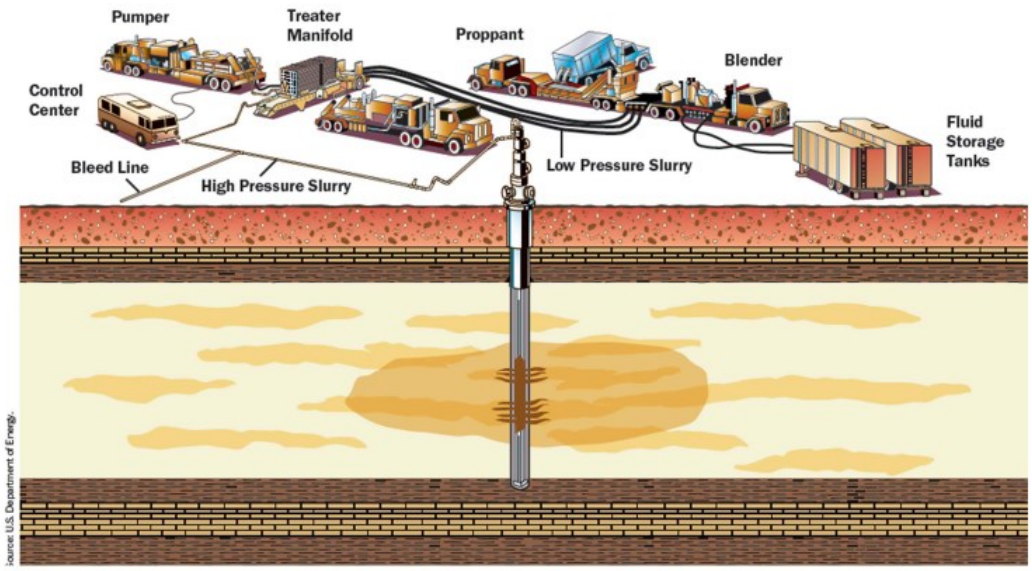

Figure 1.1: Frac-Packing Treatment (Weng & Klein, 1998)

The final distribution of the proppant bed in the fracture may be affected by several processes. These are:

1. Leak-off of the carrying fluid through the fracture walls into the formation.
2. Settling of proppant particles due to gravity.
3. Variation in the rheology of the carrying fluid
4. Difference in the velocity of proppants and carrying fluid
5. Extra drag force exerted on the particles by the walls of the fracture

The majority of the current proppant transport models do not calculate the fracture dimensions numerically but rather they use analytical equations. None of the available frac-pack models are able to capture geomechanical effects in the fracturing process. In the current research, an intensive literature survey was carried out to investigate the results of laboratory experiments on particle motion to be able to simulate the proppant distribution more accurately. The objective is to gather all the mechanisms previously studied at the laboratory scale in our numerical model.

In this research, a 3D numerical proppant transport model is coupled to our developed numerical fracture simulator to properly investigate proppant transport phenomenon in hydraulic fractures. A smeared fracture approach will be implemented and utilized in a numerical model based on the continuum mechanics assumption. This is the first model that couples the fluid flow, solid

deformation, proppant transport, and mechanics of fracture growth to create a numerical tool for fracture creation when proppants are injected. This is the first and only model that links numerical fracture geometry calculations with a proppant transport model.

The model can be used by operators to design and optimize frac-pack treatments in a systematic way. The simulator will aid in identifying the important parameters for frac-packing, leading to improvements in fracture design and proppant transport.

1.2 Problem Statement

Proppant transport models in hydraulic fracturing have been developed with various levels of success. Fracture simulation in these models usually has some serious shortfalls that lessen their suitability for field applications. Regarding the way that these models simulate the fracture, two different categories can be recognized: models with constant rectangular or elliptical width (slot experiment simulations) and models with the fracture geometry coming from an analytical equation (like PKN, P3d or PL3D). These models simulate a planar fracture in a pre-determined direction; In addition, they are unable to capture plastic deformations in the reservoir which are very important in weak formations. Regarding solid transport simulations, they do not include simultaneous settling velocity corrections for fracture wall, proppant concentration and inertia, fracture closure on the proppants and mobility reduction as a function of proppant concentration among others. Although these aspects have been studied separately, a numerical model that takes account of all these effects has not been published. Also, the numerical methods used in the published models are not accurate for transport problems.

We propose to develop a coupled hydro-mechanical, multi-module numerical model to capture the abovementioned processes that occur during the frac-packing. The model will interface a numerical hydraulic fracture model to a reservoir simulator and a proppant transport simulator. A very accurate finite volume numerical technique for transport problem was combined with the dimensional splitting method to reduce the running time of multi-dimensional simulations.

1.3 Background

A typical hydraulic fracturing treatment consists of three steps: (1) a fluid pad without proppant is pumped down the well under high pressure to initiate and extend the induced fractures. (2) A high-viscosity fracturing fluid containing proppant is pumped to extend the fracture and place

proppants. Proppant is transported into the fracture by the proppant laden fluid, and its function is to prop the fractures and keep the created fractures open after the pumping stops. (3) A fluid pad without proppant is pumped following the proppant to displace all the proppant laden slurry in the well-bore into the fracture (Brannon et al., 2009; Cipolla, 2009; Grieser et al., 2009; Crafton, 2008; Fisher, et al., 2004; Wiley et al., 2004). Usually the fluid which carries the proppant is required to have a high viscosity, so that the proppant can be distributed uniformly inside the fracture and form a high-conductivity path. Fracture conductivity and propped fracture length are the two main factors determining the productivity of fractured wells. In high-permeability reservoirs, fracture conductivity is more important to enhance well productivity than fracture length, while for low-permeability reservoirs, the fracture length is more important. Both of these factors are dependent on proppant transport. Ideally the proppant should distribute uniformly across the production interval. This requires that the fluid have good proppant suspension capability to keep the proppant from settling. In all the fracturing treatments, proppant transport is a key issue because it determines whether or not a large amount of proppant settles down to the fracture bottom and forms a proppant bed. Horizontal transport of the proppant determines how far the proppant is transported into the fracture and how long the propped portion of the fracture is. In this research models are proposed and implemented to show the impact of proppant transport on fracture geometry.

Though different approaches have been implemented for studying sediment transport and developing sediment transport functions, basic aspects of sediment transport due to fluid movement remain the same. The transport of sediment particles by a flow of liquid can be in the form of bed-load and/or suspended-load, depending on the particle characteristics (particle size distribution and concentration) and flow conditions (the velocity profile, bed-shear stress and shear velocity). Typically, three modes of sediment motion have been observed: 1) traction motion, 2) saltation motion, and 3) suspended motion. When the bed-shear stress exerted on an individual particle exceeds the critical value for initiation of motion (referred to as Shields parameter or Shields criterion), the particle starts to move by rolling and/or sliding, and is referred to as traction motion. During traction motion, the particles pivot out of the position and move in the direction of the flow while maintaining contact with the channel bed.

As the bed-shear velocity increases, the particles start moving along the bed in the form of regular jumps, which are referred to as saltations (Brannon et al., 2005). During the saltation

motion, the turbulence tries to lift the particle into suspension, but the particle weight is too heavy to be in a suspended state, and thus, falls back to the channel bed. Usually, the transport of particles by rolling, sliding, and saltating is commonly referred to as the bed-load transport. When the bed-shear velocity exceeds the particle settling velocity, the turbulent forces become higher than the particle weight and the particles move by suspended motion (van Rijn, 1984). The mechanics of sediment transport are controlled mainly by the horizontal fluid velocity. At low velocities, the sediments mainly move as a result of sliding and/or rolling. At intermediate velocities, a fluidized layer is formed which promotes bed-load transport. At higher velocities, sediments are transported due to suspended motion (Biot & Medlin, 1985).

Our model numerically solves the mass balance of proppant and slurry during the packing process. The developed proppant model accounts for the leak off of fracturing fluid from the fracture, effects of fracture walls on settling velocity, changes in settling velocities caused by changes in proppant concentration and inertial effects associated with large relative velocities between the proppant and the fluid. The model also accounts for the formation of proppant bed at the bottom of the fracture. The most important input of the tool is the fracture geometry, which can be assessed analytically (e.g., through PKN fracture model), or by using a numerical fracture model. The distribution of the proppant concentration in the fracture is the main output of this model. The model has been verified against numerical slot test simulations. The model has been used in a sensitivity analysis to study how the final proppant distributions are impacted by the proppant size and density, carrying fluid viscosity and fluid flow rate. The new tool is a noticeable step towards improving the efficiency and consistency of proppant transport modeling. The model can be used to improve proppant placement under a given set of in-situ conditions.

1.4 Research Objective

Significant amounts of research have been directed towards understanding the hydraulic fracturing and solid transport mechanisms in underground formations. Yet, several aspects of the process remain unclear.

The main objective of the research is to develop the capability to simulate hydraulic fracturing and frac-packing in reservoirs using a coupled multi-module numerical model. The model consists of a smear fracture simulator and a proppant transport module. The model can be used to

investigate the effect of proppant injection on fracture width, length, and mobility. We have also investigated the effect of various proppant and pad parameters on frac-pack performance. This study is a unique approach for further understanding of the proppant transport process to allow for possible enhancements of frac-packing performance. The sensitivity analysis is one of the significance of this research. Modeling the field problem due to the lack of data and variability of properties is so complex that makes the simulation almost impossible. Therefore, the purpose of our sensitivity analysis is establishing trends based on which optimizations and recommendations can be made. Besides, by performing a parametric analysis, the impact of such factors as flow rate, and fracturing fluid rheology and proppant properties on proppant transport is assessed. This model provides a platform to analyze the fracturing response of field operations as well.

Smeared fracture approach has been used to develop our numerical fracture module, which is capable of simulating multiple shear and tensile fractures and rotating fractures. The results of this research can provide valuable information for field fracturing practices, optimization and management of fracturing jobs.

To the best of our knowledge, such a model that incorporates numerical fracture simulation and a proppant transport model has not been developed or published. The important features of the proposed numerical model include:

1. Explicit modeling of fracturing phenomenon (avoiding predetermined geometries for fractures)
2. Capability for capturing plastic deformations in the reservoir
3. Comprehensive modeling of proppant injection, by including Stokes velocity corrections for inertia, wall and concentration effects, retardation factor, and for the first time, fracture closure on proppant,
4. Applying an accurate form of finite volume method that has been proposed specifically for hyperbolic (transport) partial differential equations

This research will help in the understanding of the mechanisms involved in the process of proppant transport in hydraulic fractures. The main questions to be answered in this research are:

1. What are the physical phenomena that have an impact on the proppant distribution inside the fractures?
2. How can the results of experiments on transport of proppants, fluidization and sedimentation be applied in a flexible manner in a numerical model?
3. How the design of the frac-packing treatments can be optimized with our numerical tool?

The results of this research will provide valuable information for field frac-packing practices, optimization and management of the jobs.

1.5 Research Hypothesis

This research focuses on the study of mechanisms of proppant transport in reservoirs during frac-packing operation. According to laboratory experiments several factors affect the final distribution of proppants in the fracture. Inertia, fracture walls and presence of other particles have an effect on the settling velocity of the particles. The relationship between Reynolds number and drag coefficient exerted on particles changes with increasing inertia. Fracture walls significantly reduce settling velocity of particles due to extra drag force they exert on particles. Proppant concentration has a similar effect to walls. However, after concentration reaches a certain level, the packed fracture behaves like a porous medium and no more proppant particles can be injected into this packed system. The existence of the proppants changes the mobility of the fluid since the viscosity of carrying fluid is enhanced. The higher the concentration, the higher the slurry viscosity, net pressure and fracture width. The length of the fracture, on the other hand, shortens due to the higher pressure losses inside the fracture.

Several design parameters, such as injection rate, proppant density and diameter and injection fluid viscosity affect the final concentration of proppants inside the fractures. According to the published numerical works on proppant transport in slots, viscosity of injection fluid shows a strong impact on the concentration distribution (by changing settlement and convection) and shape of the fracture. Increased flow rate causes the fracture to fill up faster and reduces both convection and settlements. Proppant density and diameter have a moderate effect on settlement only. The combined effect of these parameters can be obtained by looking at the Buoyancy number of the system. The Buoyancy number is an important factor in determining the shape of concentration plume. Very different design parameters, if provide similar Buoyancy number, are

expected to result in similar distribution of proppants. Unfortunately, the Buoyancy number cannot be defined for geometries other than fixed shape slots and has to be determined through numerical simulations.

Advanced numerical techniques and state of the art in solid transport experiments were combined to develop an efficient numerical tool. Our developed tool helps the understanding of the relationship between fluid and proppant properties and reduces the existing uncertainty in the underground proppant distribution.

1.6 Methodology

The methodology in this research consists of developing a 2D continuum-based numerical frac-pack model capable of simulating hydraulic fracturing and proppant transport. Finite Difference software FLAC (ITASCA Consulting Group, 2006) is the platform for stress/strain analysis. A single-phase finite difference fluid flow analysis code has been developed in MATLAB to perform flow simulations. The third module is a proppant transport simulator, which maps conductivity to the fluid flow module, while receiving geometry of the fracture from geomechanics module. In other words, FLAC geomechanical tool is linked to a proppant and reservoir flow simulator, developed in MATLAB, using an iterative coupling scheme, to capture the mechanical and fluid flow aspects of the process.

The modules are as follows:

- Mechanical module (FLAC)
- Fluid flow module (in-house program coded in MATLAB)
- Proppant module (in-house program coded in MATLAB)
- Linking interface (MATLAB)

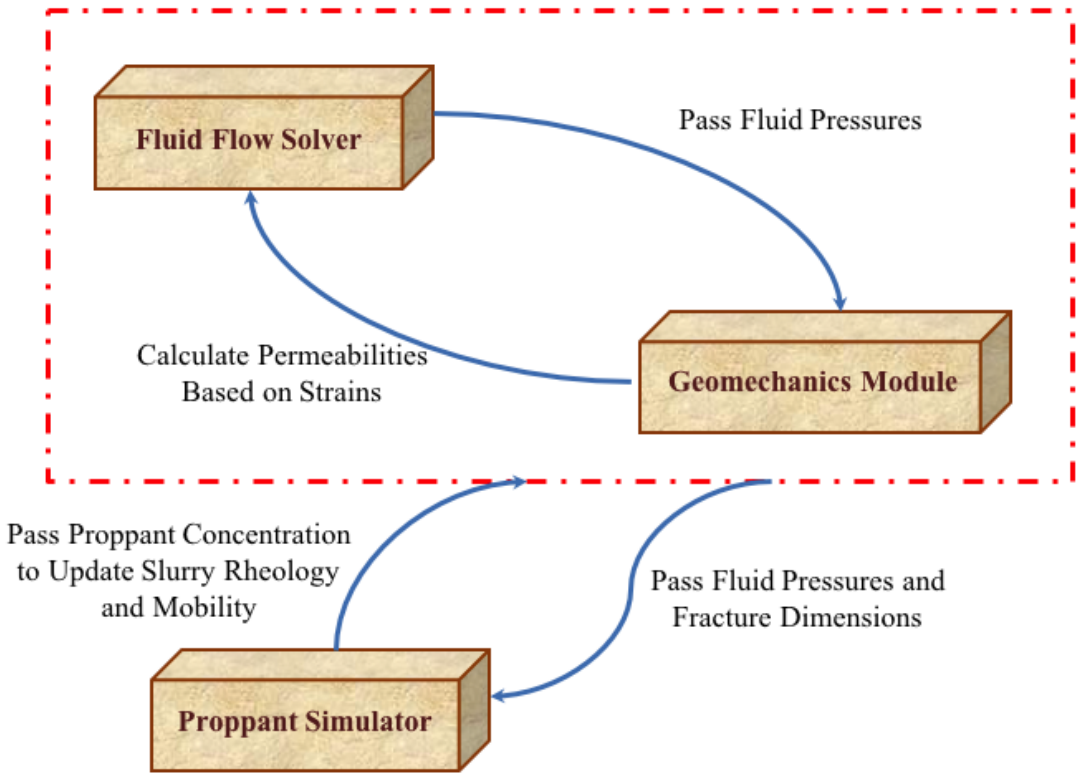

Figure 1.2: Interaction between different modules

Different parameters are transferred among the modules (Fig. 1.2). The fracture module produces the fracture geometry for fracture flow analysis and proppant transport analysis and also provides the fluid flow module with permeability and porosity, which are required to calculate the pore pressure and fluid flow. The proppant module calculates the fracture face pressure and proppant concentration, which are then fed into the fracture module as the mobility increase or decrease (fracture creation or closure).

The main outputs of the model are:

- Stress/strain distribution
- Pore pressures
- Fracture geometry
- Fracture conductivity
- Proppant concentration along the fracture

To develop the smeared-based numerical tool for simulation of proppant transport, the following steps have been taken:

- A smeared hydraulic fracture model that was previously developed by Taghipoor et al. (2013), is our numerical fracture model. In this model, a permeability model for tensile fracturing is utilized to relate the permeability of the fractured element to its deformation in the continuum model. In addition, the coupled mechanism between shearing and the concomitant permeability evolution has been considered in this hydraulic fracture model. The details of Taghipoor et al. (2013) model are outside the scope of this work.
- From a numerical point of view, we have utilized different techniques to reduce the expected long run-time of the model. Dimensional splitting and sparse method of solving matrix equations are employed to optimize the running time of the model.
- Geomechanics and fluid mechanics equations are solved by finite difference. A full permeability tensor is used in the fluid flow simulations. The proppant mass balance equation forms a non-linear hyperbolic PDE, which needs to be solved by high-resolution methods of finite volume through the application of flux limiters. The slurry mass balance equation forms an elliptical PDE, which can be solved implicitly by finite difference method. The procedure of solving the two equations is similar to IMPES method in reservoir simulations and iterations are performed to achieve convergence.

The developed model has two stages. The first stage is during the pad flow before the onset of proppant injection. Fig. 1.3a shows the calculation scheme for this stage. The second stage is after the proppant injection for which proppant transport simulation is necessary. The calculation procedure is depicted in Fig. 1.3b.

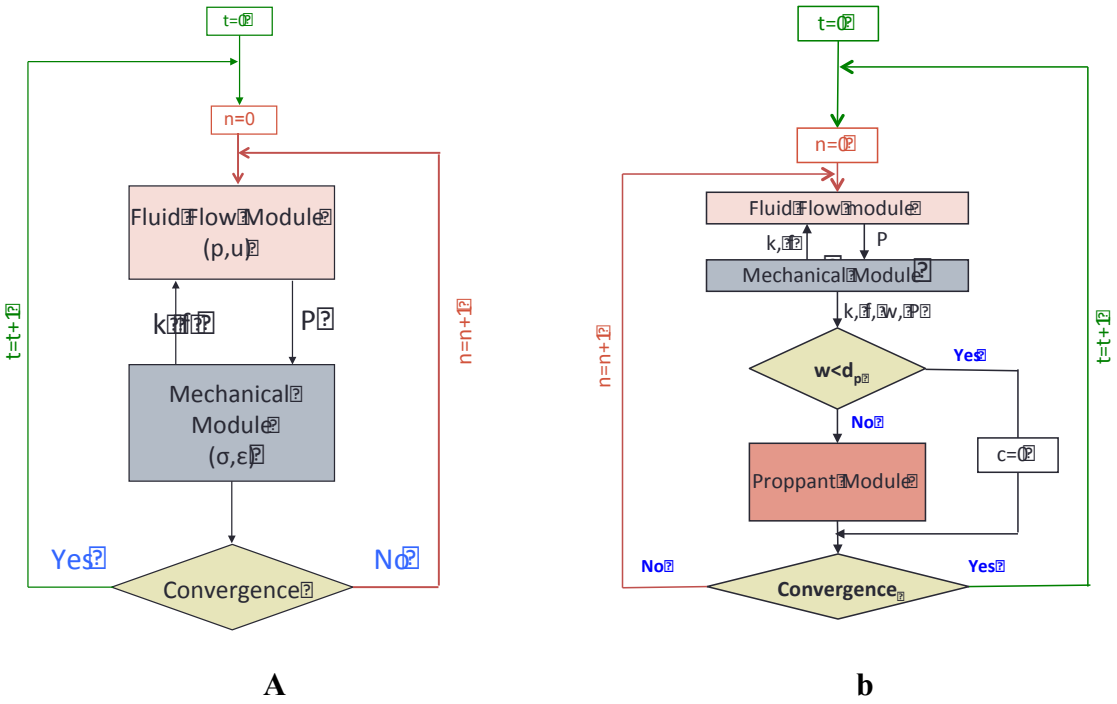

Figure 1.3: Modeling flow chart for the a) injection of the initial fracking pad, b) injection of proppants

To carry out the simulation some simplifications have been made:

A vertical hydraulic fracture is considered. In the proppant module, the dominant flow in the fracture can be two or three dimensional in the horizontal and vertical directions. Therefore, our proppant code considers a 3D geometry. The proppant motion inside the fracture occurs horizontally, caused by fluid flow, and vertically (downward), caused by gravity. The horizontal velocity of the proppant is related to horizontal fluid velocity through the retardation factor. The vertical sand velocity (usually referred to as "hindered settling velocity") is governed by fluid properties as well as particle size and specific gravity.

The fracture plane is a horizontal section of the 3D vertical fracture. We have assumed 2D plain strain geometry for fracture simulation. The flow rate is assumed to be uniformly distributed over the fracture height. With this simplification, the 3D fluid/proppant flow problem is reduced to a 2D problem in the horizontal plane. This greatly reduces the complexity of the numerical problem and makes the computation feasible. In addition, extending this model to full 3D will be easier in the future, since our proppant model is written for a 3D geometry.

Modeling the field problem due to the lack of data and variability of properties is so complex that makes the validation of the model by actual treatment jobs almost impossible. Therefore, we simulated a slot test flow and compared the results of our simulations with commercial software COMSOL.

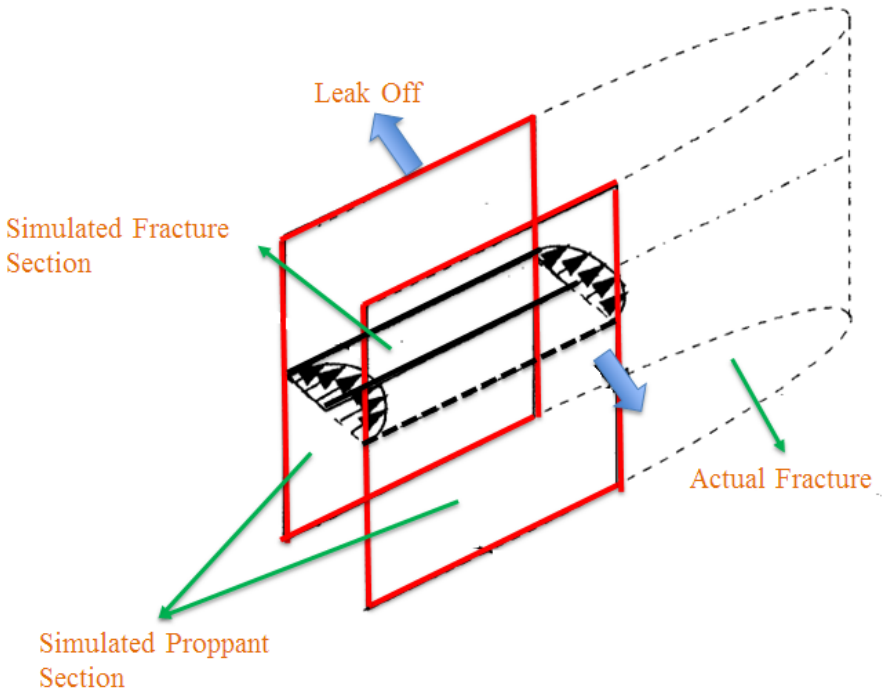

Figure 1.4: Geometry of Our Field Model

1.7 Thesis Layout

The research discussed here forms the basis of a multi-module numerical hydraulic fracture and proppant transport simulator. The research methodology consists of numerical model development, model verification against analytical solutions, published simulations, and commercial software, and application examples to field size models. The research is divided into the following chapters:

In Chapter 2, a literature survey is carried out to investigate the results of small- and large-scale laboratory experiments on proppant transport and sedimentation and fluidization. The objective was to study the physical phenomena that occur at the laboratory scale and capture them in our numerical tool. Proposed correlations for the effect of inertia, concentration and fracture wall on settling velocity and also correlations regarding viscosity evolution of slurry is summarized. In

Chapter 5, the effect of these correlations are reviewed in slot test simulations, and in Chapter 6, some of these correlations are implemented into our flexible numerical tool which can accommodate any other correlation. A literature survey is also carried out in Chapter 2 on the existing numerical proppant transport models with the focus on the type of hydraulic fracture considered. Various features of the numerical tools were evaluated particularly those related to the accuracy, flexibility and comprehensiveness of the models.

Chapter 3 presents the assumptions, mathematical formulations and theories of fracture, fluid flow and proppant simulations and covers all the computational aspects that are essential when developing the proppant transport code. Different solution techniques of transport partial differential equations are compared with the focus on their accuracy close to proppant front, with the objective of implementing the most accurate technique in our tool.

Chapter 4 concentrates on the verification of our proppant transport simulator. Commercial software COMSOL is used for the verification of our developed tool. Also, a sensitivity analysis was performed to distinguish the errors by finding unexpected results and relationships between inputs and outputs. Also, the results of this chapter show how much difference in proppant placement can be obtained if convection and gravity settling are changed.

Chapter 5 describes the numerical algorithm based on which our hydraulic fracture tool is developed. In addition, after discussing different methods of numerical coupling, the transfer of information between the modules and our convergence criteria are discussed. Also, our proposed permeability modifications are verified against analytical, static hydraulic fracture equations.

Chapter 6 is a compilation of example runs that show how the model works for field applications. The model is used in a comprehensive sensitivity analysis to show its capabilities in providing practical recommendations and trends in a better design of the frac-pack operation. This sensitivity study includes a comparison between different components and properties of fluid and proppant and shows which parameters have a dominant effect on the final proppant distribution.

Chapter 7 is a summary of conclusions from each chapter and it also outlines recommendations for future work involving this subject.

1.8 Significance

The main requirements of any completion technique are effective, long life span and proper support during high-rates of production. Frac-packing not only has these two requirements, but it also ensures lower average skin values. When compared to other sand control completion techniques, this method delivers consistently higher flow efficiencies (Ghalambor and Norman, 2009). Moreover, the failure rate of frac-packing is about a quarter of that for cased hole gravel-pack and half that for water-pack completion (Ghalambor and Norman, 2009).

The mechanisms involved in the proppant transport in hydraulic fracturing are very complex both experimentally and numerically, although significant amounts of research have been directed towards understanding these mechanisms. Additionally, the lack of numerical tools specifically suited for transport PDEs, has hindered the optimized design and the field implementation of the treatment.

Since the fracture width is typically so much smaller than other dimensions, a large number of elements will be needed to simulate a field treatment. By applying a partially decoupled numerical approach, we were able to overcome this deficiency in numerical modeling.

Moreover, the transport phenomenon of proppants in a fracture caused by hydraulic fracturing is described by a hyperbolic PDE. The solution of this kind of PDEs may encounter smooth transition or there can be large gradients of the field variables. The numerical challenge posed in a shock situation is that high-order finite difference schemes lead to significant oscillations in the vicinity of shocks despite that such schemes result in higher accuracy in smooth regions. On the other hand, first-order methods provide monotonic solution convergences near the shocks, while giving poorer accuracy in the smooth regions. Accurate numerical simulation of such systems is a challenging task using conventional numerical methods. Therefore, application of accurate and efficient shock capturing numerical techniques is crucial in obtaining a solution for this class of problems.

The model developed in this research will greatly increase the understanding of the mechanisms involved in proppant transport in hydraulic fractures. Such improved understanding can help in management and optimization of fracturing jobs.

Chapter 2: Review of Numerical and Experimental Works on Proppant Transport

2.1 Introduction

Fundamental aspects of fluid-particle interactions have long been the subject of applied mathematics and applied physics. The particles can be gas (bubbles), liquid (drops or droplets) or solid. For example, operations such as distillation, absorption, flotation in chemical and metallurgical engineering rely on bubbles and drops, while chemical catalysts or reactants use solid particles. Droplet behaviors in combustion operation, and bubbles in electro-machining and boiling are studied in mechanical engineering. In all these particle-fluid interactions, there exists a relative motion between the particle and the surrounding fluid. In this chapter, we focus on such relative motion and try to do a comprehensive literature on the experiments performed on the flow of solid particles in fluids.

To increase the well productivity, which is the final goal of hydraulic fracturing, the fractures should be propped open by some granular materials called proppants. Proppants prevent fracture closure after pumps are shut down and at the same time act as a filling with high permeability inside the fracture. The proppant pack inside the fracture should provide high permeability compared to the formation so that the flow from the reservoir to the well faces little resistance and can be facilitated. Proppant particles should also satisfy other requirements such as having enough compressive strength to withstand in-situ stresses and remaining firmly in place at flowback. Therefore, it is obvious how strongly the properties of proppant bed, proppant transport, placement and deposition affect the well productivity.

In the proppant transport literature, accurate determination of settling velocity still remains a problem, despite the fact that all aspects of particle settlement have been studied in other areas like sedimentation and fluidization for many years. Results of these studies, although can be applied to proppant transport application without loss of accuracy, is neglected in proppant related studies. Therefore, the need for such a review seems necessary.

We assume that the surrounding liquid or the continuous phase is a Newtonian fluid. Another assumption we use throughout this research is that the solid particles or the dispersed phase are rigid particles meaning that they can withstand large normal and shearing stresses without a noticeable deformation. It is also assumed that all the particles have the same size, while in

reality proppants with different sizes may be injected sequentially which can further complicate the movement of the suspended particles.

2.2 Past Numerical Works on Proppant Transport

This section is a quick literature review on the limited numerical proppant transport simulations that have been published and their shortcomings. From a mathematical point of view, three proppant transport models have been proposed in the literature since 1970. The type of modeling can be categorized based on the type of the hydraulic fracture description or based on the equations that describe transport phenomena. Based on transport equations the modeling types are: simplified proppant transport and settling model, mixture models and granular kinetic theory models. Our model is a mixture type model with the same formulations that exist in the literature. However, we are improving this type of modeling by including more physical transport processes in the model and applying a more accurate numerical solution technique. In addition, we are modeling the geomechanical effects associated with the injection process inside underground formations, and accounting for its effects in transport simulation.

2.2.1 Simplified Proppant Transport and Settling Model

Simplified models of proppant transport and deposition assume a vertical fracture and discretize it into vertical elements (columns) as shown in Fig. 2.1 (Novotny 1977, Daneshy 1978). Generally, in this type of modelling, proppant concentration in each element is calculated based on the fluid loss and injected amount of fluid at each time step. Empirical settling velocity equations can also be included in the model. Then, in the next step, the amounts of deposited and suspended proppants are calculated. Finally, the results are presented in the form of bed profile showing suspended and deposited proppants as well as the shape of the bank bed.

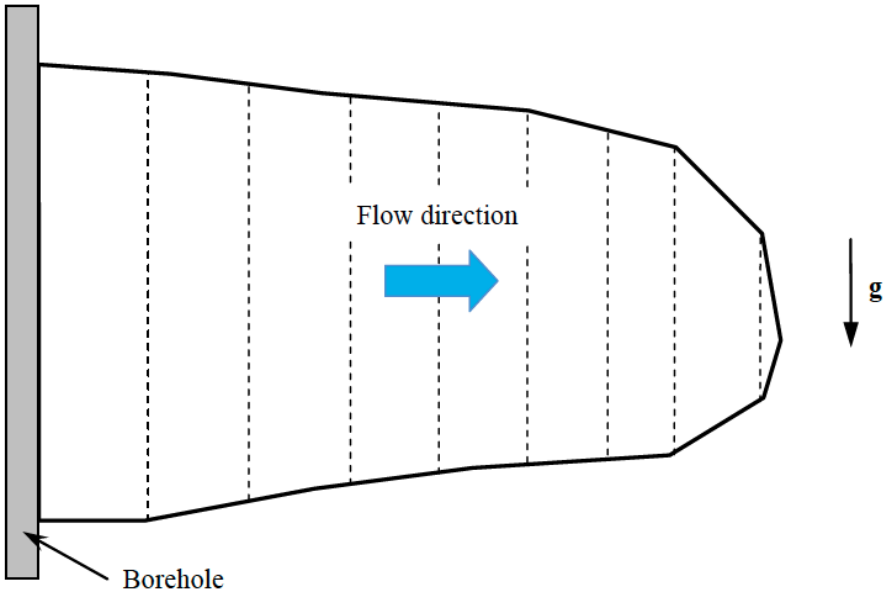

Figure 2.1: fracture discretization employed in simplified proppant transport and settling models (Lavrov, 2011)

Novotny (1977) used the simplified approach and presented one of the early simulations of proppant transport. To obtain the dimensions of the hydraulic fracture, he used the analytical equations of Geertsma and de Klerk (1969) for fracture width and length. Then he applied a simple volume balance on the amount of fluid that enters a given fracture segment and the amount lost to the formation. He also extended the model by incorporating heat transfer between the slurry and the formation and investigated the temperature variation effects on fluid loss, viscosity and settling velocity.

Daneshi (1978) simulated proppant transport in a hydraulic fracture by using the simplified approach. The fracture length and width in his modeling were derived from a simple material balance on the injected and lost fluid and the height of the fracture was assumed to be constant. He also used a lower limit for the volume of injected pad in the simulations to make sure the width of the created fracture is at least two or three times bigger than the particle diameters and particle bridging is avoided. He computed a hindered settling velocity for proppants due to the concentration effects.

It is evident from the brief description above that these models are limited to planar vertical fractures and many details of fluid flow and geomechanics are being neglected.

2.2.2 Mixture Models

The second type of numerical proppant transport model, which is more general than the previous model, is called mixture-type model. Our numerical tool falls within this category and all the details of this modelling type will be discussed later in this thesis. However, we briefly describe the evolution of this type of modelling.

Typically, in mixture-type modelling, the slurry flow inside the fracture is described by the lubrication theory. An essential element of this theory is the averaging of the variables such as concentration and velocities, in the fracture width direction. As a result, it is implied that the concentration of proppant is constant across the fracture aperture in any cross-section or the variation is insignificant and can be neglected. This simplification resolves a huge modeling complication: since the fracture width is typically so much smaller than other dimensions, discretizing an actual size fracture in a field treatment across its width requires a large number of elements to keep the element aspect ratio reasonably small. Among other assumptions of this modeling (that was removed in later simulations), we can mention no slip condition and thus no momentum transfer between the carrying fluid and the granular phase. The consequence of this assumption was that, originally, the proppant velocity was assumed to be equal to the carrying fluid velocity. In addition, the diffusion is assumed to be negligible and thus the front of the proppant concentration profile remains sharp (Adachi et al., 2007). The flow is assumed to be incompressible and the proppant particles are small compared to the fracture aperture.

Many modifications have been made in the original mixture models by different researchers to better simulate the transport phenomena. Settari et al. (1990) was the first to propose the concept of partially decoupled fracture modeling. In his approach, they linked a fracture simulator to a fluid flow simulator and mapped the fracture geometry in terms of permeability and porosity onto the reservoir simulator grids. Later, several researchers used this approach in their numerical simulation of proppant transport. Miranda et al. (2010), Shaoul et al. (2007) and Behr et al. (2006) linked a commercial reservoir simulator to a commercial fracture and proppant simulator and used the same concept that Settari et al. (1990) had used for frac-pack analysis. Later, other methods were proposed for numerical simulations of proppant transport (Friehauf, 2009; Liu, 2006; Sharma & Gadde, 2005; Gadde et al., 2004; Ouyang, 1994). These new class of

simulations can be categorized as fully decoupled models in which only the fracture and proppant distribution is simulated, without paying attention to the reservoir-fracture interactions. Ouyang (1994) proposed an adaptive meshing technique for the hydraulic fracture simulation that was adopted in a later work by Rebeiro, (2013) for proppant injection simulations. Friehauf (2009), Liu (2006) and Gadde et al. (2004) used PKN fracture geometry and included some of the experimental works in the literature related to proppant transport in their numerical model.

Adachi (2007) in his proppant transport modeling assumed the incompressibility of the proppant and the slurry, which is an acceptable assumption, but further he assumed that the only mechanism to account for ‘‘slip’’ between the proppant and the carrying fluid is gravity-induced settling. This implies that, in the absence of gravity, the proppant and fluid move at the same velocity at any given point. He did not discuss the type of settling equation, if any, that he has used. In addition, he employed an analytical integral equation between width and pressure in his fracture simulator.

Another major work in this context is the work published by Barrie and Conway in 1994 and 1995. These two documents served as a validation to their commercial proppant simulator GOHFER. From the very basic theory they have published about GOHFER, it can be understood that they have corrected Stokes equation for the effect of concentration, but they did not correct it for wall and inertial effects and they have employed only one simple equation for this correction. They applied the same correlation to account for the unequal horizontal velocity of proppant and fluid. Barrie and Conway fracture simulator again uses an integral equation between width and pressure (integral of the displacement for the point load over the surface of the fracture). There are some simulations done with GOHFER (Al-quraishi et al., 1999, Shokir et al., 2007) and the same limitation exists in them.

Mobbs et al. (2001), Unwin et al. (1995) and Hammond (1995) published their simulations with the objective of investigating the effect of fluid flow profile on final proppant distribution. They considered homogeneous flow (in which proppant particles are uniformly distributed across the fracture width) and sheet flow (in which some unspecified, but rapid process has caused all proppant to migrate across the fracture width into a close-packed sheet at the fracture center). They assumed constant rectangular and elliptical PKN type fracture width. They also neglected the retardation phenomenon and did not modify the Stokes law.

Probably, the most complete works in proppant transport simulation are the ones published by Rebeiro (2013), Freihauf (2009), Liu (2006), and Gadde (2004). All these works were done at the University of Texas at Austin. Each work is a gradual improvement to the previous one. The main deficiency of these models is the analytical PKN fracture geometry assumption. Although Rebeiro (2013) did not use this assumption and employed an adaptive re-meshing technique to couple a fully 3D fracture model with the proppant transport model, yet the model was fully elastic. Assuming minor effects of formation plasticity, these models neglect the plastic deformations in the medium.

Du et al. (2011) from Schlumberger developed another totally different methodology to model the hydraulic fracturing network, and, subsequently, simulated a shale gas reservoir as a dual-porosity system. Microseismic (MS) responses were used to delineate stimulated reservoir volumes. Microseismic events and/or natural fracture intensity were utilized to estimate the initial intensity of this induced fracture network. They assumed a simplistic in-situ fracture network geometry (elliptical shape) with the average width coming from the PKN equation. From MS mapping data, they calibrated a parameter called fracture network intensity. They did not solve any PDE for proppant distribution estimation and the calculation was very approximate in their work.

Our proposed work incorporates a numerical fracture simulator and a proppant simulator, whereas most existing models utilize an analytical (e.g., PKN) fracture model. Our model is also linked to a reservoir and a geomechanics simulator for flow and stress analysis during the life of the wellbore. Moreover, we have done an extensive literature on the settling corrections and retardation factors and coded them in our simulator.

In all the numerical models proposed in the literature, the transport and placement of proppant within the fracture is usually modeled by representing the slurry as a two-component, interpenetrating continuum. This implies that the fluid flow equations (i.e., conservation of mass and conservation of momentum) are solved for the mixture, and not for each individual component. We will follow the same procedure and solve the mass balance equation of the proppant and slurry through the method of mixture models. However, we will improve the current proppant modeling by capturing much more phenomena than the current models. This of

course, requires an extensive literature review on the experimental works in this area which is the topic of Section 2.3.

2.2.3 Granular Kinetic Theory Models

The third class of proppant transport modeling in a fracture is based on the concepts of granular kinetic theory (Gidaspow, 1994) and was proposed by Eskin and Miller (2008). They considered steady-state flow of slurry in the fracture with flat faces without including leak-off effects on slurry dynamics. In this modelling, micro-level particle dynamics is taken into account. Due to the particle migration from zones of high shear rate at the fracture walls towards the center of the fracture where shear rates are lower, non-uniform solid concentration across the fracture width will characterize the slurry flow. Kinetic theory is using Maxwellian velocity distribution for particle fluctuations and assumes that particles move like ideal gas, i.e. do not interact with each other. The intensity of particle fluctuations is determined by a parameter called granular temperature.

Eskin and Miller (2008) were not the first who used kinetic theory for modelling particle transport, although they were the first who applied it for proppants. As an example, Nott and Brady (1994) or Leighton and Acrivos (1987), used the kinetic approach for modeling particle migration across a flat channel in a Newtonian slurry flow.

The model by Eskin and Miller (2008) is for steady state only and extending it to transient flows may make it computationally prohibitive for any practical use in a hydraulic fracturing coupled simulator. As the authors of the model pointed out, application of the granular kinetic theory, though mature for gas-solids flows, is still in its infancy for liquid-solids flows since the original kinetic theory was developed mainly for gas–particle flows.

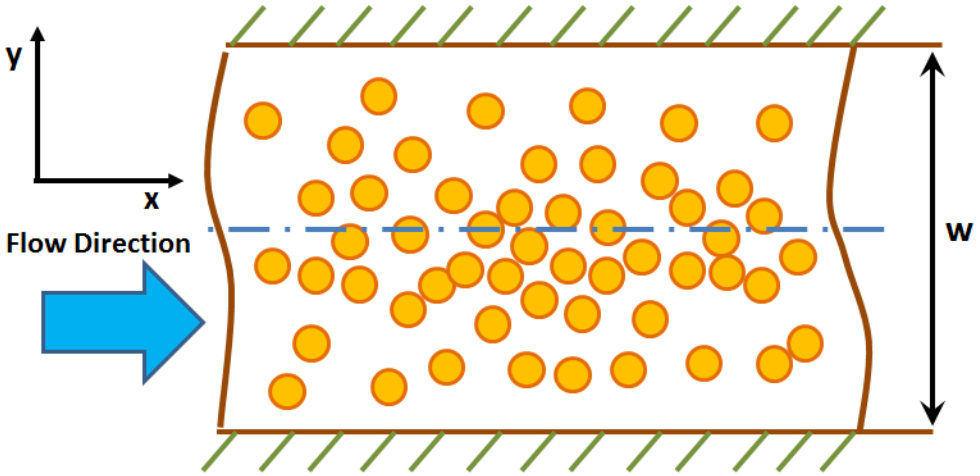

Figure 2.2: solid-liquid flow in fracture, yellow circles represent sand particles

In the model of Eskin and Miller (2008), many of the equations make use of empirical laws and correlations and are therefore valid only within certain ranges. Leak-off was neglected in the numerical computations (its introduction should be straightforward, if needed, though).

2.3 Experimental Works on Proppant Transport

In early experimental investigations of proppant transport, settling velocity and the size of proppant bed bank at the bottom of fracture was the focus of all the researches. Kern et al. (1959) studied sand movement through a simulated fracture in the laboratory. They concluded that if injection rate per foot of formation is very high, the proppant bed will not form at the bottom of a vertical fracture. Babcock et al. (1967) through their experiments identified the equilibrium velocity (velocity required to keep proppants suspended) and bank build-up constant as the two important parameters affecting propping agents' distribution. Clark et al. (1977) used a large vertical slot model with no fluid loss to evaluate the effect of fluid type and viscosity, proppant concentration and flow rate on proppant bed growth. Schols and Visser (1974) experimentally and theoretically explored the build-up of a proppant bank in a slot without leak off, using a low-viscosity fracturing fluid. They proposed three consecutive phases for the proppant bank build-up. During the first phase, bed build-up gradually occurs until an equilibrium height is reached near the wellbore after which the growth stops because of erosion. In the second phase, the bank grows only in height until it reaches an equilibrium height over its full length. Finally, in the third phase the proppants saltate toward the front of the bed, increasing its length in the direction of flow.

After 1980, many investigators turned their attention to convection flow and settling of the proppants, inertia, fracture wall and proppant concentration effects on settling.

Cleary and Fonseca (1992) concluded that most important consideration in uncontained vertical hydraulic fractures should be convection of heavier proppant-laden stages. They also mentioned that even in simple fluid treatments, convection dominates settling. Barree and Conway (1994) performed an experimental study of slurry transport in a large slot model in an attempt to develop a numerical simulator that captures particle settling and density driven flow. They observed vertical convective proppant velocities can be hundreds of time faster than single particle settling velocities. Al-quraishi and Christiansen (1999) investigated a wide variety of flow conditions using small glass models. In their observations, significant convection could occur even with small density differences. Clark and Zhu (1996) through a series of slot experiments developed a useful dimensionless group called Buoyancy number in predicting the importance of convection, for Newtonian and Non-Newtonian fluids.

Brannon et al. (2006) performed over 20 large-scale slot flow tests to investigate an extensive range of proppant transport parameters. Using the information obtained, an empirical proppant transport model was developed that could provide the length of propped fracture. They claimed their model could optimize effective fracture length and well performance by using the most favorable combination of slurry and proppant properties.

In actual field treatments, thousands of liters of slurry can be injected (Adachi et al., 2007), with a proppant mass concentration ranging from 2 to 3 lb/gal (0.24-0.36 kg/l) or proppant volume concentration of 0.1-0.15 (Novotny, 1977). This concentration may reach 11 lb/gal, i.e. a volume fraction of above 0.5 as the proppants move along the fracture.

The movement of carrier fluid and the forces of gravity acting on the proppant particles bring about the movement of proppant particles. As mentioned before, the topic of sediment transport has been studied in other areas beside the petroleum industry. Though different approaches have been implemented for studying sediment transport, basic aspects of sediment transport due to fluid movement remain the same and the results, without loss of generality can be applied to proppant transport in hydraulic fractures. The purpose of this section is providing a comprehensive literature on experimental works that has been performed on solid-fluid systems. In the next chapter, we describe how the correlations presented in this section can be included in

our numerical tool, so that more physical phenomena that happen during transport process can be captured. Including these physical parameters that govern proppant movement and settling in our numerical tool will lead to an improved understanding of proppant transport inside hydraulic fractures, improved simulations, and finally more efficient treatment designs.

2.3.1 Effect of Inertia on Proppant Settling

To calculate the hydrodynamic drag force exerted on a suspended solid particle in a fluid, a relationship between Reynolds number and a coefficient called drag coefficient is needed. The form of this relationship is different in different flow regimes. These flow regimes are distinguished by the value of particle Reynolds number and are called "Stokes" or "creeping flow" regime, "intermediate" regime and "Newtonian" regime. The expression of drag force in the intermediate and Newtonian flow regimes, unlike Stokes regime, does not have a satisfactory theoretical form and many different experimental relations have been proposed, some spanning only for a limited range of Reynolds number. In this section, we investigate the drag force expressions in different flow regimes as it is very important in calculating the proppant settling velocity. We don't intend to construct new formulas nor do we want to compare the performance of different proposed equations here, but only to provide a simple method of calculating the settling velocity over the whole Reynolds range.

Newton's second law governs the motion of immersed particles in fluids. Applying this law to an infinitesimal control volume of an incompressible Newtonian fluid (our focus) leads to Navier-Stokes equation. Exact analytical solution to Navier-Stokes equation is only possible under very restricted conditions or to the cases in which certain terms in the equation can be omitted or modified. More often, numerical techniques are necessary to obtain a solution to the problem at hand. The Navier-Stokes equation is expressed as:

$$\rho\left(\frac{\partial u}{\partial t} + u.\nabla u\right) = \rho g - \nabla p + \mu\nabla^2 u \tag{2.1}$$

where ρ is fluid density, μ is fluid viscosity, p is pressure and u is velocity. The terms on the left-hand side, arises from the product of mass and acceleration. The first term, which is a local derivative, represents changes at a fixed point in the fluid while the second term which is the convective term, accounts for changes due to the motion of the fluid. The first term on the right-

hand side is the gravity force acting on unit volume of the fluid and the final two terms represent the surface force on the element of the fluid (Bird et al., 1976; Schlichting, 1979).

The velocity and pressure fields are the unknowns of the Navier-Stokes equation. A solution can be obtained if the overall continuity equation is also considered. Application of the conservation of mass to an incompressible fluid leads to continuity equation:

$$\nabla . u = 0 \tag{2.2}$$

Solving these two equations are outside the scope of our research and therefore, we will not discuss more details such as boundary conditions and analytical or numerical techniques of the solution here.

2.3.1.1 Drag Force at Low Reynolds Numbers

As mentioned before, analytical solution to Eq. 2.1 and 2.2 can be obtained with certain assumptions. For example, in certain conditions, such as flow at high Reynolds number, viscosity terms in the equation will be negligible compared to inertia terms for which the idealized inviscid flow concept has been proposed. Another example would be boundary layer theory in which viscosity effects are neglected in large regions of the flow field and in these regions the fluid is treated as if it is inviscid. However, in very thin regions adjacent to the boundary, the effect of viscosity must be considered. Many simplifications can be made due to thinness of this layer.

Another important simplification which is more relevant to our research is known as the creeping flow approximation which applies at very low Reynolds number and velocities. In this case the convective term can be neglected from the Navier-Stokes equation. This means that fluid inertia is completely neglected (Clift et al., 1978). The creeping flow approximation has found wide application in flow through porous media. In this chapter, we discuss its application relevant to proppant transport.

In creeping flow regime, the Reynolds number is very low and the solution to Navier-Stokes equation for the drag force F_D on a sphere gives (Stokes, 1851, Batchelor, 1967):

$$F_D = 3\pi\mu d_p u \tag{2.3}$$

Drag coefficient is expressed in terms of resistance force per unit projected area in a plane perpendicular to the direction of motion, which, for a sphere, is always the area of a circle.

$$f = \frac{F_D}{(\pi d_p^2/_4)} = \frac{12\mu u}{d_p} \tag{2.4}$$

This equation can be written based on two dimensionless groups as:

$$\frac{f}{\rho u^2} = \frac{12\mu}{\rho d_p u} \tag{2.5}$$

It is noted that the Reynolds number appears on right-hand side of the equation and the left-hand side appears in the definition of dimensionless drag coefficient. That is:

$$C_D = \frac{f}{\frac{1}{2}\rho u^2} = \frac{24}{Re} \tag{2.6}$$

As mentioned earlier, the second equality is valid only in the Stokes region which is up to Re=0.2, when the error is about 4% (Clift et al., 1978).

In proppant transport application, what we are more interested in is the settling velocity of the proppants rather than the amount of drag force exerted on the particles. To convert the relationship between the drag coefficient and Reynolds number to a relation between the settling velocity and fluid parameters, another definition of drag coefficient is needed. As explained in Appendix A, the second expression of drag force which is valid for all the flow regimes is:

$$C_D = \frac{f}{\frac{1}{2}\rho u^2} = \frac{4}{3}\frac{d_p g(\rho_p - \rho_f)}{u_t^2 \rho_f} \tag{2.7}$$

Substituting Eq. 2.7 into Eq. 2.6, the corresponding terminal velocity in viscous regime would be (described in the next section):

$$u_t = \frac{g d_p^2(\rho_p - \rho_f)}{18\mu} \tag{2.8}$$

Obtaining the settling velocity from drag coefficient-Reynolds number relationship is not always this simple since most of the time we are dealing with highly non-linear C_D-Re equations. In Section 2.3.5, we will discuss this topic in detail and introduce another dimensionless variable that is more useful than C_D in proppant applications.

In obtaining this relationship between drag force and Reynolds number, the inertia terms in Navier-Stokes equation were neglected and only viscous terms were retained. There is a fundamental difficulty in this approach as first noted by Oseen (1910): this approximation is invalid at higher distances from the particle. The ratio of neglected inertia term to retained viscous term becomes high at higher distances from the particle which means for any Reynolds number, at higher distances, the neglected inertia terms dominate and the approximation is only valid for distances less than the order d_p/Re. To solve this problem, Oseen (1910) simplified the Navier Stokes equation rather than neglecting inertia terms and obtained a drag coefficient greater than Stokes law value which is applicable to Reynolds number up to 0.1. Oseen's modification is:

$$C_D = \frac{24}{Re}(1 + \frac{3}{16}Re) \tag{2.9}$$

To extend the applicability of Oseen's relationship to higher Reynolds number, several series solutions have been suggested to simplify Navier-Stokes equation that Oseen used, including one with 24 terms (Dyke, 1970). As another example, Goldstein (Goldstein, 1929) proposed an expression involving Reynolds numbers up to the power of 5:

$$C_D = \frac{24}{Re}(1 + \frac{3}{16}Re - \frac{19}{1280}Re^2 + \frac{71}{20408}Re^3 - \frac{30179}{34406400}Re^4 + \frac{122519}{550502400}Re^5) \tag{2.10}$$

Although the series solutions are accurate representatives to the Oseen's drag, the Oseen's drag itself is only an approximation to the exact drag value and all these solutions diverge rapidly from the experimental data at higher Reynolds numbers. Lewis and Carrier (1949) multiplied the final term in Oseen's equation by a parameter C_L which is a weak function of Reynolds, to improve the approximation and obtained a semi-empirical modification:

$$C_D = \frac{24}{Re}(1 + \frac{3}{16}C_L Re) \tag{2.11}$$

They proposed a value of 0.43 for C_L.

Proudman and Pearson (1957) suggested successive approximations to Navier-Stokes equation rather than obtaining accurate solutions to Oseen's equation. He defined a stream function using Stokes approximation near the sphere and Oseen's approximation away from the sphere:

$$C_D = \frac{24}{Re}(1 + \frac{3}{16}Re + \frac{9}{160}Re^2 \ln\frac{Re}{2} + O[Re^2]) \tag{2.12}$$

Chester and Breach (1969) improved the approximation by reducing the order of error:

$$C_D = \frac{24}{Re}(1 + \frac{3}{16}Re + \frac{9}{160}Re^2\left[\ln Re + \gamma + \frac{2}{3}\ln 2 - \frac{323}{360}\right] + \frac{27}{640}Re^3 \ln(\frac{Re}{2}) + O[Re^3]) \quad (2.13)$$

where γ is Euler's constant equal to 0.5772157.

Applying the same approach, Chester et al. (1969) proposed the following expression:

$$C_D = \frac{24}{Re}(1 + \frac{3}{16}\varepsilon + \frac{9}{160}\varepsilon^2\left[\ln \varepsilon + \gamma + \frac{2}{3}\ln 2 - \frac{548}{360} + \frac{5m}{8}\right] + \frac{27}{640}\varepsilon^3 \ln(\frac{\varepsilon}{2}) + O[\varepsilon^3]) \quad (2.14)$$

where:

$$\varepsilon = Re(\frac{C_D}{\frac{24}{Re}})^{-m} \quad (2.15)$$

Pruppacher et al. (1970) suggested a value of 5 for parameter m.

Liao (2002) also proposed an analytical solution to 10th order of approximation for the steady-state laminar viscous flow past a sphere in a uniform stream governed by the exact, fully non-linear Navier-Stokes equations which is applicable in a region of Re < 30 that is broader than the previous theoretical laws.

Figure 2.3 plots the proposed equations, except for Eq. 2.14 which is not explicit in drag coefficient and needs trial and error.

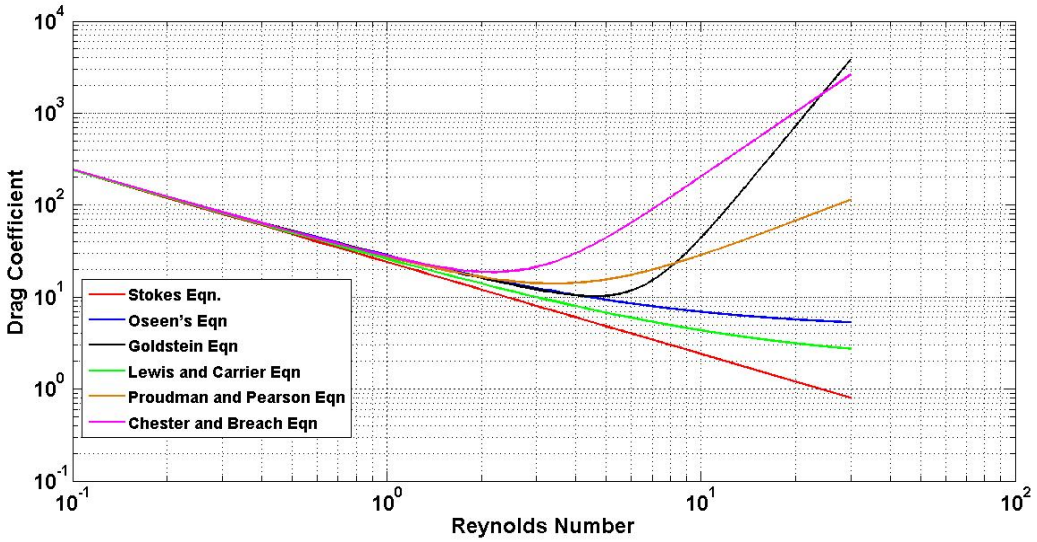

Figure 2.3: Comparing Proposed Equations of Drag Coefficient in Viscous Flow Regime

As it can be seen from Fig. 2.3, all these complex equations do not provide a huge improvement over Stokes equation. Also, they diverge very rapidly at higher Reynolds numbers. Thus, analytical solutions for flow around a spherical particle have little value at Re > 1. In this

situation, the flow field can be represented most accurately by numerical solution to Navier-Stokes equation, while empirical forms should be used for drag coefficient.

2.3.1.2 Drag at Intermediate High Reynolds Number

At high Reynolds numbers (Re > 1), no analytical solution exists for the flow of fluid past a sphere. At intermediate Reynolds number (1 < Re < 1000) for steady axisymmetric flow, numerical solutions provide more information than experiments. At unsteady state flow regime, numerical calculation of flow field is no longer feasible and experimental results possess more value (Clift et al., 1978).

Different forms of curve fitting for terminal falling velocities experimental data has been carried out (Lapple and Shepherd, 1940, Tanaka and linoya, 1970, Vlajinac and Covert, 1972). Based on experimental data of Allen (1900), Wieselsberger (1922), Prandtle and Tietjens (1931), and Schiller (1932), which have been corrected for the effect of walls, a log-log graph of drag coefficient versus Reynolds number has been well established (Fig. 2.4). This graph is called "standard drag curve" where C_D is plotted against Reynolds number.

As previously described, there are only three theoretical methods for the calculation of C_D: The Stokes law, the Oseen law, and the Goldstein law which are only applicable for limited ranges of Reynolds number and none of them can precisely agree with experimental data of Fig. 2.4. There are many empirical equations in the literature based on this graph that have varying complexity and contain many constants. Most of them are listed in Table 2.1. The emergence of all these empirical formulas is due to various attempts to obtain a better match for wider ranges of Reynolds number.

One of the most accurate expressions is the one proposed by Clift et al. (1978) in which they provided their correlations for 10 Reynolds subintervals.

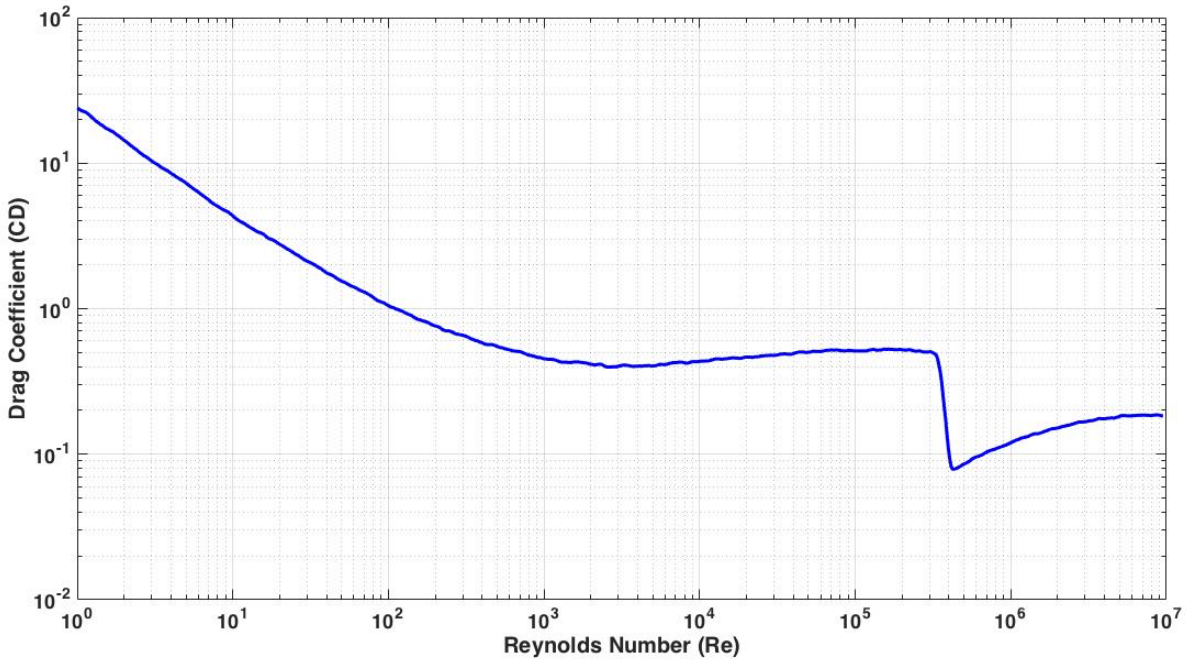

Figure 2.4: Standard Drag Curve

Although the improvement of high-performance computers has helped in further development of many complex empirical equations which are approaching experimental values, most of the empirical expressions, are based on the three abovementioned theoretical methods in Stokes region. For example, Flemmer and Banks (1986), Turton and Levenspiel (1986), Brown and Lawler (2003), and Cheng (2009) are based on Stokes law and Dou (1981) expression which is an addition type equation (explained below in this section) is based on Oseen's law. Despite the low Reynolds numbers for which the theoretical laws are applicable, empirical expressions for C_D should be based on these classical theoretical laws.

Table 2.1: Drag Coefficient as a Function of Reynolds Number

Researcher	Reynolds No. Range	Drag Coefficient
Allen (1900)	$\begin{cases} 2 < Re < 500 \\ 1 < Re < 1000 \end{cases}$	$\begin{cases} 10Re^{-0.5} \\ 30Re^{-0.625} \end{cases}$
Schiller and Naumann (1933)	$0.2 < Re < 500 - 1000$	$\frac{24}{Re}(1 + 0.15Re^{0.687})$
Wadell (1934)	$10^{-2} < Re < 10^5$	$(0.63 + \frac{4.8}{\sqrt{Re}})^2$
Rouse (1938)	$Re < 2 \times 10^5$	$\frac{24}{Re} + \frac{3}{\sqrt{Re}} + 0.34$
Dallavalle (1948)	$\begin{cases} 10^{-4} < Re < 2 \\ 2 < Re < 500 \\ 500 < Re < 10^5 \end{cases}$	$\begin{cases} \frac{24}{Re} \\ 0.4 + \frac{24}{Re} \\ 0.44 \end{cases}$
Langmuir and Blodgett (1948)	$1 < Re < 100$	$\frac{24}{Re}(1 + 0.197Re^{0.63} + 2.6 \times 10^{-4}Re^{1.38})$
Lappel (1951)	$0.2 < Re < 1000$	$\frac{24}{Re}(1 + 0.125Re^{0.72})$
Fair and Geyer (1954)	$Re < 10^4$	$\frac{24}{Re} + \frac{3}{\sqrt{Re}} + 0.34$
Gilbert et al. (1955)	$0.2 < Re < 2000$	$0.48 + \frac{28}{Re^{0.85}}$
Torobin et al. (1959)	$1 < Re < 100$	$\frac{24}{Re}(1 + 0.197Re^{0.63} + 0.0026Re^{1.38})$
Kurten et al. (1966)	$0.1 < Re < 4000$	$0.28 + \frac{6}{\sqrt{Re}} + \frac{21}{Re}$
Kurten et al. (1966)	$\begin{cases} Re < 10 \\ Re < 100 \\ Re < 10^5 \end{cases}$	$\begin{cases} 2 + \frac{24}{Re} \\ 1 + \frac{24}{Re} \\ 0.5 + \frac{24}{Re} \end{cases}$
Clift and Gauvin (1970)	$Re < 3 \times 10^5$	$\frac{24}{Re}(1 + 0.15Re^{0.687}) + \frac{0.42}{1 + 4.25 \times 10^4 Re^{-1.16}}$
Tanaka and Linoya (1970)	$\begin{cases} Re < 10 \\ Re < 100 \\ Re < 1000 \\ 1 < Re < 1000 \\ 10 < Re < 1000 \\ 10 < Re < 1000 \\ 10 < Re < 1000 \end{cases}$	$\log_{10} C_D = aw^2 + bw + c$ a: 0.07595304, 0.0930571, 0.1015314, 0.1118878, 0.1126893, 0.1132479, 0.1180904, 0.1 b: -0.8840749, -0.8850516, -0.8922549, -0.9263436, -0.9278250, -0.9112787, -0.9222214, -0.9 c: 1.421616, 1.414214, 1.408914, 1.427460, 1.426984, 1.401578, 1.399194, $\sqrt{2}$

Table 2.1: Continued

Researcher	Reynolds No. Range	Drag Coefficient
Abraham (1970)	$Re < 10^4$	$0.2924(1 + \frac{9.06}{\sqrt{Re}})^2$
Brauer and Mewes (1972)	$Re < 3 \times 10^5$	$0.4 + \frac{4}{\sqrt{Re}} + \frac{24}{Re}$
Ihme et al. (1972)	$Re < 10^4$	$0.36 + \frac{5.48}{Re^{0.573}} + \frac{24}{Re}$
Morsi and Alexander (1972)	$Re < 0.1$ $0.1 < Re < 1$ $1 < Re < 10$ $10 < Re < 10^2$ $10^2 < Re < 10^3$ $10^3 < Re < 5 \times 10^3$ $5 \times 10^3 < Re < 10^4$ $10^4 < Re < 5 \times 10^4$	$\frac{24}{Re}$ $\frac{22.73}{Re} + \frac{0.0903}{Re^2} + 3.69$ $\frac{29.1667}{Re} - \frac{3.8889}{Re^2} + 1.222$ $\frac{46.5}{Re} - \frac{116.67}{Re^2} + 0.6167$ $\frac{98.33}{Re} - \frac{2778}{Re^2} + 0.3644$ $\frac{148.62}{Re} - \frac{4.75 \times 10^4}{Re^2} + 0.357$ $-\frac{490.546}{Re} + \frac{57.87 \times 10^4}{Re^2} + 0.46$ $-\frac{1662.5}{Re} + \frac{5.4167 \times 10^6}{Re^2} + 5191$
Clift et al. (1978)	$Re < 0.01$ $0.01 < Re \leq 20$ $20 \leq Re \leq 260$ $260 \leq Re \leq 1500$ $1.5 \times 10^3 \leq Re \leq 1.2 \times 10^4$ $1.2 \times 10^4 < Re < 4.4 \times 10^4$ $4.4 \times 10^4 < Re \leq 3.38 \times 10^5$ $3.38 \times 10^5 < Re \leq 4 \times 10^5$ $4 \times 10^5 < Re \leq 10^6$ $10^6 < Re$	$C_D = \frac{3}{16} + \frac{24}{Re}$ $\log_{10}\left[\frac{C_D Re}{24} - 1\right] = -0.881 + 0.82w - 0.05w^2$ $\log_{10}\left[\frac{C_D Re}{24} - 1\right] = -0.7133 + 0.6305w$ $\log_{10} C_D = 1.6435 - 1.1242w + 0.1558w^2$ $\log_{10} C_D = -2.4571 + 2.5558w - 0.9295w^2 + 0.1049w^3$ $\log_{10} C_D = -1.9181 + 0.6370w - 0.0636w^2$ $\log_{10} C_D = -4.3390 + 1.5809w - 0.1546w^2$ $C_D = 29.78 - 5.3w$ $C_D = 0.1w - 0.49$ $C_D = 0.19 - 8 \times \frac{10^4}{Re}$
Concha and Almendra (1979)	$Re < 10^5$	$0.28(1 + \frac{9.06}{\sqrt{Re}})^2$

Table 2.1: Continued

Researcher	Reynolds No. Range	Drag Coefficient
Due (1981)	$Re < 2 \times 10^5$	$\frac{24}{Re}\left(1+\frac{3}{16}Re\right)cos^3\theta + 0.45sin^2\theta$ $\theta = \begin{cases} 0 & Re \le 0.5 \\ \frac{\ln 2Re}{\ln 5000}\frac{\pi}{2} & 0.5 \le Re \le 2500 \\ \frac{\pi}{2} & Re \ge 2500 \end{cases}$
Concha and Barrientos (1982)	$Re < 3 \times 10^5$	$C_D = 0.284153\left(1+\frac{9.04}{Re^{0.5}}\right)^2 \sum_{i=0}^{5} B_i Re^i$ $B_0 = 9.620833 \times 10^{-1}$ $B_1 = 2.736461 \times 10^{-5}$ $B_2 = -3.938611 \times 10^{-10}$ $B_3 = 2.476861 \times 10^{-15}$ $B_4 = -7.159345 \times 10^{-21}$ $B_5 = 7.437237 \times 10^{-27}$
Flemmer and Banks (1986)	$0.1 < Re < 10^5$	$\log_{10}(\frac{Re\ C_D}{24}) = 0.261Re^{0.369} - 0.105Re^{0.431} - \frac{0.124}{1+w^2}$
Turton and Levenspiel (1986)	$10^{-2} < Re < 2 \times 10^5$	$\frac{24}{Re}(1+0.173Re^{0.657}) + \frac{0.413}{1+16300Re^{-1.09}}$
Khan and Richardson (1987)	$0.01 < Re < 3 \times 10^5$	$(2.25Re^{-0.31} + 0.36Re^{0.06})^{3.45}$
Haider and Levenspiel (1989)	$Re < 2.6 \times 10^5$	$\frac{24}{Re}(1+0.1806Re^{0.6459}) + \frac{0.4251}{1+\frac{6880.95}{Re}})$
Swamee and Ojha (1991)	$Re < 1.5 \times 10^5$	$0.5\{16[\left(\frac{24}{Re}\right)^{1.6} + \left(\frac{130}{Re}\right)^{0.72}]^{2.5} + [(\frac{40000}{Re})^2 + 1]^{-0.25}\}^{0.25}$
Hesketh et al. (1991)	$0.1 < Re < 10^4$	$[0.352 + \sqrt{0.124 + \frac{24}{Re}}]^2$
Ceylan et al. (2001)	$0.1 < Re < 10^6$	$C_D = 1 - 0.5e^{0.182} + 10.11Re^{-2/3}e^{0.952Re^{0.25}} - 0.03859Re^{-4/3}e^{1.3Re^{0.5}} + 0.037 \times 10^{-4}Re \times e^{-0.125\times10^4 Re} - 0.116 \times 10^{-10}Re^2e^{-0.444\times10^5 Re}$
Brown and Lawler (2003)	$Re < 2 \times 10^5$	$\frac{24}{Re}(1+0.150Re^{0.681}) + \frac{0.407}{1+8710Re^{-1}}$ $\frac{24}{Re}(1+0.152Re^{0.677}) + \frac{0.417}{1+5070Re^{-0.940}}$ $(2.49Re^{-0.328} + 0.340Re^{0.0670})^{3.18}$ $\frac{24}{Re}10^{(0.383Re^{0.356} - 0.207Re^{0.396} - 0.143/1+(\log Re)^2)}$

Table 2.1: Continued

Researcher	Reynolds No. Range	Drag Coefficient
Almedeij (2008)	$Re < 10^6$	$[\frac{1}{(\varphi_1+\varphi_2)^{-1}+\varphi_3^{-1}}+\varphi_4]^{0.1}$ $\varphi_1 = (\frac{24}{Re})^{10} + (\frac{21}{Re^{0.67}})^{10} + (\frac{4}{Re^{0.33}})^{10} + (0.4)^{10}$ $\varphi_2 = \frac{1}{(0.148Re^{0.11})^{-10}+(0.5)^{-10}}$ $\varphi_3 = (1.57\times10^8 Re^{-1.625})^{10}$ $\varphi_4 = \frac{1}{(6\times10^{-17}Re^{2.63})^{-10}+(0.2)^{-10}}$
Cheng (2009)	$2\times10^{-3} < Re < 2\times10^5$	$\frac{24}{Re}(1+0.27Re^{0.43}) + 0.47[1-e^{-0.04Re^{0.38}}]$
Mikhailov and Freire (2013)	$Re < 118{,}300$	$\frac{3808[(^{1{,}617{,}933}/_{2030}) + (^{178{,}861}/_{1063})Re + (^{1219}/_{1084})Re^2]}{681Re[(^{77{,}531}/_{422}) + (^{13{,}529}/_{976})Re - (^{1}/_{71{,}154})Re^2]}$
Morrison (2013)	$Re < 10^6$	$\frac{24}{Re} + \frac{2.6(\frac{Re}{5})}{1+(\frac{Re}{5})^{1.52}} + \frac{0.411(\frac{Re}{263{,}000})^{-7.94}}{1+(\frac{Re}{263{,}000})^{-8.00}} + (\frac{Re^{0.8}}{461{,}000})$
Terfous et al. (2013)	$0.1 < Re < 5\times10^4$	$2.689 + \frac{21.683}{Re} + \frac{0.131}{Re^2} - \frac{10.616}{Re^{0.1}} + \frac{12.216}{Re^{0.2}}$
Where	$w = \log_{10} Re$	

One of the best classifications of the drag coefficient empirical equations has been suggested by Hongly (2015). He classified the equations based on the fact that they are either of multiplication type, the addition type or rational type. If for example, the Stokes law is multiplied by a power function or exponential function, the multiplication equations are obtained while if the same law is added by a growing function, the addition formulas are obtained.

The multiplication equations based on analytical laws can be expressed as:

$$C_D = \frac{24}{Re} f_1(Re), \text{ Stokes Law} \tag{2.16}$$

$$C_D = \frac{24}{Re}\left(1+\frac{3}{16}Re\right) f_1(Re), \text{ Oseen's Law} \tag{2.17}$$

And the addition equations based on analytical laws can be expressed as:

$$C_D = \frac{24}{Re} f_2(Re) + f_3(Re), \text{ Stokes Law} \tag{2.18}$$

$$C_D = \frac{24}{Re}(1+\frac{3}{16}Re) f_2(Re) + f_3(Re), \text{ Oseen's Law} \tag{2.19}$$

where $f_1(Re)$, $f_2(Re)$ and $f_3(Re)$ are empirical expressions. Table 2.2 summarizes Hongly's (2015) equations. The applicable range of Reynolds number for all the equations is $Re < 2\times10^5$.

Table 2.2: Hongly's (2015) Expressions for Drag Coefficient

Type	Correlation	Law
Multiplication	$C_D = \frac{24}{Re}(100Re)^{\phi}$ $\phi = 0.3492\chi + 0.8736\chi^7 - 1.3123\chi^8 + 0.4998\chi^9$	Stokes
Multiplication	$C_D = \frac{24}{Re}(1 + 0.201Re)^{\phi}$ $\phi = 0.6983 - 1.0552\chi + 1.3822\chi^2 - 0.3129\chi^4$	Stokes
Multiplication	$C_D = \frac{24}{Re}(1 + \frac{3}{16}Re)(\frac{Re}{10^7})^{\phi}$ $\phi = 0.0486\chi + 2.4265\chi^3 - 3.6319\chi^4 + 1.5393\chi^5$	Oseen
Multiplication	$C_D = \frac{24}{Re}(1 + \frac{3}{16}Re)(1 + 0.0725Re)^{\phi}$ $\phi = -0.966 + 0.3656\chi + 0.4747\chi^2 - 0.1923\chi^4$	Oseen
Addition	$C_D = \frac{24}{Re} + 2.462e^{\phi}$ $\phi = 0.2638 - 2.0658\chi + 2.5562\chi^2 - 0.9286\chi^3$	Stokes
Addition	$C_D = \frac{24}{Re}(1 + 0.2949Re)^{0.4133} + 0.4722(1 - \exp(-\beta))$ $\beta = 0.0437Re^{0.3707}$	Stokes
Addition	$C_D = \frac{24}{Re}(1 + 0.3628Re)^{0.3603} + 0.4578(1 - \exp(-\beta))$ $\beta = 1.1802\chi + 1.0587\chi^{10}$	Stokes
Addition	$C_D = \frac{24}{Re}\frac{(1 + {}^3/_{16}Re)^{0.3603}}{(1 + 0.1063Re)^{0.6919}} + 0.4623(1 - \exp(-\beta))$ $\beta = 1.3283\chi + 0.9352\chi^{10}$	Oseen
Addition	$C_D = \frac{24}{Re}(1 + \frac{3}{16}Re)^{0.635}cos^3\alpha + 0.468sin^2\alpha$ $\alpha = (1 - e^{-3.24\chi^2 + 8\chi^4 - 6.5\chi^5})\frac{\pi}{2}$	Oseen
where	$\chi = \ln\frac{1+Re}{10}$	

Hongly (2015) also provided rational type expressions based on Goldstein law, but the topic is out of the scope of this research and for brevity, we don't describe rational type expressions here.

2.3.1.3 Terminal Velocity of Single Particle in Infinite Medium

In proppant transport simulations, the drag exerted on the particles is not as important as the terminal velocity of the particles. As we will discuss the transport partial differential equations, we will see that terminal velocity is the parameter that appears in the equations and not the drag force. On the other hand, all the expressions proposed in the fluidized bed expansion studies give a relationship between the Reynolds number and drag coefficient (e.g. Clift et al., 1978; Liao, 2002; Hongly et al., 2015). The calculation of settling velocity from Re-CD relationship is

always not an easy task because the drag coefficient (CD) is not a constant over a wide range of Reynolds number (Re) and there is no definite formula for the calculation of CD.

In this section, we use a simple method to express these expressions in terms of terminal velocity.

At very low Reynolds numbers (Re<0.1), as stated earlier:

$$C_D = \frac{24}{Re} \tag{2.20}$$

and

$$C_D = \frac{4}{3}\frac{d_p g(\rho_p - \rho_f)}{u_t^2 \rho_f} \tag{2.21}$$

After substitution:

$$u_t = \frac{g d_p^2(\rho_p - \rho_f)}{18\mu} \tag{2.22}$$

Also, for 750 <Re <3.5×10^5 C_D is constant and equal to 0.445 (Clift et al. 1978). Therefore, with the same approach, terminal velocity in this range will be:

$$u_t = 1.73[\frac{g d_p(\rho_p - \rho_f)}{\rho_f}]^{\frac{1}{2}} \tag{2.23}$$

Outside these ranges of Re, in intermediate regime, or even when more accurate predictions are required, the relationships between Reynolds number and drag coefficient are inconvenient in giving explicit expressions of terminal velocity, since in both dimensionless numbers terminal velocity is involved and an iterative procedure is needed. However, the terminal velocity can be omitted by defining another dimensionless parameter:

$$Ga = \frac{3}{4} C_D Re^2 = \frac{d_p^3 g \rho_f(\rho_p - \rho_f)}{\mu^2} \tag{2.24}$$

where Ga is Galileo Number (Clift et al., 1978). It can be seen that Galileo number is independent of terminal velocity and can be evaluated from physical properties of the proppant and carrying fluid. Therefore, for proppant transport simulations, it is more satisfactory to express Galileo number rather than drag coefficient as a function of Reynolds number. In this case:

$$Re = f(Ga) \tag{2.25}$$

or

$$u_t = \frac{\mu}{\rho d_p} f(Ga) \tag{2.26}$$

In Table 2.3, we mentioned the empirical equations which were proposed in terms of Galileo number and Reynolds number. Most of the researchers did not provide such a relationship and most of the time, obtaining this form of the equations becomes very complex and impractical to use.

Table: 2.3: Reynolds Number as a Function of Galileo Number

Researcher	Reynolds No. Range	Expression
Allen (1900)	$\begin{cases} 2 < Re < 500 \\ 1 < Re < 1000 \end{cases}$	$Re = (\frac{2}{15} Ga)^{\frac{2}{3}}$ $Re = (\frac{2}{45} Ga)^{\frac{8}{11}}$
Oseen (1910)	$Re < 0.1$	$C_D = \frac{432}{Ga}(0.5 + 0.5\sqrt{1 + \frac{Ga}{24}})^2$
Dallavalle (1948)	$\begin{cases} 10^{-4} < Re < 2 \\ 2 < Re < 500 \\ 500 < Re < 10^5 \end{cases}$	$Re = \frac{Ga}{18}$ $Re = \frac{5}{2}(\frac{8Ga}{15} + 144)^{0.5} - 30$ $Re = \frac{10}{33}(33Ga)^{0.5}$
McGauhey (1956)	$Re < 0.1$	$Re = \frac{Ga^{7/3}}{18 + 0.17\sqrt{18Ga}}$
Al-Salim and Geldart (1969)	$0.1 < Re < 1000$	$\frac{576}{Re^2} = \frac{3.318 \times 10^5}{(N_D)^2} + \frac{2.954 \times 10^4}{(N_D)^{1.5928}} + \{\frac{9.479 \times 10^{11}}{(N_D)^{4.1949}} + \frac{8.440 \times 10^{10}}{(N_D)^{3.7877}}\}^{0.313}$
Turian et al. (1971)	$Re < 10^5$	$\log_{10} Re = -1.38 + 1.94N_D - 8.6 \times 10^{-2} N_D^2 - 2.52 \times 10^{-4} N_D^3 + 9.19 N_D^4 + 5.35 \times 10^{-4} N_D^5$
Fouda and Capes (1976)	$10^{-2} < Re < 10^5$	$y = \sum_{i=0}^{5} a_i x^i$ $y = \log_{10}(N_D)^{\frac{1}{3}}$ $\quad$ $y = \log_{10}(N_D)^{\frac{1}{3}}$ $x = \log_{10}(K_D)^{-\frac{1}{3}}$ $\quad$ $x = \log_{10}(N_D)^{\frac{1}{3}}$ $a_0 = -1.37323$ $\quad$ $a_0 = 0.785724$ $a_1 = 2.06962$ $\quad$ $a_1 = 0.684342$ $a_2 = -0.453219$ $\quad$ $a_2 = 0.168457$ $a_3 = -0.0334612$ $\quad$ $a_3 = 0.103834$ $a_4 = -0.00745901$ $\quad$ $a_4 = 0.20901 \times 10^{-1}$ $a_5 = 0.00249580$ $\quad$ $a_5 = 0.57664 \times 10^{-2}$

Table: 2.3: Continued

Researcher	Reynolds No. Range	Expression
Clift et al. (1978)	$\begin{cases} N_D \le 73;\ Re \le 2.37 \\ 73 \le N_D \le 580; 2.37 \le Re \le 12.2 \\ 580 \le N_D \le 1.55 \times 10^7; \\ 12.2 \le Re \le 6.35 \times 10^3 \\ 1.55 \times 10^7 \le N_D \le 5 \times 10^{10}; \\ 6.35 \times 10^3 \le Re \le 3 \times 10^5 \end{cases}$	$\begin{cases} Re = N_D 24 - 1.7569 \times 10^{-4} N_D^2 + 6.9252 \times 10^{-7} N_D^3 \\ -2.3027 \times 10^{-10} N_D^4 \\ \log_{10} Re = -1.7095 + 1.33438W - \\ 0.11591W^2 \\ \log_{10} Re = -1.81391 + 1.34671W - \\ 0.12427W^2 + 0.006344W^3 \\ \log_{10} Re = 5.33283 - 1.21728W + 0.19007W^2 - \\ 0.007005W^3 \end{cases}$ $W = \log_{10} N_D$
Concha and Almendra (1979)	$Re < 10^5$	$K_D = [\frac{22.58}{(N_D)^{1/3}}[\sqrt{1 + 0.0921\sqrt{N_D} - 1}]^2]^{-3}$
Zigrang and Sylvester (1981)	$Re < 10^5$	$Re = [\sqrt{14.51 + 1.83\sqrt{Ga}} - 3.81]^2$
Slot (1984)	$Re < 2000$	$Re = [\frac{C_D}{24} - 0.0125 - 0.348(\frac{\pi}{8}N_D)^{-1/3}]^{-1}$
Turton and Clark (1987)	$Re < 2 \times 10^5$	$Re = Ga^{1/3}[\left(\frac{18}{Ga^{2/3}}\right)^{0.824} + (\frac{0.321}{Ga^{1/3}})^{0.412}]^{-1.214}$
Khan and Richardson (1987)	$10^{-1} < Ga < 10^{10}$ $Re < 3 \times 10^5$	$Re = [2.33Ga^{0.018} - 1.53Ga^{-0.016}]^{13.3}$
Brown and Lawler (2003)	$Re < 10^5$ $Re < 3 \times 10^5$ $Re < 2 \times 10^5$ $Re < 2 \times 10^5$ $Re < 5 \times 10^3$	$Re = [\sqrt{14.82 + 1.92\sqrt{Ga}} - 3.85]^2$ $Re = [2.63Ga^{0.0159} - 1.82Ga^{-0.0117}]^{13.6}$ $Re = Ga^{1/3}[\left(\frac{18}{Ga^{2/3}}\right)^{0.901} + (\frac{0.330}{Ga^{1/3}})^{0.440}]^{-1.110}$ $Re = Ga^{1/3}[\left(\frac{18}{Ga^{2/3}}\right)^{\left[0.936Ga^{1/3}+1\right/_{Ga^{1/3}+1}]^{0.898}} + (\frac{0.317}{Ga^{1/3}})^{0.449}]^{-1.114}$ $Re = \frac{Ga(22.5 + Ga^{0.682})}{0.0258Ga^{1.349} + 2.81Ga^{1.015} + 18Ga^{0.682} + 405}$

Table: 2.3: Continued

Researcher	Reynolds No. Range	Expression
Almedeij (2007)	$Re < 10^6$	$Ga^{\frac{1}{3}} \times [\frac{1}{\left(\frac{1}{{\varphi_1}^{-1} + {\varphi_2}^{-1}} + \varphi_3\right)^{-1} + \varphi_4^{-1}}]^{0.1}$ $\varphi_1 = \frac{1}{(0.055Ga^{2/3})^{-10} + (0.126Ga^{1.256/3})^{-10} + (0.518Ga^{0.8/3})^{-10} + (1.826Ga^{0.5/3})^{-10}}$ $\varphi_2 = (2.834Ga^{0.422/3})^{10} + (1.633Ga^{0.5/3})^{10}$ $\varphi_3 = (3 \times 10^{-22} Ga^{7/3})^{10}$ $\varphi_4 = (3393Ga^{-0.352/3})^{10} + (2.582Ga^{0.5/3})^{10}$
Cheng (2009)	$2 \times 10^{-3} < Re < 2 \times 10^5$	$C_D = \frac{432}{Ga}(1 + 0.022Ga)^{054} + 047[1 - \exp(-0.15Ga^{0.15})]$
Hongli (2015)	$Re < 2 \times 10^5$	$C_D = \frac{432}{Ga}\left(0.5 + 0.5\sqrt{1 + \frac{Ga}{24}}\right)^{1.554} cos^3\alpha + 0468sin^2\alpha$ $\alpha = (1 - e^{-6.7\chi^2 + 39\chi^5 - 75\chi^7})\frac{\pi}{2}$ $\chi = \ln(1 + Ga^{\frac{1}{3}})/10$
Where:	$N_D = C_D Re^2 = \frac{4d_p^3 g\rho_f(\rho_p - \rho_f)}{3\mu^2} = \frac{4}{3}Ga$	
and	$K_D = \frac{3}{4}\frac{C_D}{Re} = \frac{g\mu(\rho_p - \rho_f)}{\rho_f^2 u_t^3}$	

As it can be seen from Table 2.3, the expressions that relate Galileo number to Reynolds number are very complex. Instead of using these relationships in our numerical code, we plotted Reynolds number as a function of Galileo number, from data in Fig. 2.4. Using this graph will be more accurate than fitting a complex equation that always contains some degree of errors.

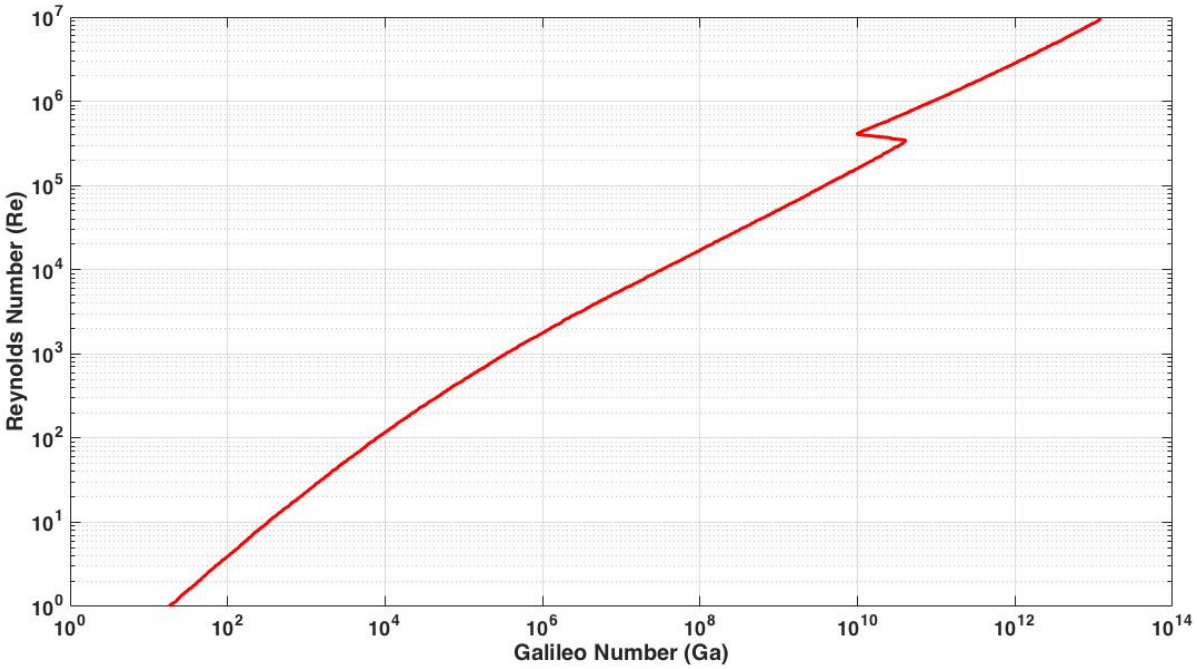

Figure 2.5: Reynolds Number vs Galileo Number

2.3.2 Effect of Fracture Walls on Proppant Settling

It is well stablished that when a particle is settling in a liquid, the confining walls around the system produce retardation effect on the particle. In other words, terminal settling velocity of proppants is known to be lower in a confined liquid compared to the case that no walls are present under identical conditions. This retardation of the motion of particles in confined medium is due to the backflow of the fluid caused by a falling sphere through the annular region between the sphere and the wall and the corresponding increase in the drag force acting on sphere. The smaller the available space for fluid counter flux compared to the particle size, the more important the phenomenon. Furthermore, the walls also change the onset of flow separation and subsequently the boundaries between flow regimes. Regarding analytical solutions, the confining walls change the boundary conditions of the equations of motion and continuity of the continuous phase and the condition of uniform flow far from the particles does not exist as in infinite mediums. The obvious outcome of these boundary conditions is changes in the exerted drag force on the particles and the reduction in the settling velocity of proppants. In our study, we will only consider the simplest case of a sphere settling on the axis of a long cylindrical tube. There are little studies on the other geometrical shapes like parallel plates (Staben, 2003) or in

triangular and square cylinders (Miyamura et al., 1981), which for the completeness of our discussion, we will review them very quickly, but not as detailed.

The severity of the wall effect is dependent on the size and the shape of the confining walls. The location of the sphere, i.e., whether the sphere is falling on the axis of the cylindrical tube, also influences the severity of the wall effect. In this work, however, we mostly consider the prediction of the wall effect for a sphere falling through a long tube, which is the topic of most of the investigations in the literature. This effect has been studied both theoretically and experimentally for many years. Knowledge of this retardation effect is necessary in calculating the net hydrodynamic drag and in turn the settling velocity of the falling particles in bounded media. Some researchers considered settling of a single sphere in Newtonian fluids (Miyamura et al., 1981; Machac and Lecjaks, 1995; Balaramakrishna and Chhabra, 1992), some focused on the settling of the non-spherical particles (Chhabra, 1995) and some concentrated on non-Newtonian Fluids (Lali et al., 1989; Venu Madhav and Chhabra, 1994; Chhabra, 1996; Ataide et al., 1999; Chhabra and Uhlherr, 1980; Song et al., 2009).

In this section, we only consider settling of a spherical particle in a Newtonian, incompressible fluid. There are different useful ways to quantify the retardation effects of the walls. As the drag force ratio, based on the same particle properties at the same fluid velocity (Latto et al., 1973; Duduković, and Končar-Djurdjević, 1981; Iwaoka and Ishii, 1979):

$$f_F = \frac{\text{drag in bounded fluid}}{\text{drag in infinite fluid}} = \frac{F_{D\infty}}{F_D} \tag{2.27}$$

as the velocity ratio based on constant particle dimensions,

$$f_u = \frac{\text{terminal velocity in bounded fluid}}{\text{terminal velocity in infinite fluid}} = \frac{u_t}{u_{t\infty}} \tag{2.28}$$

or as the viscosity ratio (Clift et al., 1978),

$$f_\mu = \frac{\mu}{\mu_s} \tag{2.29}$$

Where μ is the actual fluid viscosity and μ_s is the viscosity of the unbounded fluid which would give the observed Stokes velocity:

$$\mu_s = \frac{d^2 g(\rho_p - \rho_f)}{18 u_{Stokes}} \tag{2.30}$$

It should be noted in some literature the inverse of Eqs. 2.27 to 2.29 is considered as the wall factor.

In creeping flow regime, all the three ratios are equal but at higher Reynolds numbers, the relationships become complex.

The simplest and most relevant to proppant transport way of describing wall effect is by defining the wall factor as a velocity ratio:

$$f_w = \frac{u_w}{u_\infty} \tag{2.31}$$

where u_w and u_∞ are the settling velocity of the sphere with and without the presence of the walls. Dimensional analysis suggests that if the container is long enough for the end effects to be negligible (which is the case for hydraulic fractures) the wall factor, f_w, will be a function of only Reynolds number and the ratio of the diameters of the spheres and container, λ:

$$f_w = f(\lambda, Re), \qquad \lambda = \frac{d_p}{D_c} \tag{2.32}$$

where D_c is the container diameter (or the width of hydraulic fracture) and d_p is the diameter of proppant. Two boundary conditions must be satisfied for any meaningful wall factor. For $\lambda = 0$ the settling velocity should become the settling velocity in infinite medium and for $\lambda = 1$ the value of settling velocity must become zero.

Except for the creeping flow regime, little analytical work has been reported on the motion of contained fluids past the rigid spheres. However, according to the considerable experimental literature (Clift et al., 1978; Di Felice, 1996; Chhabra et al., 2003), it is now well known that the wall factor does not depend on the Reynolds number at very low and very high values of the Reynolds number. However, in the intermediate regime, the wall factor is a function of both λ and Reynolds number. It should be noted that the value of Reynolds number marking the transition between viscous to intermediate and then from intermediate to Newton flow regime is different for confined and unconfined mediums. In the presence of walls the Reynolds number boundaries for flow regimes is a function of λ. Different methods have been proposed in the literature on how to distinguish these boundaries. As an example, Clift et al. (1978) noticed the walls increase the point of transition between the regimes. Coutanceau (1972) based on visualization of the flow around a sphere moving along the axis of a tube containing a stationary

fluid, noticed a delay in the formation of the attached recirculatory wake, and the onset of separation (start of intermediate region) was given by:

$$Re_s = 20(1-\lambda)^{-0.56} \tag{2.33}$$

Using the detectable departure from front and rear symmetry of streamlines around the sphere, he defined the following expression for finding the upper limit of Stokes flow:

$$Re_w = \left(\frac{Re}{7}\right) - 2.75, \qquad \lambda \leq 0.8 \tag{2.34}$$

Table 2.4 summarizes some of the best-known correlations of the wall factor with their range of applicability. The purpose is not to compare the accuracy of many proposed correlations in the literature, but to provide a way of including this phenomenon in the numerical work.

Chhabra et al. (2003) by reviewing many experimental data on wall effects for a sphere falling in incompressible Newtonian media in cylindrical tubes, recommended the use of Haberman and Sayre equation (1958) in the viscous regime, and the Newton equation (1678) for the turbulent regime. According to their work, the Di Felice equation (1996) correlates most of the literature data in the transition regime with an overall minimum error of about 12.5%. However, deviations increase steeply with increasing values of λ and/or the Reynolds number. They also suggested that for λ >0.88 only limited data is available and any expression in this condition should be used with extreme caution.

During most of the experiments, researchers ignored data when the particles showed zigzag or spiral movement and rotation. Only runs in which the particle moves approximately along a straight line without rotation in the tube axis according to visual observations were considered in the analysis.

Table 2.4: Correlations for the wall factor

Author	Wall Factor	Note
Newton (1687)	$f = (1-\lambda^2)(1-0.5\lambda^2)^{0.5}$	Turbulent Regime, $0 \le \lambda \le 1$
Munroe (1889)	$f = 1-\lambda^{1.5}$	Turbulent Regime, $0.11 \le \lambda \le 0.83, 943 \le Re_{t\infty} \le 11000$
Ladenburg (1907)	$f = \frac{1}{1+2.105\lambda}$	Viscous Regime
Faxen (1923)	$f = \frac{1}{1+2.1\lambda}$	$\lambda \le 0.1$
Faxen (1923)	$f = (1-2.1044\lambda+2.089\lambda^3-0.948\lambda^5)$	Viscous Regime $\lambda \le 0.3$
Lunnon (1928)	$f = 1-0.23\lambda$	Viscous Regime $\lambda \le 0.1$
Suga (1931)	$f = (1-\lambda)^{2.1/(1-\lambda^2)}$	$\lambda \le 0.371$
Francis (1933)	$f = (\frac{1-\lambda}{1-0.475\lambda})^4$	Viscous Regime $Re_{t\infty} \le 0.2$
Lee (1948)	$f = \frac{1-\frac{9}{4}\lambda+\frac{5}{2}\lambda^3-\frac{9}{4}\lambda^5+\lambda^6}{1-\frac{1}{4}\lambda}$ $f = \frac{1}{1+\frac{9}{4}\lambda+(\frac{9}{4}\lambda)^2}$ $f = \frac{(1-\lambda)^{2.5}}{(3\sqrt{2}\frac{\pi}{8})}$	$\lambda \le 0.3$ $\lambda \le 0.3$ $0.7 \le \lambda \le 1$
Mott (1951)	$f = \sqrt{\frac{1}{1+A\lambda^2}} \quad 1.8 \le A \le 3.2$ $f = \sqrt{\frac{1}{1+16\lambda^4}}$	$0.2 \le \lambda \le 0.5$ $0.5 \le \lambda \le 0.7$
Happle and Byrne (1954)	$f = 1-2.105\lambda+2.087\lambda^3$	$\lambda \le 0.3$
Haberman and Sayre (1958)	$f = \frac{1-2.105\lambda+2.0865\lambda^3-1.7068\lambda^5+0.72603\lambda^6}{1-0.75857\lambda^5}$	Viscous Regime, $\lambda \le 0.8$
Bohlin (1960)	$f = 1-2.10443\lambda+2.08877\lambda^3-6.94813\lambda^5-1.372\lambda^6+3.87\lambda^8-4.19\lambda^{10}$	$\lambda \le 0.3$
Fidleris and Whitmore (1961)	Graphical Method	All Regimes $0.05 \le Re_{t\infty} \le 2\times10^4$
Happel and Brenner (1965)	$f = 1-2.1044\lambda+2.089\lambda^3-0.948\lambda^5$	Viscous Regime
Achenbach (1974)	$f = \frac{(1-\lambda^2)^2}{1+1.45\lambda^{4.5}}$	Turbulent Regime, $\lambda \le 0.92, Re_{t\infty} \le 10^5$
Happel and Bart (1974)	$f = 1-1.9033\lambda+3.623\lambda^2$	Viscous Regime $\lambda \le 0.1$
Garside (1977)	$f = \frac{1}{(1+2.35\lambda)}$	Viscous Regime

Table 2.4: Continued

Author	Wall Factor	Note
Clift et al. (1978)	$f = (1 - 1.6\lambda^{1.6})$	$\lambda \leq 0.06, 10^2 \leq Re_{t\infty} \leq 10^4$
Iwaoka and Ishi (1979)	$f = 1.000000 + 1.137853\lambda - 0.2644559 \times 10^{-2}\lambda^2 + 0.8474067 \times 10^2\lambda^3 + 0.1128310 \times 10^3\lambda^4 - 0.1003350 \times 10^4\lambda^5 + 0.1252298 \times 10^4\lambda^6 + 0.1922832 \times 10^4\lambda^7 - 0.6372137 \times 10^4\lambda^8 + 0.5989260 \times 10^4\lambda^9 - 0.1967150 \times 10^4\lambda^{10}$	$0 \leq \lambda \leq 1$
Khan and Richardson (1989)	$f = 1 - 1.15\lambda^{0.6}$	$0.001 \leq \lambda \leq 0.2,\ 0.01 \leq Re_{t\infty} \leq 7000$
Almeida (1995)	$f = \frac{10}{1 + ARe^B}$ $A = 8.91e^{2.79\lambda}$ $B = 1.17 \times 10^{-3} - 0.281\lambda$	
Di Felice (1996)	$f = (\frac{1-\lambda}{1-0.33\lambda})^{2.7}$	Viscous Regime
Di Felice (1996)	$f = (\frac{1-\lambda}{1-0.33\lambda})^{\alpha}$ $\frac{3.3-\alpha}{\alpha-0.85} = 0.1Re_{t\infty}$	Intermediate and Turbulent Regime, $0.08 \leq \lambda \leq 0.7, Re_{t\infty} \leq 200$
Di Felice (1996)	$f = (\frac{1-\lambda}{1-0.33\lambda})^{0.85}$	Turbulent Regime
Wham et al. (1996)	$f = \frac{1 + 0.03708(0.5Re_\infty)^A}{C[1 + 0.03708(0.5fRe_\infty)^B]}$ $A = 1.5844 - 0.1016\ln(Re_\infty)$ $B = 1.5844 - 0.1016\ln(fRe_\infty)$ $C = \frac{1 - 0.75857\lambda^5}{1 - K\lambda + 2.0865\lambda^3 - 1.7068\lambda^5 + 0.72603\lambda^6}$ $K = 0.6628 + 1.458\exp(-0.028175fRe_\infty)$	Intermediate Regime, $0.08 \leq \lambda \leq 0.7, Re_{t\infty} \leq 200$
Ataide et al. (1999)	$f = \frac{1.0920}{1 + ARe^B}$ $A = 0.1e^{8.541\lambda}$ $B = -0.042 - 0.939\lambda$	$0 \leq \lambda \leq 0.61$ $0.38 \leq Re \leq 310.7$
Kehlenbeck and Di Felice (1999)	$f = \frac{1-\lambda^p}{1 + (\frac{\lambda}{\lambda_0})^p}$ $\frac{\lambda_0 - 0.283}{1.2 - \lambda_0} = 0.041{Re_{t\infty}}^{0.524}$ $p = 1.44 + 0.5466{Re_{t\infty}}^{0.434},\ Re_{t\infty} < 35$ $p = 2.3 + 37.3{Re_{t\infty}}^{-0.8686},\ Re_{t\infty} > 35$	Intermediate Regime $\lambda \leq 0.85$
Arsenijević et al. (2010)	$f = (1 - 1.12\lambda^{1.26})^{0.7}$	$0.0032 \leq \lambda \leq 0.873, 53 \leq Re_{t\infty} \leq 15100$

Haberman and Sayre (1958) theoretical expression has gained a wide acceptance in the literature and it was initially thought to be applicable up to λ=0.8. However, subsequent numerical studies

(Paine et al., 1975; Bowen and Sharif, 1994; Higdon and Muldowney, 1995) extended its applicability to λ =0.9.

Extensive comparisons between the data of circular and square cross-section fall containers have clearly shown that the Newton expression is the most reliable at high Reynolds number. Although there is no detail about its range of applicability, it is usually assumed to be applicable over the complete range, namely $0 < \lambda < 1$. Newton's expression (1678) applies to more general cases other than a cylindrical tube as well. His original expression is:

$$f = \left(\frac{A - \frac{\pi d^2}{4}}{A}\right)\left(\frac{A - \frac{\pi d^2}{8}}{A}\right)^{0.5} \tag{2.35}$$

where A is the cross section of the container. The prediction of Munroe's equation (1889) and Newton's equation (1687) differ only marginally.

Obviously, the Wham et al. (1996) equation is implicit in terms of f and an iterative procedure is needed to obtain f from known λ and Reynolds number. Also, this equation reduces to Haberman and Sayre (1958) expression as the Reynolds number is reduced.

As for inertial effects, analytic solutions have not been extended beyond the creeping flow range. For example, Faxen (1923) using Oseen's linearization made predictions for drag force exerted on a sphere moving axially in a tube which were not reliable in higher Reynolds number situations (Fidleris and Whitmore, 1961; Happel and Brenner, 1973; Sutterby, 1973). However, there are considerable experimental results which are in remarkably good agreement for freely settling spheres (McNown et al., 1948; Fidleris and Whitmore, 1961; Sutterby 1973) and spheres fixed in a fluid flow (McNown et al., 1948; Achenbach, 1974).

Miyamura et al. (1981) performed experiments on the wall correction factor in various geometries other than cylinders and proposed a 19th order equation as:

$$f = R_0 + \sum_{i=1}^{19} R_i \lambda^i \tag{2.36}$$

with coefficients in Table 2.5.

Table 2.5: Coefficients of Equation (2.36)

Coefficient	Triangular Cylinder	Square Cylinder	Parallel Plates
R_0	1.0000000	1.0000000	1.0000000
R_1	-0.1524694×10^{1}	-0.1923777×10^{1}	-0.4027060×10^{0}
R_2	-0.9356945×10^{1}	0.1649393×10^{1}	-0.8435362×10^{1}
R_3	0.6788950×10^{2}	-0.1153624×10^{2}	0.3487996×10^{2}
R_4	-0.1634936×10^{3}	0.2682020×10^{2}	-0.2359584×10^{2}
R_5	0.6563649×10^{2}	0.1367386×10^{2}	-0.1193919×10^{3}
R_6	0.1929998×10^{3}	-0.5060226×10^{2}	0.1362242×10^{3}
R_7	0.4729873×10^{2}	-0.1042480×10^{3}	0.1601959×10^{3}
R_8	-0.3751033×10^{3}	0.1170802×10^{3}	-0.4106427×10^{1}
R_9	0.2752887×10^{3}	0.2395431×10^{3}	-0.3171554×10^{3}
R_{10}	-0.1190656×10^{4}	-0.1757552×10^{3}	-0.1989548×10^{3}
R_{11}	0.6542166×10^{3}	0.1097079×10^{2}	0.4608181×10^{2}
R_{12}	0.2075038×10^{4}	-0.2409061×10^{3}	0.3581750×10^{3}
R_{13}	0.3268518×10^{3}	-0.9802373×10^{2}	0.2128604×10^{3}
R_{14}	-0.2014247×10^{4}	0.1344775×10^{3}	0.2338137×10^{3}
R_{15}	-0.2869939×10^{4}	0.2037087×10^{3}	-0.8912624×10^{2}
R_{16}	0.1553641×10^{4}	0.9298401×10^{2}	-0.6472198×10^{2}
R_{17}	0.1483049×10^{4}	-0.1153909×10^{3}	-0.2528621×10^{3}
R_{18}	0.2078562×10^{4}	0.2791606×10^{3}	0.2000882×10^{3}
R_{19}	-0.2211987×10^{4}	-0.3434466×10^{3}	0.2897953×10^{3}

The work of Fidleris and Whitmore (1961) is probably the most thorough investigation of the wall effect for spheres. They interpreted the results of over 3,000 velocity measurements and presented wall effect correction factors graphically. Fidleris and Whitmore's graph is reproduced here in Fig. 2.6. According to the figure, the wall effect is highest at high diameter ratios and at low Reynolds numbers.

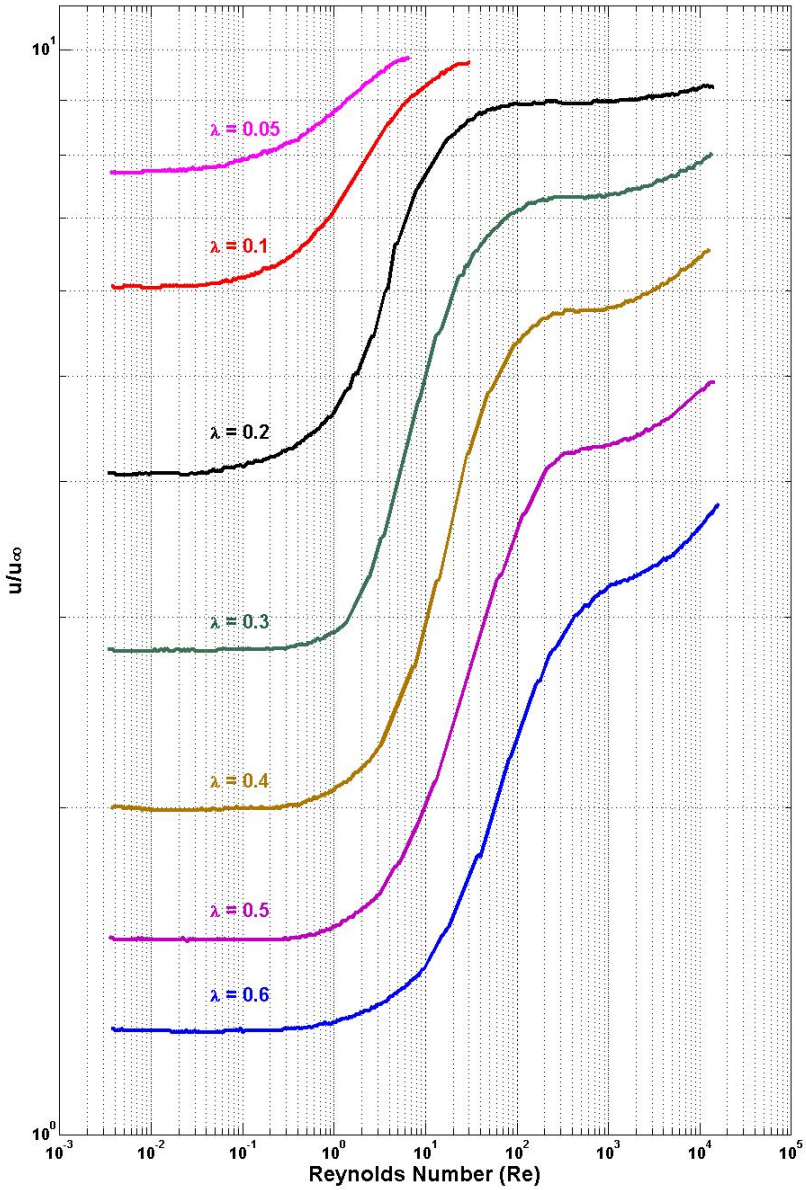

Figure 2.6: Fidleris and Whitmore, 1961 Graphical Method in determining Wall Factor

2.3.3 Effect of Concentration on Particle Settling

The settling velocity in suspensions has been the subject of many studies for more than a half century. Many empirical expressions that were proposed in fluidization can be applied to the proppant settling inside the fractures as both phenomena are following the same physics. In this section, we investigate the deviation of settling velocity from single terminal velocity due to the presence of other particles which in turn modifies the flow field. Other interactions such as wall effects are not considered here. In addition, the many empirical relations that have been proposed in fluidization context are examined in this section and an attempt is made to classify these

expressions by the method that they were obtained and also, by the graphical shape of the expressions.

In proppant transport application, we are dealing with a multi-particle system. The presence of other particles changes the drag force exerted on each particle. The motion of other particles creates a "return flow" of carrying fluid. Moreover, presence of other particles increases the viscosity of the suspension.

In fluidization research, the ratio of the terminal drag force in a multi-particle system to the drag force exerted on a single particle is called voidage function or concentration function (voidage is defined as 1-c) and is used to measure the concentration effects:

$$f(c) = \frac{F_{Dt}}{F_{Ds}} \tag{2.37}$$

where F_{Dt} and F_{Ds} are terminal drag force in multi-particle and single-particle systems, respectively. Obviously, the value of the concentration function depends on the particle concentrations, and drag forces in calculating this function should be evaluated at the same velocity. In different applications and problems this ratio may be expressed in other forms than forces to investigate different quantities. For example, in sedimentation research this ratio is used to calculate piezometric pressure drop through the bed of particles. In proppant transport studies the main application of this term is the calculation of the hindered settling velocity. Therefore, it is more convenient to express this ratio in terms of velocities rather than forces. Furthermore, here all the voidage function formulas are expressed in terms of concentration rather than voidage.

De fellice (1994), based on particles momentum equation and the drag force equation, showed that the concentration function can be expressed in terms of velocities as:

$$f(c) = \left(\frac{u_t}{u}\right)^2 \frac{C_{Dt\infty}}{C_{Dt}}(1-c) \tag{2.38}$$

In Stokes region or creeping flow region ($Re_p < 0.1$):

$$\frac{C_{Dt\infty}}{C_{Dt}} = \frac{\frac{24}{Re_t}}{\frac{24}{Re}} = \frac{u}{u_t} \tag{2.39}$$

Therefore:

$$f(c) = \frac{u_t}{u}(1-c) \tag{2.40}$$

In Newton's region or turbulent region (500 < Rep < 200,000):

$$C_{Dt} = 0.44 \tag{2.41}$$

Therefore:

$$\frac{C_{Dt\infty}}{C_{Dt}} = 1 \tag{2.42}$$

Substituting:

$$f(c) = \left(\frac{u_t}{u}\right)^2 (1-c) \tag{2.43}$$

The first type of approaches in finding voidage function is fully theoretical approach in which a solution for Navier-Stokes equation for multi-particle system is proposed. Exact solution of fluid-solid interaction force can only be obtained for very low Reynolds number or dilute suspensions. As an example, we can mention Barnea and Mizrahi (1973) voidage function expression for fixed spatial particle arrangements:

$$f(c) = [1 + K(c)^{1/3}](1-c) \tag{2.44}$$

with K having values ranging between 1 and 2. For random particle arrangements, Batchelor (1972) obtained:

$$f(c) = \frac{(1+4.7c)(1-c)}{1-1.83c} \tag{2.45}$$

Happel (1958) proposed the following expression:

$$f(c) = \frac{(3+2c^{5/3})(1-c)}{3-4.5c^{1/3}+4.5c^{5/3}-3c^2} \tag{2.46}$$

Some researchers, with limited success, tried to utilize theoretical approaches and extend the applicability of the equations to higher Reynolds number. The reader is referred to the work of LeClair and Hamielec (1968) or El-Kaissy and Homsy (1973).

The limited range of applicability of theoretical solutions leaves ample space for less exact approaches to be carried out in multi-particle-fluid systems. In completely empirical approaches, the proposed expressions relating velocity to concentration are derived exclusively from experimental data. Experimental data in this regard over the full range of flow regime are abundant. For example, if we use Rechardson-Zaki, (1954), correlation:

$$\frac{u_t}{u} = (1-c)^{-n} \tag{2.47}$$

$n = 4.65 \qquad Re_t < 0.2, \qquad n = 2.4 \qquad 500 < Re_t$

Hence for low Reynolds regime:

$$f(c) = (1-c)^{1-n} = (1-c)^{-3.65} \tag{2.48}$$

And for high Reynolds regime:

$$f(c) = (1-c)^{1-2n} = (1-c)^{-3.7} \tag{2.49}$$

These two famous correlations show that for extremely low or high Reynolds conditions the concentration function has almost the same form. Based on this conclusion, some researchers proposed that the concentration function is independent of Reynolds number due to constancy of the exponent in the above expressions. Therefore, the same type of expression can be used for intermediate flow regime as well (Richardson and Jeronimo, 1979; Foscolo et al., 1983; Kmiec, 1976).

Khan and Richardson (1990) calculated the drag coefficient of a sphere in a concentrated suspension of particles as a function of concentration. They observed inconsistency between abovementioned generalization and the behavior of fluidized beds. They were the first researchers who modified the expression of concentration function in intermediate regime. For intermediate flow regimes, De fellice (1994) using Dalla valle (1948) drag coefficient correlation for spherical particles obtained:

$$C_D = (0.63 + \frac{4.8}{Re^{0.5}})^2 \tag{2.50}$$

Richardson and Zaki (1954) equation for hindered settling velocity can be expressed as:

$$\frac{Re}{Re_t} = (1-c)^n \tag{2.51}$$

and Rowe (1987) correlation for exponent n in Richardson-Zaki correlation is:

$$\frac{4.7-n}{n-2.35}=0.175Re_t^{0.75} \tag{2.52}$$

De fellice (1994) concluded that the exponent is not a constant and it varies depending on the Reynolds number. He proposed the following expression for the concentration function:

$$f(c)=(1-c)^{-\beta} \tag{2.53}$$

where exponent β changes with the Reynolds number:

$$\beta=\{3.7-0.65e^{(1.5-log\,Re)^2/2}\} \tag{2.54}$$

There are also semi-empirical approaches in which the parameters in the existing theoretical models are adjusted. In approaches based on single-particle-fluid systems, in order to extend the single particle equations to multi-particle systems, a "pseudo-fluid" whose density and viscosity is such that it gives the same fluid dynamic effect on the single particle as the presence of neighboring particles, is considered. In these early studies, some researchers were using Stokes equation with modified viscosity and density of slurry rather than the fluid (Robinson, 1926, Steinour 1944). Robinson (1926) published this idea which was later adopted by Steinour (1944). Hawksley (1951), assuming pseudo fluid density to be equal to the suspension density and its viscosity is calculated from Vand equation (mentioned later in this chapter), obtained the following expression for particle settling velocity:

$$\frac{u}{u_t}=(1-c)^2e^{\left(-2.5c/1-\frac{39}{64}c\right)} \tag{2.55}$$

which is strictly valid for the creeping flow regime. Barnea and Mizrahi (1973) using similar approach provided voidage function for the entire flow regime, which can only be stated explicitly for low and high Reynolds numbers:

$$f(c)=\frac{1+c^{1/3}}{(1-c)}e^{[5c/3(1-c)]} \tag{2.56}$$

$$f(c)=\frac{1+c^{1/3}}{(1-c)^2} \tag{2.57}$$

Other examples of this approach can be found in the work of Letan (1974), Ishii and Zuber (1979), Patwardhan and Chi Tien (1985a). This approach gives a fair agreement with the published experimental data for a wide range of flow regimes.

There are approaches with the analogy with fluid flow in pipes in which the relationship between pressure drop and concentration is given. More complete reviews are reported by Dullien (1975) and Barnea and Mednick (1978).

There are many studies in the literature that were trying to formulate the effect of particle concentration on settling velocity. Many of the proposed correlations apply over a restricted range of Reynolds number. Table 2.6 summarizes these equations with their range of applicability.

Table 2.6: Expressions for Effect of Particle Concentration on Settling Velocity

Researcher	Range of Applicability	Equation
Steinour (1944)	$Re_t < 0.2, c > 0.15$	$\frac{u}{u_t} = (1-c)^2 e^{-4.19c}$
Brinkman (1947)	$Re_t < 2$	$\frac{u}{u_t} = [1 + 0.75c(1 - \sqrt{\frac{8}{c} - 3})]$
Lewis et al. (1949)	$1.1 < Re_t < 26$	$\frac{u}{u_t} = (1-c)^{4.65}$
Hawksley (1951)	$10^{-3} < Re_t < 58$	$\frac{u}{u_t} = (1-c)^2 \mathrm{e}^{[\frac{-2.5c}{1-\frac{39}{64}c}]}$
Jottrand (1952)	$10^{-3} < Re_t < 0.4$	$\frac{u}{u_t} = (1-c)^{5.6}$
Lewis and Bowerman (1952)	$2 < Re_t < 500$ $Re_t > 500,\ \ c > 0.1$	$\frac{u}{u_t} = 0.9(1-c)^{2.97}$ $\frac{u}{u_t} = 0.72(1-c)^{2.32}$
Richardson and Zaki (1954)		$\frac{u}{u_t} = (1-c)^n$
	$Re_t < 0.2$	$n = 4.65 + 20\frac{d_p}{D}$
	$0.2 < Re_t < 1$	$n = (4.4 + 18\frac{d_p}{D}) \Big/ Re_t^{0.03}$
	$1 < Re_t < 200$	$n = (4.4 + 18\frac{d_p}{D}) \Big/ Re_t^{0.1}$
	$200 < Re_t < 500$	$n = 4.4 Re_t^{-0.1}$
	$Re_t > 500$	$n = 2.4$

Table 2.6: Continued

Researcher	Range of Applicability	Equation
Happel (1958)	$Re_t < 0.2$	$\frac{u}{u_t} = \frac{3 - \frac{9}{2}c^{\frac{1}{3}} + \frac{9}{2}c^{\frac{5}{3}} - 3c^2}{3 + 2c^{\frac{5}{3}}}$
Loeffler and Ruth (1959)	$Re_t < 0.5$	$\frac{u}{u_t} = \frac{\frac{(1-c)^3}{c}}{5.7 + \frac{(1-c)^2}{c}}$
Oliver (1961)	$Re_t < 0.4$	$\frac{u}{u_t} = (1 - 2.15c)(1 - 0.75c^{\frac{1}{3}})$
Wen and Yu (1966)	$10^{-2} < Re_t < 10^4$	$Ga = (18Re_t + 2.7Re_t^{1.687})(1-c)^{-4.7}$
Gelperin et al. (1972)	$Re_t < 500$	$Ga = (18Re_t + 0.36Re_t^2)(1-c)^{-4.76}$
Ramamurthy and Sabbaraju (1973)	$Ga\frac{\rho_p - \rho_f}{\rho_f} < 18$ $18 < Ga\frac{\rho_p - \rho_f}{\rho_f} < 10^5$ $Ga\frac{\rho_p - \rho_f}{\rho_f} > 10^5$	$Ga = 18Re\frac{\rho_f}{\left(1 - 1.21c^{\frac{2}{3}}\right)^{1.56}(\rho_p - \rho_f)}$ $Ga = 19Re^{1.4}\frac{\rho_f}{\left(1 - 1.21c^{\frac{2}{3}}\right)^{2.18}(\rho_p - \rho_f)}$ $Ga = \frac{1}{3}Re^2\frac{\rho_f}{\left(1 - 1.21c^{\frac{2}{3}}\right)^{3.12}(\rho_p - \rho_f)}$
Barnea and Mizrahi (1973)	$10^{-3} < Re_t < 3 \times 10^4$	$C_{D\phi} = (0.63 + \frac{4.8}{\sqrt{Re_\phi}})^2$ $C_{D\phi} = \frac{C_D(1-c)^3}{(1 - c^{\frac{1}{3}})}$ $Re_\phi = \frac{Re}{(1-c)e^{\frac{5c}{3(1-c)}}}$ $\left[\frac{4d_p(\rho_p - \rho_f)g}{3\mu u_\infty^2}\right]\left[\frac{1-c}{1 + c^{\frac{1}{3}}}\right] = 0.63 + \frac{4.8}{\sqrt{Re_\phi}}$
Letan (1974)	$1.5 < Re_t < 2200$	$\frac{u}{u_t} = \frac{(1 + 0.15Re_t^{0.687})(1-c)^{4.5}}{1 + 0.15\left(Re_t\frac{u}{u_t}\right)^{0.687}(1-c)^{1.72}}$
Wen and Fan (1974)	$18 < Ga < 10^5$ $i.e. 1 < Re_t < 550$ $Ga > 10^5$ $i.e. Re_t > 550$	$Ga = [13.9Re_t^{1.4}\phi_c^{3.026}(1 + 1.13 \times 10^{-3}\phi_c^{4.025})]^{\frac{1}{[1+0.0463(\phi_c-1)]}}$ $Ga = [\frac{1}{3}Re_t^2\phi_c^{3.819}(1 + 1.5 \times 10^{-3}\phi_c^{3.102})]^{\frac{1}{[1+0.0384(\phi_c-1)]}}$ $\phi_c = \frac{1}{(1 - 1.21c^{\frac{2}{3}})}$

Table 2.6: Continued

Researcher	Range of Applicability	Equation
Garside and Al-Dibouni (1977)	$B = 0.8(1-c)^{1.28} \quad c > 0.15$ $B = (1-c)^{2.65} \quad c < 0.15$	$0.6Re_t^{(1.2-c)} = \dfrac{\frac{u}{u_t} - (1-c)^{4.14}}{B - \frac{u}{u_t}}$
Riba and Couderc (1977)	First Equation: $(1-c) < 0.85$ Second Equation: $(1-c) > 0.85$	First form: $Ga = \dfrac{\rho_f}{\rho_p - \rho_f} 1.9(1-c)^{-3.77}(18Re + 2.7Re^{1.687})$ $Ga = \dfrac{\rho_f}{\rho_p - \rho_f} 1.3(1-c)^{-6.17}(18Re + 2.7Re^{1.687})$ Second form: $c = 1 - 1.58Re^{0.33}Ga^{-0.21}\left(\dfrac{\rho_f}{\rho_p - \rho_f}\right)^{-0.22}$ $c = 1 - 1.2Re^{0.17}Ga^{-0.11}\left(\dfrac{\rho_f}{\rho_p - \rho_f}\right)^{-0.12}$ Third form: $\begin{cases} Ga = 21.8Re\phi_c^{1.28}\dfrac{\rho_f}{\rho_p - \rho_f} \\ Ga = 13.9Re\phi_c^{2.7}\dfrac{\rho_f}{\rho_p - \rho_f} \end{cases} \quad Ga\dfrac{\rho_p - \rho_f}{\rho_f} < 18$ $\begin{cases} Ga = 18.2Re^{1.4}\phi_c^{1.79}\dfrac{\rho_f}{\rho_p - \rho_f} \\ Ga = 9.6Re^{3.78}\phi_c^{3.78}\dfrac{\rho_f}{\rho_p - \rho_f} \end{cases} \quad 18 < Ga\dfrac{\rho_p - \rho_f}{\rho_f} < 10^5$ $\begin{cases} Ga = 0.49Re^2\phi_c^{2.56}\dfrac{\rho_f}{\rho_p - \rho_f} \\ Ga = 0.2Re^2\phi_c^{5.4}\dfrac{\rho_f}{\rho_p - \rho_f} \end{cases} \quad Ga\dfrac{\rho_p - \rho_f}{\rho_f} > 10^5$ $\phi_c = \dfrac{1}{(1 - 1.21c^{\frac{2}{3}})}$
Ganguly (1980)	$L_e = \dfrac{1.27W}{\rho_f D^2(1 - 1.762U + 0.95U^2)}$ $U = \dfrac{u - u_m}{u_t - u_m}$	$0.12 < Re_t < 43.66$ u_m: minimum fluidization velocity L_e: height of expansion bed W: mass of feed

Table 2.6: Continued

Researcher	Range of Applicability	Equation
Limas-Ballesteros et al. (1982)	$6 \times 10^4 < Ga < 5.6 \times 10^7$	$Ga = \frac{\rho_f}{\rho_p - \rho_f}[1.21\psi^{1.35}(1-c)^{-4.94}(24Re + C_l Re^2)]$ $\psi = 1.0$ $C_l = 0.8(\frac{100}{Re})^{0.35} \quad 200 < Re < 500$ $C_l = 0.7(\frac{10}{Re})^{0.0876} \quad 200 < Re < 500$ $C_l = 0.439 \quad 200 < Re < 500$
Foscolo et al. (1983)	$Re_t < 0.2$ $0.2 < Re_t < 500$ $Re_t > 500$	$\frac{u}{u_t} = \frac{(1-c)^4}{4c + (1-c)^3}$ $\frac{u}{u_t} = \frac{0.0777 Re_t (1 + 0.01941 Re_t)(1-c)^{4.8} - 1}{0.0388 Re_t}$ $\frac{u}{u_t} = [\frac{(1-c)^4}{3.55c + (1-c)^3}]^{0.5}$
Jean and Fan (1989)	$Re_t < 0.2$	$\frac{u}{u_t} = \frac{3 - 4.5c^{1/3} + 4.5c^{5/3} - 3c^2}{3 + 2c^{5/3}}$
Hirata and Bulos (1990)	As Rechardson and Zaki	$\varepsilon = \varepsilon_{pk} + (1 - \varepsilon_{pk})\varepsilon_{RZ}\exp[B(1 - \varepsilon_{RZ})]$ $A = 2.2n + \frac{8d_p}{D}$ $B = 2.1n$ ε_{pk}: Static Bed Voidage ε_{RZ}: Bed Voidage Calculated from Richardson-Zaki Equation

As it can be seen, there is a large amount of published correlations on the effect of concentration on settling velocity. There are wide discrepancies between the prediction of these published correlations. However, Di felice (1995) provided a more systematic approach in categorizing different correlations based on the shape of the correlations when u/u_t vs. voidage is plotted on a log-log scale. Di felice (1996) recognized four different types of behavior as shown in Fig. 2.7.

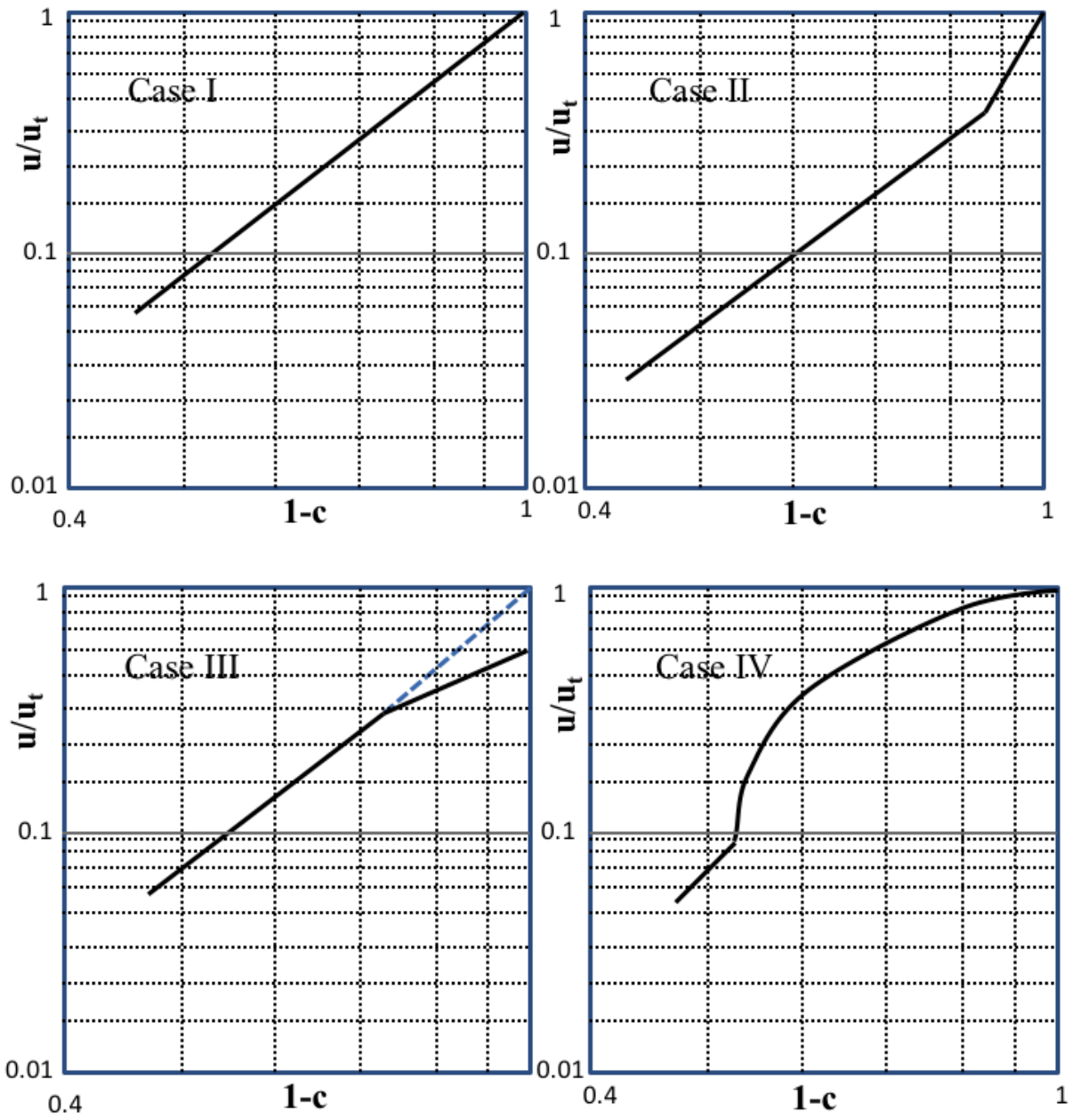

Figure 2.7: Different Classes of Velocity vs Concentration Correlations

In Case I, the plot is smooth and linear and the extrapolation of experimental points to c = 0, corresponds to the single particle velocity. The main characteristic of Case II is that the plot is divided into two regions with different slopes. For high concentrations, the extrapolation of the straight line coincides with a velocity well below the single particle terminal velocity. However, the slope increases in the second region and the extrapolated line approaches the correct value of single particle settling velocity. Case III is similar to Case II but in the second region the slope is

decreasing. In Case IV the first part of the plot is linear, while the second part is concave, approaching the unhindered settling velocity.

2.3.4 Random Close Packing Concentration and Maximum Close Packing Concentration

The maximum volume fraction of solids (proppants) obtained, when they are packed randomly, gives a parameter called random close packing (RCP). A clear geometric point at which proppants are in a densely packed but non-crystalline state gives random close packing concentration (c_{RCP}). The empirical nature of RCP and whether it is a well-defined property or dependent on shear history of suspension and precise definition of end of randomness and crystallinity start is very controversial (Torquato et al., 2000; Mewis and Wagner, 2009). However, there are several predictive theoretical models that can determine c_{RCP} from particle size distribution (Phan et al., 1998; Kansal et al., 2002; Farr and Groot, 2009; Brouwers, 2011), the topic of which is beyond the scope of this work. In addition, increasing size dispersity of the system, increases c_{RCP} (Chong et al., 1971; Farr and Groot, 2009; Mewis and Wagner, 2011).

It should be noted that c_{RCP} is the most "geometrical" consolidated packing that can be achieved by tapping or vibrating a large container of spheres. (Mewis and Wagner, 2011) and has a highly repeatable experimental value. Depending on the size of the particles, different values for random close pack concentration is reported in the literature (for example Shapiro and Probstein (1992) reported $c_{RCP} = 0.52$ and Chong and Christiansen (1971) reported $c_{RCP} = 0.61$). Later in our numerical code, we assume a value of 0.66 for this parameter. On the other hand, there is another parameter called maximum packing concentration (c_m) at which suspensions become highly viscous. This parameter is defined from a "thermodynamic" point of view, however, for the mono-disperse suspensions it is very close to c_{RCP}. In the next section, one approach of determining this parameter will be discussed.

An overview of random close packing is given by Koos (2009). It should be noted that another packing which is called random loose packing (concentration in the range 0.55-0.61) also exists which is defined as the loosest state that particles can obtain while they are still in contact.

In our numerical code, maximum packing concentration (sometimes called saturation concentration in proppant applications) is important in determining the evolution of slurry viscosity (as will be discussed in the next section) and also gives the point at which fracture is

filled with proppant and should be treated like a porous medium. Although, there are very few models that can predict maximum packing concentration, in this research, we assume it is equivalent to c_{RCP}, which is easier to determine. An approach which is also supported by theoretical and experimental literature (Brady, 1993; Quemada and Berli, 2002; Mendoza and Santamaria-Holek, 2009).

2.3.5 Viscosity Evolution of Slurries

Rheology of suspensions is a rapidly increasing function of particle concentration which is also sometimes called phase volume (c, phase volume is the volume of suspending particles divided by the total volume of suspension). The reason is that the transfer of momentum between each particle and fluid is effected by the presence of other particles, which is equivalent to the increase of the apparent bulk viscosity of the slurry, a phenomenon more evident when the bulk slurry is sheared.

Another factor that also effects slurry viscosity is the particle diameter. In high viscosity liquids, the effect of particle diameter is negligible while in low viscosity liquids, slurry viscosity is weakly dependent on the diameter of the proppants. Effect of particle shape and particle size distribution is totally neglected in our work since we are assuming uniform spherical proppants are being injected inside the formation. Present section is focusing on the flow behavior of proppant laden slurries, since viscosity evolution of such fluids strongly modify the mobility of fluids inside the fractures. Obviously, the focus would be on slurries with large particles and high solid fraction. The assumption of random position of the particle, with no segregation comes closer to reality for narrow size distributions and highly concentrated suspensions. Flocculating, colloidal and aggregating suspensions are beyond the scope of our study. Assumptions mentioned above are common to almost all previous publications in proppant laden slurries.

There has been a vast number of theoretical and experimental studies on the subject of viscosity of suspensions. Many theoretical and semi-empirical closed form expressions have been proposed for viscosity evolution with concentration. A complete overview has been given by Rutgers (1962) and Horri et al. (2011). The most common way of describing slurry viscosity evolution is by introducing a parameter called relative viscosity which is the ratio of dynamic viscosity of slurry to dynamic viscosity of the carrying fluid:

$$\mu_{rel} = \frac{\mu_{sl}}{\mu_0} \tag{2.58}$$

Relative viscosity is an indication of the factor by which the viscosity of the liquid is increased due to the presence of proppants.

Over 100 years ago, Einstein (1906) theoretically derived his famous viscosity equation for dilute suspensions of rigid particles:

$$\mu_{rel} = 1 + Kc \tag{2.59}$$

He proposed a value of 2 for K (intrinsic viscosity) for spherical particles. Einstein work is based on the dissipated energy from suspending particles in the liquid, which is assumed to take place in the portion occupied by the particles. This assumption is permissible only in the case of dilute suspensions and very small particles. When the particles are densely populated, the calculation of the dissipated energy is overestimated since dissipation does not occur in the portion occupied by the particles. Einstein equation is valid for very dilute suspensions when concentration is around 0.01-0.02 (Rutgers, 1962). The possibility of a higher K value, e.g. 4.5 or 5.5 has been mentioned repeatedly, e. g. by Hatschek (1913) or Happel (1957).

The viscosity-concentration correlations can be categorized according to the type of the proposed equation. Rutgers (1962) classified the correlations in terms of their mathematical forms. Table 2.7 shows a summary of the famous proposed equations.

Table 2.7: Summary of Different Viscosity Models for Suspensions

Author	Formula	Comment
Einstein (1906)	$\mu_{rel} = 1 + Kc$	K=2.5 for spheres, c < 0.02
Baker (1913)	$\mu_{rel} = (1 + kc)^n$	Whole concentration range
Kunitz (1926)	$\mu_{rel} = \frac{1 + 0.5c}{(1 - c)^4}$	Valid for large c
Bredee (1933)	$\frac{\mu_{rel} - 1}{\sqrt{\mu_{rel}}} = Kc$	Whole concentration range
Phillipoff and Hess (1935)	$\mu_{rel} = (1 + \frac{k}{n}c)^n$	Whole concentration range
Papkow and Kunststoffe (1935)	$\ln \mu_{rel} = Kc^n$	n = 1.2; K = 2.3
Guth and Simha (1936)	$\mu_{rel} = \frac{1 + 0.5c - 0.5c^2}{1 - 2c - 9.6c^2}$	c < 0.08

Table 2.7: Continued

Author	Formula	Comment
Eiler (1941)	$\mu_{rel} = (1 + \frac{1.25c}{1-c})^2$	Whole concentration range
Arrhenius (1942)	$\ln \mu_{rel} = Kc$	K = 2.78, Low concentration
Vand (1948)	$\mu_{rel} = \exp(\frac{2.5c}{1-0.609c})$	No attraction or repulsion between the particles
Vand (1948)	$\mu_{rel} = \exp(\frac{2.5c + 2.7c^2}{1-0.609c})$	No triplets collisions
Mooney (1951)	$\mu_{rel} = \exp(\frac{2.5c}{1-Kc})$	0.75< K < 1.5
Weissberg and Simha (1951)	$\frac{\mu_{rel}-1}{kc} = \frac{1}{kc}(1 + \frac{k}{n}c)^n - 1$	Whole concentration range
Simha (1952)	$\mu_{rel} = 1 + 2.5c(1 + \frac{25c}{4f^3} \ldots)$	For dilute suspensions
Simha (1952)	$\lim_{c \to c_m} \mu_{rel} = 1 + \frac{54}{5f^3}\left(\frac{c}{1-(c/c_m)^3}\right)$	For very concentrated suspensions only
Rosco (1952)	$\mu_{rel} = (1 - 1.35c)^{-2.5}$	High Concentrations
Oliver and Ward (1953)	$\mu_{rel} = 1 + \sum_{n=1}^{\infty}(kc)^n$	Low to moderate concentrations (c < 0.2)
Flory (1953)	$\log \mu_{rel} = A + kc^{1/2}$	n = 1.13, K = 2.3
Maron and Pierce (1956)	$\mu_{rel} = (1 - \frac{c}{c_m})^{-2}$	c > 0.2
Happel (1957)	$\mu_{rel} = 1 + 5.5c(\frac{4c^{7/3} + 10 - (84/11)c^{2/3}}{10(1 - c^{10/3} - 25c(1 - c^{4/3}))})$	Approximated by (if c < 0.3): $\mu_{rel} = \exp(4.58c)$
Krieger and Dougherty (1959)	$\mu_{rel} = (1 - \frac{c}{c_m})^{Bc_m}$	B = 2.5 for solid spheres
Thomas (1965)	$\mu_{rel} = 1 + 2.5c + 10.05c^2 + 0.00273\exp(16.6c)$	Whole concentration range
Frankel and Acrivos (1967)	$\mu_{rel} = \frac{1.125(c/c_m)^{1/3}}{1-(c/c_m)^{1/3}}$	Whole concentration range
Frankel and Acrivos (1967)	$\mu_{rel} = C\left\{1 - (\frac{c}{c_m})^{1/3}\right\}^{-1}$	For concentrated suspensions only,

Table 2.7: Continued

Author	Formula	Comment
Chong et al. (1971)	$\mu_{rel} = (1 + 0.75 \frac{c/c_m}{1 - c/c_m})^2$	High concentrations
Nicodemo and Nicolais (1974)	$\mu_{rel} = (1 - \frac{c}{c_m})^{-2.5}$	Whole concentration range
Batchelor (1977)	$\mu_{rel} = 1 + 2.5c + Ac^2$	A = 6.2 for spheres
Dabak and Yucel (1986)	$\mu_{rel} = (1 + \frac{2.5cnc_m}{n(c_m - c)})^n$	High concentrations, Low to high shear rates
Barree, (1994)	$\mu_{rel} = (1 - \frac{c}{c_m})^{-1.5}$	Whole concentration range
Mendoza and Santamaria-Holek (2009)	$\mu_{rel} = (1 - c_{excl})^{2.5}$ $c_{excl} = \frac{c}{1 - [\frac{(1 - c_m)c}{c_m}]}$	c_{excl}: Excluded Volume
Brouwers (2010)	$\mu_{rel} = (\frac{1 - c}{1 - c/c_m})^{2.5c_m/1 - c_m}$	High concentrations, Mono-sized, spherical particles

The most commonly used equation involves the maximum solid fraction. The maximum solid fraction is the concentration at which viscosity of the slurry becomes infinity, as shown in the Fig. 2.8. It should be noted that concentrated suspensions above maximum packing concentration can exist under compression. The behavior of such suspensions is defined by inter-particle interactions and micro-structure through theoretical and semi-empirical approaches and definition of suspension modulus (G'), the topic of which is beyond the scope of our work.

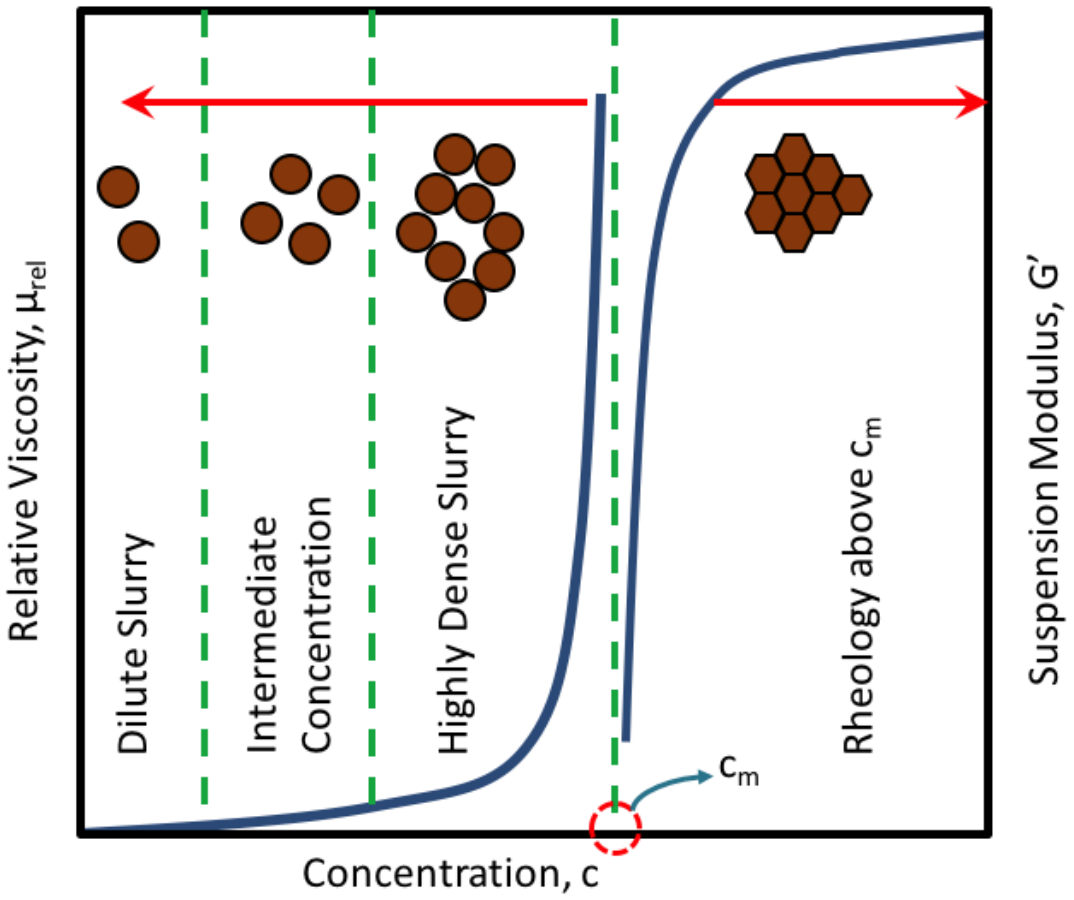

Figure 2.8: Rheological Behavior of Suspensions

2.4 Conclusion

Only a limited number of approaches are available for numerical simulations of particle transport. Although the application of granular kinetic theory for gas-liquid systems has been successful, the approach is still insufficient for solid-liquid systems. On the other hand, mixture models can be easily modified to accommodate different physical phenomena occurring during proppant placement. To this purpose, various aspects of hydrodynamics of solid settling in fluids were investigated. Laboratory investigations have shown that concentration, wall and inertial effects are among the most key factors that control the settling velocity of proppants. However, there still are some disagreements between proposed correlations.

In particle-fluid systems, the effect of inertia on drag force exerted on particles has been thoroughly studied. Based on many experimental data of different researchers, a standard graph of drag coefficient versus Reynolds number has been established. Since the effect of inertia on

settling velocity cannot be explicitly recognized from standard drag curve, we re-plotted this graph in terms of Galileo number and Reynolds number. Galileo number can be easily obtained from the physical properties of fluid and particles.

Fracture walls cause a hydrodynamic retardation that significantly reduce settling velocity, especially when particle diameter becomes comparable to slot width.

Increased particle concentration generally hinders settling rate. As the concentration reaches to maximum packing concentration, settling velocity becomes zero. At this point, packed fracture can be treated like porous medium. Moreover, the viscosity of the proppant laden slurry significantly increases as concentration increases. The effect would be a huge change in mobility and consequently, pressure field inside the fracture.

Incorporation of the state of the art in proppant transport laboratory experiments enables the numerical simulators to routinely design and evaluate field size stimulation and proppant injection. The current tools have not reached a fully foretelling capability which would allow for daring optimization schemes. Most of our effort was devoted to developing a robust numerical tool that captures physical phenomena and facilitates predictive designs.

Chapter 3: Mathematical Formulation of the Proppant Transport Simulator

3.1 Introduction

The transport phenomenon of proppants in hydraulic fractures is described by hyperbolic partial differential equations (PDE). Hyperbolic PDEs are based on conservation laws and describe a wide range of wave propagation and transport phenomena arising in practical engineering problems (Leveque, 2004).

The solution to this kind of PDEs is highly dependent on the specified initial conditions. Solution to hyperbolic PDEs simply transports the initial condition within the model. On the other hand, it is well known that the hyperbolic partial differential equations (PDE) accept both smooth as well as discontinuous solutions. A discontinuous solution, also referred to as a shock, is characterized by large gradients in the variables such as velocity, density (concentration), depth or pressure. Even with smooth initial conditions, discontinuities may develop with time (Chen, 2006). Accurate numerical simulation of such systems is a challenging task using conventional numerical methods. The numerical challenge in the vicinity of large gradients (shocks) is that high order FD schemes lead to significant oscillations despite the fact that such schemes result in higher accuracy in smooth regions. On the other hand, first-order methods provide non-oscillatory (monotonic) solution near the shocks, while giving poorer accuracy in the smooth regions.

In this chapter, we investigated several shock-capturing schemes. The competency of each scheme was tested against a 1D benchmark problem. The main purpose of this chapter is to provide a step-by-step description of the numerical solution to proppant transport PDE, since such a description, although exists in related math textbooks, is missing in the hydraulic fracturing context. It should be noted that the classification of PDEs can be found in Appendix B.

3.2 Theory and Governing Equations of Slurry Proppant Transport

In this section, we derive the most general form of mass conservation equation for proppant transport. For this purpose, we need to define several terms. If we assume a control volume of dimensions dx, dy and w (width of the fracture), according to Fig. 3.1, the rate of change of proppant mass inside the element will be:

$$\frac{\partial m_p}{\partial t} = \frac{\partial \rho_p V_p}{\partial t} \tag{3.1}$$

where m_p, ρ_p and V_p are proppant mass, density and volume respectively. On the other hand, proppant volume, Vp can be related to total element volume, V, by proppant concentration, c:

$$V_p = cV = cdxdyw \tag{3.2}$$

Since we assume proppant density is not changing with time, the rate of change of proppant mass can be written as:

$$\frac{\partial m_p}{\partial t} = \rho_p \frac{\partial [cdxdyw]}{\partial t} \tag{3.3}$$

The mass rate entering the system in the x-direction, from the left boundary of the element will be:

$$\frac{\partial m_p}{\partial t} = \rho_p u_p cA = \rho_p u_p cdyw \tag{3.4}$$

where u_p is proppant horizontal velocity. With the same reasoning, proppant mass rate in the y-direction entering from bottom boundary of the system can be written as:

$$\frac{\partial m_p}{\partial t} = \rho_p v_p cA = \rho_p v_p cdxw \tag{3.5}$$

where v_p is proppant vertical velocity. The proppant mass rate leaving the system from right and top boundaries can be written as:

$$\frac{\partial m_p}{\partial t} = \rho_p u_p cdyw + \frac{\partial [\rho_p u_p cdyw]}{\partial x} dx \tag{3.6}$$

$$\frac{\partial m_p}{\partial t} = \rho_p v_p cdxw + \frac{\partial [\rho_p v_p cdxw]}{\partial y} dy \tag{3.7}$$

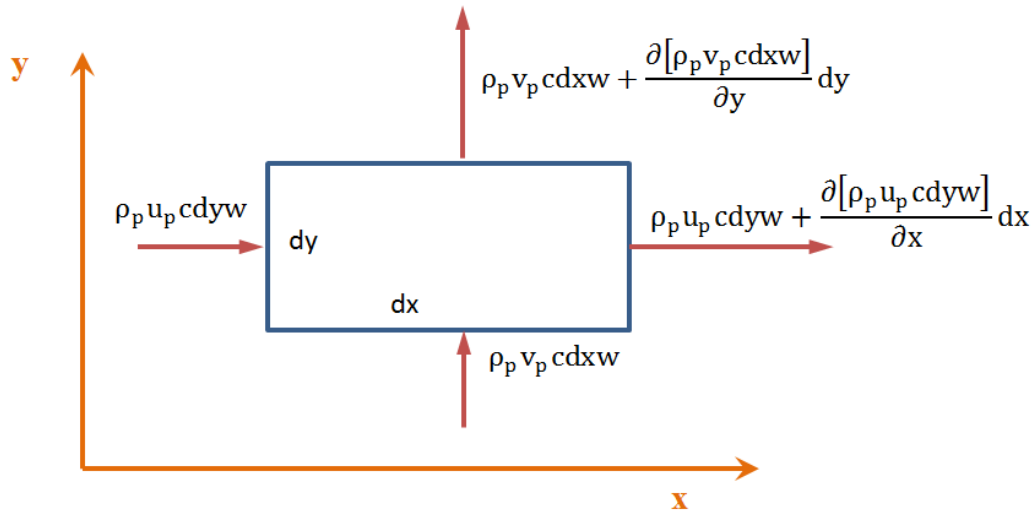

Figure 3.1: Small Control Volume

Now according to the law of conservation of mass, proppant mass entering the system minus proppant mass leaving the system plus source or sink term during a certain amount of time will give the change of mass in the system in that time:

$$\rho_p u_p cdyw - \left[\rho_p u_p cdyw + \frac{\partial[\rho_p u_p cdyw]}{\partial x} dx\right] + \rho_p v_p cdxw - \left[\rho_p v_p cdxw + \frac{\partial[\rho_p v_p cdxw]}{\partial y} dy\right] + c.q_{inj} = \rho_p \frac{\partial[cdxdyw]}{\partial t} \tag{3.8}$$

After some simplification and dividing by dxdy:

$$\rho_p \frac{\partial[cw]}{\partial t} + \frac{\partial[\rho_p u_p cw]}{\partial x} + \frac{\partial[\rho_p v_p cw]}{\partial y} + cq_{inj} = 0 \tag{3.9}$$

It should be noted that u_p and v_p can be related to fluid velocities. In fact, proppant and fluid are not moving at the same velocities in horizontal and vertical directions. Therefore, defining:

$$R_{ret} = \frac{u_p}{u_f} \tag{3.10}$$

where u_f is horizontal fluid velocity and R_{ret} is called retardation factor which is the ratio of proppant to fluid horizontal velocities and:

$$v_p = v_f - v_{set} \tag{3.11}$$

where v_f is fluid vertical velocity and v_{set} is proppant settling velocity. Therefore, Eq. 3.9 can be written as:

$$\rho_p \frac{\partial[cw]}{\partial t} + \frac{\partial[\rho_p R_{ret} u_f cw]}{\partial x} + \frac{\partial[\rho_p (v_f - v_{set}) cw]}{\partial y} + cq_{inj} = 0 \tag{3.12}$$

Now, this form of mass conservation is categorized as pure advection since no diffusion term exists in the PDE expression. The solution to pure advection PDE simply translates the specified initial condition along the model, without smearing. Bird et al (1976) applied Fick's law of mass diffusion for binary systems to proppant flow and obtained the following relationship for the diffusion of proppants in the bulk flow of slurry as:

$$Proppant\ Diffusion\ = \nabla.(\rho_{sl} w D_{pf} \nabla \omega_p) \tag{3.13}$$

where ρ_{sl} is slurry density, D_{pf} is diffusivity coefficient and ω_p is mass fraction of the proppant and is defined as:

$$\omega_p = c\frac{\rho_p}{\rho_{sl}} \tag{3.14}$$

Applying the diffusion term in the mass balance Eq. 3.12, we get:

$$\rho_p \frac{\partial[cw]}{\partial t} + \frac{\partial[\rho_p R_{ret} u_f cw]}{\partial x} + \frac{\partial[\rho_p (v_f - v_{set}) cw]}{\partial y} + cq_{inj} = \nabla.(\rho_{sl} w D_{pf} \nabla \omega_p) \tag{3.15}$$

Bird et al. (1976) mentioned that the diffusivity coefficient, D_{pf}, can be broken into three sources: molecular movement, D_{pf}^{mo}, turbulent flow, D_{pf}^{tu} and temperature gradient, D_{pf}^{te}. In other words:

$$D_{pf} = D_{pf}^{mo} + D_{pf}^{tu} + D_{pf}^{te} \tag{3.16}$$

The diffusion associated with molecular movement is very small in hydraulic fracturing problems. Also, in our modeling, assumptions are made that the flow of frac-fluid is laminar and that the entire field is in a constant temperature field. For these reasons, the diffusive term can be dropped. The obvious outcome of neglecting diffusion is that the advancing front of proppant will be a ''sharp'' front, without any diffusion ahead. In addition, we are assuming proppant grains are incompressible and ρ_p can also be omitted from the equations. Therefore:

$$\frac{\partial[cw]}{\partial t} + \frac{\partial[R_{ret} u_f cw]}{\partial x} + \frac{\partial[(v_f - v_{set}) cw]}{\partial y} + cq_{inj} = 0 \tag{3.17}$$

Law of mass conservation can also be written for fluid injected into the wellbore. Again, for brevity, we don't bring the full derivation of the equation as it is very similar to proppant mass conservation.

$$\frac{\partial[(1-c)w]}{\partial t}+\frac{\partial[u_f(1-c)w]}{\partial x}+\frac{\partial[v_f(1-c)w]}{\partial y}+(1-c)q_{inj}=0 \tag{3.18}$$

If we consider Eqs. 3.17 and 3.18, we will be dealing with a system of hyperbolic PDEs. To avoid solving a complicated system of hyperbolic PDEs, we can do some manipulations. If we add proppant and fluid mass conservation equations, we obtain slurry mass conservation equation:

$$\frac{\partial[cw]}{\partial t}+\frac{\partial[u_pcw]}{\partial x}+\frac{\partial[v_pcw]}{\partial y}+\frac{\partial[(1-c)w]}{\partial t}+\frac{\partial[u_f(1-c)w]}{\partial x}+\frac{\partial[v_f(1-c)w]}{\partial y}+q_{inj}=0 \tag{3.19}$$

or:

$$\frac{\partial w}{\partial t}+\frac{\partial\{[u_pc+u_f(1-c)]w\}}{\partial x}+\frac{\partial\{[v_pc+v_f(1-c)]w\}}{\partial y}+q_{inj}=0 \tag{3.20}$$

Slurry velocity can be viewed as a volume fraction weighted sum of proppant and fluid velocities:

$$u_{sl}=u_pc+u_f(1-c) \tag{3.21}$$

$$v_{sl}=v_pc+v_f(1-c) \tag{3.22}$$

After substitution of slurry velocities given in Eqs. 3.21 and 3.22 into Eq. 3.20, we obtain:

$$\frac{\partial w}{\partial t}+\frac{\partial[u_{sl}w]}{\partial x}+\frac{\partial[v_{sl}w]}{\partial y}+q_{inj}=0 \tag{3.23}$$

To obtain a solution to our system of equations we need another expression which is Navier-Stokes equation (conservation of momentum for incompressible flow of Newtonian fluid). In the next section, we will see that combining Navier-Stokes equation with slurry transport equation leads to an elliptic type PDE, the solution of which would be easier to obtain compared to a system of hyperbolic PDEs.

The Navier-Stokes equations can be expressed as:

$$\rho\left(\frac{\partial u_i}{\partial t}+u_x\frac{\partial u_i}{\partial x}+u_y\frac{\partial u_i}{\partial y}+u_z\frac{\partial u_i}{\partial z}\right)=-\frac{\partial p}{\partial x_i}-\left(\frac{\partial\tau_{xi}}{\partial x}+\frac{\partial\tau_{yi}}{\partial y}+\frac{\partial\tau_{zi}}{\partial z}\right)+\rho g_i \tag{3.24}$$

where u is the velocity, g is the gravitational acceleration and i is x, y or z. p is pressure and τ represent different stress components.

In hydraulic fracturing applications, the solution to the Navier-Stokes equation is called cubic law. The derivation of cubic law can be found elsewhere (e.g. Economides and Nolte, 2000).

$$u_{sl} = -\frac{w^2}{12\mu}\frac{\partial p}{\partial x} \tag{3.25}$$

Similarly, for y direction:

$$v_{sl} = -\frac{w^2}{12\mu}\frac{\partial (p - \rho g y)}{\partial y} \tag{3.26}$$

where μ is the equivalent viscosity of the slurry. The second term in Eq. 3.26 is convection velocity. If we substitute Eq. 3.25 and 3.26 in Eq. 3.23, we obtain:

$$\frac{\partial}{\partial x}\left(\frac{w^3}{12\mu}\frac{\partial p}{\partial x}\right) + \frac{\partial}{\partial y}\left(\frac{w^3}{12\mu}\frac{\partial (p - \rho g y)}{\partial y}\right) + q_{inj} = \frac{\partial w}{\partial t} \tag{3.27}$$

This PDE is now of elliptic class and simple finite difference schemes can be used to solve it to obtain the fluid pressures. In addition, the rheology of the slurry which is affected by the proppant concentration, inertia or walls of the fracture can be included in the model by their effect on settling velocity, through any of the correlations provided in Chapter 2.

3.3 Convective Flow

Settling and convection are the two controlling mechanisms in proppant placement. Proppant settling velocity was extensively discussed in Chapter 2 and it was mentioned that uncorrected Stokes settling can be expressed as:

$$u_t = \frac{g d_p^2 (\rho_p - \rho_f)}{18\mu} \tag{3.28}$$

On the other hand, as the proppants are injected inside the fracture, the density of the carrying fluid starts to increase, generating a density gradient along the fracture. This density gradient, even in its moderate amount, can generate large scale fluid movement which dominates particle settling in most field scale conditions. This complex phenomenon causes vertical segregation of suspensions of different density.

In this section, we explain how convective flow can be quantified and measured for slot flow based on fluid rheological properties and local proppant concentration, just like settlement of particles. We will further present simulation results that confirm the theory that we discuss here

later in Chapter 4. The simulations are aimed to investigate the concurrent occurrence of particle settlement and convective movement.

Based on the cubic law, the horizontal flow of a fluid down a slot as a function of pressure drop can be expressed as (Bird et al., 1976):

$$Q_h = \frac{w^3 h}{12\mu}\frac{\Delta p}{l} \tag{3.29}$$

Solving for pressure gradient yields:

$$\frac{\Delta p}{l} = \frac{12\mu Q_h}{w^3 h} \tag{3.30}$$

In addition, the force on the fluid per unit length, in the horizontal direction is given by:

$$F_h = \frac{\Delta p}{l}.A \tag{3.31}$$

Combining the above equations:

$$F_h = \frac{12\mu Q_h}{w^2} \tag{3.32}$$

On the other hand, the vertical force on a fluid section of unit length is expressed as:

$$F_v = \frac{\Delta\rho.g.V}{l} = \Delta\rho.g.h.w \tag{3.33}$$

The ratio of the horizontal force to vertical force yields a dimensionless group called Buoyancy number which is useful in predicting dominance of horizontal or vertical flow:

$$N_{Bu} = \frac{12\mu}{\Delta\rho.g.w^3}.\frac{Q_h}{h} \tag{3.34}$$

Buoyancy number is the ratio of the axial flow velocity to the typical convection velocity, driven by gravity due to density differences. The lower the Buoyancy number, the stronger the convection mechanism. This dimensionless parameter is an indicator of the relative importance of convection and horizontal flow. It can be observed from Eq. 3.34 that N_{Bu} is extremely sensitive to changes in the width of the fracture.

As mentioned before, in real placement designs, it is assumed that proppants are uniformly distributed inside the fracture. However, strong gravity driven motions can cause this distribution uniformity to be lost over the total or part of the fracture height. Production from the upper section of the pay-zone can be dramatically reduced if proppants did not extend vertically through the fracture height and instead misplaced at the bottom of the fracture.

Comparing settling and convection velocities (Eqs. 3.28 and second term of Eq. 3.26), it can be concluded that convection is scaled to fracture width while settling is scaled to proppant diameter. Since proppant entry requirement states that the fracture width should be at least 4 to 5 times larger than the proppant diameter and also convection is related to width to the power of two, while settling is related to proppant diameter to the power of two, it is reasonable to expect that convection has a much larger effect than settling on proppant placement.

As mentioned before, convection transport depends on the density difference, which is a function of concentration. Therefore, a correct modelling of convectively driven flow requires that the numerical method of solution has the capability of capturing sharp concentration fronts.

3.4 Finite Volume Formulation of Proppant Transport Equation

In mathematical books, hyperbolic PDEs which describe the process of transport of material are generally written as:

$$\frac{\partial q}{\partial t}+\frac{\partial f}{\partial x}+\frac{\partial g}{\partial y}=0 \tag{3.35}$$

where q is the conservative variable to be advected and f and g are the flux vector. Comparing Eqs. 3.30 and 3.48, we can say that in proppant transport, the conserved variable is:

$$q = cw \tag{3.36}$$

And the components of proppant mass flux vector are:

$$f = u_p cw = u_p q = R_{ret} u_f cwq \tag{3.37}$$

$$g = v_p cw = v_p g = (v_f - v_{set})cw \tag{3.38}$$

Proppant velocities in these equations determine the speed of information propagation.

As a starting point, we consider the 1-Dimensional form of Eq. 3.35:

$$\frac{\partial(\mathrm{cw})}{\partial \mathrm{t}}+\frac{\partial(\mathrm{u_p cw})}{\partial \mathrm{x}}=0 \tag{3.39}$$

All the subsequent materials can be extended to multi-dimensional problems without the loss of generality. In finite volume method, integral form of conservation laws is dealt with. In Eqs. 3.36 and 3.37, we know that the terms (cw) and ($u_p$cw) are functions of x and t (time). So, we will use the following notations for these two parameters:

$$cw = c(x,t)w(x,t) \tag{3.40}$$

$$u_p cw = u_p(x,t)c(x,t)w(x,t) \tag{3.41}$$

If we consider the grid shown in Fig. 3.2 and integrate Eq. 3.39 from $x_{i-0.5}$ to $x_{i+0.5}$ we will obtain:

$$\frac{d}{dt}\left[\int_{x_{i-\frac{1}{2}}}^{x_{i+\frac{1}{2}}} c(x,t)w(x,t)dx\right] + \int_{x_{i-\frac{1}{2}}}^{x_{i+\frac{1}{2}}}[\frac{d}{dx}(u_p(x,t)c(x,t)w(x,t))]dx = 0 \tag{3.42}$$

However, we know that:

$$\int_{x_{i-\frac{1}{2}}}^{x_{i+\frac{1}{2}}}[\frac{d}{dx}(u_p(x,t)c(x,t)w(x,t))]dx \tag{3.43}$$

$$= u_p(x_{i+\frac{1}{2}},t)c(x_{i+\frac{1}{2}},t)w(x_{i+\frac{1}{2}},t) - u_p(x_{i-\frac{1}{2}},t)c(x_{i-\frac{1}{2}},t)w(x_{i-\frac{1}{2}},t)$$

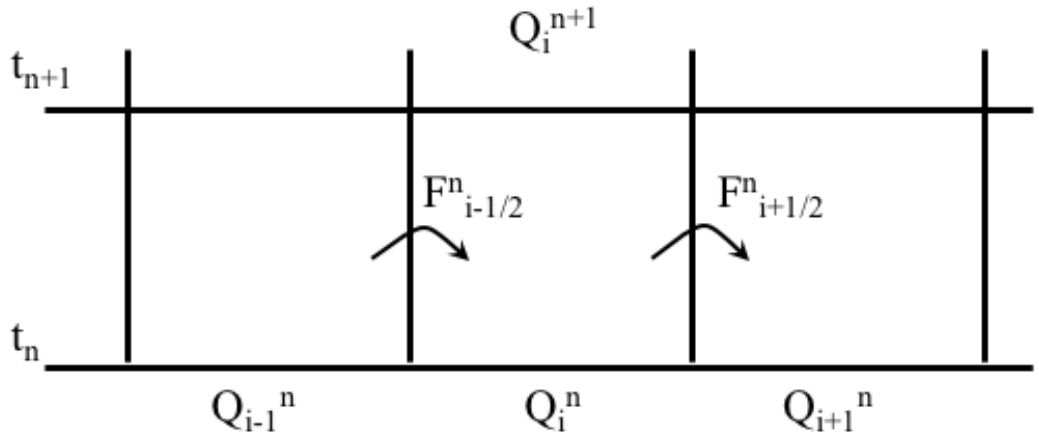

Figure 3.2: Illustration of a FVM for updating the cell average $Q^i_{n^i}$ by Fluxes at the Cell Edges. Shown in x–t Space

Now integrating Eq. 3.42 in time from t_n to t_{n+1} yields:

$$\int_{t_n}^{t_{n+1}} \frac{d}{dt}\left[\int_{x_{i-\frac{1}{2}}}^{x_{i+\frac{1}{2}}} c(x,t)w(x,t)dx\right]dt + \int_{t_n}^{t_{n+1}}\left[u_p(x_{i+\frac{1}{2}},t)c(x_{i+\frac{1}{2}},t)w(x_{i+\frac{1}{2}},t)\right]dt \tag{3.44}$$

$$-\int_{t_n}^{t_{n+1}}\left[u_p(x_{i-\frac{1}{2}},t)c(x_{i-\frac{1}{2}},t)w(x_{i-\frac{1}{2}},t)\right]dt = 0$$

Again we know that the first term can be written as:

$$\int_{t_n}^{t_{n+1}} \frac{d}{dt}\left[\int_{x_{i-\frac{1}{2}}}^{x_{i+\frac{1}{2}}} c(x,t)w(x,t)dx\right]dt \tag{3.45}$$

$$= \int_{x_{i-\frac{1}{2}}}^{x_{i+\frac{1}{2}}} c(x,t_{n+1})w(x,t_{n+1})dx - \int_{x_{i-\frac{1}{2}}}^{x_{i+\frac{1}{2}}} c(x,t_n)w(x,t_n)dx$$

We can use this expression to develop a time marching algorithm as:

$$\int_{x_{i-\frac{1}{2}}}^{x_{i+\frac{1}{2}}} c(x,t_{n+1})w(x,t_{n+1})dx \tag{3.46}$$

$$= \int_{x_{i-\frac{1}{2}}}^{x_{i+\frac{1}{2}}} c(x,t_n)w(x,t_n)dx$$

$$-\{\int_{t_n}^{t_{n+1}} \left[u_p(x_{i+\frac{1}{2}},t)c(x_{i+\frac{1}{2}},t)w(x_{i+\frac{1}{2}},t)\right]dt$$

$$-\int_{t_n}^{t_{n+1}} \left[u_p(x_{i-\frac{1}{2}},t)c(x_{i-\frac{1}{2}},t)w(x_{i-\frac{1}{2}},t)\right]dt\}$$

Now, if we use the fact that the average value of a conserved quantity over a gridblock i at time t_n can be expressed as:

$$Q_i^n \approx \frac{1}{\Delta x}\int_{x_{i-\frac{1}{2}}}^{x_{i+\frac{1}{2}}} c(x,t_n)w(x,t_n)dx \tag{3.47}$$

$$Q_i^{n+1} \approx \frac{1}{\Delta x}\int_{x_{i-\frac{1}{2}}}^{x_{i+\frac{1}{2}}} c(x,t_{n+1})w(x,t_{n+1})dx \tag{3.48}$$

and divide Eq. 3.46 by Δx, the above averaging definitions gives:

$$Q_i^{n+1} = Q_i^n - \frac{\Delta t}{\Delta x}(F_{i+\frac{1}{2}}^n - F_{i-\frac{1}{2}}^n) \tag{3.49}$$

where:

$$F_{i-\frac{1}{2}}^n = \frac{1}{\Delta t}\int_{t_n}^{t_{n+1}} \left[u_p\left(x_{i+\frac{1}{2}},t\right)c\left(x_{i+\frac{1}{2}},t\right)w\left(x_{i+\frac{1}{2}},t\right)\right]dt \tag{3.50}$$

$$F_{i+\frac{1}{2}}^n = \frac{1}{\Delta t}\int_{t_n}^{t_{n+1}} \left[u_p\left(x_{i-\frac{1}{2}},t\right)c\left(x_{i-\frac{1}{2}},t\right)w\left(x_{i-\frac{1}{2}},t\right)\right]dt \tag{3.51}$$

The function F can be seen as an approximation to the average flux along boundary.

Eq. 3.39 is a non-linear advection equation since velocity of proppant changes with space and time. Therefore, special techniques suitable for non-linear hyperbolic problems must be utilized. In solving this kind of hyperbolic PDEs, different capturing schemes have been developed which can be classified as classical or traditional and modern techniques.

In the traditional techniques, the finite difference method is employed, while in the modern techniques, the finite volume method (which for rectangular grids can be viewed as a generalization of the finite difference method) is used. Here, we briefly present the finite volume discretization of the hyperbolic equations presented above. The finite difference discretizations can also be explained in the more general finite volume discretization.

In the finite volume method, the integral form of the partial differential equations is developed. As we explained, in one dimensional space, the finite volume discretization of Eq. 3.39 is:

$$Q_i^{n+1} = Q_i^n - \frac{\Delta t}{\Delta x}(F^n_{i+\frac{1}{2}} - F^n_{i-\frac{1}{2}}) \tag{3.52}$$

All the terms in the above discretization are average values of the variables over the i^{th} interval and at time t_n. e.g.:

$$\mathrm{Q_i^n} \approx \frac{1}{\Delta \mathrm{x}} \int_{\mathrm{x_{i-\frac{1}{2}}}}^{\mathrm{x_{i+\frac{1}{2}}}} \mathrm{q(x, t_n)dx} \tag{3.53}$$

$$F^n_{i-\frac{1}{2}} \approx \frac{1}{\Delta t} \int_{t_n}^{t_{n+1}} f(q\left(x_{i-\frac{1}{2}}, t\right))dt \tag{3.54}$$

Any numerical method for solving hyperbolic equations depends on the choice of F, which is called the numerical flux function.

Since the solution of this kind of PDE may involve shocks or steep gradients, shock capturing methods with the ability of tracking discontinuity and maintaining accuracy and stability in smooth regions have been developed (Leveque, 2004). In the next section, a review of the conventional finite difference methods and recent shock capturing methods is provided. Our approach should not be confused with shock tracking or front tracking methods in which a combination of the finite difference or finite volume methods (in smooth regions) with an explicit method of tracking the location of discontinuity is employed. The goal of shock-capturing methods is to automatically capture discontinuities in the solution, without having to explicitly track them (Davis, 1992).

3.5 Review of Numerical Methods in Solving Hyperbolic PDEs

In solving the hyperbolic equations, traditional finite difference methods generate either non-physical oscillations or numerical diffusion in the presence of shocks (Leveque, 2004). This large error in the solution technique was the motivation behind the development of shock capturing schemes. In spectral methods, these oscillations are called Gibbs phenomena and their magnitudes do not reduce by refining the mesh. Application of such methods to simulate proppant transport often leads to instabilities since transport of proppant is a non-linear problem and contains discontinuities. In this section, we review some of the most important techniques in solving the first-order hyperbolic problems and apply them in a numerical experiment to investigate the capability of each method.

Before 1987, two numerical methods were largely used to reduce or eliminate the spurious oscillations near shocks. The first method is called artificial viscosity and as the name implies a diffusive term is added to the discretization scheme. The amount of diffusion added in artificial viscosity methods is problem dependent. In other words, the smearing of the solution can be too large that it sacrifices the accuracy. The second method was application of flux limiters which uses total variation diminishing (TVD) property. In these methods, the discretization scheme is non-oscillatory near the discontinuity. However, these methods are first-order accurate near smooth regions as well. We will describe some of the artificial viscosity and flux limiter (they are also called slope limiter) methods in this section.

The first proposed successful idea in obtaining a uniformly high order accurate, yet non-oscillatory results was proposed by Harten et al. in 1987 (Harten et al., 1987). The method was named ENO which stands for essentially non-Oscillatory. These researchers used Newton divided differences to measure the local smoothness of the stencils. Later on WENO schemes (Weighted ENO) were developed based on ENO schemes to reduce the computational cost and increase the order of the accuracy (Liu et al., 1994, Jiang and Shu, 1996). We will discuss the application of these state of the art methods to the hyperbolic transport equations in the following section.

It should be mentioned that the study of ENO and WENO method is still very active. For example, ENO schemes based on point values and TVD Runge-Kutta time discretizations (Shu and Osher, 1989, Osher, 1991), Biased ENO (Shu, 1990, Fatemi et al., 1991), ENO based on

other than polynomial building blocks (Christofi, 1995, Iske and Soner, 1996), or combination of ENO with spectral methods (Cai and Shu, 1993) have been proposed with applications in many different fields. Obviously, we cannot describe nor apply all the methods and modifications in this short chapter. Only the original ENO and WENO methods will be used in later chapters to simulate the process of proppant transport.

3.5.1 Benchmark Test to Evaluate Different Solution Techniques

To test the capability of the capturing techniques discussed here, we use a numerical benchmark test with known exact solution. We consider a 1D linear advection equation (Eq. 3.55) with unit velocity (Garcia-Navarroa and Vazquez-Cendon, 2000).

$$\frac{\partial q}{\partial t}+\frac{\partial q}{\partial x}=0, \qquad -1<x<1 \tag{3.55}$$

For the initial condition of our numerical experiment, we consider a combination of a Gaussian wave, a square wave, a sharp triangle and a half ellipse:

$$q(x,0)=q_0(x) \tag{3.56}$$

$$q_0(x)=\begin{cases}\frac{1}{6}(G(x,\beta,z-\delta)+G(x,\beta,z+\delta)+4G(x,\beta,z)), & -0.8\le x\le -0.6\\ 1, & -0.4\le x\le -0.2\\ 1-|10(x-0.1)|, & 0\le x\le 0.2\\ \frac{1}{6}(H(x,\alpha,a-\delta)+H(x,\alpha,a+\delta)+4H(x,\alpha,a)), & 0.6\le x\le 0.8\\ 0, & otherwise\end{cases} \tag{3.57}$$

The functions G and H are defined as:

$$G(x,\beta,z)=e^{-\beta(x-z)^2} \tag{3.58}$$

$$H(x,\alpha,a)=\sqrt{max(1-\alpha^2(x-a)^2),0} \tag{3.59}$$

Also we set:

$$z=-0.7,\delta=0.005,\beta=\frac{log(2)}{36\delta^2},a=0.5,\alpha=10 \tag{3.60}$$

The exact solution of this problem is the translation of the initial solution at unit speed:

$$q(x,t)=q_0(x-t) \tag{3.61}$$

In other words, the shape of the initial condition does not change with time and it simply translates in the model. Fig. 3.3 shows a schematic of the initial condition.

We used a periodic boundary condition on the left and right sides of the model and ran the simulation for 2 seconds. For this model problem, we assigned a Courant number of 0.9 for all the schemes.

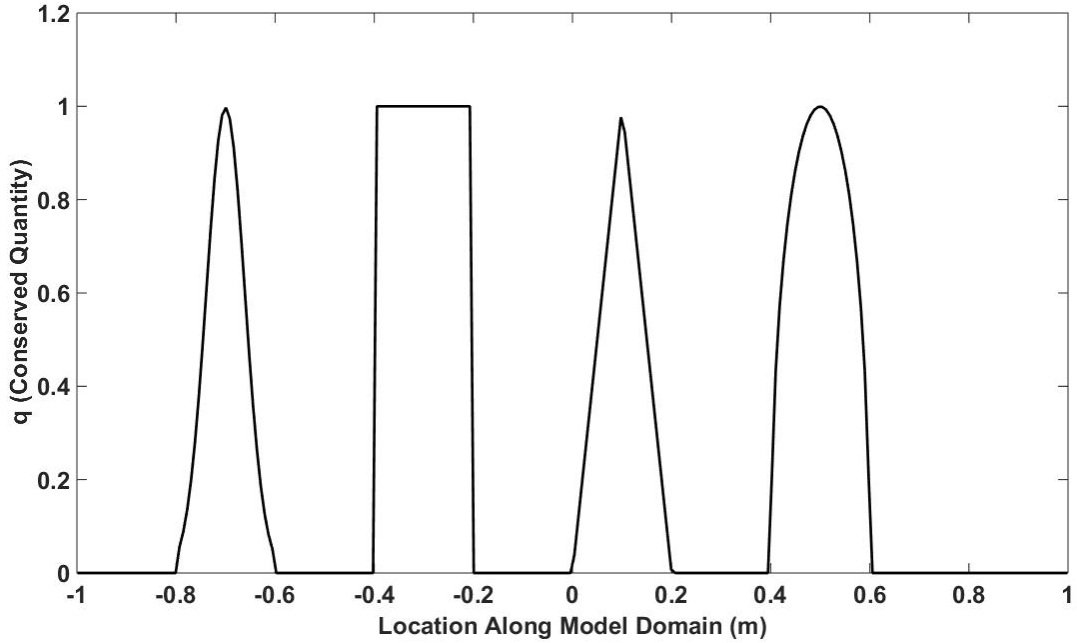

Figure 3.3: Numerical Experiment with Gaussian, Square, Sharp Triangle, and Half Ellipse Initial Waves

3.5.2 First-Order Finite Difference Schemes

First or second-order finite difference methods have been traditionally used in capturing shocks. A very important family of the first-order schemes is the upwind methods which in its most general case becomes Godunov scheme (Fennema and Chaudhry, 1987). Upwind schemes can cause strong diffusion and significant smearing in the solutions. In addition, the numerical method becomes very complex for non-linear problems. Godunov scheme applies to system of hyperbolic equations and it reduces to upwind method if applied to a single PDE. The numerical flux of both methods depends on the direction of propagation of information or the sign of velocity. The numerical flux of upwind method in Eq. 3.49 can be written as:

$$\begin{cases} F^n_{i-\frac{1}{2}} = \bar{u}Q_{i-1} & if\ u > 0 \\ F^n_{i-\frac{1}{2}} = \bar{u}Q_i & if\ u < 0 \end{cases} \tag{3.62}$$

which can be written as a single equation:

$$F^n_{i-\frac{1}{2}} = \bar{u}^- Q_i + \bar{u}^+ Q_{i-1} \tag{3.63}$$

where

$$\bar{u}^+ = \max(\bar{u}, 0) \tag{3.64}$$

$$\bar{u}^- = \min(\bar{u}, 0) \tag{3.65}$$

and the final discretization of upwind method would be:

$$Q_i^{n+1} = Q_i^n - \frac{\Delta t}{\Delta x}[\bar{u}^+(Q_i^n - Q_{i-1}^n) + \bar{u}^-(Q_{i+1}^n - Q_i^n)] \tag{3.66}$$

Besides upwind method, Lax method is another popular first-order scheme. The centered difference discretization of advection equation is unconditionally unstable. In Lax or Lax-Friedrichs scheme (Lax, 1954), the central difference scheme is stabilized by replacing Q_i^n term with the average $0.5(Q_{i+1}^n + Q_{i-1}^n)$ term in the discretization. Lax method is known for its large dissipation error when Courant number is not 1 and produces a leading phase error (Pletcher et al., 1997). The numerical flux and final discretization of Lax-Friedrichs scheme are:

$$F^n_{i-\frac{1}{2}} = \frac{1}{2}(u_{i-1}Q^n_{i-1} + u_i Q^n_i) - \frac{\Delta x}{2\Delta t}(Q^n_i - Q^n_{i-1}) \tag{3.67}$$

$$Q_i^{n+1} = \frac{1}{2}(Q^n_{i-1} + Q^n_{i+1}) - \frac{\Delta t}{2\Delta x}[u_{i+1}Q^n_{i+1} - u_{i-1}Q^n_{i-1}] \tag{3.68}$$

From Fig. 3.4, it is evident that first-order upwind and Lax-Fridrichs methods are monotone everywhere. In other words, they do not lead to oscillations anywhere in the solution. However, they have poor accuracy due to large dissipation.

The reason that each of these schemes lead to smearing of the solution can be explained by utilizing modified equation concept. Here we describe the modified equation (Warming and Hyett, 1974) of upwind method, but for brevity skip the modified equation of other techniques.

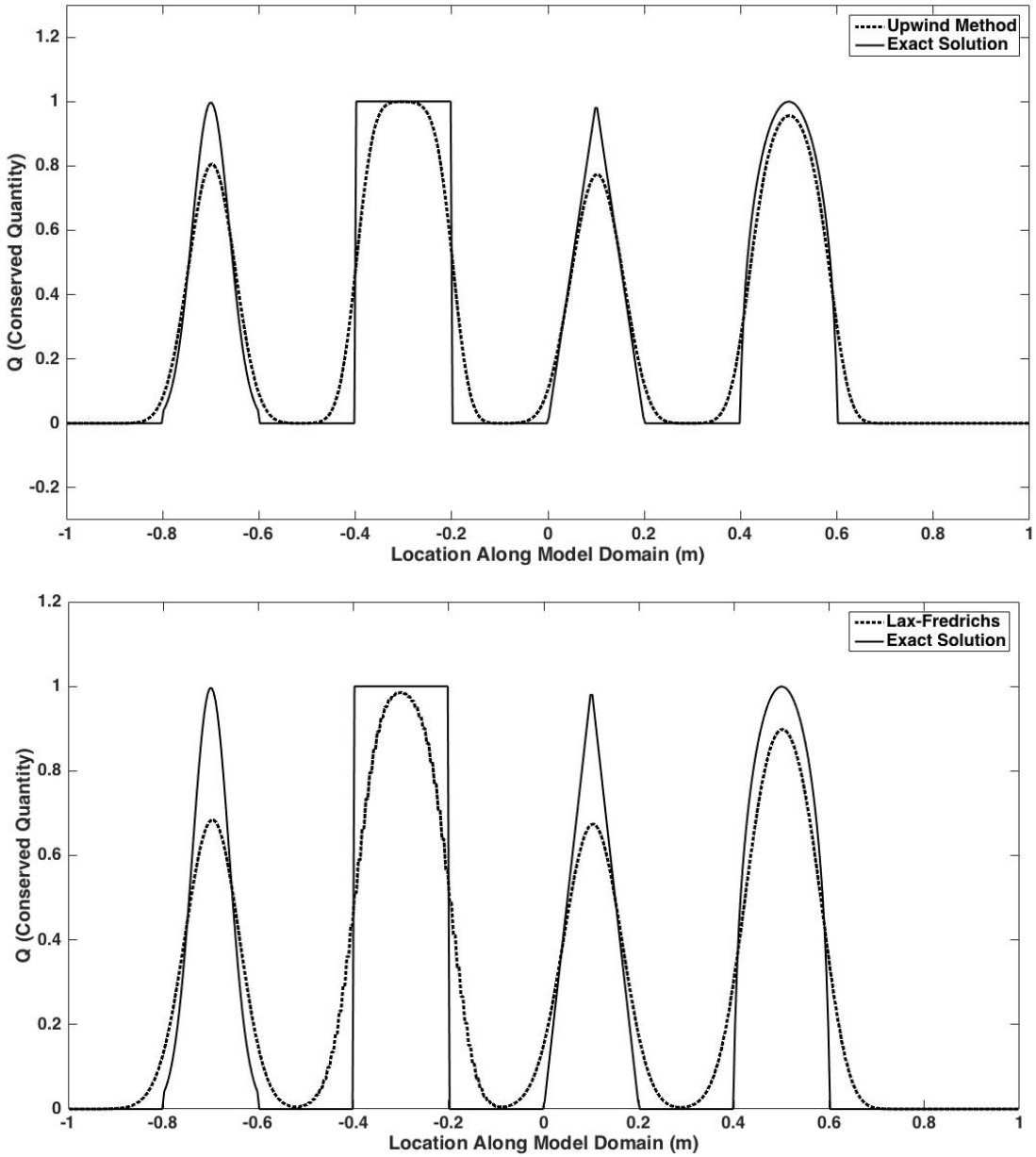

Figure 3.4: Results of First-Order Schemes after 2 Seconds, Upwind (Top) and Lax-Fredrichs (Bottom), Monotonic without Oscillation

From Taylor series expansion, we know that:

$$Q_i^{t+\Delta t} = Q_i^t + \Delta t \frac{\partial Q_i^t}{\partial t} + \frac{(\Delta t)^2}{2}\frac{\partial^2 Q_i^t}{\partial t^2} + \frac{(\Delta t)^3}{6}\frac{\partial^3 Q_i^t}{\partial t^3} + \cdots \tag{3.69}$$

$$Q_{i-\Delta x}^t = Q_i^t - \Delta x \frac{\partial Q_i^t}{\partial x} + \frac{(\Delta x)^2}{2}\frac{\partial^2 Q_i^t}{\partial x^2} - \frac{(\Delta x)^3}{6}\frac{\partial^3 Q_i^t}{\partial x^3} + \cdots \tag{3.70}$$

Now, if we substitute above formulations in upwind discretization equation, assuming u > 0, after some manipulation we obtain:

$$\frac{\partial Q_i^t}{\partial t} + u\frac{\partial Q_i^t}{\partial x} = -\frac{\Delta t}{2}\frac{\partial^2 Q_i^t}{\partial t^2} + \frac{u\Delta x}{2}\frac{\partial^2 Q_i^t}{\partial x^2} - \frac{(\Delta t)^2}{6}\frac{\partial^3 Q_i^t}{\partial t^3} - \frac{u(\Delta x)^2}{6}\frac{\partial^3 Q_i^t}{\partial x^3} + \cdots \tag{3.71}$$

The left-hand side of the above equation corresponds to the original hyperbolic PDE, however, substituting Taylor series expansion in upwind scheme did not obtain a zero right hand side. The result can be better interpreted if we also substitute all the time derivatives with space derivatives. Taking the partial time derivative of above equation yields:

$$\frac{\partial^2 Q_i^t}{\partial t^2} + u\frac{\partial^2 Q_i^t}{\partial x \partial t} = -\frac{\Delta t}{2}\frac{\partial^3 Q_i^t}{\partial t^3} + \frac{u\Delta x}{2}\frac{\partial^3 Q_i^t}{\partial x^2 \partial t} - \frac{(\Delta t)^2}{6}\frac{\partial^4 Q_i^t}{\partial t^4} - \frac{u(\Delta x)^2}{6}\frac{\partial^4 Q_i^t}{\partial x^3 \partial t} + \cdots \tag{3.72}$$

and taking the partial space derivative of the same equation and multiplying by –u gives:

$$-u\frac{\partial^2 Q_i^t}{\partial t \partial x} - u^2\frac{\partial^2 Q_i^t}{\partial x^2} = \frac{u\Delta t}{2}\frac{\partial^3 Q_i^t}{\partial t^2 \partial x} - \frac{u^2\Delta x}{2}\frac{\partial^3 Q_i^t}{\partial x^3} + \frac{u(\Delta t)^2}{6}\frac{\partial^4 Q_i^t}{\partial t^3 \partial x} + \frac{u^2(\Delta x)^2}{6}\frac{\partial^4 Q_i^t}{\partial x^4} - \cdots \tag{3.73}$$

Adding the two equations gives:

$$\frac{\partial^2 Q_i^t}{\partial t^2} = u^2\frac{\partial^2 Q_i^t}{\partial x^2} + \Delta t\left(-\frac{\partial^3 Q_i^t}{2\partial t^3} + \frac{u}{2}\frac{\partial^3 Q_i^t}{\partial t^2 \partial x} + O[\Delta t]\right) + \Delta x\left(\frac{u}{2}\frac{\partial^3 Q_i^t}{\partial x^2 \partial t} - \frac{u^2}{2}\frac{\partial^3 Q_i^t}{\partial x^3} + O[\Delta x]\right) \tag{3.74}$$

In a similar manner, the following equations can be obtained for other time derivatives:

$$\frac{\partial^3 Q_i^t}{\partial t^3} = -u^3\frac{\partial^3 Q_i^t}{\partial x^3} + O[\Delta t, \Delta x] \tag{3.75}$$

$$\frac{\partial^3 Q_i^t}{\partial t^2 \partial x} = u^2\frac{\partial^3 Q_i^t}{\partial x^3} + O[\Delta t, \Delta x] \tag{3.76}$$

$$\frac{\partial^3 Q_i^t}{\partial x^2 \partial t} = -u\frac{\partial^3 Q_i^t}{\partial x^3} + O[\Delta t, \Delta x] \tag{3.77}$$

Substituting all the time derivatives of Eq. 3.71 with above relationships we obtain:

$$\frac{\partial Q_i^t}{\partial t} + u\frac{\partial Q_i^t}{\partial x} = \frac{u\Delta x}{2}(1-v)\frac{\partial^2 Q_i^t}{\partial x^2} - \frac{u(\Delta x)^2}{6}(2v^2 - 3v + 1)\frac{\partial^3 Q_i^t}{\partial x^3} + O[(\Delta x)^3, (\Delta x)^2\Delta t, \Delta x(\Delta t)^2, (\Delta t)^3] \tag{3.78}$$

where v is the Courant number. Eq. 3.78 is called the modified equation of upwind scheme. It is obvious that when upwind discretization is used, it is actually Eq. 3.78 that is solved and not Eq. 3.68. The right-hand side of the modified equation contains both even and odd derivatives. The effect of even derivatives on solution is similar to the diffusion equation that was discussed

earlier in this chapter. Even derivatives are called artificial viscosity and they reduce all the gradients in the solution, similar to Eq. B-12 in Appendix B. This effect is also called numerical dissipation. The direct effect of odd derivatives is distortion of the phase relations between various wave. This effect is called numerical dispersion. The combined effect of dissipation and dispersion is referred to as numerical diffusion, which spread out sharp fronts in the solution.

3.5.3 Higher Order Finite Difference Schemes

In most cases 1st-order schemes, are not employed to solve PDEs due to their intrinsic inaccuracy. Higher order shock capturing techniques are utilized to obtain better accuracy. Perhaps the simplest second-order scheme is the Leap Frog method. Applying this scheme to 1st order hyperbolic equation gives:

$$Q_i^{n+1} = Q_i^{n-1} - \frac{u\Delta t}{\Delta x}(Q_{i+1}^n - Q_{i-1}^n) \tag{3.79}$$

A disadvantage of this method is that for the first time step two initial conditions should be specified at two time levels.

Lax-Wendroff scheme (Lax and Wendroff, 1960), which is one of the earliest 2nd order finite difference schemes, can be obtained from Taylor series expansion. This scheme can be written as:

$$F_{i-\frac{1}{2}}^n = \frac{1}{2}u(Q_{i-1}^n + Q_i^n) - \frac{1}{2}\frac{\Delta t}{\Delta x}u^2(Q_i^n - Q_{i-1}^n) \tag{3.80}$$

$$Q_i^{n+1} = Q_i^n - \frac{\Delta t}{2\Delta x}u(Q_{i+1}^n - Q_{i-1}^n) + \frac{1}{2}\left(\frac{\Delta t}{\Delta x}u\right)^2(Q_{i-1}^n - 2Q_i^n + Q_{i+1}^n) \tag{3.81}$$

The Lax-Wendroff scheme has predominantly lagging phase error except for large wave numbers with $0.5 < \nu < 1$, where ν is Courant number. It is second-order accurate in both space and time.

There is another version of the Lax-Wendroff scheme, which is called Richtmyer two-step Lax-Wendroff. This scheme is more suitable for nonlinear problems. It is second-order accurate with the same amplification factor and relative phase shift error as the original Lax-Wendroff. In the first step of this scheme a Lax- Friedrichs scheme is applied at the mid-point for the half time step:

$$Q_{i-\frac{1}{2}}^{n+\frac{1}{2}} = \frac{1}{2}(Q_{i-1}^{n} + Q_{i}^{n}) - \frac{\Delta t}{2\Delta x}[f(Q_{i}^{n}) - f(Q_{i-1}^{n})] \tag{3.82}$$

For the remaining of the time step, a leap-frog scheme is applied.

$$F_{i-\frac{1}{2}}^{n} = f(Q_{i-\frac{1}{2}}^{n+\frac{1}{2}}) \tag{3.83}$$

The Lax-Wendroff and two-step Lax-Wendroff schemes are equivalent when applied to linear advection equations.

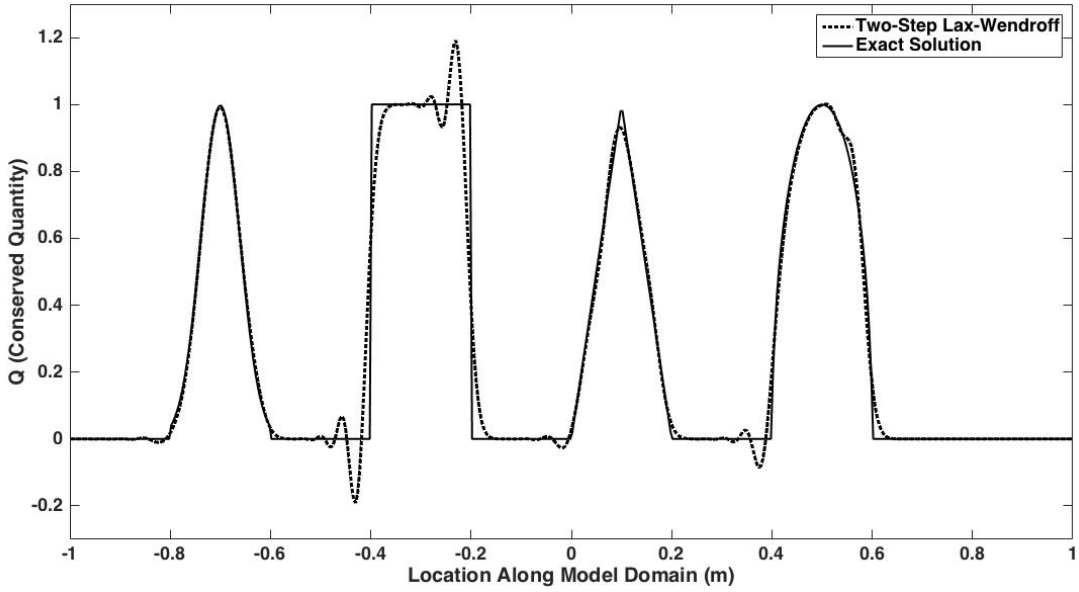

Figure 3.5: Two-step Lax-Wendroff Richtmyer Method, Good Accuracy in Smooth Regions, Oscillations Near the Shocks

The MacCormack method (Wesseling, 2001) is a modified form of two-step Lax-Wendroff scheme in which a temporary value of Q^{n+1} is calculated in the first step and is corrected in the second step. In the predictor equation, a forward difference for space derivative is employed, while in the corrector equation a backward difference is used. The differencing scheme can be reversed, depending on the problem at hand:

Predictor: $\overline{Q_i^{n+1}} = Q_i^n - \frac{u\Delta t}{\Delta x}(Q_{i+1}^n - Q_i^n)$ (3.84)

Corrector: $Q_i^{n+1} = \frac{1}{2}[Q_i^n + \overline{Q_i^{n+1}} - \frac{c\Delta t}{\Delta x}(\overline{Q_i^{n+1}} - \overline{Q_{i-1}^{n+1}})]$ (3.85)

Beam-Warming scheme (Beam and Warming, 1978) is a variation of MacCormack method, which uses the same differencing in the predictor and corrector steps, depending on the sign of the velocity.

$$F^n_{i-\frac{1}{2}} = uQ^n_{i-1} + \frac{1}{2}u(1 - \frac{\Delta t}{\Delta x}u)(Q^n_{i-1} - Q^n_{i-2}) \tag{3.86}$$

$$Q^{n+1}_i = Q^n_i - \frac{\Delta t}{2\Delta x}u(3Q^n_i - 4Q^n_{i-1} + Q^n_{i-2}) + \frac{1}{2}\left(\frac{\Delta t}{\Delta x}u\right)^2 (Q^n_i - 2Q^n_{i-1} + Q^n_{i-2}) \tag{3.87}$$

This scheme, which is a 2nd order upwind scheme, has a predominantly leading phase error for $0<\nu<1$ and predominantly lagging phase error for $1<\nu<2$. On the other hand, the Lax-Wendroff method has opposite phase error for $0<\nu<1$. Therefore, a linear combination of the two methods can reduce dispersive error of the scheme. Fromm's method of zero-average phase error (Wesseling, 2001) is based on this observation:

$$Q^{n+1}_i = Q^n_i - \frac{\Delta t}{\Delta x}u(Q^n_{i+1} + 3Q^n_i - 5Q^n_{i-1} + Q^n_{i-2}) - \left(\frac{\Delta t}{2\Delta x}u\right)^2 (Q^n_{i+1} - Q^n_i - Q^n_{i-1} + Q^n_{i-2}) \tag{3.88}$$

Figure 3.6 is another example of application of 2nd order methods to advection equation. These methods provide good accuracy in smooth regions, while giving oscillations close to discontinuity. The oscillations happening in the vicinity of the discontinuity show the dispersive nature of these methods.

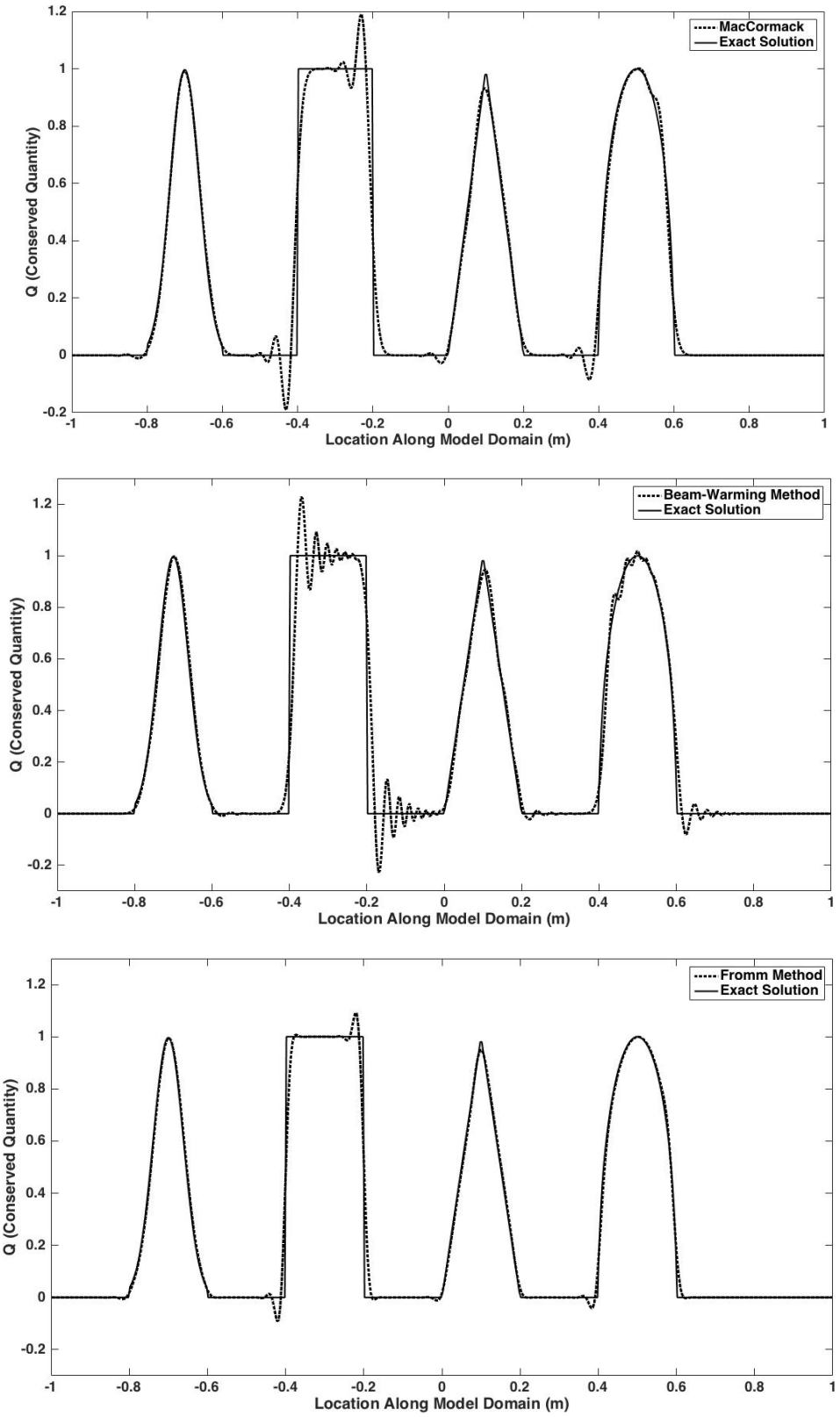

Figure 3.6: MacCormack Method (Top), Beam-Warming Method (Middle) and Fromm's Method (Bottom) Good Accuracy in Smooth Regions, Oscillations Near the Shocks

The methods presented so far were either first-order or second-order accurate. There are a small number of 3rd order methods in the literature. Rusanov, (1970) and Burstein and Mirin, (1970), separately developed the following third-order three-step scheme:

$$Step\ 1: \quad Q_{i+1/2}^{(1)} = \frac{1}{2}(Q_{i+1}^{n} + Q_{i}^{n}) - \frac{1}{3}\frac{u\Delta t}{\Delta x}(Q_{i+1}^{n} - Q_{i}^{n}) \tag{3.89}$$

$$Step\ 2: \quad Q_{i}^{(2)} = Q_{i}^{n} - \frac{2}{3}\frac{u\Delta t}{\Delta x}(Q_{i+1/2}^{(1)} - Q_{i-1/2}^{(1)}) \tag{3.90}$$

$$Step\ 3: \quad Q_{i}^{n+1} \tag{3.91}$$
$$= Q_{i}^{n} - \frac{1}{24}\frac{u\Delta t}{\Delta x}(-2Q_{i+2}^{n} + 7Q_{i+1}^{n} - 7Q_{i-1}^{n} + 2Q_{i-2}^{n})$$
$$- \frac{3}{8}\frac{u\Delta t}{\Delta x}\left(Q_{i+1}^{(2)} - Q_{i-1}^{(2)}\right) - \frac{\omega}{24}(Q_{i+2}^{n} - 4Q_{i+1}^{n} + 6Q_{i}^{n} - 4Q_{i-1}^{n} + Q_{i-2}^{n})$$

where for stability requirements:

$$4\left(\frac{u\Delta t}{\Delta x}\right)^{2} - (\frac{u\Delta t}{\Delta x})^{4} \leq \omega \leq 3 \tag{3.92}$$

Another famous third-order method was developed by Warming et al. in 1973 and is called Warming-Kutler-Lomax. The method can be written as:

$$Step\ 1: \quad Q_{i}^{(1)} = Q_{i}^{n} - \frac{2}{3}\frac{u\Delta t}{\Delta x}(Q_{i+1}^{n} - Q_{i}^{n}) \tag{3.93}$$

$$Step\ 2: \quad Q_{i}^{(2)} = \frac{1}{2}\left(Q_{i}^{n} + Q_{i}^{(1)}\right) - \frac{2}{3}\frac{u\Delta t}{\Delta x}(Q_{i}^{(1)} - Q_{i-1}^{(1)}) \tag{3.94}$$

$$Step\ 3: \quad Q_{i}^{n+1} \tag{3.95}$$
$$= Q_{i}^{n} - \frac{1}{24}\frac{u\Delta t}{\Delta x}(-2Q_{i+2}^{n} + 7Q_{i+1}^{n} - 7Q_{i-1}^{n} + 2Q_{i-2}^{n})$$
$$- \frac{3}{8}\frac{u\Delta t}{\Delta x}\left(Q_{i+1}^{(2)} - Q_{i-1}^{(2)}\right) - \frac{\omega}{24}(Q_{i+2}^{n} - 4Q_{i+1}^{n} + 6Q_{i}^{n} - 4Q_{i-1}^{n} + Q_{i-2}^{n})$$

High order finite difference schemes are non-dissipative with good accuracy near the smooth regions. However, they are prone to generating spurious oscillations across discontinuities or in the vicinity of large gradients in the solution (Leveque, 2004). In case the numerical oscillation becomes large, then the numerical method becomes inefficient to capture an accurate solution.

3.5.4 Artificial Viscosity

Lax- Friedrichs, Lax-Wendroff, and MacCormack methods belong to a class of solution methods that use artificial viscosity. This property is employed to introduce enough dissipation near

discontinuities to smear oscillations (Fig. 3.7). The amount of this artificial viscosity should be negligible close to smooth regions (Fennema and Chaudhry, 1990).

However, the difficulty with this approach is that it is hard to determine the amount of dissipation needed without causing unnecessary smearing. For this reason, the high-resolution methods were developed.

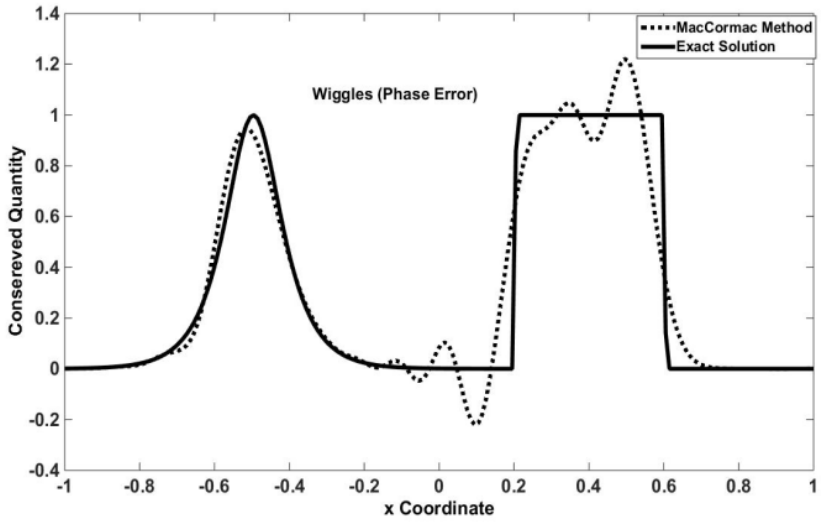

(a)

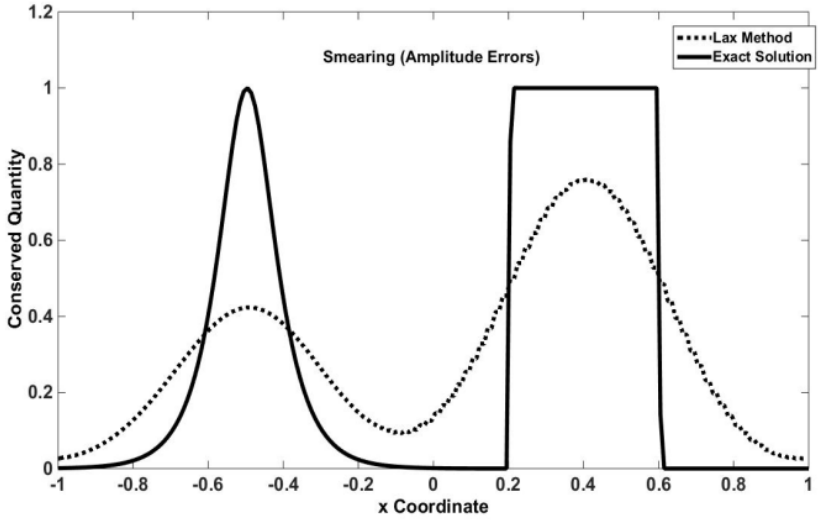

(b)

Figure 3.7: a) Comparison of MacCormack Method Result with Exact Solution Showing Numerical Distortion and b) Comparison of Lax Method Result with Exact Solution Showing Numerical Distortion Dissipation

3.5.5 High-Resolution Methods

In the past decade, attempts have been made to devise a method that can combine the monotone feature of first-order methods with high accuracy of higher order methods. This was achieved through high-resolution methods which are at least 2nd order accurate in smooth regions and non-oscillatory at discontinuities (Leveque, 2004). A measure of the oscillation in the total variation is given by:

$$TV(Q^n) = \sum_{i=-\infty}^{+\infty} |Q_i^n - Q_{i-1}^n| \tag{3.96}$$

It is obvious that in this definition more oscillations will give rise to more total variations. Therefore, to avoid oscillations it is necessary that the total variation decreases with time. Any numerical scheme that has this capability is called Total Variation Diminishing (TVD) scheme. In flux limiter schemes, limiters are imposed on numerical flux function such that higher order schemes are used in smooth regions, while lower order schemes are employed close to the discontinuity. This combination can be achieved through:

$$F_{i+\frac{1}{2}}^n = F_L(Q_i, Q_{i+1}) + \phi_{i+\frac{1}{2}}^n [F_H(Q_i, Q_{i+1}) - F_L(Q_i, Q_{i+1})] \tag{3.97}$$

where F_L denotes lower order flux function and F_H denotes higher order flux function. $\phi_{i+\frac{1}{2}}^n$ is called flux limiter which will be near zero closer to the discontinuities and around 1 close to the smooth data.

The definition of the limiter leads to a wide variety of other methods of this form. Flux Corrected Transport (FCT) scheme of Boris and Book (1973) is one of the earliest limiter applications. Other popular choices of limiters include the Superbee limiter (Roe, 1985), van Leer limiter (Van Leer, 1977), the Woodward limiter (Colella, 1985), the Minmod limiter (Colella, 1985) and the Monotone Upstream-centered Scheme for Conservation Laws (MUSCL) by van Leer (Colella, 1985). To be able to apply simpler 1D flux limiter schemes to advection equation, we utilized dimensional splitting, a description of which is given in section 3.5.6.

3.5.6 Dimensional Splitting

Dimensional splitting is a type of fractional step methods which can be used to transform a PDE with source term to a homogeneous and ordinary differential equation. The two sub-problems can be solved independently, with any scheme for each sub-problem. It can also be applied in

converting a multi-dimensional problem into several one-dimensional problems. The advection equation in 2D with source term can be written as:

$$\frac{\partial q}{\partial t} + u(x,y)\frac{\partial q}{\partial x} + v(x,y)\frac{\partial q}{\partial y} = \psi(x) \tag{3.98}$$

where u and v are velocities in the x and y directions and ψ(x) is a source term. In proppant injection application the source term is the injection rate of proppants. Now, applying dimensional splitting to Eq. 3.98, we obtain:

$$\frac{\partial q}{\partial t} = \psi(x) \tag{3.99}$$

$$\frac{\partial q}{\partial t} + u(x,y)\frac{\partial q}{\partial x} = 0 \tag{3.100}$$

$$\frac{\partial q}{\partial t} + v(x,y)\frac{\partial q}{\partial y} = 0 \tag{3.101}$$

Eq. 3.99 is an ordinary differential equation and can be integrated using standard methods for solving ODEs (e.g. Euler or Runge-Kutta methods, explained later in section 3.5.7. In the next step, the high-resolution methods can be applied to Eqs. 3.100 and 3.101 to advect the solution.

Figures 3.8 and 3.9 present the results of the simulations with high-resolution methods. It is evident from figures that the first-order schemes non-oscillatory property along with good accuracy of higher order methods is obtained in the higher order schemes.

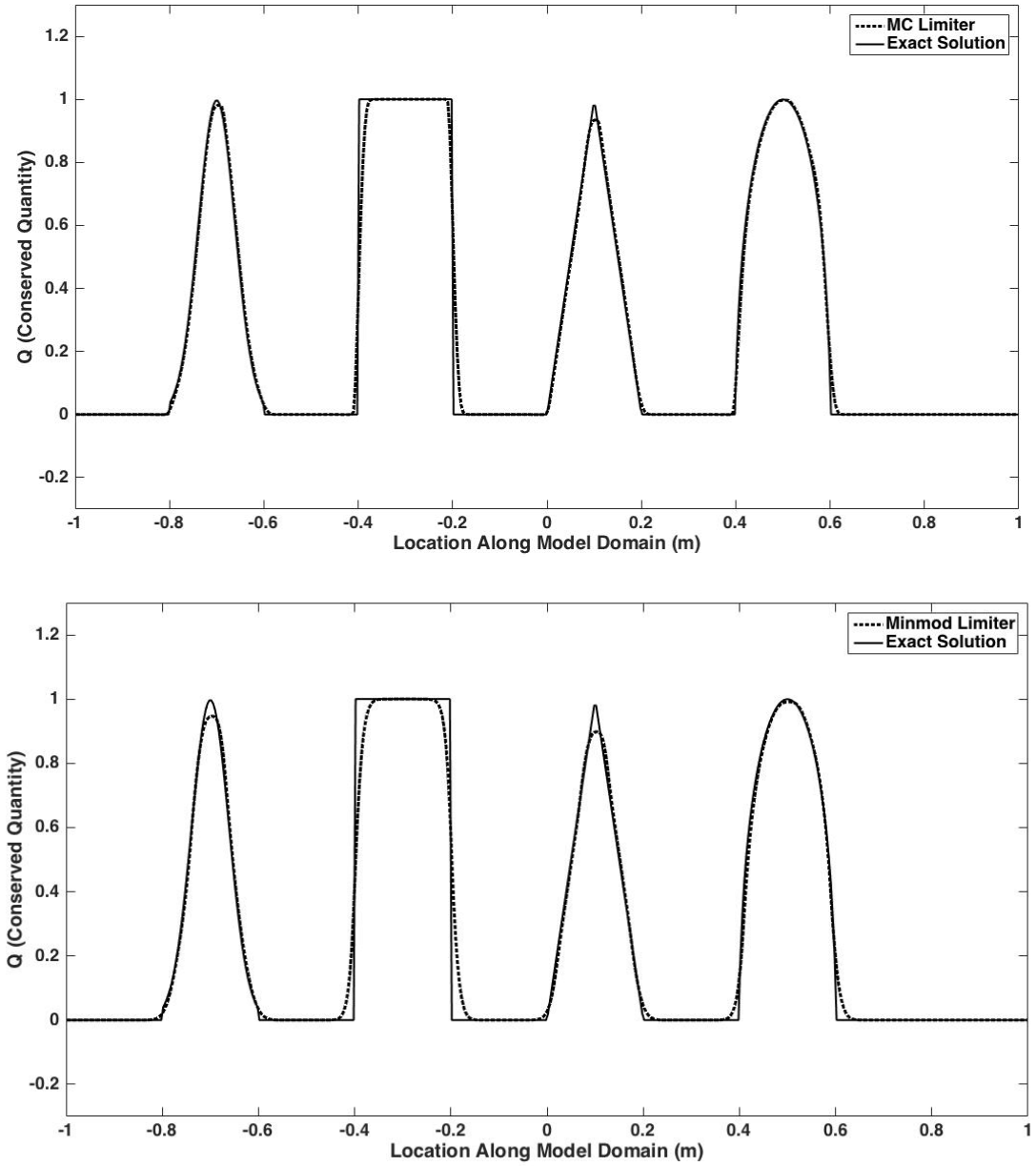

Figure 3.8: Flux Limiter Schemes: Accurate in Smooth Regions and 1st OrderNear Shocks

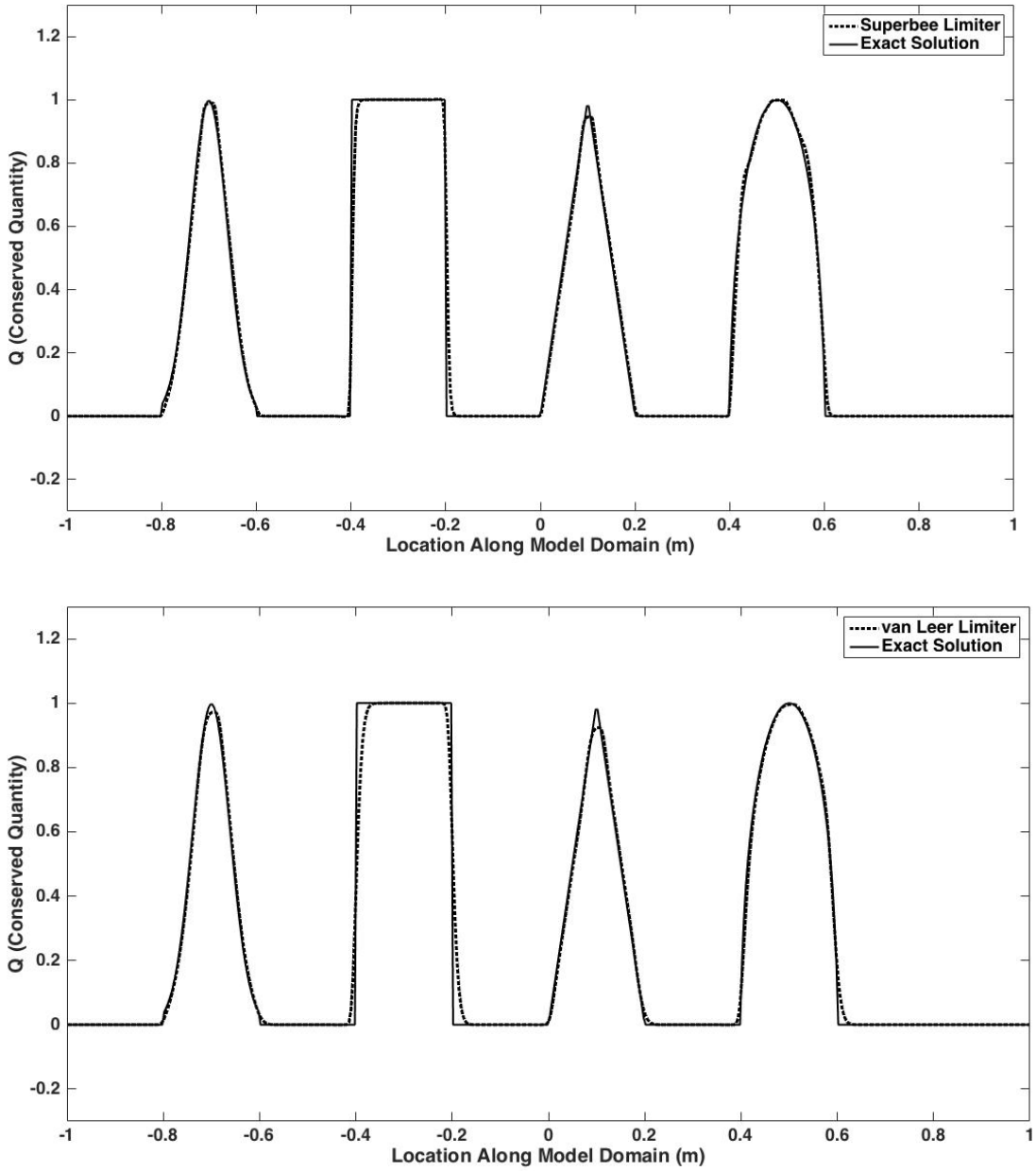

Figure 3.9: Flux Limiter Schemes: Accurate in Smooth Regions and 1st Order Near Shocks

3.5.7 Runge-Kutta Methods

It should be noted that ENO or WENO schemes are frequently used with Runge-Kutta methods and a flux differencing scheme. Therefore, before explaining ENO and WENO, we briefly describe Runge-Kutta methods and some of the flux differencing methods.

Runge-Kutta methods are a family of iterative methods that are used for temporal discretization of ordinary differential equations. Jameson et al. in 1981 applied these methods to PDEs as well.

In the first step of the method, the PDE will be converted to a pseudo ODE. For wave equation the pseudo ODE takes the following form:

$$q_t = R(q) \tag{3.102}$$

$$R(q) = f_x \tag{3.103}$$

f_x will be obtained by ENO or WENO and q_t will be obtained by Runge-Kutta methods. The first-order Runge-Kutta method is also called Euler method:

$$Q_i^{n+1} = Q_i^n + \Delta t f(t^n, Q^n) \tag{3.104}$$

Here we only introduce 3rd and 4th order Runge-Kutta methods.

3rd order:

$$k_1 = Q_i^n + \Delta t f(t^n, Q^n) \tag{3.105}$$

$$k_2 = \frac{3}{4}Q_i^n + \frac{k_1}{4} + \frac{1}{4}\Delta t f(t^n, k_1) \tag{3.106}$$

$$Q_i^{n+1} = \frac{1}{3}Q_i^n + \frac{2}{3}k_2 + \frac{2}{3}\Delta t f(t^n, k_2) \tag{3.107}$$

4th order:

$$k_1 = Q_i^n + \Delta t f(t^n, Q^n) \tag{3.108}$$

$$k_2 = \frac{1}{2}Q_i^n + \frac{k_1}{2} - \frac{1}{4}\Delta t f(t^n, Q^n) + \frac{1}{2}\Delta t f(t^n, k_1) \tag{3.109}$$

$$k_3 = \frac{1}{9}Q_i^n + \frac{2}{9}k_1 + \frac{2}{3}k_2 - \frac{1}{9}\Delta t f(t^n, Q^n) - \frac{1}{3}\Delta t f(t^n, k_1) + \Delta t f(t^n, k_2) \tag{3.110}$$

$$Q_i^{n+1} = \frac{1}{3}k_1 + \frac{1}{3}k_2 + \frac{1}{3}k_3 + \frac{1}{6}\Delta t f(t^n, k_1) + \frac{1}{6}\Delta t f(t^n, k_3) \tag{3.111}$$

3.5.8 Essentially Non-Oscillatory (ENO) Schemes

The idea of essentially non-oscillatory schemes, as mentioned before, was developed by Harten et al. in 1987. The accuracy of these schemes does not depend on the location of discontinuity as they are uniformly high order and non-oscillatory. In ENO, the magnitude of highest degree Newton divided differences is compared to measure the local smoothness of the stencil, although other methods could also be utilized for such a purpose.

In this section, we briefly describe the construction of ENO schemes for hyperbolic partial differential equations. However, detailed mathematical proofs will not be addresses here, as they can be found in other related textbooks.

ENO starts by finding a polynomial $p_i(x)$, of degree at most k-1, based on cell averages $Q_i^n(x)$, such that it is a k[th] order accurate approximation of the unknown function $q(x)$:

$$Q_i^n \approx \frac{1}{\Delta x}\int_{x_{i-\frac{1}{2}}}^{x_{i+\frac{1}{2}}} q(x,t_n)dx \tag{3.112}$$

$$p_i(x) = q(x) + O(\Delta x^k) \tag{3.113}$$

In other words, the unique polynomial $p_i(x)$ has the following property:

$$\frac{1}{\Delta x_i}\int_{x_{i-\frac{1}{2}}}^{x_{i+\frac{1}{2}}} p(x,t_n)dx = Q_i \tag{3.114}$$

We show the stencil based on r cells to the right and s cells to the left:

$$S(i) = \{I_{i-r}, \dots., I_{i+s}\} \tag{3.115}$$

and we know that:

$$r + s = k - 1 \tag{3.116}$$

It can be shown that the k[th] order accurate polynomial that we are looking for can be found by:

$$p_i\left(x_{i+\frac{1}{2}}\right) = q_{i+\frac{1}{2}} = \sum_{j=0}^{k-1} c_{rj} Q_{i-r+j} \tag{3.117}$$

where c_{rj} are the constant coefficients of the polynomial. Shu (1997) using the Lagrange form of the interpolation polynomial obtained the following expression for non-uniform grids:

$$c_{rj} = \left(\sum_{m=j+1}^{k} \frac{\sum_{l=0}^{k}\prod_{p=0}^{k}(x_{i+\frac{1}{2}} - x_{i-r+p-\frac{1}{2}})}{\prod_{l=0}^{k}(x_{i-r+m-\frac{1}{2}} - x_{i-r+l-\frac{1}{2}})}\right)\Delta x_{i-r+j} \tag{3.118}$$

For a uniform grid, above expression reduces to:

$$c_{rj} = \left(\sum_{m=j+1}^{k} \frac{\sum_{l=0}^{k}\prod_{p=0}^{k}(r-p+1)}{\prod_{l=0}^{k}(m-l)}\right) \tag{3.119}$$

In solving a hyperbolic PDE, we know that we have the point values of the unknown at the nodes, from initial conditions. In ENO method, these nodal values are used to approximate a high order accurate derivative of the function. In other words, knowing the point values:

$$q_i = q(x_i), \quad i = 1, 2, \dots, N \tag{3.120}$$

a numerical flux function should be found based on nodal values:

$$\hat{Q}_{i+\frac{1}{2}} = \hat{Q}(Q_{i-r}, Q_{i-r+1}, \dots, Q_{i+s}), \quad i = 0, 1, 2, \dots, N \tag{3.121}$$

such that the flux difference approximates the function derivative to the k^{th} order accuracy:

$$\frac{1}{\Delta x_i}\left(\hat{Q}_{i+\frac{1}{2}} - \hat{Q}_{i-\frac{1}{2}}\right) = Q'(x_i) + O(\Delta x^k), \quad i = 0, 1, 2, \dots, N \tag{3.122}$$

A major difference between ENO and flux limiter schemes is the fact that ENO is based on point values (finite difference) rather than cell averages (finite volume). Again, it can be shown that the coefficients c_{rj} defined above can be used to achieve such a property:

$$\hat{Q}_{i+\frac{1}{2}} = \sum_{j=0}^{k-1} c_{rj} q_{i-r+j} \tag{3.123}$$

All the traditional finite difference or finite volume schemes can be derived by the above approach.

As explained earlier in this chapter, fixed stencil approximations with orders higher than one lead to spurious oscillations. In ENO schemes, Newton divided differences, which are a measure of the smoothness of a function, are used to create an adaptive stencil, namely, the left shift, r, changes with the location of the gridcell.

Forward Newton divided differences are defined as:

$$Q\left[x_{i-\frac{1}{2}}\right] = Q(x_{i-\frac{1}{2}}) \tag{3.124}$$

$$Q\left[x_{i-\frac{1}{2}}, \dots, x_{i+j-\frac{1}{2}}\right] = \frac{Q\left[x_{i+\frac{1}{2}}, \dots, x_{i+j-\frac{1}{2}}\right] - Q\left[x_{i-\frac{1}{2}}, \dots, x_{i+j-\frac{3}{2}}\right]}{x_{i+j-\frac{1}{2}} - x_{i-\frac{1}{2}}} \tag{3.125}$$

Large Newton divided differences imply large or discontinuous derivatives. On the other hand, the smaller the divided difference, the smoother the function will be in the interval. ENO schemes make the stencil adaptive by using this property of Newton divided differences and

choosing the smoothest stencil compared to other stencils in the interval. As the first step, a two-point stencil is selected:

$$S(i) = \{x_{i-\frac{1}{2}}, x_{i+\frac{1}{2}}\} \tag{3.126}$$

In the next step one point should be added to this stencil. This point can be on the right-hand side or left hand side of the stencil. To decide which point to add, we compare the Newton divided differences:

$$S(i) = \left\{x_{i-\frac{3}{2}}, x_{i-\frac{1}{2}}, x_{i+\frac{1}{2}}\right\} \quad if \ \left|Q[x_{i-\frac{3}{2}}, x_{i-\frac{1}{2}}, x_{i+\frac{1}{2}}]\right| < \left|Q[x_{i-\frac{1}{2}}, x_{i+\frac{1}{2}}, x_{i+\frac{3}{2}}]\right| \tag{3.127}$$

$$S(i) = \left\{x_{i-\frac{1}{2}}, x_{i+\frac{1}{2}}, x_{i+\frac{3}{2}}\right\} \quad if \ \left|Q[x_{i-\frac{3}{2}}, x_{i-\frac{1}{2}}, x_{i+\frac{1}{2}}]\right| > \left|Q[x_{i-\frac{1}{2}}, x_{i+\frac{1}{2}}, x_{i+\frac{3}{2}}]\right| \tag{3.128}$$

This procedure is repeated with one point added to the stencil until the desired order of accuracy is reached.

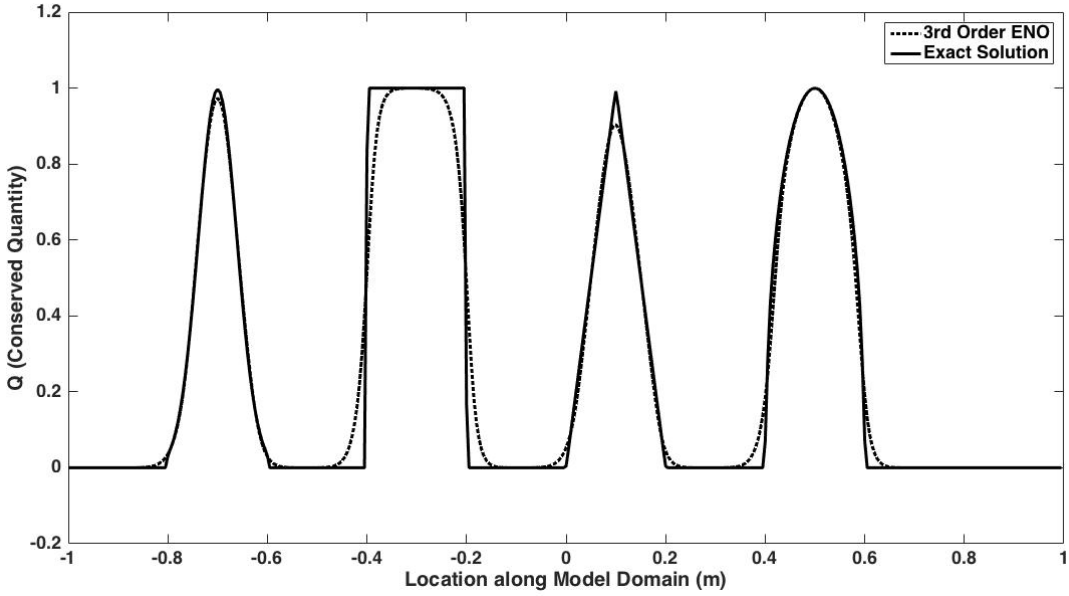

Figure 3.10: 3rd Order ENO Scheme: High Order in Smooth Regions and Near Shocks

3.5.9 Weighted Essentially Non-Oscillatory (WENO) Schemes

As stated earlier, ENO is uniformly high order everywhere in the model right next to the discontinuity. WENO method has been created based on ENO, with an attempt to remove some of the disadvantages of ENO. In ENO, the free adaptation of the stencil is not needed in smooth regions. In addition, applying adaptation of stencil to hyperbolic PDEs may cause some loss of

accuracy [Shu, 1990, Rogerson and Meiberg, 1990). Moreover, the numerical flux that is obtained by changing the stencil based on its smoothness may have different form at neighboring points. Last but not least, one of the main advantages of WENO over ENO is the order of accuracy. In ENO if for example 2k-1 cells are used to give k stencil candidates, only one of them is chosen to give k^{th} order accuracy. In WENO, on the other hand, all k stencil candidates are used to give 2k-1 order accuracy. To be more precise, a convex combination of all the candidate stencils is used. If we show all the stencil candidates by:

$$S_r(i) = \{x_{i-r}, \dots, x_{i-r+k}\}, \quad r = 0, \dots, k-1 \tag{3.129}$$

and k different numerical fluxes by:

$$\hat{Q}^{(r)}_{i+\frac{1}{2}} = \sum_{j=0}^{k-1} c_{rj} q_{i-r+j} \tag{3.130}$$

WENO uses a convex combination of all the candidates as:

$$\hat{Q}_{i+\frac{1}{2}} = \sum_{r=0}^{k-1} \omega_r \hat{Q}^{(r)}_{i+\frac{1}{2}} \tag{3.131}$$

For stability and consistency, weights ω should follow below requirements:

$$\omega_r \geq o, \qquad \sum_{r=0}^{k-1} \omega_r = 1 \tag{3.132}$$

The way that the weights are defined is different in smooth regions and near discontinuity. In smooth regions the weights are shown by d_r:

$$\hat{Q}_{i+\frac{1}{2}} = \sum_{r=0}^{k-1} d_r \hat{Q}^{(r)}_{i+\frac{1}{2}} \tag{3.133}$$

d_r weights are always positive. As an example, d_r values are calculated for k between 1 to 3:

$$k = 1, \qquad d_0 = 1 \tag{3.134}$$

$$k = 2, \qquad d_0 = \frac{2}{3}, \quad d_1 = \frac{1}{3} \tag{3.135}$$

$$k = 3, \qquad d_0 = \frac{3}{10}, \quad d_1 = \frac{3}{5}, \quad d_2 = \frac{1}{10} \tag{3.136}$$

When a discontinuity exists in the region, the corresponding weights ω_r would be zero, to emulate ENO idea. Originally, polynomials or rational functions were used to define weights since they are computationally efficient:

$$\omega_r = \frac{\alpha_r}{\sum_{s=0}^{k-1} \alpha_s}, \quad r = 0, \dots, k-1 \tag{3.137}$$

with

$$\alpha_r = \frac{d_r}{(\varepsilon + \beta_r)^2} \tag{3.138}$$

In the above equation ε is introduced to avoid denominator from becoming zero. A value of $\varepsilon = 10^{-6}$ has been suggested for this purpose. In WENO method, similar to ENO the smoothness of each stencil is measured. However, in WENO Newton divided differences are not used and β_r which is called smooth indicator is employed. Jiang and Shu, (1996) after extensive experiments, proposed following relationship for smooth indicators:

$$B_r = \sum_{l=1}^{k-1} \int_{x_{i-\frac{1}{2}}}^{x_{i+\frac{1}{2}}} \Delta x^{2l-1} \left(\frac{\partial^l p_r(x)}{\partial x^l}\right)^2 dx \tag{3.139}$$

Again, as an example, if k = 2, we will have the following interpolating polynomials:

$$p_0(x) = Q_i + \frac{Q_{i+1} - Q_i}{\Delta x}(x - x_i) \tag{3.140}$$

or

$$p_1(x) = Q_i + \frac{Q_i - Q_{i-1}}{\Delta x}(x - x_i) \tag{3.141}$$

Therefore,

$$\beta_0 = (Q_{i+1} - Q_i)^2 \tag{3.142}$$

$$\beta_1 = (Q_i - Q_{i-1})^2 \tag{3.143}$$

If k = 3, we will have:

$$p_0(x) = \frac{Q_{i+2} - 2Q_{i+1} + Q_i}{2\Delta x^2}(x - x_{i+1})^2 + \frac{Q_{i+2} - Q_i}{2\Delta x}(x - x_{i+1}) + Q_{i+1} - \frac{Q_{i+2} - 2Q_{i+1} + Q_i}{24} \tag{3.144}$$

$$p_1(x) = \frac{Q_{i+1} - 2Q_i + Q_{i-1}}{2\Delta x^2}(x - x_i)^2 + \frac{Q_{i+1} - Q_{i-1}}{2\Delta x}(x - x_i) + Q_i - \frac{Q_{i+1} - 2Q_i + Q_{i-1}}{24} \tag{3.145}$$

$$p_2(x) = \frac{Q_i - 2Q_{i-1} + Q_{i-2}}{2\Delta x^2}(x - x_{i-1})^2 + \frac{Q_i - Q_{i-2}}{2\Delta x}(x - x_{i-1}) + Q_{i-1} - \frac{Q_i - 2Q_{i-1} + Q_{i-2}}{24} \tag{3.146}$$

and the three indicators of smoothness will be:

$$\beta_0 = \frac{(Q_{i+1} - Q_i)^2 + (Q_{i+2} - Q_{i+1})^2}{2} + (Q_{i+2} - 2Q_{i+1} + Q_i)^2 \tag{3.147}$$

$$\beta_1 = \frac{(Q_i - Q_{i-1})^2 + (Q_{i+1} - Q_i)^2}{2} + (Q_{i+1} - 2Q_i + Q_{i-1})^2 \tag{3.148}$$

$$\beta_2 = \frac{(Q_{i-1} - Q_{i-2})^2 + (Q_i - Q_{i-1})^2}{2} + (Q_i - 2Q_{i-1} + Q_{i-2})^2 \tag{3.149}$$

Figure 3.11 is an example of the application of 5th order WENO to our numerical experiment. High order accuracy of this scheme in smooth regions is apparent.

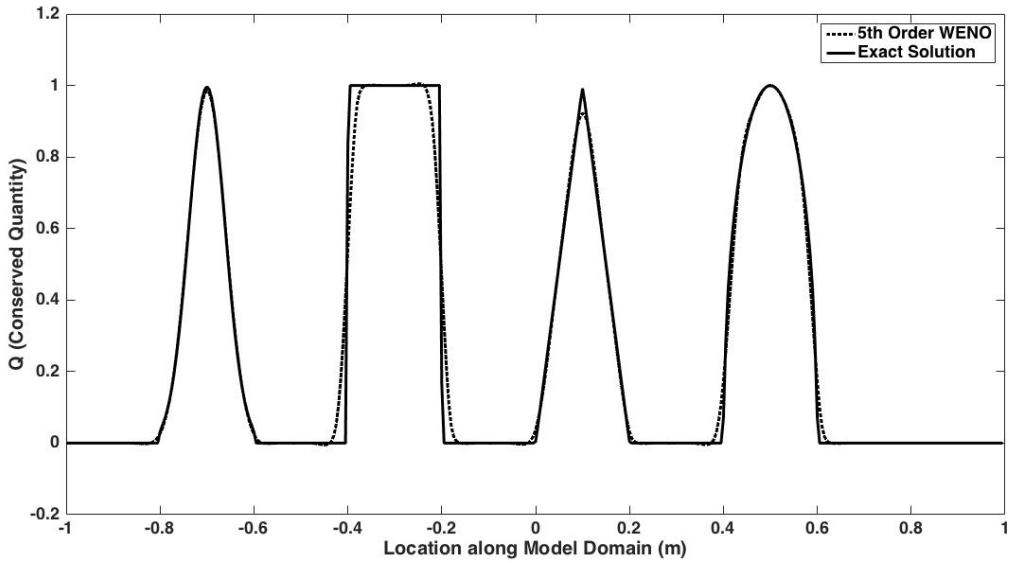

Figure 3.11: 5th Order WENO Scheme: High Order in Smooth Regions and Near Shocks

3.6 Conclusion

In this chapter, the capability of several FD and FV schemes for capturing shocks in hyperbolic conservation PDEs was investigated. The solution methods available to this kind of problem are

numerous in the literature and the subject is still very active. The application of many of the proposed methods requires advanced mathematical backgrounds. Here, we only tried to introduce and later apply the most famous methods of solution to proppant injections in hydraulic fractures. Based on the numerical example of this chapter, the following can be concluded regarding the competency of the applied solution methods:

1) First-order finite difference schemes are always monotonic preserving. However, they are not accurate enough near smooth regions of solution.

2) Although higher order finite difference schemes give good accuracy in smooth regions, they produce spurious oscillations near regions with high gradients in the solution.

3) High resolution method of finite volume through the application of flux limiters are always non-oscillatory (total variation diminishing) and 1^{st}-order accurate near the location with large gradients. These schemes also produce accurate results in the smooth regions.

4) ENO and WENO schemes are uniformly high order accurate and resolve shocks with sharp and monotone transitions. They are especially suitable for problems containing both shocks and complicated smooth solutions like proppant injection in hydraulic fractures.

5) Godunov splitting technique is very effective in simulating multi-dimensional problems. Applying this method eliminates unnecessary complexity of the un-split methods and makes modeling easier for coding.

Chapter 4: Verification and Sensitivity Analysis of Proppant Injection into a Slot

4.1 Introduction

Various physical aspects of slurry and proppant transport have been discussed in Chapter 2 based on a review of literature and experimental studies. It is now well realized that different physics of proppant transport such as hindered settling velocity of proppants or slurry flow viscosity evolution, as some examples, should be addressed in a well-established modelling tool. The numerical solution of the first-order hyperbolic transport equation has also been described in Chapter 3. Considering these two chapters, we have directed the current chapter at the development of a numerical tool of proppant transport that incorporates physical aspects of the process, while applies an accurate and proper numerical technique.

In this chapter, we will introduce the mathematical equations of motion of a slurry and boundary conditions that govern proppant injection into a fixed dimension fracture. As a starting point of code development, we tried to develop a numerical tool for simple slot flow. This gave us the chance to verify our proppant transport module by the results of available simulations in the literature.

In the design of hydraulic fracture treatment, volumetric average fluid velocity is typically used in the calculations of fluid transport since it is implicitly assumed that solid proppants which are carried by the injection fluid are moving at that calculated average velocity and therefore particles are uniformly distributed. This simple assumption is the base of many design decisions like total fluid requirements, pad size and proppant staging.

A series of sensitivity analysis using realistic parameter values was conducted to explore the legitimacy of these assumptions and to provide better guidelines that allow more accurate predictions of the proppant and fluid transfer. In addition, we will also investigate the amount of gravity driven vertical motion of proppant which is driven by density differences (convection) and compare it to a second gravity driven motion which is proppant settlement. Both of these two well recognized mechanisms can occur inside a fracture during proppant placement, however, the importance of each mechanism as a function of proppant injection design parameters is not fully understood. In addition to considering a rectangular channel width, we

also investigate proppant placement in an elliptic fracture cross section since this shape is predicted by many idealized analytical fracture propagation models such as PKN.

4.2 Mathematical Formulation and Solution Technique

The governing equations of a proppant transport model are: a) conservation of mass for the injection fluid, which yields the pressure distribution, b) conservation of mass for the solid proppants which yields the proppant concentration distribution during the simulation, c) momentum equations which for the case of flow between parallel plates leads to the cubic law, a relation between pressure gradient and fluid velocity and d) proppant settling velocity or the terminal velocity of the proppant particles inside the fracture. The main output of this kind of modelling is the distribution of the proppant that is given by its volumetric concentration (defined as the volume of the proppant over the volume of the slurry).

In our simulations, we have neglected flocculation and slumping of the particles and we assumed uniform concentration across the width of the fracture (slot). This assumption avoids unnecessary complications arising from large aspect ratio of elements in the numerical model or high running time of a model with large number of elements. Therefore, a 2D modeling of the problem seems sufficient.

In addition, for the binary system of proppant flow, Taylor dispersion, which consists of diffusion associated with the molecular movement, turbulent flow and temperature gradient (Bird et al., 1976) can be neglected. The most obvious consequence of these assumptions is that this moving boundary problem consists of a sharp proppant front (without any diffusion ahead) which needs special numerical techniques.

We use the Finite Volume Method (FVM) technique which minimizes numerical dispersion that occurs in traditional Finite Difference (FD) schemes. We applied WENO numerical solution of FVM which was explained in Chapter 3. This scheme gives high accuracy where the solution is smooth (away from proppant front) and non-oscillatory near discontinuities (proppant front).

4.2.1 Mass Balance (Continuity) Equations

Continuity equation is basically a statement based on the conservation of mass. In proppant transport context two mass conservation equations are required for the slurry which consists of

proppant and injection fluid. The derivation of these balance equations can be found in Chapter 3 and here we only mention these conservation equations.

For slurry:

$$\frac{\partial}{\partial x}\left(\frac{w^3}{12\mu}\frac{\partial p}{\partial x}\right)+\frac{\partial}{\partial y}\left(\frac{w^3}{12\mu}\frac{\partial(p-\rho g y)}{\partial y}\right)+q_{inj}=\frac{\partial w}{\partial t} \tag{4.1}$$

For proppant:

$$\frac{\partial}{\partial t}(cw)+\frac{\partial}{\partial x}\left(u_p cw\right)+\frac{\partial}{\partial y}\left(v_p cw\right)+cq_{inj}=0 \tag{4.2}$$

where w is the width of the fracture, c is the volumetric proppant concentration defined as the ratio of proppant volume to slurry volume and u_p and v_p are the horizontal and vertical velocities of proppant respectively.

In this set of equations, the width of the slot is constant. Therefore, the right hand side of the Eq. 4.1 disappears for the case of flow through fixed slots. We adopted the finite difference scheme to solve this elliptic PDE and obtain the fluid pressures.

In addition, the rheology of the slurry is affected by the proppant concentration. We assume that the increase in viscosity can be described by the following (Barree & Conway, 1994):

$$\mu=\frac{\mu_0}{(1-\frac{c}{c*})^{1.82}} \tag{4.3}$$

where c* is the saturation concentration and μ_0 is the initial viscosity of the clean fluid. Saturation concentration corresponds to the maximum concentration that can be achieved by random packing of regular spheres. At saturation concentration, proppant particles create a pack and behave like solid porous medium. Thereafter, only the fluid phase is able to mobilize through the pack. Saturation concentration can be determined experimentally and depends on the type of the proppant and it varies between 0.52 (loose packing) to 0.65 (dense packing). We assign a value of 0.6 to this parameter in the simulations. This apparent viscosity is used to calculate fluid transmissibilities in the pressure equation (Eq. 4.1).

Eq. 4.3 has been obtained by laboratory experiments (Barree and Conway, 1994) and lumps all the effects of interactions between particles and particles and fluid into a modified viscosity of the fluid. There are also a variety of other equations as discussed in Chapter 2.

According to Eq. 4.3, viscosity of the slurry increases with increasing concentration. This, however, imposes a limitation on the numerical implementation of this relationship. This is because the viscosity increases very rapidly when concentration approaches the saturation concentration. The most apparent solution is assigning a threshold value to the maximum viscosity or concentration.

It should be noted that our transport model consists of coupling mass balance of slurry and proppant. Slurry mass balance equation is an elliptic PDE and is solved by an implicit method and the shock capturing methods discussed earlier are not applied to solve this PDE.

4.2.2 Proppant Mass Balance

The complexity of the proppant transport problem comes from solving the hyperbolic PDE of proppant transport (Eq. 4.2). Conventional finite difference methods generate either non-physical oscillations or numerical diffusion in the presence of shocks (Leveque, 2004). We reviewed the capability of several finite difference and finite volume techniques in Chapter 2 and here we briefly describe the discretization method that we used for this work.

We can assume that the following relation exists between the slurry and particle velocities (Barree et al., 1994; Liu, 2006):

$$u_p = \alpha . u_{sl} \tag{4.4}$$

$$v_p = v_{sl} - \frac{g(\rho_p - \rho_f)d_p^2}{18\mu} e^{-5.9c} \tag{4.5}$$

where α accounts for the fact that the velocity of fluid and proppant are not the same. It should be emphasized that the first term in Eq. 4.5 which is v_{sl} includes convection velocity the second term in Eq. 4.5 accounts for particle settling velocity and is corrected for the effect of particle concentration on the settlement of of proppants (Barree & Conway, 1995). For each fluid type, a different form of such a function may be required. There are many empirical equations for settling velocity that consider the effects of proppant interactions and wall effects (Daneshy, 1978; Novotny, 1977; Baree and Conway, 1994, Clark and Quadir, 1981). A review of these equations can be found in Chapter 2.

To avoid complications arising from un-split high-resolution methods, we applied dimensional splitting method, a type of fractional step method, to solve Eq. 4.2. Using this method, a multi-dimensional PDE with source terms can be split into several 1D PDE (depending on the

dimensionality of the problem) and an ordinary differential equation. In our case, Eq. 4.2 becomes:

$$\frac{\partial(cw)}{\partial t} + cq_{inj} = 0 \tag{4.6}$$

$$\frac{\partial(cw)}{\partial t} + \frac{\partial[u_p(x,y)cw]}{\partial x} = 0 \tag{4.7}$$

$$\frac{\partial(cw)}{\partial t} + \frac{\partial[v_p(x,y)cw]}{\partial y} = 0 \tag{4.8}$$

Each of these equations can be solved by the 5th order WENO scheme combined with the 4th order Runge-Kutta method as explained in Chapter 3.

4.3 Algorithm for Coupling Slurry and Proppant Transport Equations

We designed a coupling algorithm to link the partial differential equations for fluid flow and proppant transport. Two variables are important in our coupling: proppant velocity which is a direct result of solving fluid flow and slurry mass conservation, and slurry viscosity which is adjusted for proppant concentration changes through Eq. 4.3 (or any of the empirical equations mentioned in Chapter 2). Figure 4.1 shows the coupling scheme for the slurry and proppant mass balance solvers. According to Fig. 4.1, the latest pressure distribution from Eq. 4.1 is used to calculate the proppant velocities needed in solving Eqs. 4.7 and 4.8 to obtain the latest concentration. Then the fluid rheological properties are updated as a function of this new concentration. Since the proppant transport PDE is solved explicitly, we imposed a Courant–Friedrichs–Lewy (CFL) stability condition on the time step that assures information travels within one element in each time step. Necessity of imposing CFL stability condition is explained in Appendix C.

To provide a numerical solution for the proppant transport partial differential equation, we applied a simple iteration approach. The proppant mass balance partial differential equation that we obtained in the previous section is non-linear, meaning that the coefficients of the equation depend on the unknown. At each time-step the transport problem is divided into three parts:

First, we calculate the coefficients of the slurry mass balance equation (Eq. 4.1) using viscosity of the previous time step (at time level n-1) or at the previous iteration level, k-1. We solve for the pressure field using the viscosity obtained in the previous time-step (or the initial condition for the first time-step); Next, we calculate the vertical and horizontal velocity of the proppant,

using the pressure field calculated in the previous time-step (Eqs. 4.4 and 4.5). Finally, we apply a finite-volume method to Eqs. 4.7 and 4.8 to advect the concentration of proppant.

We iterate on the solution until convergence is achieved. Figure 4.1 shows the coupling between the slurry and proppant mass balance solvers.

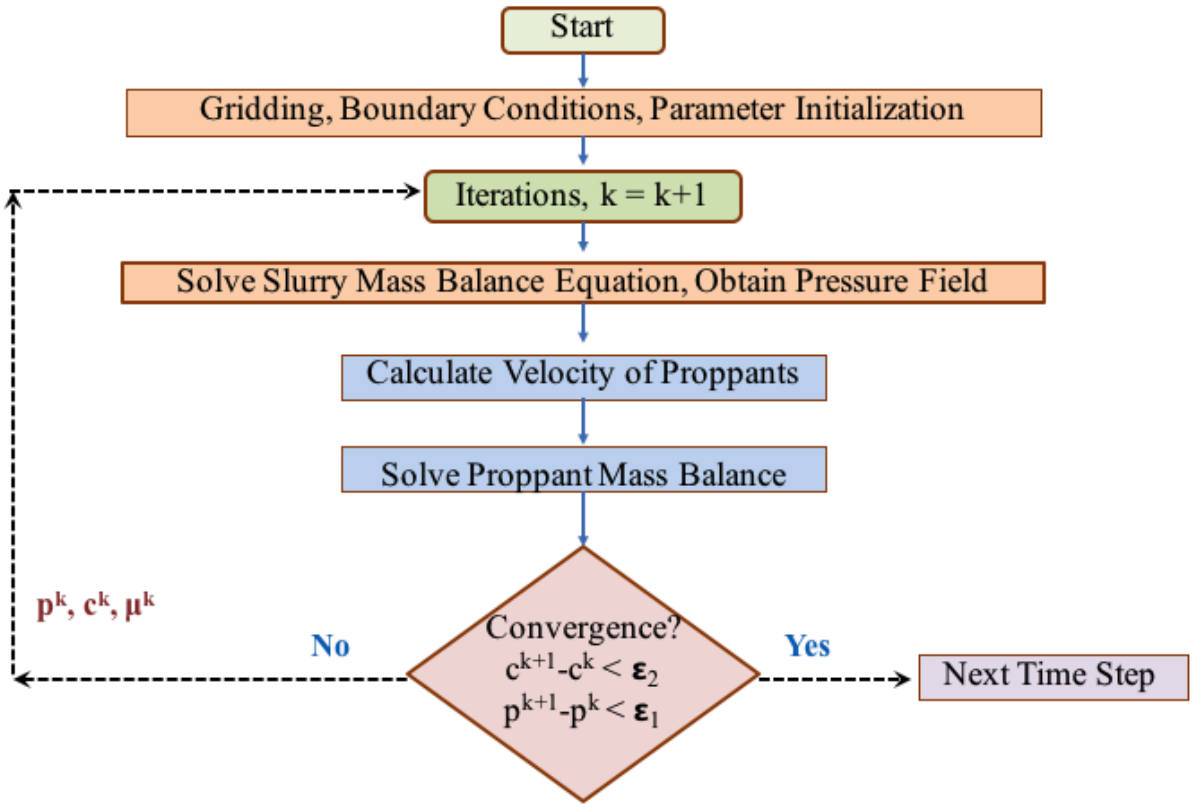

Figure 4.1: Numerical Algorithm of Solving System of Mass Balance Equations

4.4 Numerical Example

A synthetic model with realistic parameters was designed for a series of computer simulations to investigate the effects of volumetric proppant injection rate, injection fluid density, proppant size, carrying fluid viscosity, fracture shape and Buoyancy number on proppant settling and convection inside a fixed dimension slot. This section first presents the results of model verification against the results of a commercial PDE solver (COMSOL Multiphysics) for rectangular and elliptic shape fractures with constant fracture length, width and height. We first describe a base case model whose input parameters are used in the sensitivity study simulations

except for one parameter which is changed at a time. In all cases the fracture is rectangular with a uniform width of 3 mm.

4.4.1 Geometry and Boundary Conditions

For the verification simulation, the model domain is fixed at 5 m by 5 m with 3-mm uniform slot aperture. Initially the slot is filled with the injection fluid (no proppant). Figure 4.2 shows the domain and boundary conditions. The slurry injection is assigned a rate of 1.325 l/s with 0.3 proppant concentration at the left boundary (inlet) over the full slot height. Top, bottom, and right boundaries were assigned zero proppant flux. Fluid is assigned zero pressure at the right boundary and is not allowed to exit from the top and bottom boundaries. In addition, solid wall boundary condition is assigned to the top, bottom and right boundary to prevent proppant from exiting the model

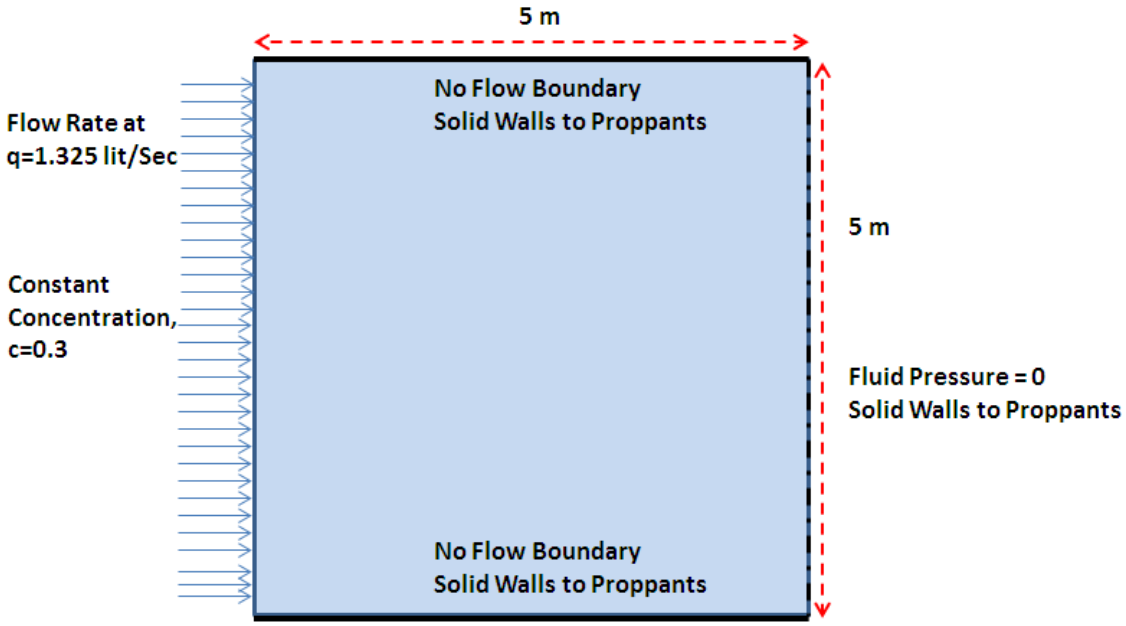

Figure 4.2: Model domain and boundary conditions for slurry and proppant transport equations

4.4.2 Model Verification

The model has been verified by comparison with the simulations conducted with COMSOL Multiphysics, which is a general-purpose software platform, for modeling physics-based problems.

Figures 4.3a and 4.3b compare the result of pressure field from COMSOL Multiphysics and our simulation when no proppant is injected at the left boundary. In this case, both COMSOL Multiphysics and our numerical simulator solve only Eq. 4.1 (slurry mass balance). Results indicate a general agreement between the predictions of the two models. In Fig. 4.4, we compare the pressure profile along the cross section shown in Fig. 4.3. The good match that is observed between these simulations results from the fact that traditional numerical schemes give accurate results when dealing with elliptic partial differential equations (Eq. 4.1).

Figures 4.5a and 4.5b show the concentration contour plot after 8 seconds from the start of proppant injection for both COMSOL and the current computer code, respectively. Figure 4.6 shows the concentration profile across the line shown in Fig. 4.5.

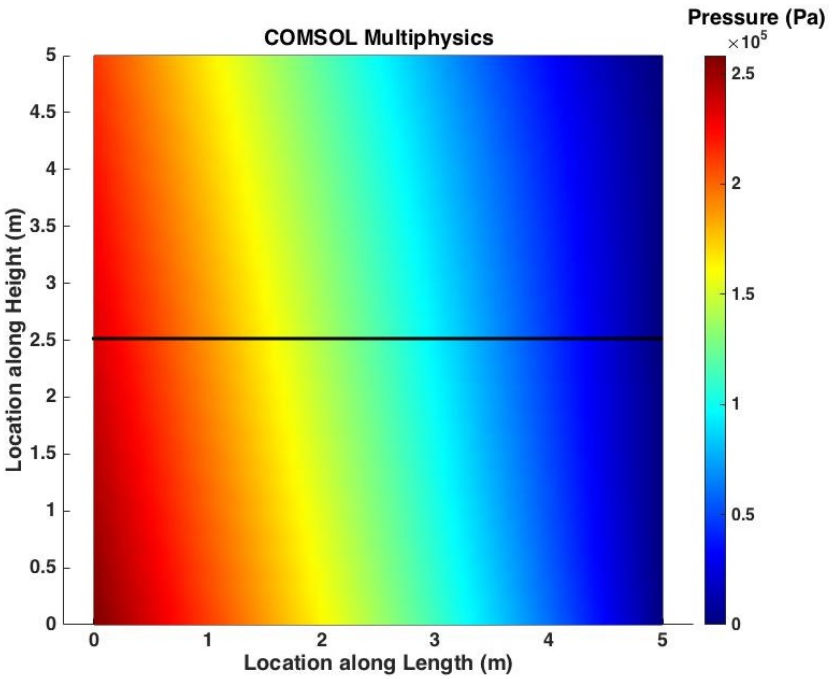

a

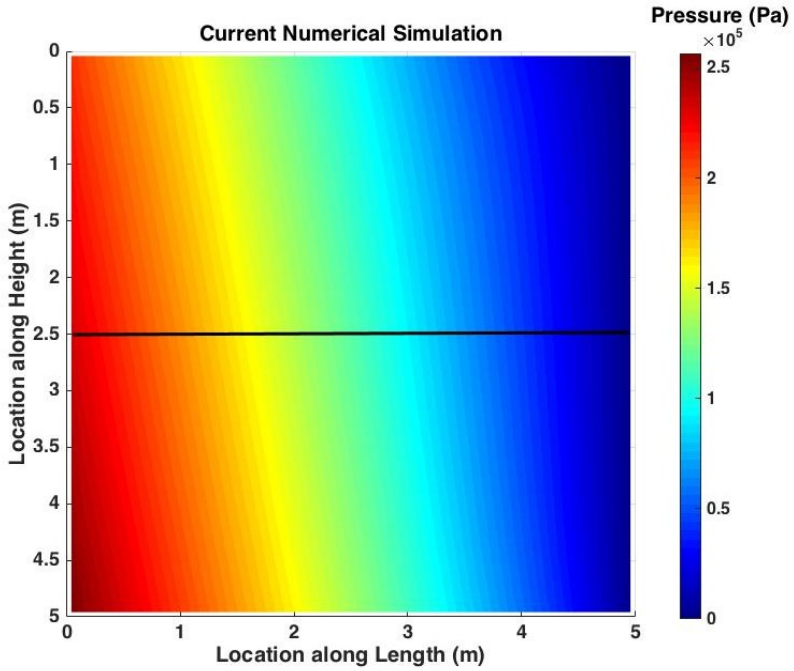

b

Figure 4.3: Pressure Distribution of a) COMSOL Multiphysics and b) presented model at 20 seconds

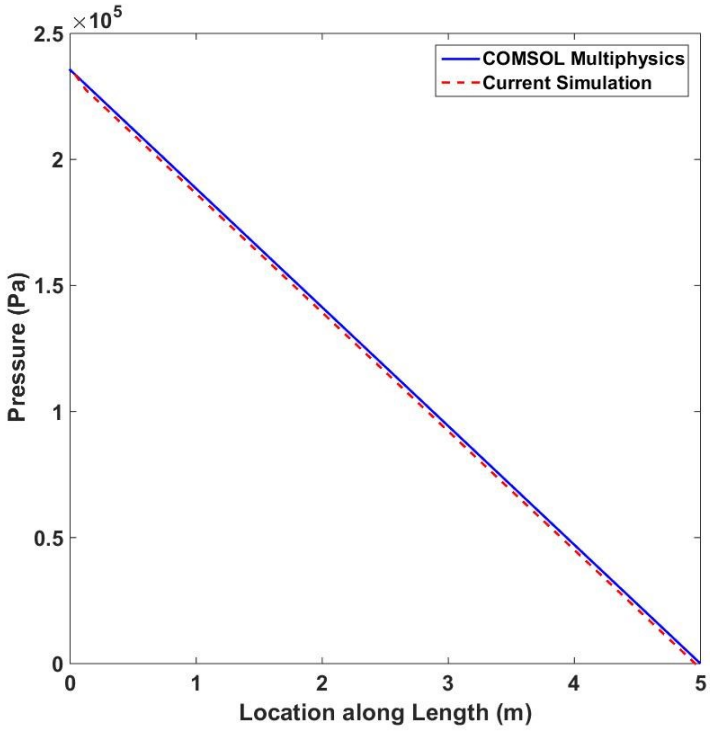

Figure 4.4: Pressure profile for a horizontal section 2.5 m from the model base

A comparison between Figs. 4.5a and 4.5b indicates that the travel distances of proppant front for both simulations are the same at approximately 2 m from the left boundary. However, COMSOL simulation shows more numerical diffusion at the proppant front, while the results of our numerical technique indicate a sharper front and less numerical diffusion. According to Eq. 4.2, there is no second-order space derivative in the proppant transport equation. Even-order derivatives indicate diffusion and, therefore, a suitable numerical technique in solving this type of problems is the one that results in minimum diffusion. According to Fig. 4.6, COMSOL Multiphysics gives more gradual change in concentration gradient compared to our simulation. We can see how traditional numerical schemes fail close to shock fronts when dealing with hyperbolic partial differential equations.

The second difference is the oscillatory nature of the solution technique in COMSOL as can be seen in Fig. 4.6. The oscillation originates from the fact that all traditional numerical techniques with orders higher than one generate oscillations in places with large gradients. This limitation does not exist in our numerical simulation as shown in Figs. 6b and 7.

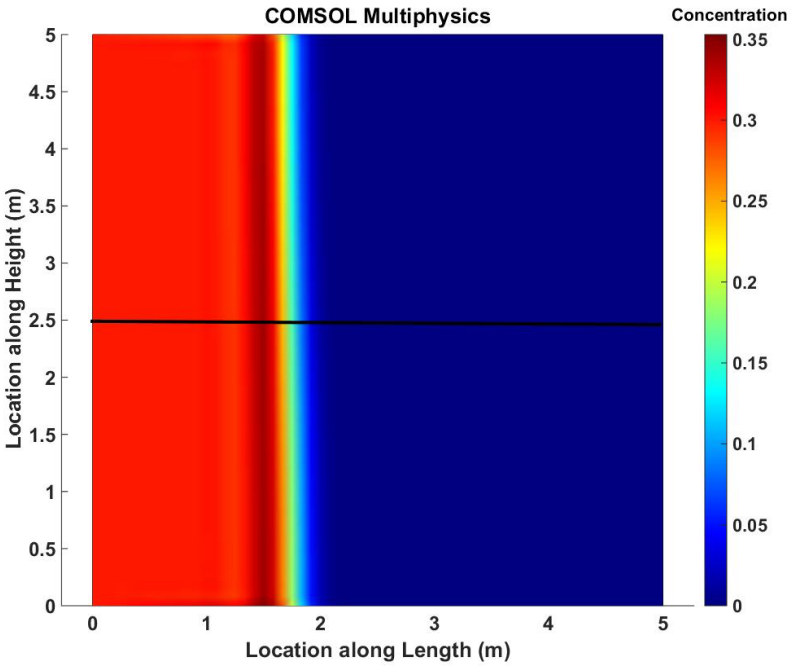

a

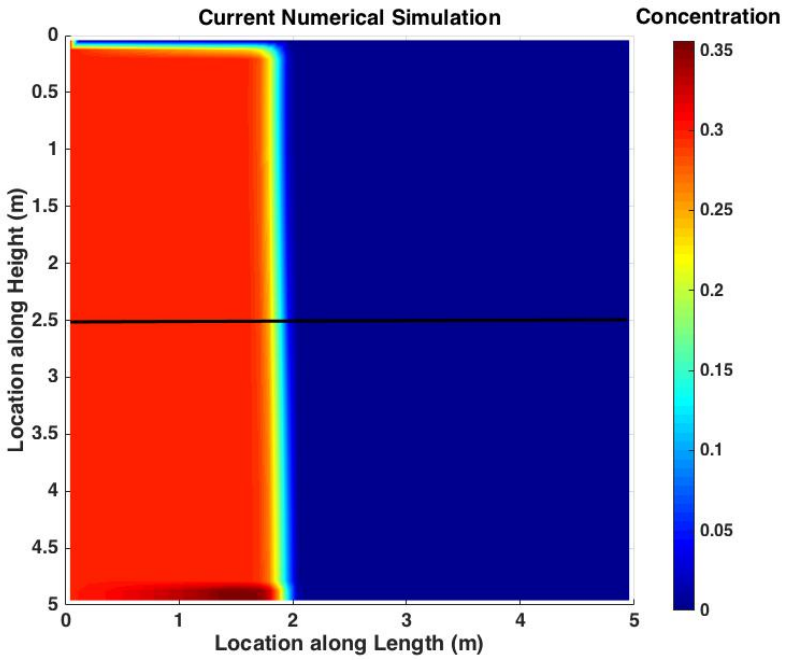

b

Figure 4.5: Result of COMSOL Multiphysics and presented model

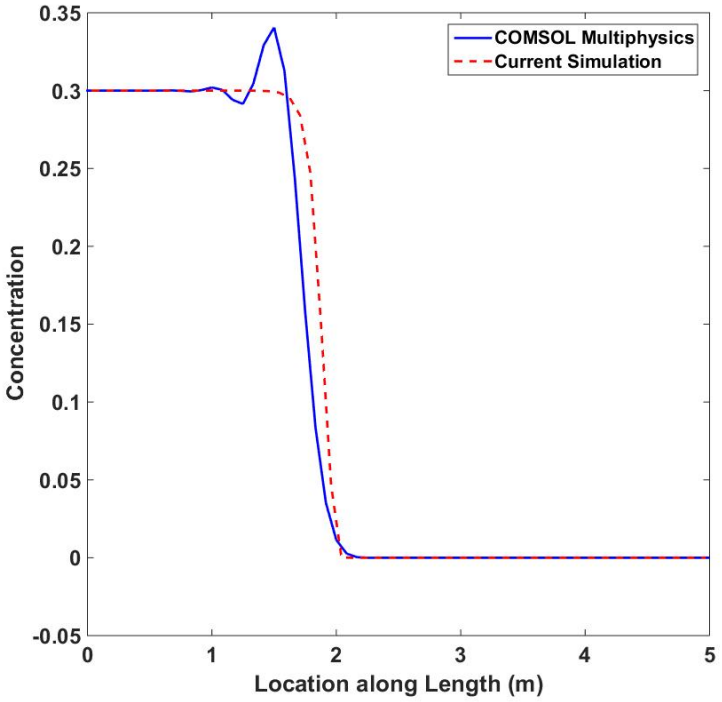

Figure 4.6: Concentration profile at horizontal cross section 2.5 m from the base

4.4.3 Base Case Model

Table 4.1 shows the input parameters of the base case model. The simulation continued until the entire slot was filled with proppant.

Table 4.1: Input parameters for the base model

Fluid Flow Rate (lit/sec)	1.325
Proppant Diameter (mm)	0.200
Proppant Density (kg/m^3)	2,600
Fluid Viscosity (Pa sec)	0.4
Saturation Concentration*	0.6

*This parameter was kept constant for all simulations.

Figure 4.7 shows the concentration maps at different times during the injection as predicted by the numerical transport model. The amount of particle concentration is indicated by the colour change in the contour plots. Figures 4.7a and 4.7b show the proppant front continues to extend with no change in concentration as the slurry travels through the length of the model.

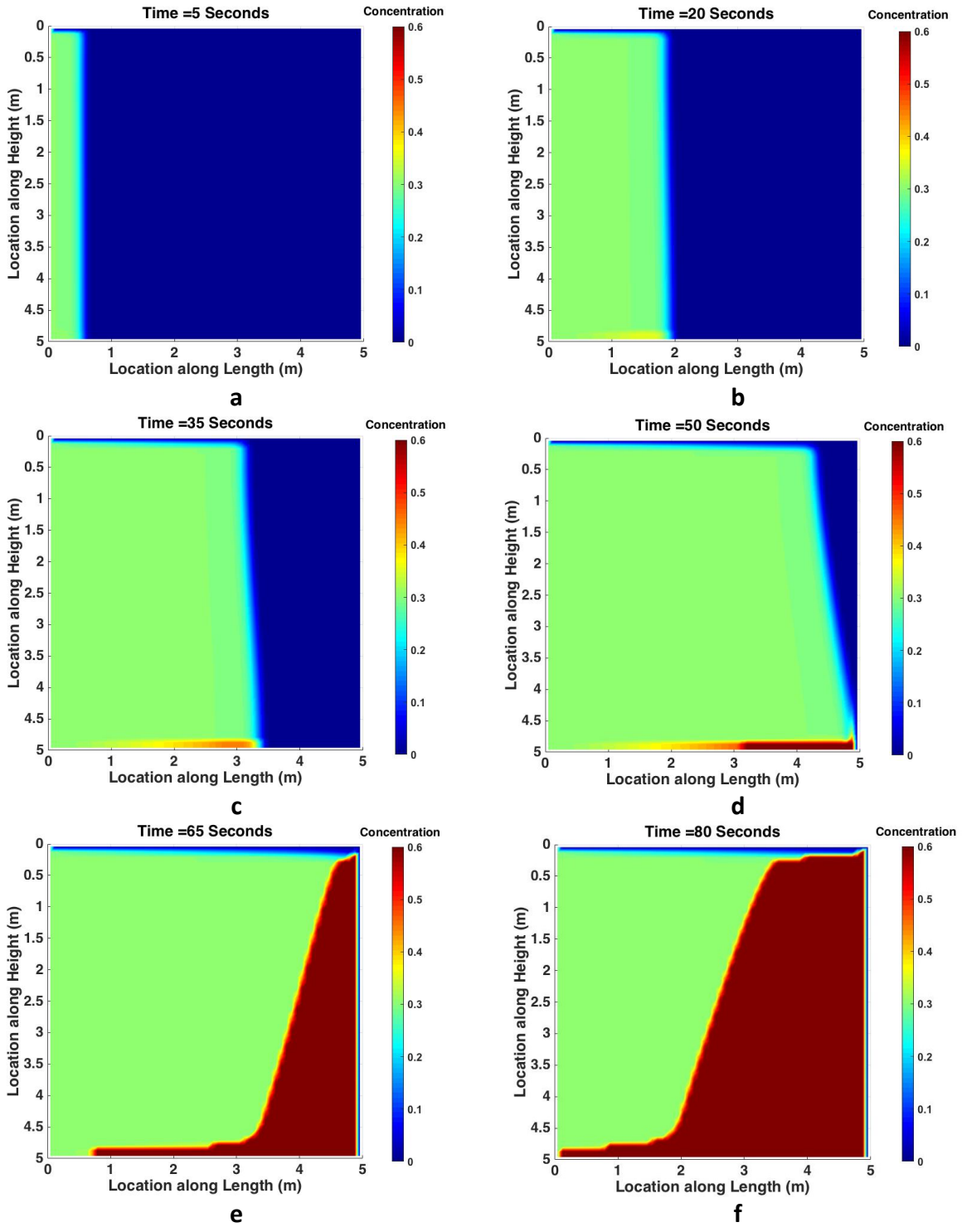

Figure 4.7: Concentration maps for the base model at different injection times

The Buoyance number of the base case according to Eq. 3.34 is 3.00 and, therefore, due to much higher proppant horizontal velocity relative to its vertical velocity in the specified condition of the simulation, little settlement is observed at the bottom of the slot before the proppant front

reaches the right boundary. However, Figs. 4.7c-4.7f show a higher proppant concentration at the bottom of the slot, indicating the formation of a sediment bed.

A proppant bank is also created at the discharge part of the model when the front reaches the right boundary (Figs. 4.7e-4.7f). The bank grows with time in an unsymmetrical manner due to proppant settlement. The proppant concentration increases to the saturation concentration after the proppant reaches the right boundary. We set the numerical proppant flux entering the element at zero when its proppant concentration reaches the saturation level.

4.4.4 Effect of Volumetric Flow Rate

Figure 4.8 shows proppant volume fraction contour plots at 8 seconds of injection for different volumetric injection rates of 1.3, 5.3, 10.6 and 15.9 lit/sec (720, 2,880, 5,760 and 8,640 bbl/day, respectively). The buoyancy number, N_{Bu} is increasing by increasing the flow rate. This means flow rate increase favors horizontal flow. Buoyancy number for different volumetric injection rates of 1.3, 5.3, 10.6 and 15.9 lit/sec is 3, 12, 24, and 36, respectively. Obviously, the slot fills up faster at higher injection rates.

Figure 4.9 shows the time that is required for the proppant front to reach 4.5 m for different flow rates. Obviously, longer injection time is needed for the lower rates. For different volumetric injection rates of 1.3, 5.3, 10.6 and 15.9 lit/sec, this time is 46, 12, 6 and 4 seconds, respectively. The amount of settling is indicated by the creation of a higher concentration bed at the bottom of the slot, which is insignificant in all cases except for the lowest flow rate, as shown in Fig. 4.9a. This is mainly because the horizontal proppant velocity for high-rate injections is one order of magnitude larger than the vertical proppant velocity.

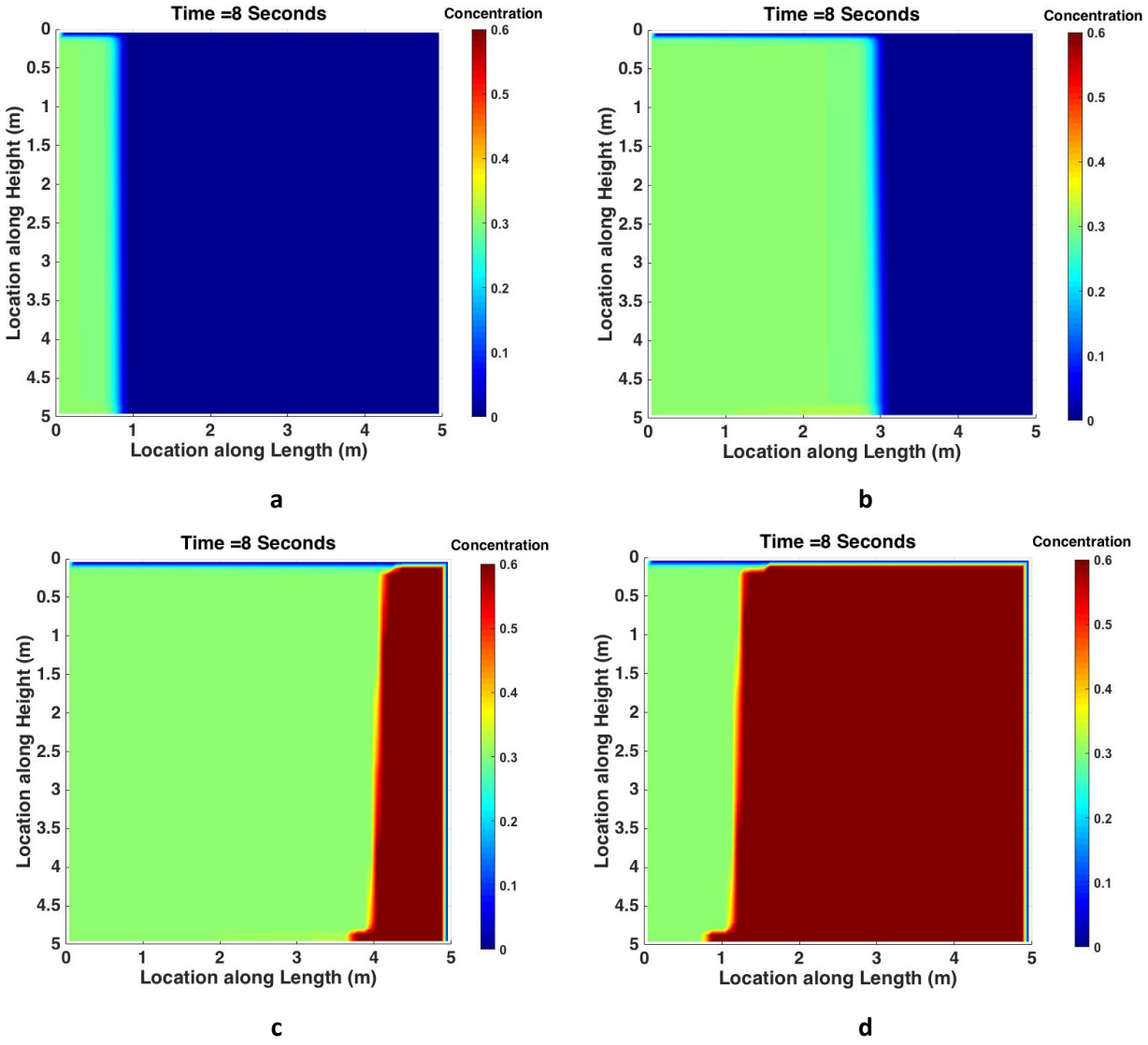

Figure 4.8: Concentration map for injecting proppant with different volumetric flow rates of a) 1.325 , b) 5.3, c) 10.6 and d) 15.9 lit/sec after 8 seconds

If in some situations bed concentration reaches the saturation concentration, the created proppant bank alters the area available for fluid flow in the fracture and may cause a blockage at the fracture entrance and possibly lead to a premature termination of the fracturing operation.

It should be noted that while the amount of settling is indicated by the size of the bed at the bottom of the fracture or the size of the region with clear fluid at the top of the fracture, the amount of convection can be recognized by the slope of the iso-concentration contours. The less this slope, the more the convection. Convection occurs because the heavier proppant slurry tends

to fall to the bottom of the fracture and the low-viscosity particle-free fluid flows more easily at the top.

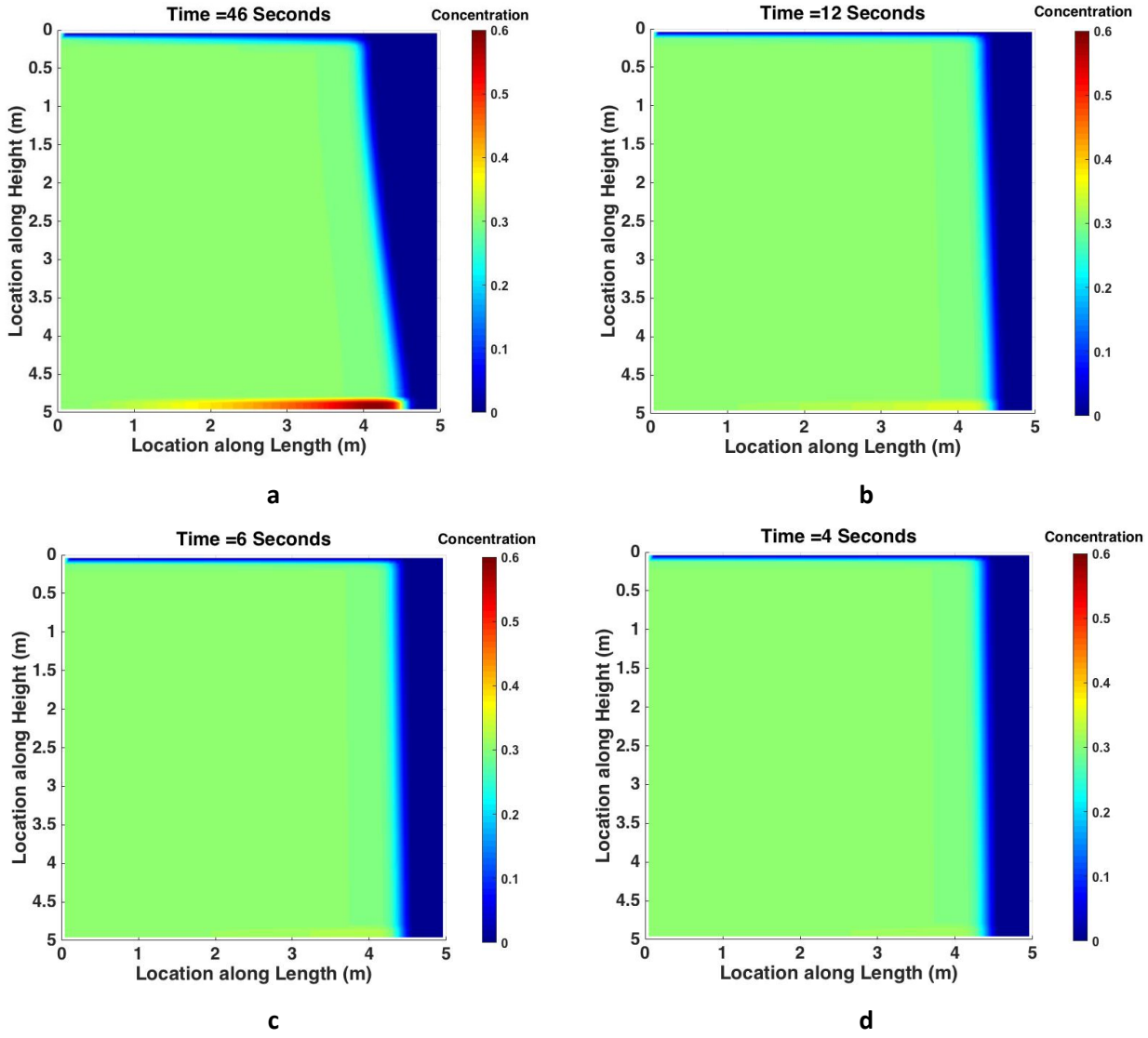

Figure 4.9: Concentration map for injecting proppant with different volumetric flow rates of a) 1.3, b) 5.3, c) 10.6 and d) 15.9 lit/sec after a) 46, b) 12, c) 6 and d) 4 seconds

Figures 4.10 and 4.11 depict the proppant front, i.e. injection concentration of 0.3, for different flow rates during the injection. Solid lines show proppant front advancement before it reaches the right boundary of the model. Dashed lines show 0.6 concentration (saturation concentration front), which seems to be steeper for higher flow rates due to less convection flow at higher horizontal velocities. For the least flow rate case, a stronger convective transport is indicated by

a smaller slope of the concentration contours. As expected, the slot is filled up faster for injection flow rates.

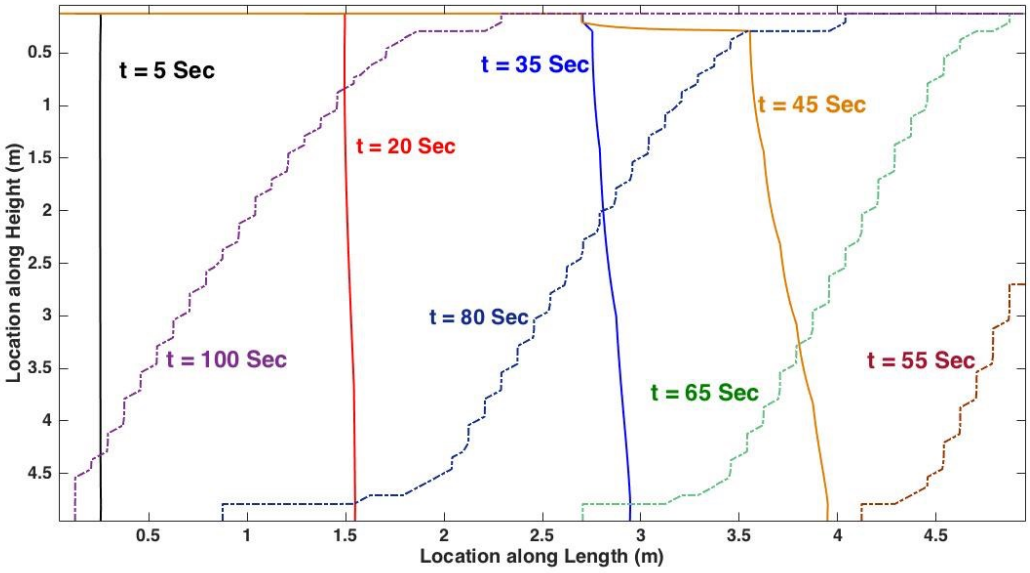

a

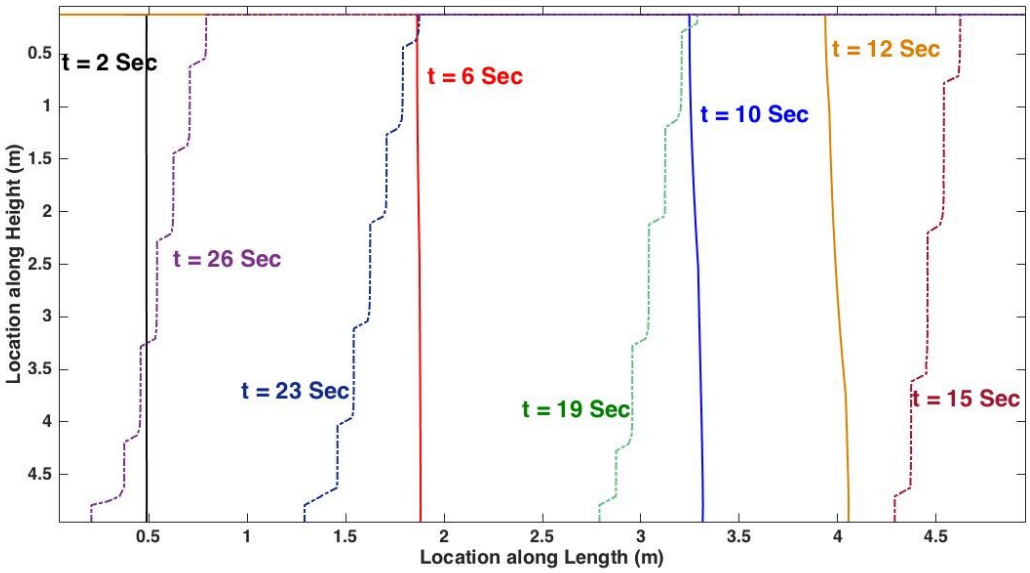

b

Figure 4.10: Proppant fronts at (a) 1.3 lit/sec, (b) 5.3 lit/sec. Solid lines show the proppant front before reaching the right boundary of the model. Dashed lines show the proppant front after reaching the right boundary.

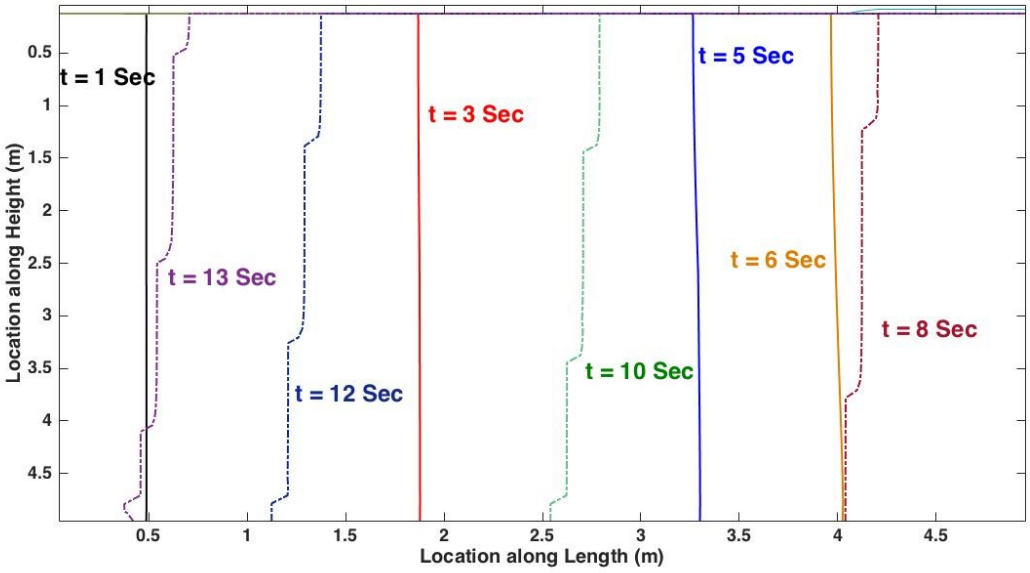

a

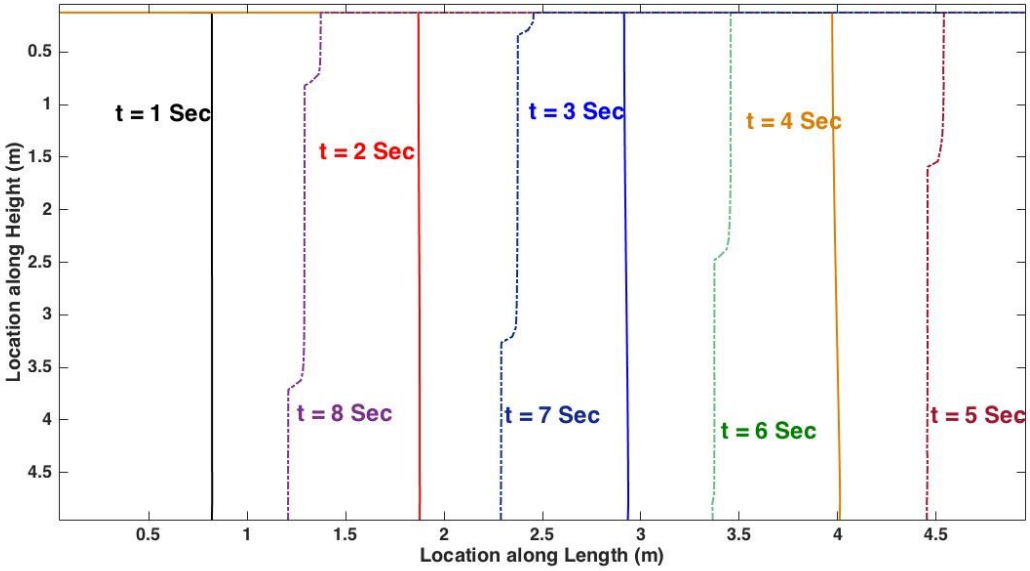

b

Figure 4.11: Proppant fronts at (a) 10.6 lit/sec, (b) 15.9 lit/sec. Solid lines show the proppant front before reaching the right boundary of the model. Dashed lines show the proppant front after reaching the right boundary.

In conclusion, it can be stated that flow rate has a strong impact on both settling and convection. Higher flow rate decreases settling and convection at the same time due to the fact that by increasing injection rate, viscous force overrides gravity force more and more. This in turn leads

to proppant placement efficiency improvement. In the design applications, applying higher injection rate can also create a wider fracture and ease proppant entry. However, higher injection rate does not necessarily yield better proppant placement when height growth is expected. In this situation, a shorter propped length might be obtained.

4.4.5 Effect of Proppant Density

We applied four different proppant densities of 2100, 2600, 3100 and 3600 kg/m^3. Figure 4.12 shows the concentration contours at 40 seconds of injection. Clearly, settlement velocity increases for heavier proppants. As it is shown in Fig. 4.12, a thin layer of proppant is formed at the bottom of the slot, before the front reaches the right boundary. For the selected input parameters in these simulations, changing the density of the proppant did not alter the proppant distribution significantly. This can be attributed to the relatively high viscosity of the injection fluid in these numerical exercises.

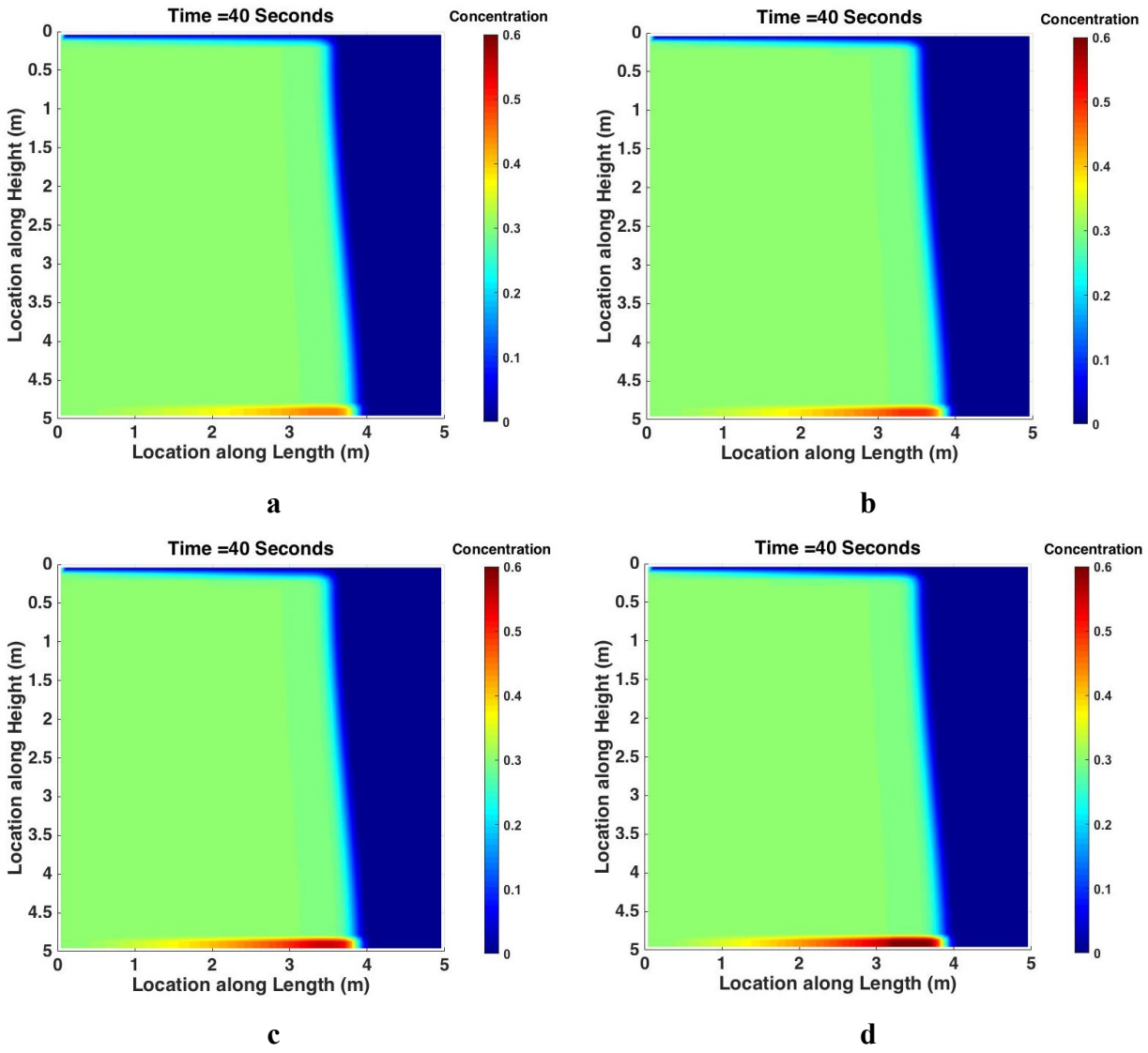

Figure 4.12: Concentration profile for different proppant densities of a) 2,100, b) 2,600, c) 3,100 and d) 3,600 kg/m^3 after 40 seconds of injection

4.4.6 Effect of Proppant Size

We applied different proppant diameters of 0.1, 0.6, 1.5 and 2.36 millimeters. These sizes are chosen based on the real proppant diameter range. It should be mentioned that in real case, the mobility of the proppants rapidly decreases when the fracture width is of the same order of magnitude as the proppant diameter. The fracture width should be 4 to 5 times bigger than the particle diameter for effective placement. However, we have neglected this fact here since our focus is to observe the settling characteristics of the particles. This effect can be accounted for by simply imposing a minimum fracture width (as a multiple of proppant diameter) required for free

proppant circulation, in the numerical code. Figure 4.13 shows the proppant concentration profiles after 40 seconds of injection. Increasing proppant diameter has the same but stronger effect as increasing proppant density and causes more settlement by increasing the vertical velocity component of proppants. This is predictable since according to Eq. 3.28, proppant settling velocity is proportional to the square of the particle diameter, while it is only proportional to the density to the power of one.

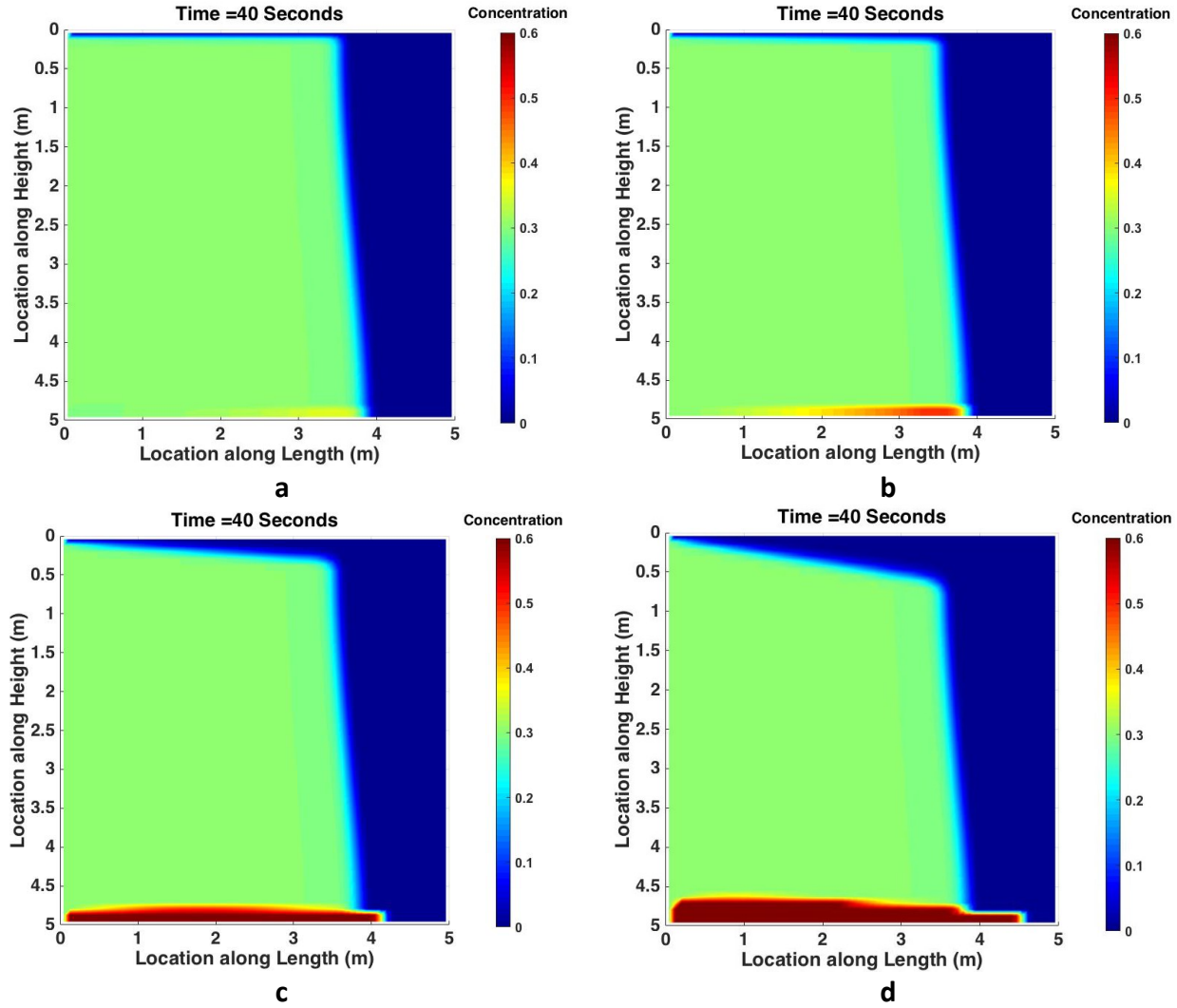

Figure 4.13: Concentration Maps for Different Proppant Diameters; a) 0.2 b) 1 and c) 2 mm, After 40 seconds of injection

4.4.7 Effect of Injection Fluid Viscosity

Figures 4.14 and 4.15 show proppant volume fraction contour plots at 50 and 65 seconds of injection for four different fluid viscosities of 0.05, 0.1, 0.4 and 1 Pa.Sec. For small values of

viscosity, settlement is very strong, resulting in a buildup of particles at the bottom of the slot. It can be observed from Figs. 4.14 and 4.15 that at lower viscosities, concentration has reached the saturation value in a large portion of the slot height. This can cause a premature termination of fracturing treatment since the carrying capacity of the injecting fluid reduces by reducing viscosity. Another issue with having low viscosity injection fluids is the creation of narrow fractures. If the width of the fracture is comparable to proppant diameter, the proppant transport can be altered significantly due to extra drag forces exerted on the proppants by the fracture walls.

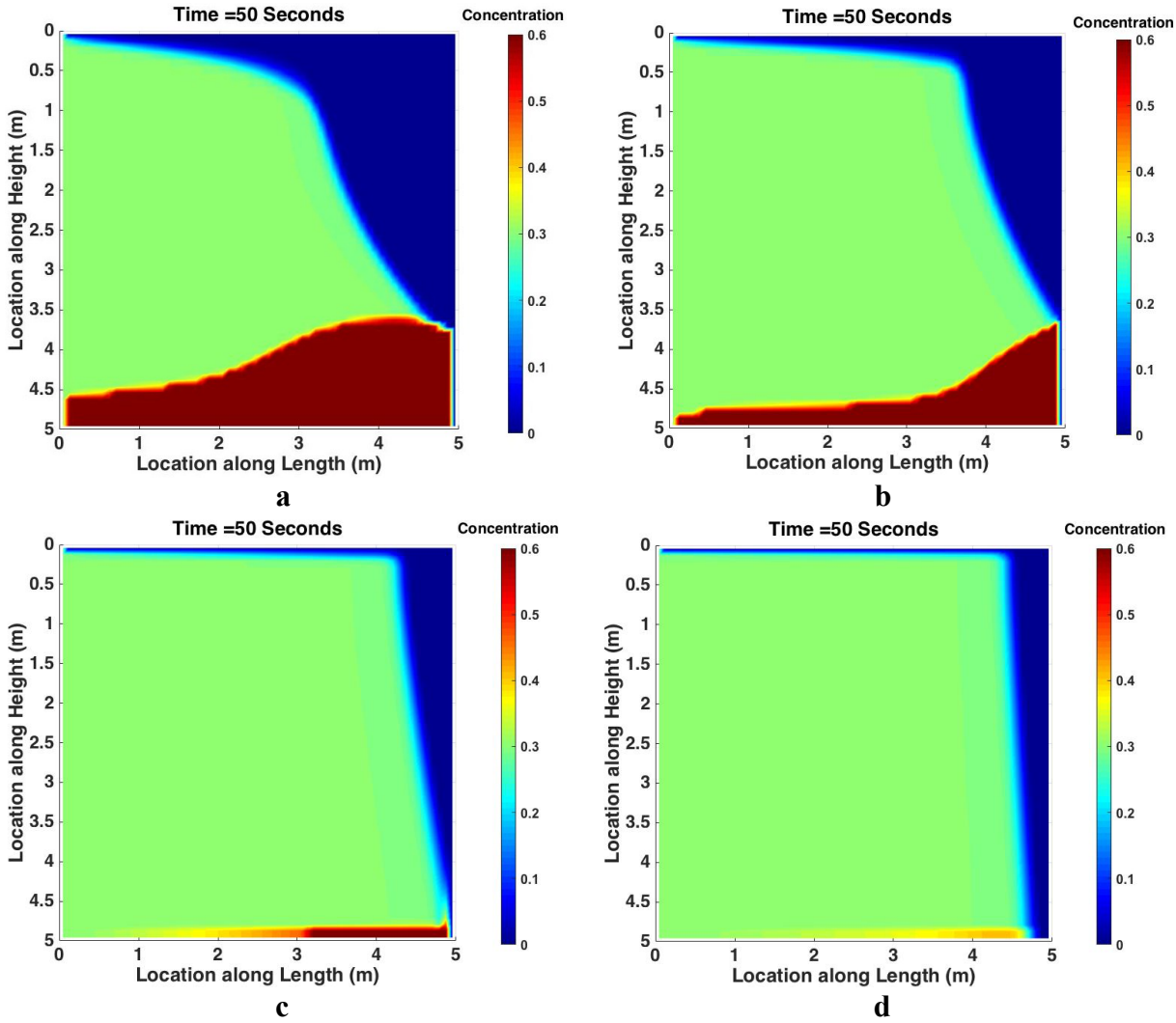

Figure 4.14: Concentration maps for different injection fluid viscosities; a) 0.01, b) 0.1, c)0.4 and d) 1 Pa.Sec, after 50 seconds of injection

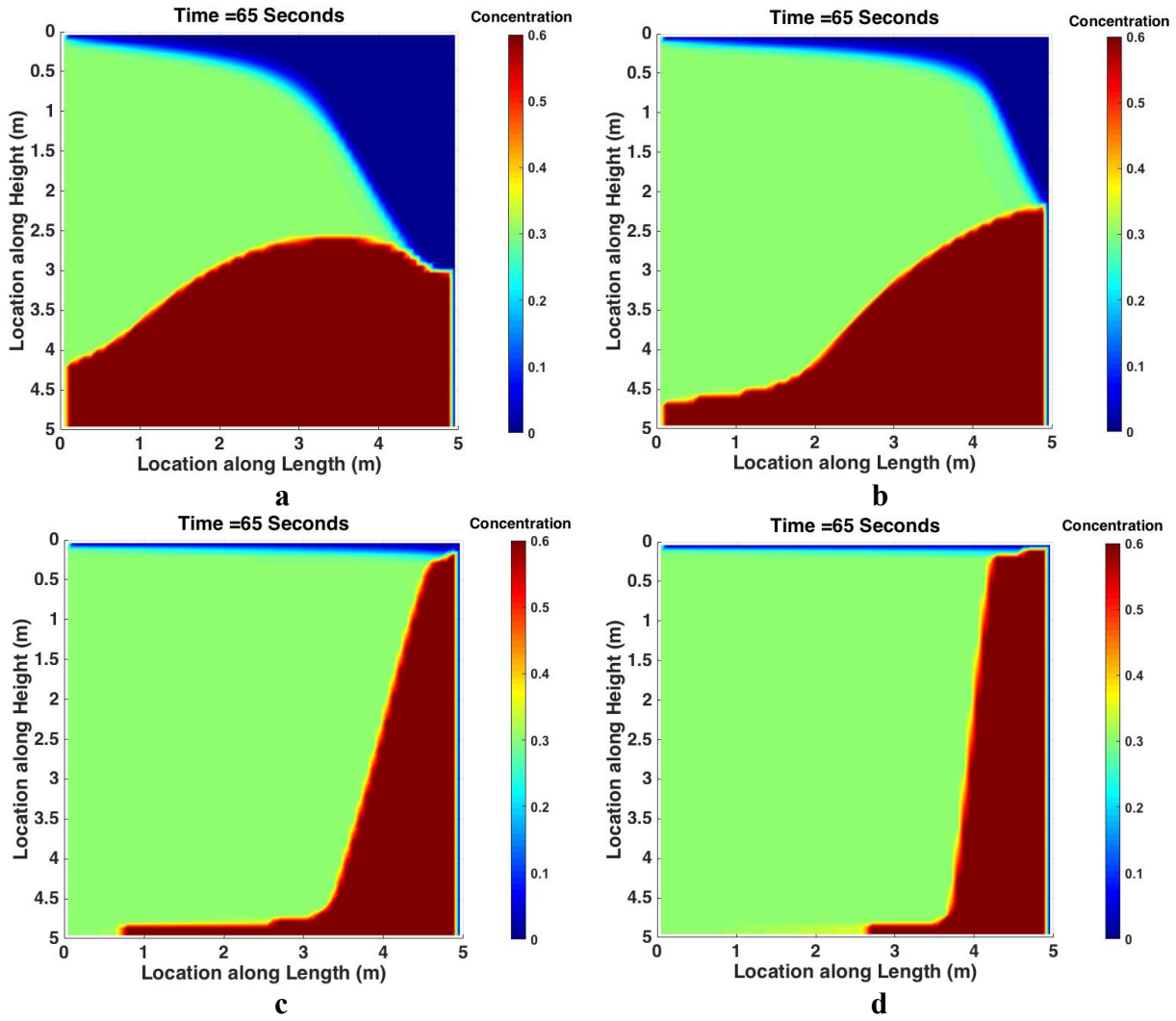

Figure 4.15: Concentration maps for different injection fluid viscosities; a) 0.01, b) 0.1, c) 0.4 and d) 1 Pa.Sec, after 65 seconds of injection

The Buoyancy number for the different simulated cases, as the viscosity increases are 0.375, 0.75, 3, and 7.5, displaying better carrying capacity for higher viscosity fluids. Based on the size of the bed at the bottom of the slot, settling is greatly enhanced in low viscosity fluids, while the slope of the concentration front in Fig. 4.14 shows convection is reduced in high viscosity fluids. Obviously, poor proppant placement should be expected specially when a long hydraulic fracture is created and a low viscosity fluid is used. Overall, viscosity is strongly effecting both settling and convection.

4.4.8 Elliptical Slot

The results presented so far related to the case of rectangular slot with a uniform width of 3 mm along the entire fracture height. In this section, we change the width of the slot from rectangular to elliptical to investigate the effect of fracture shape on proppant distribution. The width of the fracture here is calculated from:

$$w = w_{centre}[1 - (\frac{2y}{h})^2]^{0.5} \tag{4.9}$$

where w_{centre} is the maximum width of the slot in the middle (5 mm), h is the height of the model (5 m), and y is the vertical axis with the coordinate origin placed at the middle of the fracture.

Figure 4.16 shows the concentration map for the elliptic slot at different injection times. It is interesting that the concentration distribution is greatly different compared to the rectangular case. The reason is that for elliptical slots, horizontal slurry velocity is calculated from Eq. 4.10 (Nordgren, 1972) instead of Eq. 3.25:

$$u_{sl} = -\frac{\pi w^2}{64\mu}\frac{\partial p}{\partial x} \tag{4.10}$$

Obviously, proppant particles travel faster in the middle part of the slot, where the width is the greatest and offers least resistance to flow. In addition, at the top and bottom of the model the width is less than particle diameter. Therefore, both top and bottom of the slot are not covered by proppants. In real situations where there is leak off of injection fluid to formation, proppant will have some tendency to move towards the edges of the fracture. Therefore, the leak off reduces the tendency for proppant packing in the center part of the elliptic fracture to some extent.

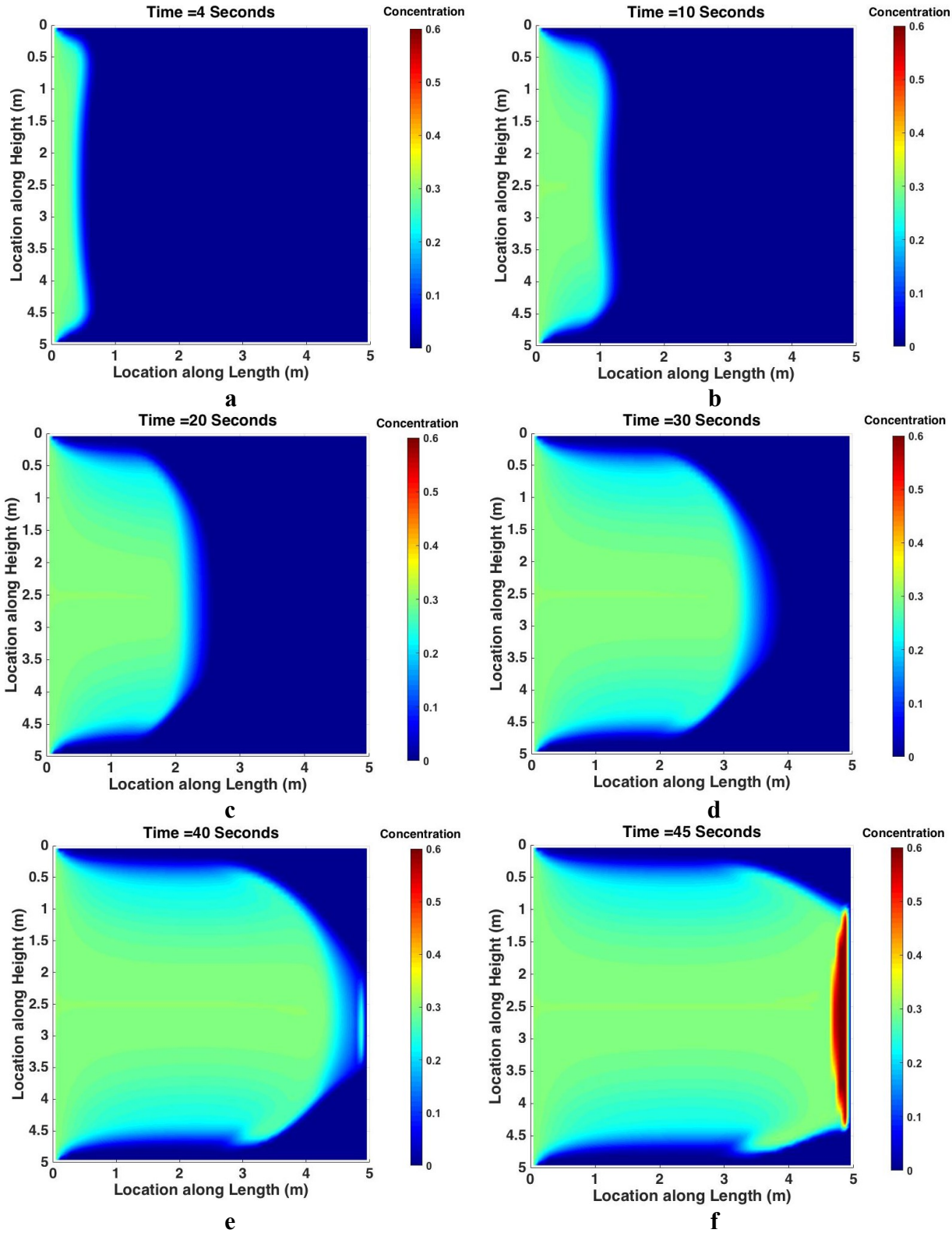

Figure 4.16: Simulation Result of Presented Model for Elliptic Slot

4.4.9 Buoyancy Number

To confirm the effectiveness of Buoyancy number in predicting the dominance of gravity over viscous forces, several simulation examples were carried out and the results are presented in this section. In the previous simulations, smaller tendency for downward slurry flow to the bottom of the slot and a more symmetrical proppant distribution were evident for higher Buoyancy numbers. To verify these phenomena, two simulations were conducted in which Buoyancy number was set to 0.1 and 1. Figure 4.17 shows the concentration distribution for abovementioned Buoyancy numbers at times that the front has advanced 2 m. As shown in Fig. 4.17, the lower slope of the concentration front indicates a higher convection. At the same time, higher convection means more lateral advancement of concentration front at the bottom of the fracture. Even at Buoyancy number of 1 the tendency of the injected slurry to go to the bottom of the slot is not diminished. Simulations at higher Buoyancy numbers result in an increased symmetry of the concentration distribution as a more uniform flow into the slot is expected for a higher N_{Bu}.

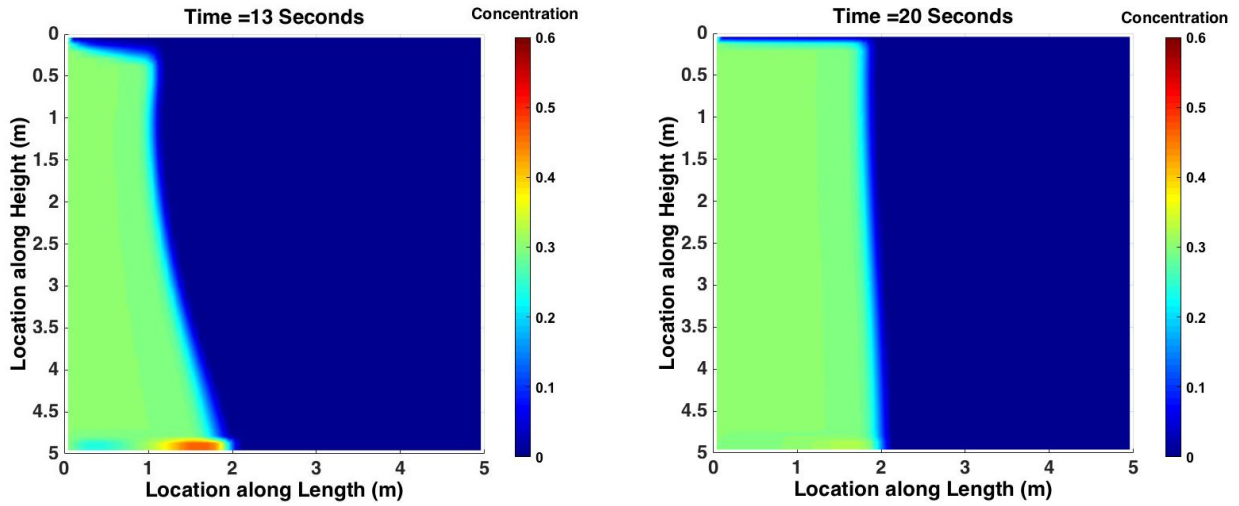

a **b**

Figure 4.17: Effect of Buoyancy number on Convective Flow: a) N_{Bu}=0.1, b) N_{Bu}=1

It is interesting to note that the shape of concentration front depends only on the value of Buoyancy number and not on a particular input parameter.

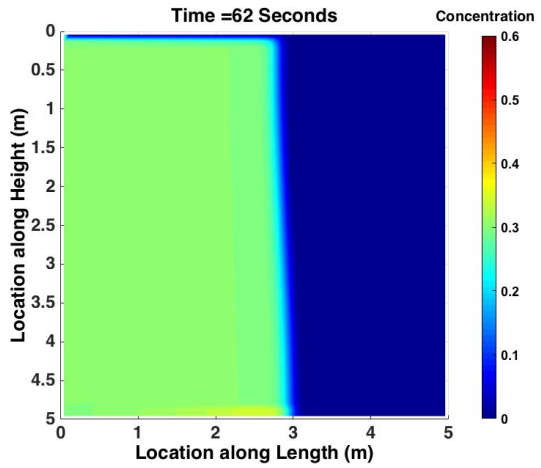

a) w=0.003×2 m, Δρ=1600/8 kg/m^3

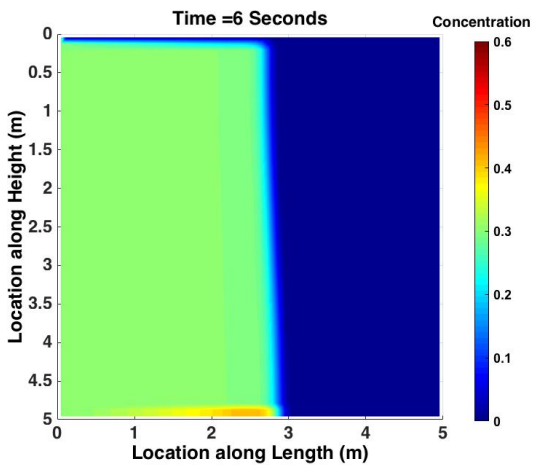

b) q=0.003×5 m^3/s, Δρ=1600×5 kg/m^3

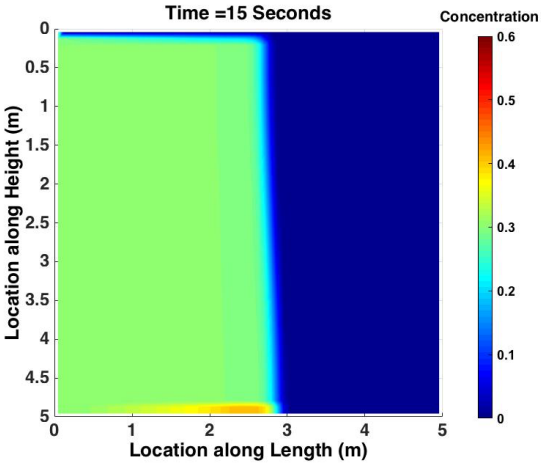

c) q=0.003×2 m^3/s, μ=0.4/2 Pa.s

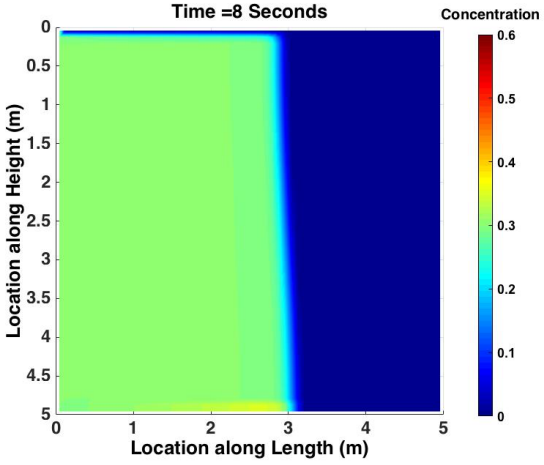

d) q=0.003×8 m^3/s, w=0.003×2 m

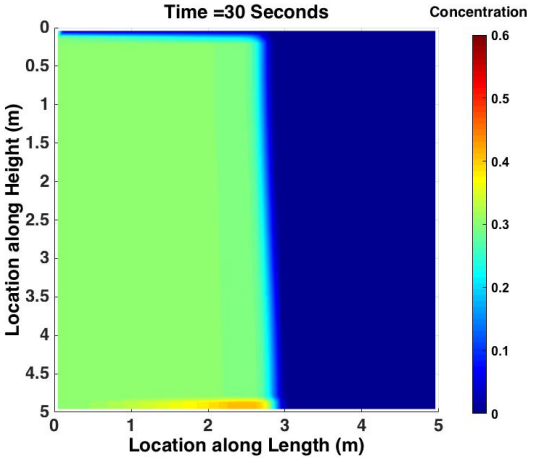

e) μ=0.4×5 Pa.s, Δρ=1600×5 kg/m^3

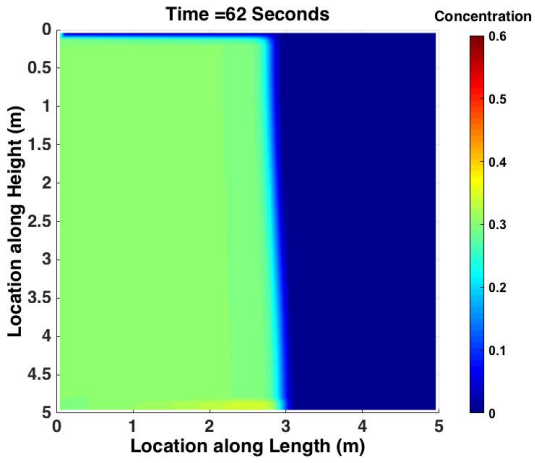

f) μ=0.4×8 Pa.s, w=0.003×2 m

Figure 4.18: Constant Buoyancy Number and Similarity of Concentration Plume

In a series of simulations, two parameters from Eq. 3.34 were changed in a way that the value

of Buoyancy number was kept constant. Figure 4.18 shows the simulation results for different density-width, flow rate-density, flow rate-viscosity, flow rate-width, density-viscosity and width-viscosity, when concentration front has advanced to 3 m from the injection boundary. The general shapes of all the concentration fronts are the same. The size of the concentration plume might vary a bit since it is difficult to capture the time at which identical sizes are obtained. The amount of settling is different in some cases and that is because Buoyancy number is not a measure of the settling. In addition, since the velocity field is different for different simulations, the time at which the concentration front reaches a certain point is also different.

4.5 Discussion of Results

During proppant injection, vertical motion of the proppants affects the final distribution and can lead to the creation of a proppant bed at the bottom of the fracture. The concentration of proppants inside the bank can reach its maximum value, which is the saturation concentration. If the bank covers a major portion of the fracture height, it can block further proppant injection leading to a premature termination of the proppant injection. The amount of vertical motion of proppants depends on the volumetric injection rate, suspending fluid viscosity, proppant density and proppant size. Overall, these parameters impact the concentration distribution by changing the proppant velocity field. Low suspending fluid viscosity, high proppant density, large proppant sizes and low injection rate can increase the proppant settlement.

According to our simulations, the viscosity of the carrying fluid is the most important parameter in controlling the lateral transport dominance over settling. Among other factors, density of the particles has a small impact on the final distribution of the proppants.

Based on the proppant distribution for elliptic slots, we can conclude that the fracture shape can affect the slurry convection and settlement. Convection was stronger than settlement in the cases we attempted since no bed was created in our simulations.

In field-scale fracture designs, the fluid velocity will be affected by several other variables such as fluid leak off, non-uniform proppant size distribution, and non-spherical particle shapes. Although we neglected these factors, our modelling results can still be used to improve treatment designs. For example, we can obtain an estimate of the flow rate which will disperse proppants

more uniformly over the fracture height, without creating a bed at the bottom. Similarly, a low pump rate in the order of leak off rate will confine the particles at the bottom of the fracture rendering an ineffective frac-packing operation.

4.6 Conclusion

We have numerically simulated proppant transport inside a slot by solving the equations of motion of slurry and proppants. We assumed incompressible and Newtonian fluid and an isothermal system. We accounted for the change of the slurry viscosity due to the change of proppant concentration. An effective numerical technique was used to capture the proppant front more precisely and with minimum oscillation and diffusion. In this numerical scheme, WENO scheme of finite volume was employed to approximate the solution of the hyperbolic transport partial differential equation. We used dimensional splitting technique to reduce the running time and complexity of solving hyperbolic partial differential equations.

We investigated the effects of injection rate, proppant density, proppant size and injection fluid viscosity on proppant placement. These parameters change the final proppant concentration distribution since they control particle settlements. Some of the conclusions from the sensitivity analysis presented in this paper include:

- The model simulated the proppant bank creation at the bottom of the fracture during the treatment time.
- The fracture fills up faster at higher injection rates with less proppant settlement.
- Viscosity of the carrying fluid has the strongest effect on the amount of proppant settlement.
- Within practical ranges, parameters such as proppant size and density only have a modest effect on proppant settlement.

As of now, there is a significant uncertainty in the effect of physical proppant and fluid parameters on the final proppant distribution. The numerical model presented here enhances our understanding of the relationship between fluid and proppant properties and the final proppant distribution that determines the conductivity of the propped fracture. The outcome is improved design and implementation of the fracpack operation and reduced uncertainty in the fracpack performance.

Chapter 5: Smeared Modeling of Hydraulic Fracture Using Partially Decoupled Modeling of Reservoir and Geomechanics Simulators

5.1 Introduction

In this chapter, we describe the numerical method of coupling between our reservoir simulator and geomechanics commercial software FLAC2D to build a smeared fracture type hydraulic fracture simulator. The new development falls within the category of partially decoupled model, and is very versatile, flexible and efficient. This approach can be used to couple any other advanced commercial fluid flow or geomechanics simulators with good accuracy to better describe the initiation and propagation of hydraulic fractures. As we will see later in the next chapter, transport of proppants inside the created fractures can also be linked to this package as a third module.

Sophisticated reservoir simulators should include not only the solution of fluid flow and stresses, but also the dependencies between the two. Such dependencies although ignored or approximated safely in elastic reservoirs, are pronounced in high-pressure injection operations like hydraulic fracturing and require the use of some sort of coupled modeling. In petroleum-related operations, many of the processes and technical problems root in interactions between flow and stress-strain response of the formation. Injection of fluids and proppants into the hydrocarbon reservoirs during hydraulic fracture treatment induces significant variations in reservoir pressures which leads to the modification of the stress state in and around the reservoir. The reservoir properties like porosity and permeability could be altered by this change in the stresses which may in turn modify the fluid flow within the reservoir. This means that in these situations, geomechanical effects (deformations and stresses) are strongly coupled to fluid flow. In numerical simulations, these interconnected effects should be captured and analyzed through the coupling of the geomechanics and reservoir fluid flow simulators.

There are many descriptions of such coupled simulators in the literature. As an example we can mention Settari and Mourits (1994) and Chin and Thomas (1999) in investigation of the effects of reservoir compaction, Chin et al. (1998) in the context of reservoir stress dependent permeability, Gutierrez and Makurat (1997) for studying fracture permeability variation of fractured reservoir, Behr et al. (2006) in the study of damage zone around a hydraulically fractured tight gas reservoir, and Miranda et al. (2010) in the study of hydraulic fracturing.

Previous works have proved that coupling of the reservoir simulation and geomechanics modeling is essential in better understanding of the hydraulic fracturing treatment. The coupling of fracture propagation with reservoir fluid flow and heat transfer were mathematically established first in 1980s (Hagoort et al, 1980, Settari, 1980, Nghiem, 1984), and more recently in Al-Thawad et al. (2004) or Longuemare (2001). In the early works, essentially two independent grid systems were used for the numerical solution of the continuity equation in the fracture and the partial differential equations for the reservoir multi-phase flow. The coupling was improved later on by using only one set of common gridblocks for both fracture and reservoir flow and considering a high permeability for the fracture (Settari et al, 1990; Weill and Latil, 1992). Further improvement was achieved by using pressure/stress dependent permeability in the coupled simulations (Garon and Dunayevsky, 1988, Settari and Mourits, 1994, 1998, Ji et al, 2004, 2006). Lebel (2002) used a type of upstream weighting in evaluating the effective permeability between fractured gridblocks. Hustedt et al. (2005) used a two-way explicit coupling approach between a reservoir simulator and a fracture simulator which was proposed by van den Hoek et al, earlier in 1996 but was using a pseudo 3-D fracture model. Ehrl (2000) optimized future field development by integrating a 3-D geologic model and a field-scale reservoir simulation model in which local grid refinements were used around the wells to remove numerical stability problems. However, the most flexible approach was suggested by the use of partially de-coupled approach (Settari et al, 1990; Weill and Latil, 1992).

Although most of the field evidence is related to the importance of coupling in unconsolidated or soft formations, where the reservoir undergoes large rock deformation, Heifer et al. (1994) showed that coupling effects can also be significant in fractured reservoirs.

Historically, numerical modeling of such coupled processes were performed in a fully decoupled manner and based on the primary purpose of the computation, were categorized into geomechanical modelling, reservoir simulation and fracture mechanics with the primary goal of computation as stress-strain behavior, flow in porous media and fracture propagation, respectively. Simplifying assumptions were inevitable about part of the problem that was not of primary interest. It is obvious that such an approach proves to be inadequate in situations where strong coupling between these processes exists. As an example, porosity and permeability of the formation may change in any type of reservoir modelling of fluid injection into the wellbore, due to the stress changes and failure of the underground formation.

This chapter describes an approach for the modular coupling of an in-house developed fluid flow code with a 2D stress/strain code (FLAC2D). In the next chapter, a 3D proppant transport simulator will be added to these modules. The iteratively coupled modules have been recognized to be equivalent to a fully coupled solution of geomechanics and fluid flow (Settari and Mourits, 1998). We discuss the partial coupling of fluid flow and geomechanics in modeling fracture initiation and propagation by considering a common gridblock for fracture and reservoir and updating porosity and permeability. The method captures the effects of fracture on reservoir fluid flow and formation geomechanics through stress dependent permeability and porosity. We also elaborate the numerical algorithm of the linkage which uses MATLAB as the interface. Several examples will be presented to show the robustness and flexibility of the approach. The hydraulic fracture simulator described in this chapter is a key step in simulating proppant transport inside fractures, which is the topic of the next chapter.

5.2 Coupling Approaches

The linkage between the simulators falls within three main categories. It can be either a fully decoupled linkage, a fully coupled type or partially decoupled type of linkage. In the first two types of linkage, an explicit fracture is simulated in the model, but in the third approach, some sort of "effect" of the fracture is included.

Traditionally, fracture mechanics in impermeable rocks has been adopted to porous media in the petroleum industry (Settari et al., 1989). In these models, stress changes around the fracture caused by geomechanical effects are estimated by simple 2D analytical approaches which decouple reservoir simulation and stress solution. Generally, in fully decoupled approach, the fracture equations are solved independently of the reservoir response. In other words, the fracture geometry is obtained by numerical or analytical methods and its effect is represented in the reservoir model by several methods, ranging from an overall leak-off or permeability modification in the reservoir block containing the fracture or increasing the wellbore radius (Vairogs, 1971; Aziz and Settari, 1979). This approach is computationally efficient; nevertheless, it is a simplistic approximation of the reservoir. The main disadvantage of this type of coupling is its restricted range of validity.

In fully coupled models, as the name implies, the fracture and reservoir equations are solved simultaneously at all times. The fracture propagation is simulated in a fixed reservoir grid.

Although the reservoir fluid flow is not simplified in this approach, the implementation of a numerical solution is cumbersome and it lacks flexibility. Simultaneous formulation of flow and geomechanics results in large matrices and the model will therefore be very computationally expensive. Moreover, in fully coupled models, iterations are needed in the same fashion as iterative coupling, and this approach does not reduce the complexity of the problem.

The third approach falls in between the other two approaches in which the fracture propagation and reservoir fluid flow are solved independently. However, the result from each module is transferred to the other simulator to improve the outcome. In this approach, which is called partially coupled or partially decoupled, the new fracture grids can be easily generated and in principal, it can be conveniently attached to any type of reservoir or fracture simulator. This greatly increases the flexibility and range of application of the method. Settari (1988) was the first researcher who proposed the modular coupling. In modular coupling information is passed between different modules and iterations are used to converge the solution. Such an approach can even use highly advanced commercial reservoir and geomechanics simulators.

Here we don't discuss fully coupled models since we are using a multi-module simulator and different modules are linked together through partially coupled principals. This approach seems to be effective when we consider proliferation of the available geomechanics codes outside the petroleum engineering. Our in-house developed fluid flow simulator, which is coded in MATLAB, is the host and is linked to the commercial stress simulator FLAC to develop our numerical hydraulic fracture simulator. After proppant injection starts, a third module, which is the proppant transport simulator, is added to the modules. In the following sections, after a quick review of various modular couplings, we describe the coupling between the fluid flow and geomechanics in developing our numerical hydraulic fracture simulator. The linkage of the proppant transport simulator to this package will be discussed in the next chapter.

5.3 Different Methods of Partial Coupling

Models can be built based on solving the fluid flow and stress equations in different modules. Our model consists of three separate simulators: fluid flow, geomechanics and proppant. In modular simulators, different strategies are applied to link the modules.

In "one way coupling", pore pressures which ae the output of reservoir simulator, are passed to the geomechanics module, but no information is passed back to the reservoir simulator (Settari

and Walters, 2001). In other words, the geomechanics module does not attempt to improve the fluid flow solution. This old-style type of coupling can lead to large errors when porosity strongly depends on the flow. In the "loose coupling", reservoir and geomechanics modules are run sequentially and the solution from each module is passed to the other one (Settari and Walters, 2001). However, this transfer of information happens one time in each time step and no iteration is performed. Such coupling cannot represent complex constitutive plasticity models of the formation. Loose coupling is also called "explicit coupling" or "sequential coupling". The type of coupling that we used is "iterative coupling" which is shown schematically in Fig. 5.1. In this type of coupling, iteration is carried out in each time step, between the fluid flow and geomechanics modules until certain convergence criteria are met. In each iteration, the previous guess of the permeability and porosity is used to solve the flow equation and the corresponding change of pore pressure is used to calculate new deformations and stresses, which in turn provide new update of permeability. Iterative coupling, when converged, gives equivalent solution to a fully coupled model, while it is much more flexible and less computational demanding.

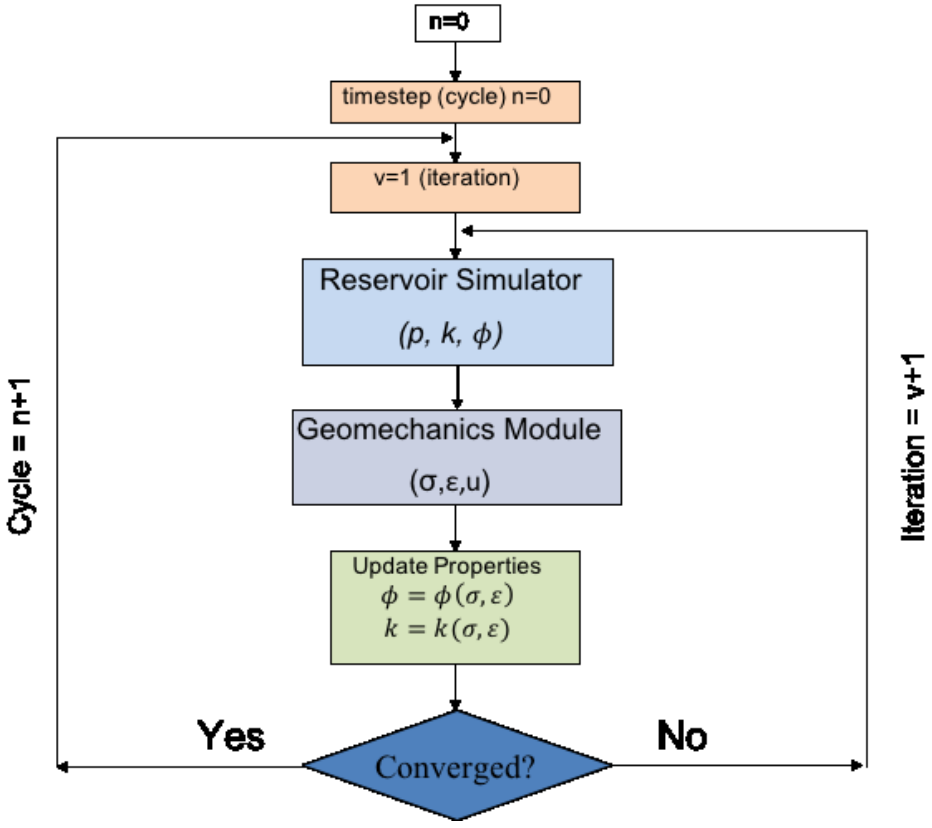

Figure: 5.1: Numerical Algorithm for Iterative Coupling

Each of the abovementioned strategies of partially coupled models can be performed in two ways: “Pore Volume Coupling” and “Flow Properties Coupling” (Settari and Mourits, 1998). The information that is updated and transferred to the other module is different in these two methods. Flow properties coupling was implemented in our linkage algorithm and therefore will be described in detail is given in the next section.

5.3.1 Flow Properties Coupling

The second type of coupling is called flow properties coupling, in which permeability is modified as a function of effective stresses. Such a relationship has been investigated for many types of formation rocks and is stronger in low permeability materials. In addition, it is now known that the tensor character of permeability may also have an important role in fractured reservoirs. Moreover, porosity dilation in soft and unconsolidated formations can also lead to permeability enhancement. Furthermore, flow properties coupling does not have any effect on the mass balance formulation, as pore volume coupling does and, therefore, is easier to apply. In the traditional approach of flow dependent coupling, tables of primary flow property, which is permeability, versus pressure is used in an uncoupled model. In those approaches, different assumptions are made about stress change during time. However, in the modern attempts of this type of coupling, stresses are obtained by including geomechanics equations. The main advantage of such coupling is its capability in predicting permeability changes from the geomechanics of opening fractures or failure (dilation) of joints. The orientation of fractures or joint requires a full tensor permeability in the flow model. Consequently, flow properties coupling, can capture the change in reservoir description through time because of geomechanics. In hydraulic fracturing simulation, the transmissibility multiplier in the potential fracture plane is dynamically changed and the changes in fracture propagation pressure with time, which may be large, can be captured.

5.4 Hydraulic Fracture Module

Our hydraulic fracture numerical simulator consists of two modules: fluid flow and geomechanics. From now on, when we use the term “hydraulic fracture module”, we refer to the coupled fluid flow and geomechanics modules.

Fluid flow simulator is the host or master module in the iteratively coupled model, which means it is run in the beginning of each time steps and it triggers (calls) the geomechanics module to

calculate stresses and displacements. In practice, as mentioned before, the iterative modular coupling has a great range of flexibility since each of the modules can be any commercial software.

It is well known that the orientation of the hydraulic fracture is determined by the in-situ stress field: the hydraulic fracture will propagate perpendicular to the minimum principal in-situ stress. In all of our simulations we assumed the minimum principal stress is horizontal and therefore the fracture plane is a vertical plane, normal to the direction of minimum stress.

For simplifying the illustrations, we assume that the minimum in-situ stress is along y direction as depicted in Fig. 5.2 and compressive stresses are negative.

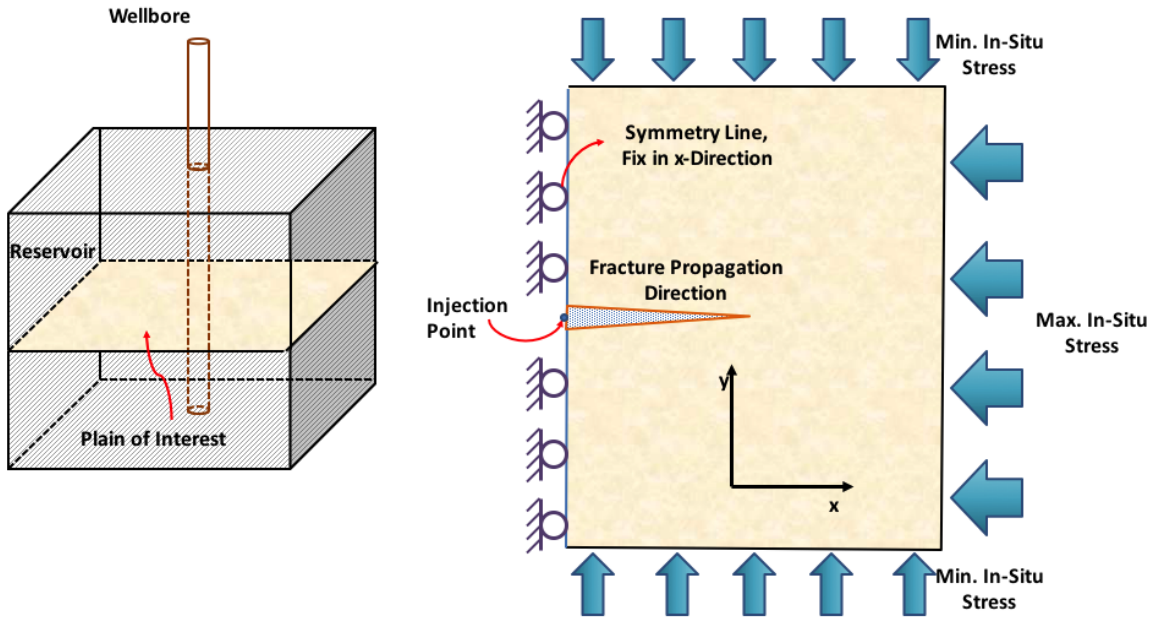

Figure 5.2: Geometry and Boundary Condition of the Model

There are many different fracture initiation and propagation criteria in the literature. In this work, we utilized the geomechanical results for this purpose and assumed that fracture initiation and propagation are determined by the effective stresses (σ_{tip}+p). The fracture initiation and propagation in this work are assumed to occur when the tensile stress exceeds the tensile strength:

$$\sigma_3 + p \geq T \tag{5.1}$$

where σ_3 is the minimum principal stress, p is the pore pressure and T is tensile strength of the rock.

Due to the fluid injection and poroelastic effects, the stress at the tip of the fracture is changing with time. This change varies along the model and is generally complex. Hence, we reformulate the initiation and propagation criterion as:

$$\sigma_{tip} + p \geq T \tag{5.2}$$

where σ_{tip} is the stress at the tip of the fracture in the minimum principal stress direction. This equation means that fracture will propagate through a gridblock if the least principal effective stress at that gridblock exceeds the tensile strength of the rock. This criterion is checked in every time step in the geomechanical module to give the dimensions of the fracture.

The total length of the fracture is determined by the sum of the length of all the elements that satisfy Eq. 5.2 criterion. There is, however, one issue that should be addressed here. There will always be a situation in which the effective stress at cell i is higher than tensile strength of the rock, while the same property at cell i+1 is less than tensile strength of the rock (Fig. 5.3). This means that the fracture tip will be somewhere between the gridblocks i and i+1.

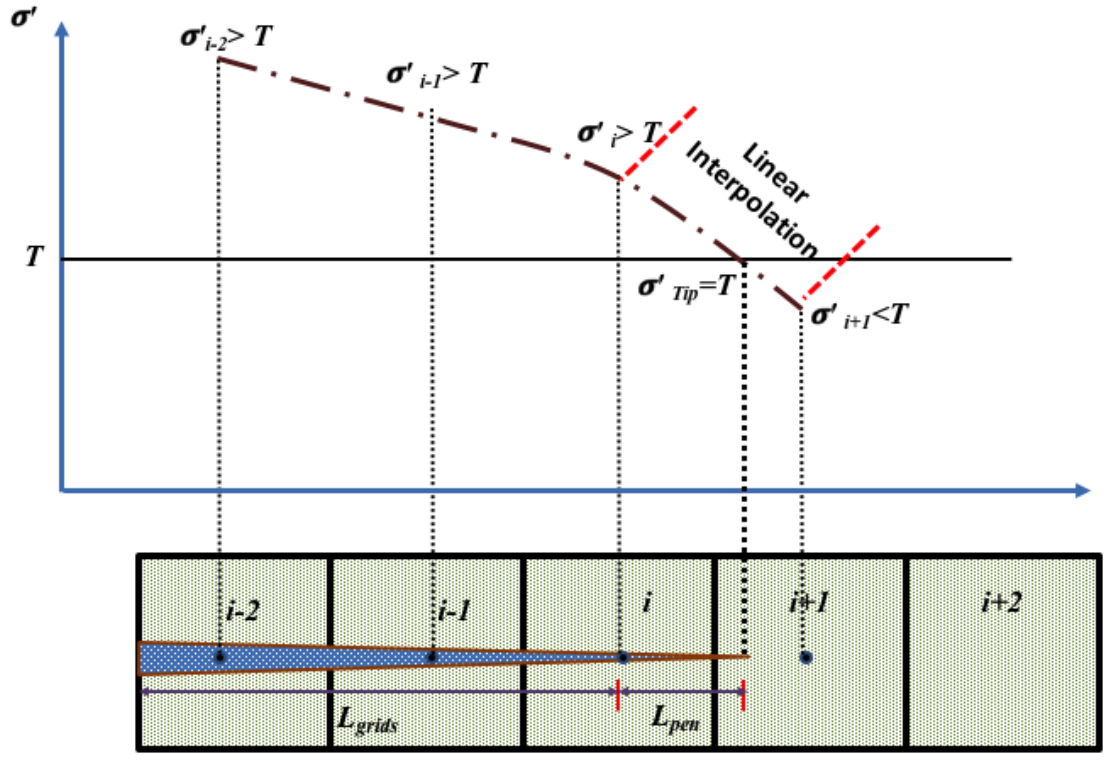

Figure 5.3: Linear Interpolation of Fracture Penetration Length

To more accurately calculate the length of the fracture, the amount of fracture penetration into the gridblock i+1 should also be considered. According to Fig. 5.3, the length of the fracture, L_f, is:

$$L_f = L_{grids} + L_{pen.} \tag{5.3}$$

where L_{grids} is the sum of the element sizes that are completely penetrated by the fracture and $L_{pen.}$ is the fracture penetration distance into the element that contains the tip of the fracture. Obviously:

$$L_{grids} = \sum_{i=0}^{N} \Delta x_i \tag{5.4}$$

where N is the number of the elements in which the effective stress is more than the tensile strength of the rock. On the other hand, the amount of fracture penetration into gridblock i+1 can be calculated by interpolation and assuming the effective stress at the tip is equal to tensile strength of the rock:

$$L_{pen.} = \frac{\sigma'_y - T}{\sigma'_{y_i} - \sigma'_{y_{i+1}}} \Delta x_{i+\frac{1}{2}} \tag{5.5}$$

The height of the fracture is assumed to be equal to the payzone thickness.

The width on the other hand can be calculated from geomechanics. If the initiation criterion is met in any gridblock, then the width of the fracture at the corresponding location is determined from nodal displacement of that gridblock in the direction normal to the minimum principal stress, as:

$$w(x, y) = 2u_y(x, y) \tag{5.6}$$

where w is fracture width and u_y is displacement perpendicular to the minimum principal stress.

5.4.1 Calculation of the Average Permeability in Fractured Gridblocks

In our hydraulic fracture simulator, only one common grid system is considered for both the reservoir and the fracture. If the fracture is modeled with its actual dimensions, a severe time step limitation arises in the simulation. Correspondingly, the permeability and porosity of the fracture is smeared in the encompassing gridblock. Based on the fluid flow cubic law, the permeability of the fracture depends on the fracture aperture or width as:

$$k = \frac{w^2}{12} \tag{5.7}$$

This equation gives a large value for the permeability and, therefore, the fracture is the highly permeable part of the encompassing gridblock. For this reason, the permeability of the fractured gridblocks should be enhanced to include the effect of fracture on fluid flow. As mentioned before, fracture can penetrate completely or partially into a gridblock. The permeability enhancement follows different formulations for these two cases.

5.4.2 Permeability Enhancement for Grids Completely Penetrated by Fracture

All the gridblocks in the reservoir simulator that contain the fracture will be completely penetrated by the fracture, except for one gridblock that contains the fracture tip. Obviously, the presence of fracture results a significant permeability enhancement. However, in smeared fracture approach, this enhancement should be averaged within the whole gridblock.

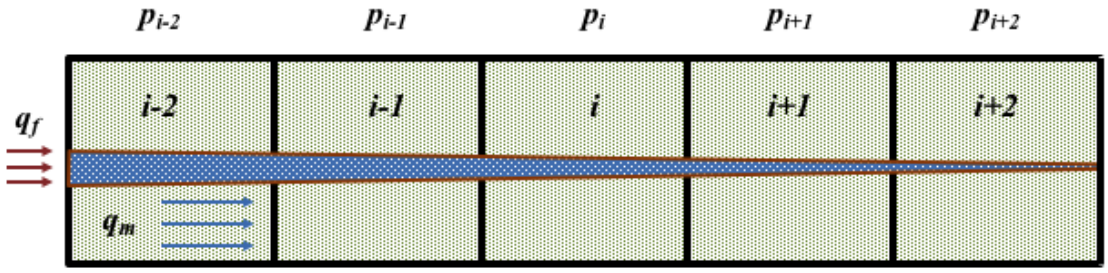

Figure 5.4: Grids Completely Penetrated by the Fracture

According to Fig. 5.4, there are two flow paths between adjacent blocks, namely through the fracture and through the matrix. Therefore, the total flow from grid i to i+1 will be the sum of the flow through matrix and fracture:

$$q_t = q_m + q_f \tag{5.8}$$

where q_m is the matrix flow rate and q_f is the fracture flow rate. According to Darcy's law, each of these flow rates can be stated as:

$$q_t = \frac{k_{avg}\Delta y \Delta z}{\mu B \Delta x}(p_{i+1} - p_i) \tag{5.9}$$

$$q_m = \frac{k_m(\Delta y - w)\Delta z}{\mu B \Delta x}(p_{i+1} - p_i) \tag{5.10}$$

$$q_f = \frac{k_f w \Delta z}{\mu B \Delta x}(p_{i+1} - p_i) \tag{5.11}$$

Substituting Eq. 5.9 to 5.11 into Eq. 5.8 gives the average permeability of the fractured block as:

$$k_{avg} = \frac{k_m(\Delta y - w) + k_f w}{\Delta y} \tag{5.12}$$

k_{avg} is the permeability of the gridblock that contains the fracture. The fracture width is usually ignored in the matrix flow rate calculation since it is generally much smaller than Δy of element. However, we keep this term in all the formulations.

5.4.3 Permeability Enhancement for Grids Partially Penetrated by the Fractures

For elements partially penetrated by the fracture, we need to define the distance, or length of fracture penetration into the gridblock. We denote this length by L_p and we know that this length is always smaller than the length of the gridblock:

$$0 \leq L_{pen.} \leq \Delta x \tag{5.13}$$

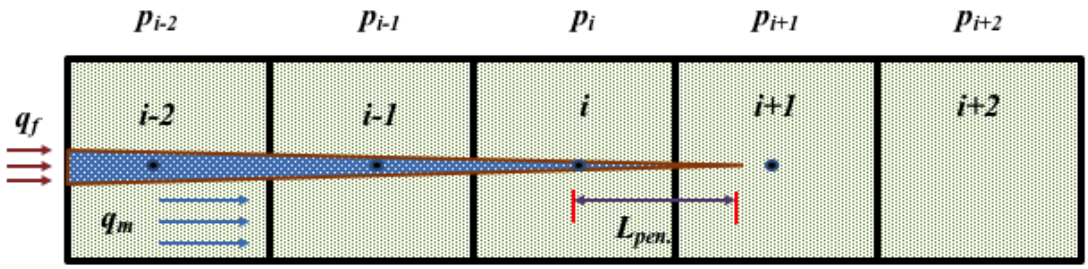

Figure 5.5: Last Grid is Partially Penetrated by the fracture

According to Fig. 5.5, the pressure drop between cells i and i+1 can be written as:

$$p_{i+1} - p_i = (p_{i+1} - p_{i+L_{pen.}}) + (p_{i+L_{pen.}} - p_i) \tag{5.14}$$

This pressure drop can be written as a function of total flow rate from cell i to cell i+1 as:

$$p_{i+1} - p_i = \frac{q_t}{\frac{k_{avg}\Delta y \Delta z}{\mu B \Delta x}} \tag{5.15}$$

Between locations $i+L_p$ (Fig. 5.5) and i+1, the flow only passes through the matrix and $q_t = q_m$. Therefore:

$$p_{i+1} - p_{i+L_p} = \frac{q_t}{\frac{k_m \Delta y \Delta z}{\mu B(\Delta x - L_{pen.})}} \tag{5.16}$$

and between points i and $i+L_p$, the pressure drop will be:

$$p_{i+L_p} - p_i = \frac{q_t}{\frac{k_m(\Delta y - w)\Delta z}{\mu B L_{pen.}} + \frac{k_f w \Delta z}{\mu B L_{pen.}}} \tag{5.17}$$

substituting these pressure drops (Eqs. 5.15 to 5.17) into Eq. 5.14 gives the smeared cell permeability when the gridblock contains fracture tip:

$$k_{avg} = \frac{k_m \Delta x[k_m(\Delta y - w) + k_f w]}{\{(\Delta x - L_{pen.})[k_m(\Delta y - w) + k_f w] + k_m \Delta y L_{pen.}\}} \tag{5.18}$$

The permeabilities of the fractured gridblocks are dynamically updated during each time step according to Eq. 5.12 and 5.18.

Fracture permeability is a function of aperture and aperture is a function of net pressure inside the fracture (or effective stress). Therefore, it can be concluded that above treatment makes the permeability pressure-dependent or effective stress-dependent. In addition, in our numerical simulations, such a dynamic calculation of permeability through time can be used to capture the change of matrix permeability due to pore pressure changes during injection (or production) in stress sensitive formations or change in fracture mobility due to proppant injection. We will discuss the reduction of propped fracture mobility in the next chapter.

5.4.4 Porosity Change

During fluid injection into the formation, porosity of the formation rock changes. It is desirable to state this change of porosity in terms of volumetric strains, so that the direct outputs of geomechanics module can be used to obtain the new porosity value in each time step. Assuming the original porosity of the formation is:

$$\phi_0 = \frac{V_t - V_g}{V_t} \tag{5.19}$$

where V_t is the total volume and V_g is grain volume, if any volume change, ΔV, occurs, the new porosity will be:

$$\phi_{new} = \frac{(V_t + \Delta V) - V_g}{(V_t + \Delta V)} \tag{5.20}$$

The volumetric strain, ε_v, on the other hand is:

$$\varepsilon_v = \frac{\Delta V}{V_t} \tag{5.21}$$

Therefore:

$$\phi_{new} = \frac{(V_t + \varepsilon_v V_t) - V_g}{(V_t + \varepsilon_v V_t)} \tag{5.22}$$

or:

$$\phi_{new} = \frac{\varepsilon_v + \phi_0}{1 + \varepsilon_v} \tag{5.23}$$

This change in porosity is due to the deformation of the rock. On the other hand, fracture porosity also needs to be included in the porosity calculation of the fracture gridblocks. Fracture volume in a given gridblock can be calculated as:

$$V_f = L_{f_i} \Delta z w \tag{5.24}$$

where L_{fi} is the fracture length in the gridblock. Therefore, the fracture porosity is:

$$\phi_f = \frac{V_f}{V_b} = \frac{L_{f_i} \Delta z w}{\Delta x \Delta z \Delta y} = \frac{L_{f_i} w}{\Delta x \Delta y} \tag{5.25}$$

where V_b is the bulk volume of the gridblock. The total porosity of a fractured gridblock will be:

$$\phi_{new} = \frac{\varepsilon_v + \phi_0}{1 + \varepsilon_v} + \frac{L_{f_i} w}{\Delta x \Delta y} \tag{5.26}$$

By treating porosity in this way, any closing or opening of the fracture which in turn results in fracture volume change, can be captured as a change of fracture porosity.

5.5 Coupling between Fluid Flow and Geomechanics Modules

In this section, we describe our numerical technique in developing a hydraulic fracture simulator through iterative coupling of a reservoir simulator and an advanced commercial geomechanics software, FLAC 2D, with considering plasticity effects. Only one grid system is used for reservoir simulation and geomechanics modeling to better evaluate the mutual influence between dynamic fracture propagation and fluid flow. Although, in theory, the stress model can have an independent mesh from the reservoir simulator mesh, it is advantageous and simpler to use the same mesh for the two modules. In this case, since the location of the nodes are the same in the two gridding systems, there is no need to map the results from one grid system to another. The

zero-displacement boundaries of the model are placed far enough from the well such that they do not influence the solution.

The communication between the simulators takes place through an interface code developed in MATLAB. The pressure changes occurring in the reservoir simulator are passed to the geomechanical simulator by the interface code and the updated stresses and displacements are passed back to the reservoir simulator and are used to evaluate coupled parameters in the reservoir formulation. Iterations are needed to ensure convergence. The interface code has enough flexibility to allow different degrees of coupling depending on the accuracy needed. Figure 5.6 is a schematic of the coupling in one iteration.

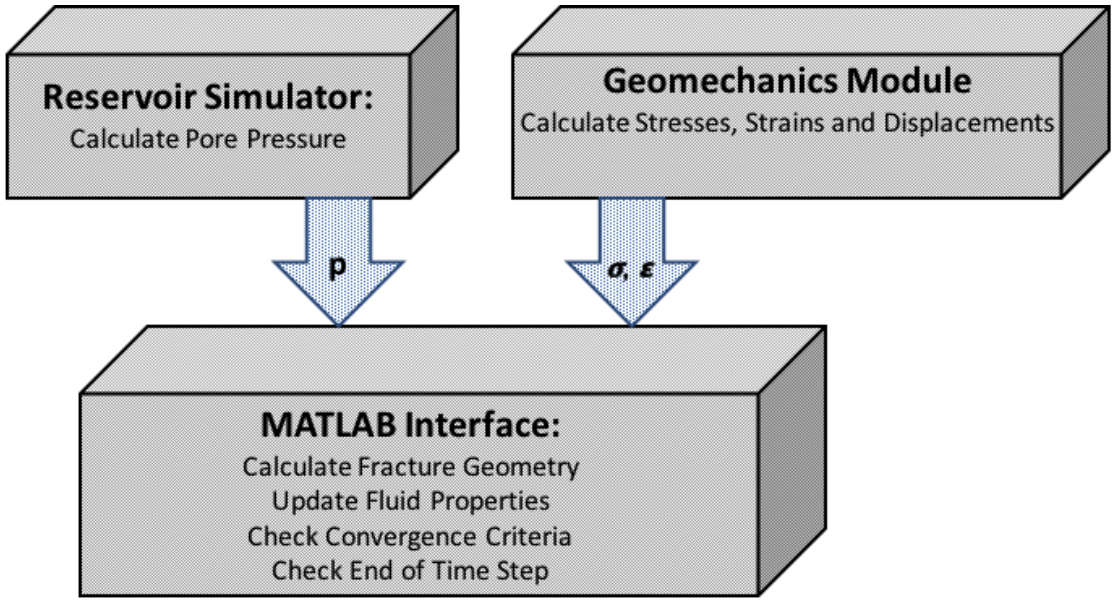

Figure 5.6: Algorithm of Coupling during Each Iteration

As it can be concluded from presented formulation of permeability and porosity, a strong dependency exists between fluid flow and geomechanics outputs; therefore, the linkage between the modules is essential. In our coupling scheme, porosity and permeability are used as the coupling parameters between the modules. Figure 5.6 illustrates the procedure of partial coupling through flow properties, between the fluid flow simulator and the stress code FLAC2D, with the reservoir simulator being the host module.

After creating model geometry and the mesh, fluid flow simulator starts the simulation to give pore pressures of the gridblocks. These pressures are transferred to the geomechanics module in which stresses and strains are calculated. The pore pressures are used to calculate effective

stresses and check the fracture initiation and propagation criteria (Eq. 5.2). If the criteria are met in any gridblock, it is marked as fractured. Next, Eq. 5.3 through 5.6 are used to obtain fracture geometry. This geometry is used to update the permeability of the gridblocks that contain the fracture, according to permeability sensitive laws described in Section 5.4.2 and 5.4.3 (Eq. 5.12 and 5.18). Also, porosity of the gridblocks is modified according to Eq. 5.26. Using the updated permeability and porosity, the reservoir simulator is run again, for the same time step, but next iteration to improve pore pressure results. This process is repeated until the maximum change in pore pressure, porosity, permeability and width falls below a certain level.

The procedure of the coupling is as follows:

1) Initialize all the reservoir and geomechanics parameters for all the gridblocks at $n = 0$, $p^{n}_{i, j, k}$, $\sigma^{n}_{i, j, k}$

2) Start the iterations, $\nu = 0$, by running the fluid flow simulator to obtain pore pressures, $p^{\nu+1}_{i, j, k}$

3) Transfer the pore pressures in all the gridblocks to the geomechanics module.

4) Calculate the stresses and displacements in geomechanics module, by calling the geomechanics module

5) Based on the effective stress, determine the fractured gridblocks and the fracture tip location.

6) Evaluate the permeability of the fractured gridblocks according to Eq. 5.12 and 5.18.

7) Calculate new value of porosity based on Eq. 5.26, as a function of volumetric strain.

8) With the new permeability and porosity, run the fluid flow simulator again for the new iteration level and obtain $p^{\nu+1}_{i, j, k}$

9) Move to next iteration if the convergence criteria are not satisfied, otherwise go to the next time step.

As it can be seen, reservoir fluid flow and geomechanics equations are solved separately in each time step, implying the name partially decoupled.

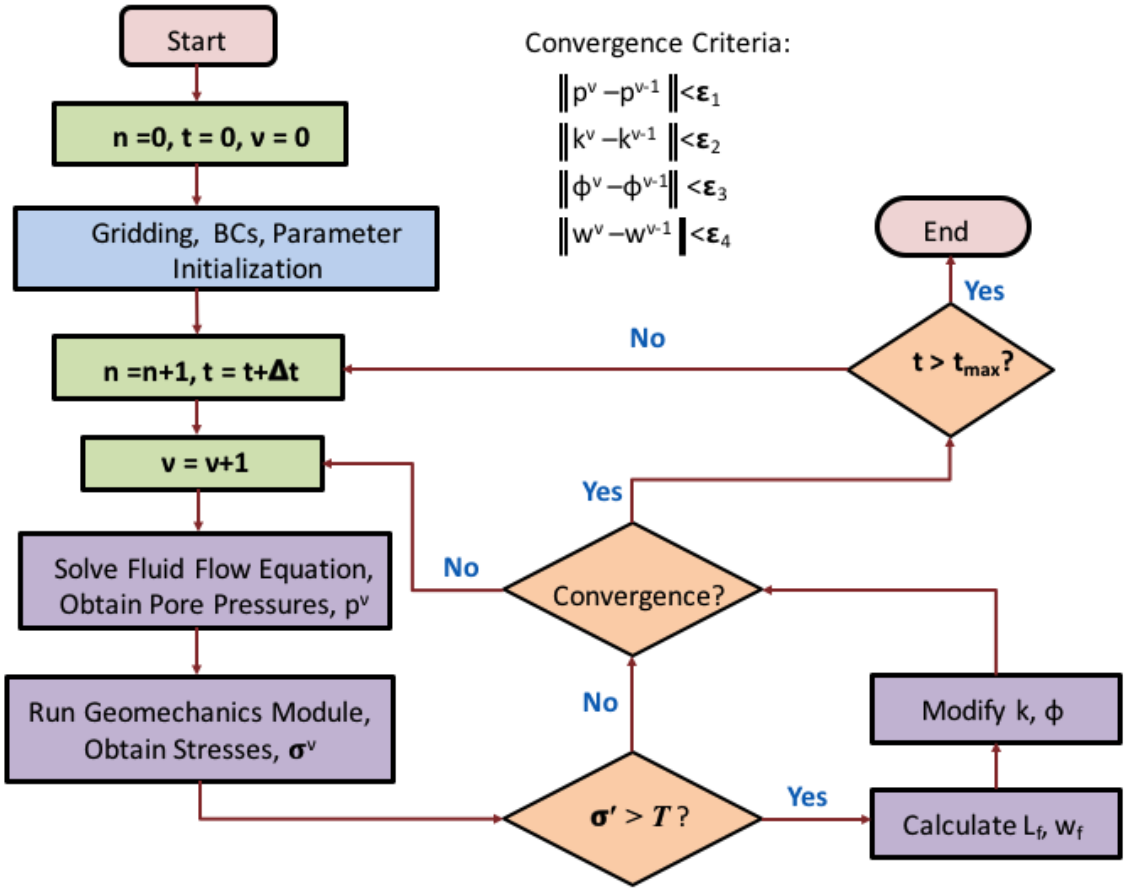

Figure 5.7: Flowchart of the Coupling Algorithm between Fluid Flow and Geomechanics Modules

5.5.1 Explicit and Implicit Treatment of permeability enhancement

Explicit treatment of permeability enhancement means evaluating average permeabilities based on fracture dimensions at previous time step. The amount of permeability enhancement is calculated only once and at the beginning of each time step and it will not change during iterations:

$$k_{avg}{}^{n+1} = \frac{k_m(\Delta y - w^n) + k_f{}^n w^n}{\Delta y} \tag{5.27}$$

or

$$k_{avg}{}^{n+1} = \frac{k_m \Delta y \Delta x [k_m(\Delta y - w^n) + k_f{}^n w^n]}{\Delta y\{(\Delta x - L_p{}^n)[k_m(\Delta y - w^n) + k_f{}^n w^n] + k_m \Delta y L_p{}^n\}} \tag{5.28}$$

Implicit treatment, however, means that the average permeability is calculated from latest iteration level of the fracture dimensions:

$$k_{avg}{}^{n+1}_{v+1} = \frac{k_m\left(\Delta y - w^{n+1}_{v}\right) + k_f{}^{n+1}_{v} w^{n+1}_{v}}{\Delta y} \tag{5.29}$$

or

$$k_{avg}{}^{n+1}_{v+1} = \frac{k_m \Delta y \Delta x[k_m\left(\Delta y - w^{n+1}_{v}\right) + k_f{}^{n+1}_{v} w^{n+1}_{v}]}{\Delta y\{\left(\Delta x - L_p{}^{n+1}_{v}\right)\left[k_m\left(\Delta y - w^{n+1}_{v}\right) + k_f{}^{n+1}_{v} w^{n+1}_{v}\right] + k_m \Delta y L_p{}^{n+1}_{v}\}} \tag{5.30}$$

where ν shows iteration level and n shows step time level.

Ji, 2008 reported that explicit treatment of permeabilities causes oscillations while the implicit treatment generates smoother results in length and in pressures. Therefore, for all HF simulations in this research, an implicit treatment of permeabilities (Eq. 5.29 and 5.30) was adopted.

5.6 Verification of the Hydraulic Fracture Model

The above formulation of permeability enhancement in fractured gridblocks was tested in a simulation of an isothermal reservoir with single-phase, slightly compressible flow. A static fracture was represented in the model by assigning higher values of permeability to the gridblocks containing the fracture. Analytical solution of such a problem exists in the literature and it is used as a validation to the permeability modification of our numerical tool. The problem description is as follows:

Figure 5.8 shows a schematic view of the reservoir simulation problem that was used for our validation purposes. A horizontal, homogeneous, isotropic reservoir, saturated with slightly compressible fluid is considered. Gravity effects are neglected and the reservoir is at an initial pressure of p_i. The well is assumed to be in a rectangular drainage area. A vertical fracture is assumed extending over the entire height of the formation, which is parallel to the drainage boundary and is located symmetrically within the square drainage area. In the numerical model, a homogeneous, isotropic, square drainage model filled with slightly compressible fluid of constant viscosity was created. The fracture was assumed to be in the center of the model, as shown in the Fig. 5.8. Table 5.1 shows the input data used in the model.

Table 5.1: Input Parameters for Infinite Conductivity Fracture Simulation

Parameter	Value
Porosity	0.25
Permeability	0.9869×10^{-13} m^2 (0.1 Da)
Viscosity	1 cp (0.001 Pa.Sec)
Fluid Compressibility	1e-10 Pa^{-1}
Injection Flow Rate	8×10^{-5} m^3/Sec
Reservoir Dimensions (Drainage Area)	300 m by 300 m (90000 m^2)
Reservoir Height	1 m
Initial Reservoir Pore Pressure	5 MPa
Grid Size	2.9412 m × 5.8824 m
Grid Number	51 by 51
Fracture Width	0.001 m
Fracture Half Length	Variable

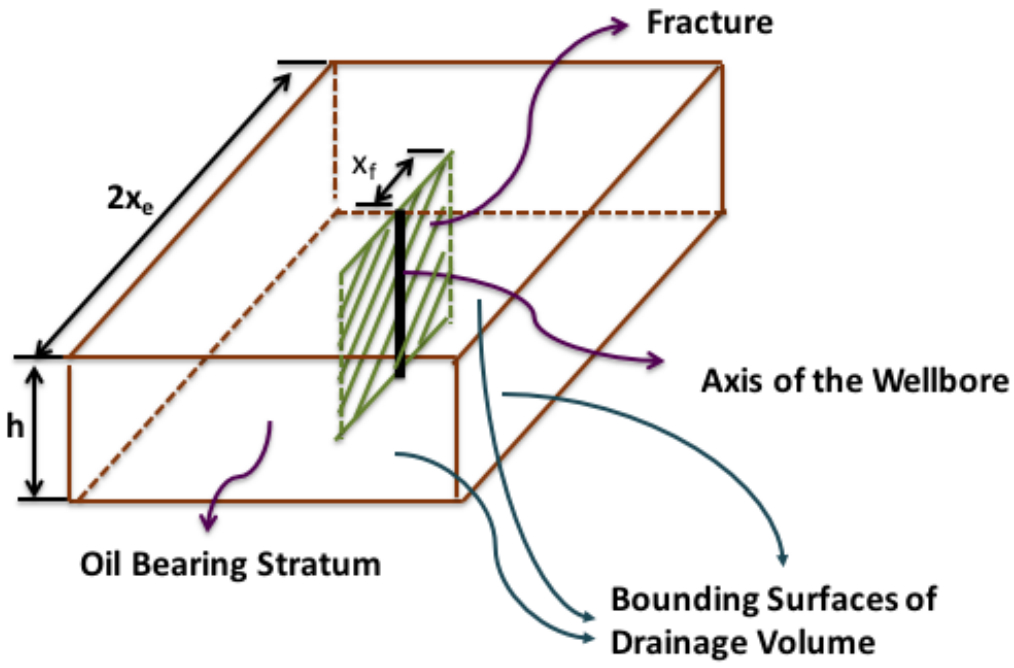

Figure 5.8: Schematic View of Fractured Well and Reservoir Drainage Volume

The boundary conditions that complete our problem are no flow boundary around the model.

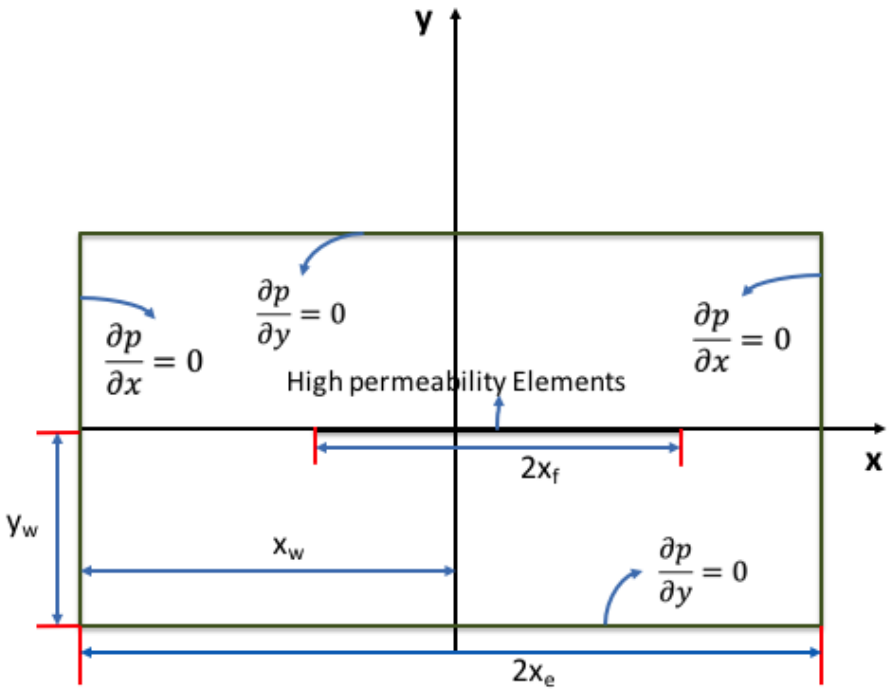

Figure 5.9: Plan View of the Fractured Reservoir

Greengarten (1974) by using Green's function and product solution method, obtained the analytical solution to pressure distribution in the abovementioned problem as:

$$p_D\left(\frac{x}{x_e}, \frac{y}{y_e}, t_{DA}\right) \tag{5.31}$$

$$= 2\pi \int_0^{t_{DA}} \left[1 + 2\sum_{n=1}^{\infty} e^{-n^2\pi^2 \frac{x_e}{y_e} t'_{DA}} cos\left(n\pi \frac{y_w}{2y_e}\right) . cos\left(n\pi \frac{y_w + y}{2y_e}\right)\right] \Bigg[1$$

$$+ 2\sum_{n=1}^{\infty} e^{-n^2\pi^2 \frac{y_e}{x_e} t'_{DA}} \frac{sin\left(n\pi \frac{x_f}{2x_e}\right)}{n\pi \frac{x_f}{2x_e}} . cos\left(n\pi \frac{x_w}{2x_e}\right) . cos\left(n\pi \frac{x_w + x}{2x_e}\right)\Bigg] dt'_{DA}$$

where:

$$t_{DA} = \frac{kt}{4\mu c\phi (x_e y_e)^2} \tag{5.32}$$

and

$$p_D(x_D, y_D, t_D) = \frac{2\pi kh}{q\mu}(p - p_i) \tag{5.33}$$

x_e and y_e are half length of reservoir drainage area and x_w and y_w show fracture axis coordinates (see Fig. 5.9), and p_i is the initial reservoir pressure. Therefore, the pressure drop at the center of a square drainage area ($x_e = y_e$, $x_w = y_w$) is:

$$p_{wD}(t_{DA}) = 2\pi \int_0^{t_{DA}} \left[1 + 2\sum_{n=1}^{\infty} e^{-4n^2\pi^2 t'_{DA}}\right] \Bigg[1 + 2\sum_{n=1}^{\infty} e^{-4n^2\pi^2 \frac{y_e}{x_e} t'_{DA}} \frac{sin(n\pi \frac{x_f}{x_e})}{n\pi \frac{x_f}{x_e}} . cos(n\pi x_D \frac{x_f}{x_e})\Bigg] dt'_{DA} \tag{5.34}$$

The pressure drop on the fracture can be obtained by setting $x_D = 0$ in Eq. 5.34. Greengarten also presented numerical results of above function which we have used for validation. Figure 5.10 is a graphical representation of the analytical solution of Greengarten.

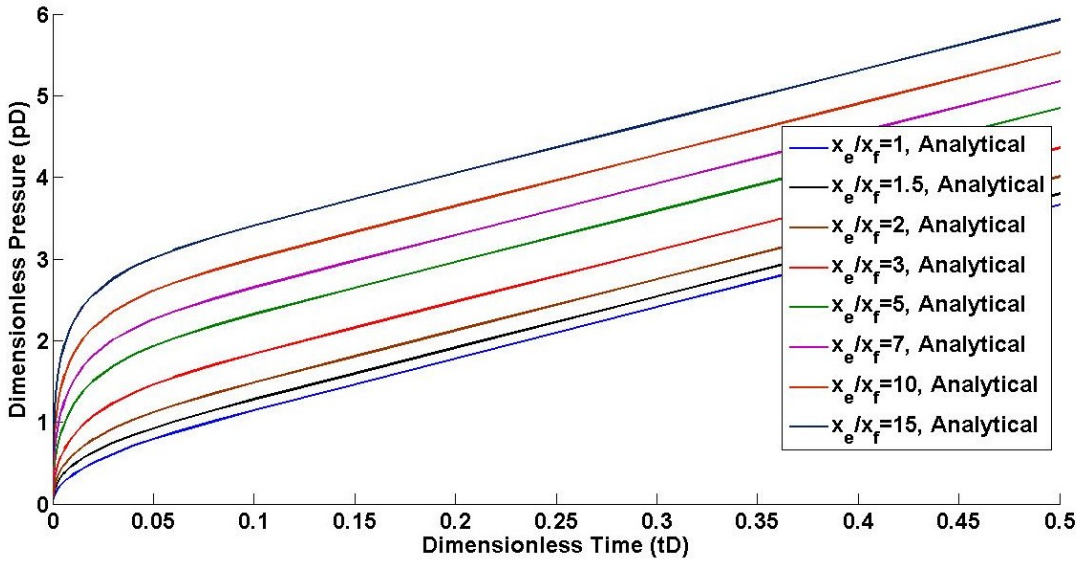

Figure 5.10: Graphical Representation of Greengarten Solution

Figure 5.11 presents a comparison between the dimensionless pressure drops from the numerical model and the analytical solution of Greengarten (1974). The results indicate that permeability enhancement method gives accurate results which match reasonably well and within 5% difference with the analytical solutions.

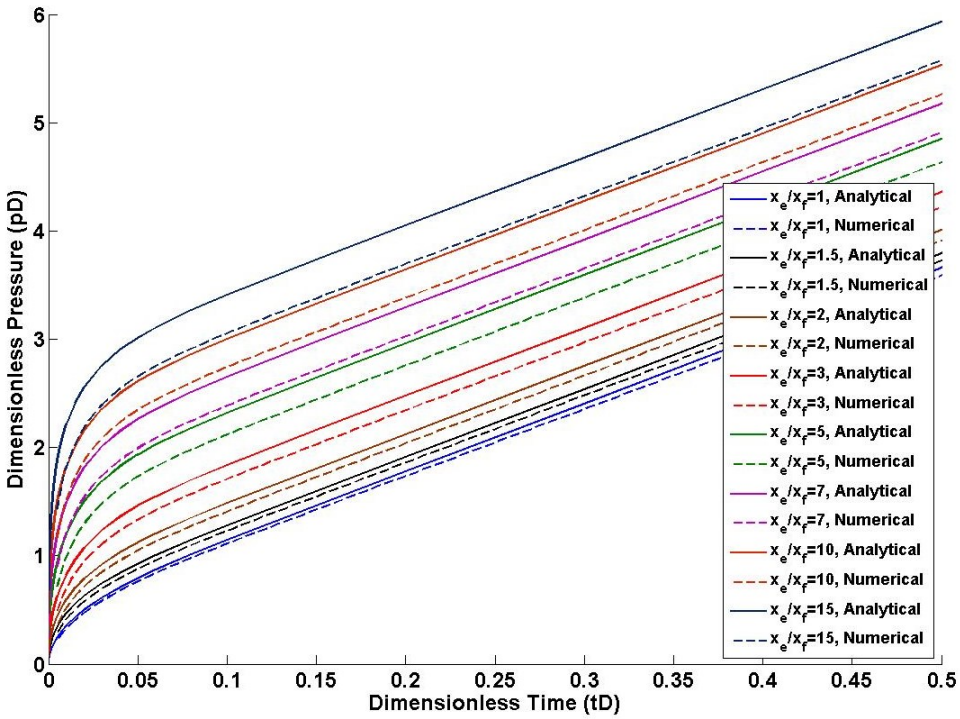

Figure 5.11: Comparison of Greengarten Analytical Solution with Numerical Simulation

5.7 Effect of Local Grid Refinement

A mesh sensitivity analysis is performed in this section to investigate the effect of different meshing strategies on the pressure response. The model input parameters are the same as in Table 5.1 and it is assumed that the ratio of reservoir drainage length to fracture length is 5 (x_e/x_f=5). In some of the simulations of this part, uniform grids are used, but the size of the grid is changing in each case. In the non-uniform case mesh (71 by 71), a locally refined mesh is designed in which the size of the mesh in an 11-meter band around the injection point is about 1 m by 1 m and then increases to 5 m by 5.5 m around the refined band, as shown in Fig 5.12.

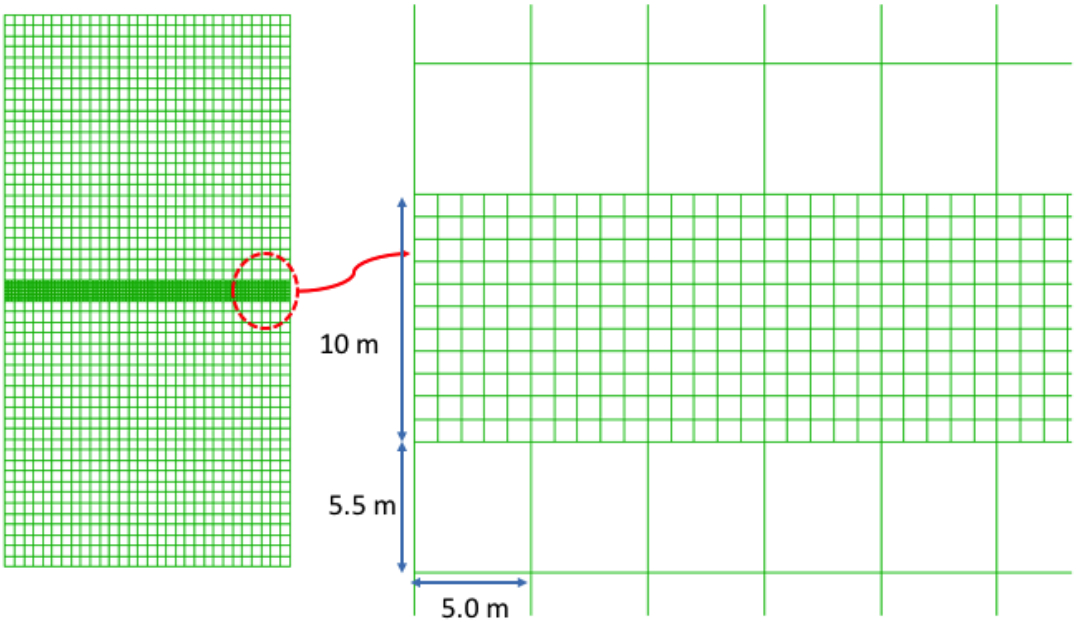

Figure 5.12: Locally Refined Mesh

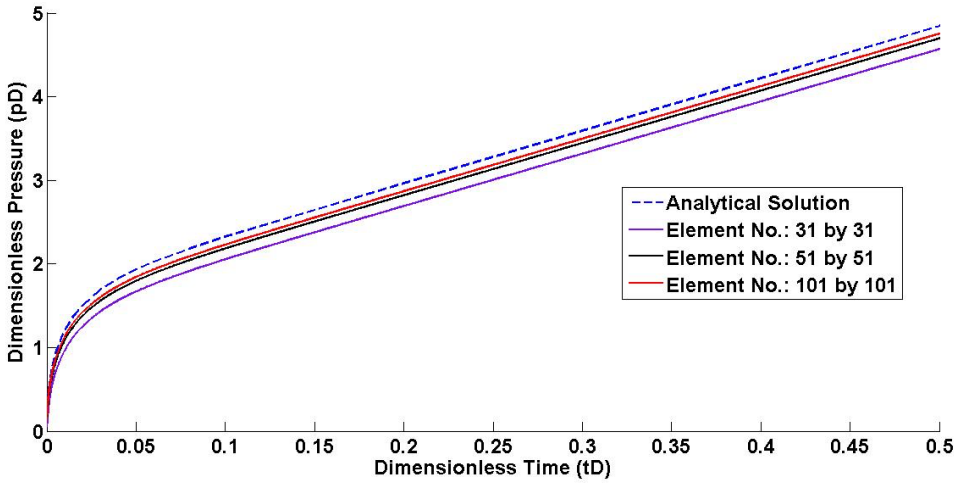

Figure 5.13: Effect of Uniform Size Mesh Refinement

As it can be seen from Fig. 5.13, as the size of the gridblock becomes smaller, the pressure response becomes closer to the analytical solution. However, when uniform grids are used, running time of the simulation becomes too expensive and still the accuracy is not desirable. On the other hand, locally refined mesh gives a high accuracy with manageable running time, as shown in Fig. 5.14.

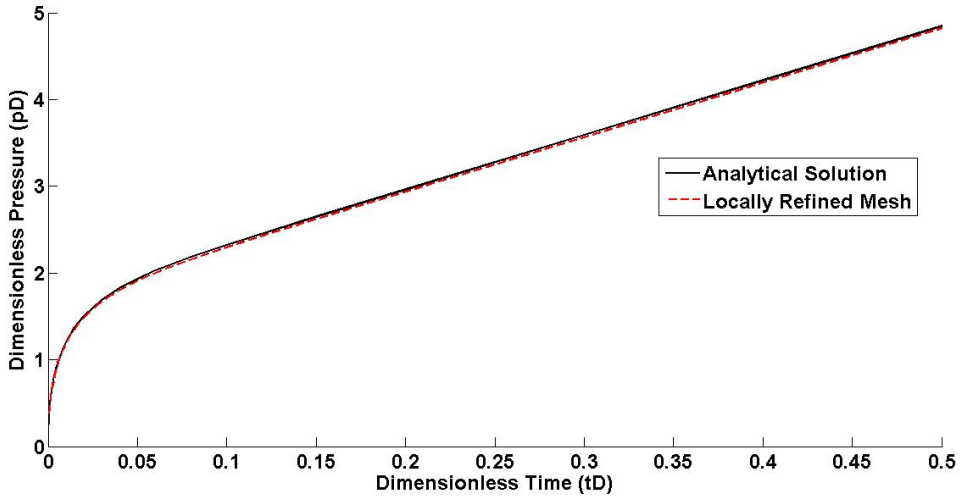

Figure 5.14: Effect of Locally Refined Mesh

5.8 Effect of Maximum Limit of Permeability

The higher the permeability of the fracture, the less the friction loss inside the fracture will be. However, it is recognized that after a certain value of permeability, increasing this parameter does not change the fracture behavior. It is because when permeability of the fracture is much higher than the matrix permeability, the majority of fluid passes through the fracture. It is well known that the permeability of the fractured elements should be gradually increased in each iteration or otherwise severe oscillations will arise (Ji, 2008). Obviously, higher value of permeability of the fracture requires higher number of iterations to bring matrix permeability to fracture permeability. Setting a maximum limit for permeability in our numerical work reduces the number of iterations and consequently running time. Therefore, it is worth to investigate the fracture permeability that leads to solutions that match reasonably well with those obtained from a model with "infinite conductivity" fracture. We investigated the effect of setting a maximum limit of permeability, both for static and dynamic fractures.

The static fracture model is the same as the model explained in Section 5.6. Figure 5.15 shows how the change of maximum permeability of the fracture changes the injection pressure. As the maximum limit of permeability is increasing, the pressure at the wellbore decreases and gets closer to the analytical solution. However, since we are using smeared approach in simulating the fracture, the numerical results and analytical solutions will never match unless a very fine grid is used.

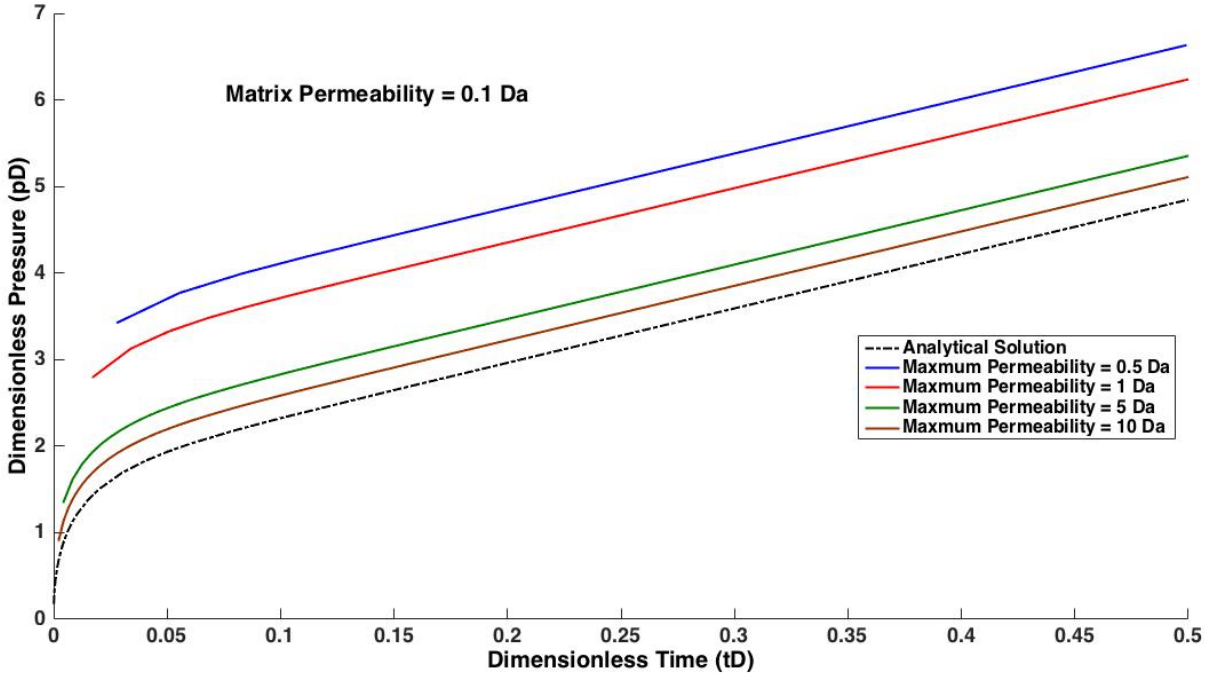

Figure 5.15: Effect of Maximum Permeability Limit on Static Fracture

For the case of dynamic fracture propagation, a 50 m by 50 m model was built and geomechanics and fluid flow modules were linked as explained in Section 5.5. Table 5.2 presents the input parameters of the model. It is assumed that formation rock follows Mohr-Coulomb plasticity model and water is used as injection fluid.

Table 5.2: Input Parameters for Dynamic Fracture Model

Parameter	**Value**
Model Dimensions	100 m by 50 m
Injecting Fluid Viscosity	0.001 Pa.Sec.
Formation Initial Porosity	0.2
Formation Initial Horizontal Permeability	0.1 Da
Formation Initial Vertical Permeability	0.1 Da
Initial Reservoir Pressure	1.6 MPa
Young's Modulus	1.785 GPa
Poisson's Ratio	0.3
Vertical Principal Stress	4 MPa
Maximum Horizontal Principal Stress	6.7 MPa
Minimum Horizontal Principal Stress	3 MPa
Cohesion	1.185 MPa
Friction Angle	20
Dilation Angle	22
Injection Time	2000 Seconds

Figure 5.16 displays the boundary conditions of the geomechanics and fluid flow simulators.

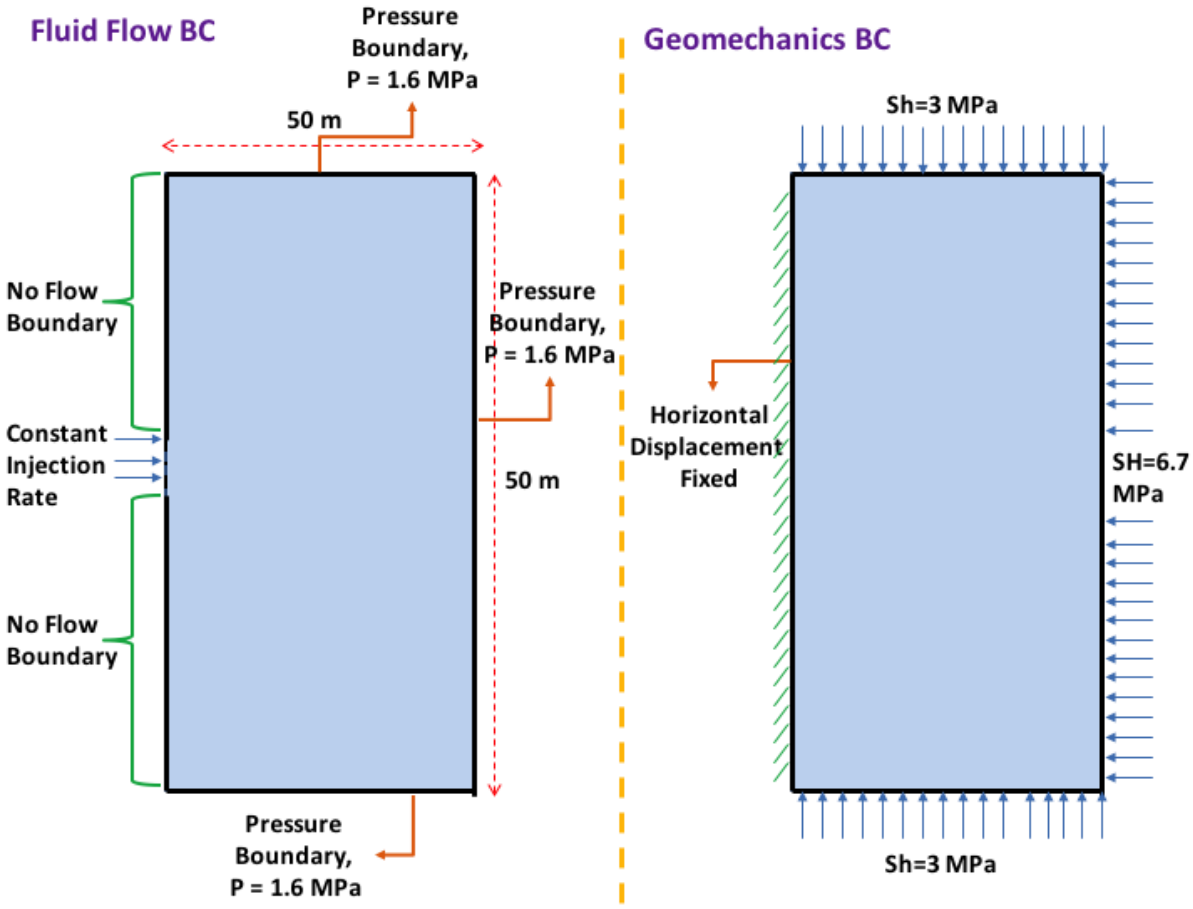

Figure 5.16: Fluid Flow and Geomechanics Boundary Conditions

In dynamic fracture case, the width changes along the fracture length and, therefore, a variable permeability limit should be assigned to fractured elements. In Figs. 5.17 and 5.18, permeability ratio means the ratio of the assigned permeability in the numerical code to the actual smeared permeability coming from Eq. 5.12 and 5.18.

Figure 5.17 compares the maximum width of the fracture while Fig. 5.18 shows fracture length for different maximum limits of permeability. Again, acceptable results are obtained even when a limit is assigned to the maximum number of permeability. However, in the dynamic fracture model, assigning a value of 0.01 to permeability ratio, leads to completely different results. Therefore, whenever fracture propagation is occurring inside the model, the maximum limit for permeability should be applied with some care.

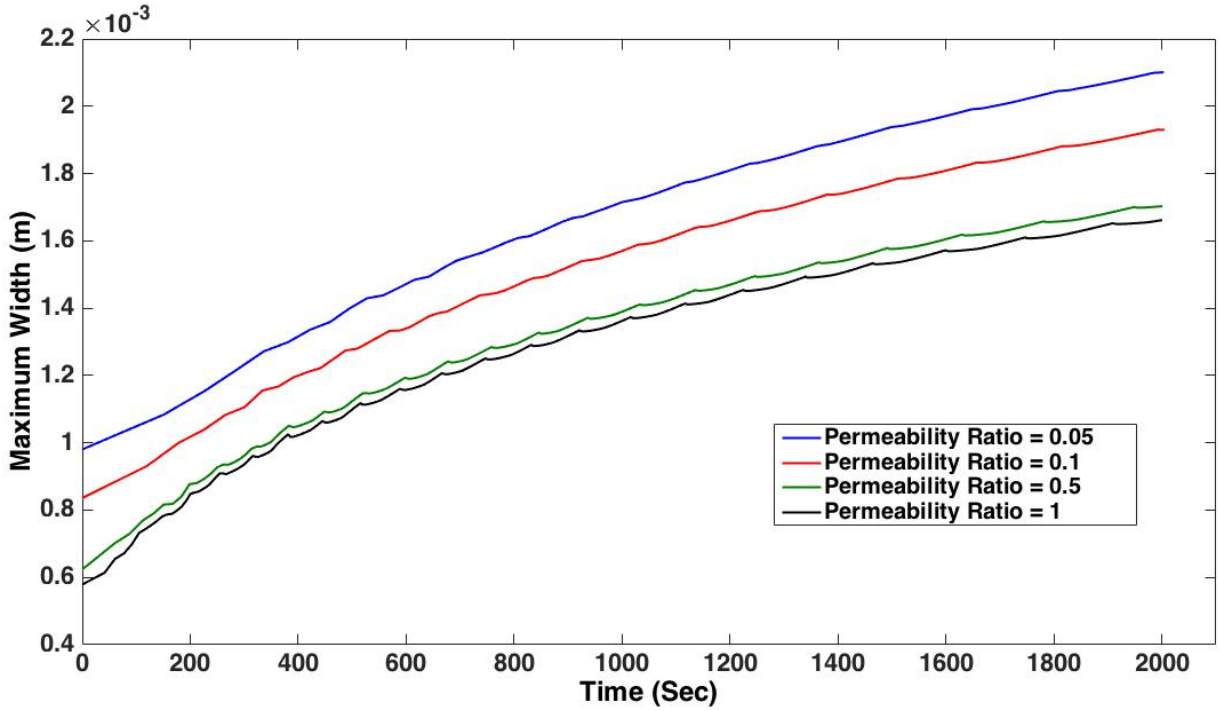

Figure 5.17: Effect of Maximum Permeability Limit on Fracture Width

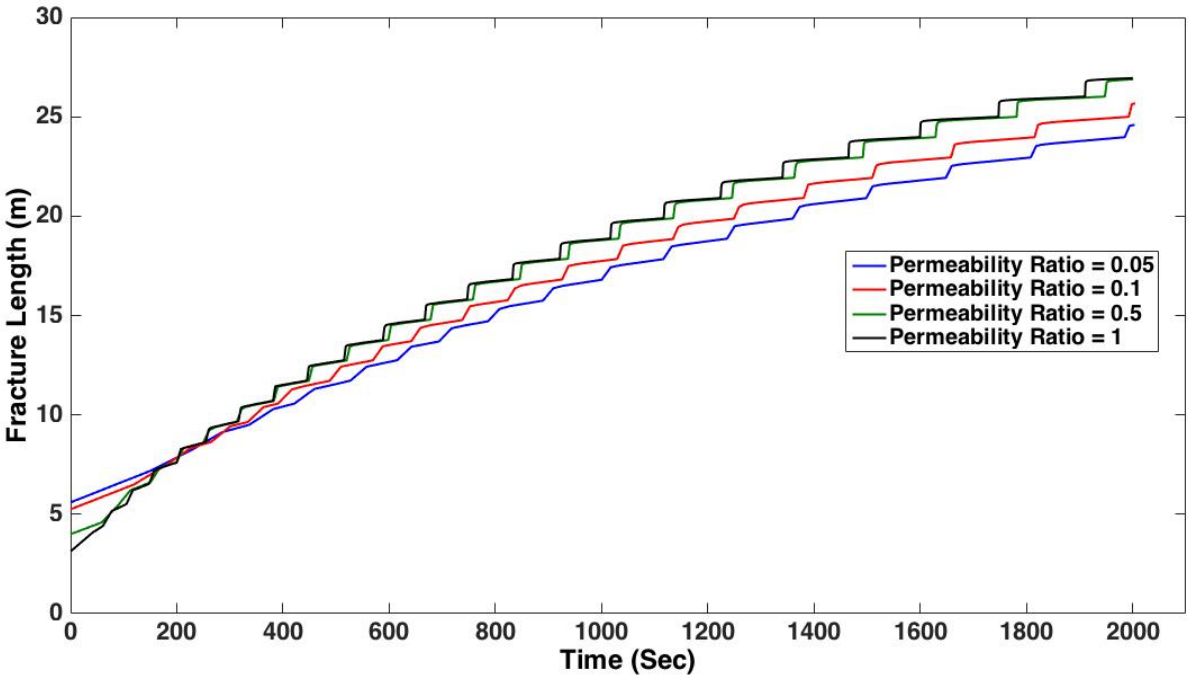

Figure 5.18: Effect of Maximum Permeability Limit on Fracture Length

5.9 Implicit versus Explicit Solutions

Our in-house fluid flow code that is developed in MATLAB can provide reservoir pressures from explicit or implicit approaches. When the permeability of the fractured element is enhanced based on the displacements, stable time step of explicit approach becomes very small accordingly. On the other hand, permeability enhancement does not influence the run time in the implicit approach and, therefore, the implicit solution seems to be more practical here. However, as we will explain in the next chapter, CFL condition put a severe restriction on the stable time step of proppant transport simulator. Having this in mind, the implicit solution time step should be reduced so that the change of properties due to proppant injection can be included in the simulation iterations in smaller time steps. Performing a HF simulation with implicit approach and small time steps will require a longer run time compared to the explicit approach, even when the permeability is high. Therefore, we decided to use the explicit method when proppants are being injected in the reservoir. Since previously all the verification and validation works of the HF simulator were done with implicit approach (Taghipoor et al., 2013), in this section, we compare the result of explicit versus implicit solutions in the dynamic fracture case.

Figure 5.19 compares the maximum width and fracture length for the explicit and implicit approaches. A good agreement for fracture dimensions is observed between the two approaches. In addition, Fig. 5.20 shows some of the main geomechanical parameters at the end of the simulation. Again, both approaches obtain almost identical results.

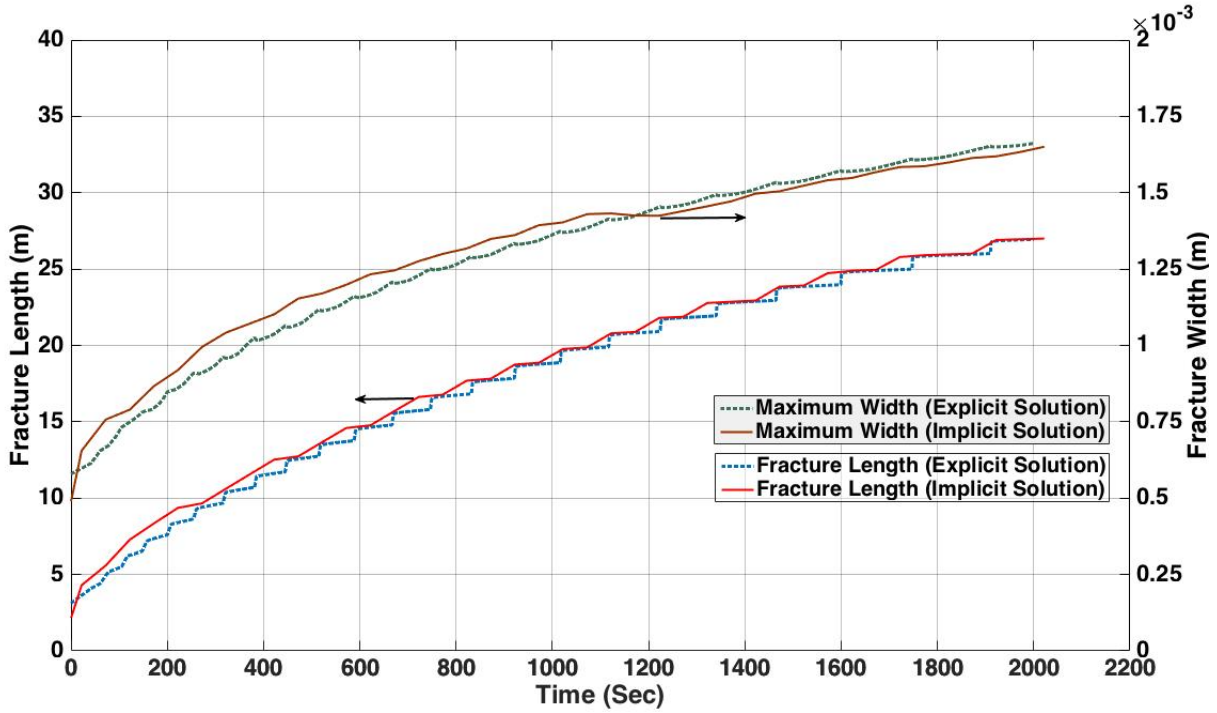

Figure 5.19: Implicit vs. Explicit Solution Technique

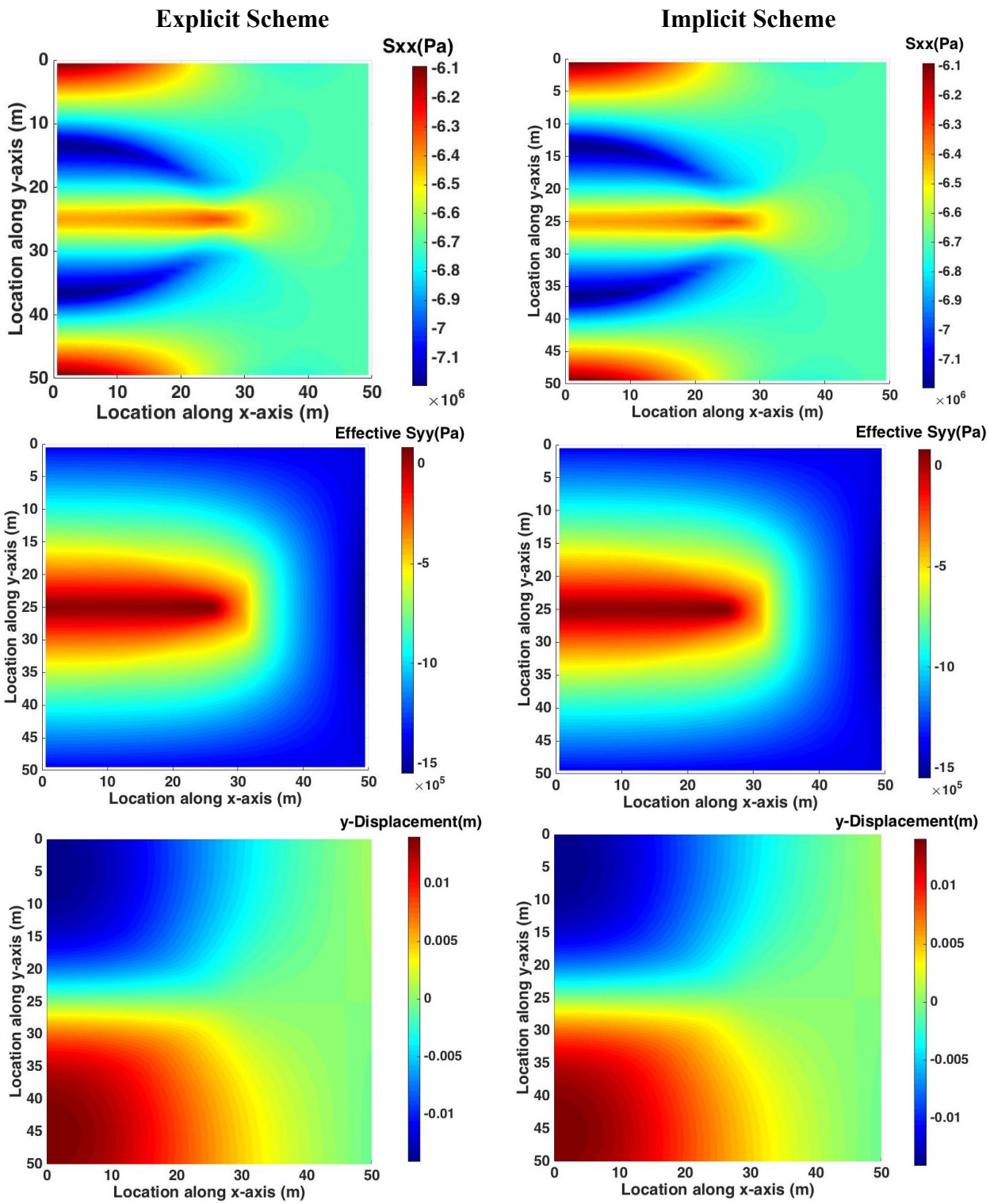

Figure 5.20: Implicit vs. Explicit Solution Technique

5.10 Conclusion

A partially decoupled hydraulic fracture simulation was described in this chapter in which the fracture was represented by enhancing the permeability in the reservoir grids. Such a detailed modelling approach can represent stimulation as well as damage in the formation and can bring the realism of hydraulic fracturing to a new level. Geomechanical effects on fracture initiation and propagation was also included in our modeling through utilizing FLAC2D. Formation displacements rigorously calculated in the geomechanics module, were utilized to give the fracture width while fracture length was calculated based on effective stresses. This can demonstrate the importance of stress change in controlling fluid flow inside the fracture. The modular coupling between fluid flow and geomechanics simulators was carried out through flow properties, i.e. pressure-dependent permeability and porosity. The extremely flexible modular structure of the system can adapt any advanced commercial geomechanics or reservoir simulator.

Gridding strategy is very important in obtaining more precise dimension of the fracture. Locally refined mesh shows accurate results and, at the same time, does not increase the run time significantly.

The work presented in this chapter is a necessary first step in developing a proppant transport simulator in hydraulic fracturing. In Chapter 6, we will develop such a numerical tool that integrates reservoir and geomechanics simulator to a proppant transport simulator at the field scale.

Chapter 6: Coupled Hydraulic Fracture and Proppant Transport Simulation

6.1 Introduction

In numerical reservoir simulation, a hydraulic fracture that extends over several gridblocks can be represented by its actual size (Dowdle and Hyde, 1977, Hoditch 1979). Since the fracture has a high permeability and a very small width, compared to the model dimensions, having one grid system for fracture and one grid system for reservoir (Konoplyov and Zazovsky, 1991, Settari et al, 1996) requires a large degree of refinement that poses serious stability and run-time limitations. To overcome these limitations, maximize the numerical stability and reduce the run time, Settari et al. (1990, 1996) proposed the use of one common grid system for both fracture and reservoir and representation of the fracture by increasing the permeability of the grids that contain the fracture. However, proppant transport simulation requires an explicit representation of the fracture. In our modular simulation, the reservoir module treats the fracture following Settari et al. (1990) approach, and the proppant module, simulates an actual fracture with its true dimensions. In other words, the benefits of the previous two approaches have been combined in our modular simulation. To include the geomechanical effects, a third module is considered that calculates stresses and displacements during fracture propagation.

This chapter presents the linkage between the three modules of fluid flow simulator, geomechanics module and proppant transport simulator. The main algorithms implemented in our numerical code such as adaptive re-meshing of the propagating fracture, moving boundary conditions, time stepping scheme and mobility averaging in the simulator, are discussed in this chapter.

6.2 Linkage Algorithm of Reservoir, Geomechanics and Proppant Modules

Although approaches that link fracture and reservoir simulators are not new, in all of them fracture simulators which are using simplified analytical or semi-analytical approaches are interfaced with a reservoir simulator. It is now amply accepted that complexity of the fractures cannot be modeled by such simple methods.

Our current approach takes the advantages of a robust and sophisticated simulator that was previously developed in our group and incorporates an in-house built proppant transport module to obtain propped fracture dimensions and concentration distribution. A smeared fracture

approach is used to model the fracture geometry, as explained in the previous chapter. Therefore, fracture propagation, proppant transport and fluid flow are solved numerically in Cartesian grid cells. The flexibility of the coupling allows any type of fracture simulator (analytical or explicitly simulated fractures) be used without a huge modification of the tool. In the developed software capability, the propped fracture geometry and proppant concentration which are the output of the proppant module, are imported to hydraulic fracture simulator through mobility modification.

There are several algorithms implemented in our tool to better capture different phenomena occurring during injection. To better illustrate the coupling of the modules, these algorithms are explained in this section before presenting the last step of our development: linkage of the modules of our numerical tool.

6.2.1 Proppant Entry Requirement

When the injection of proppants stars, the dimensions of the fracture should be known. As explained in Chapter 5, our hydraulic fracture simulator (linked reservoir and geomechanics modules) provides the created fracture length and width based on the effective stresses and nodal displacements, respectively. However, proppants cannot enter the fracture if the width is not 3 to 4 times greater than proppant diameters. This phenomenon is well known in the literature and is called fracture entry requirement.

In all our simulations, we assumed that a proppant can enter the fracture as long as its diameter is equal to the fracture width. Hence, the length of the fracture is shortened to the point that its width is equal to proppant diameters. It is this new shortened length that is discretized and used in the proppant simulator module. Figure 6.1 shows this process schematically.

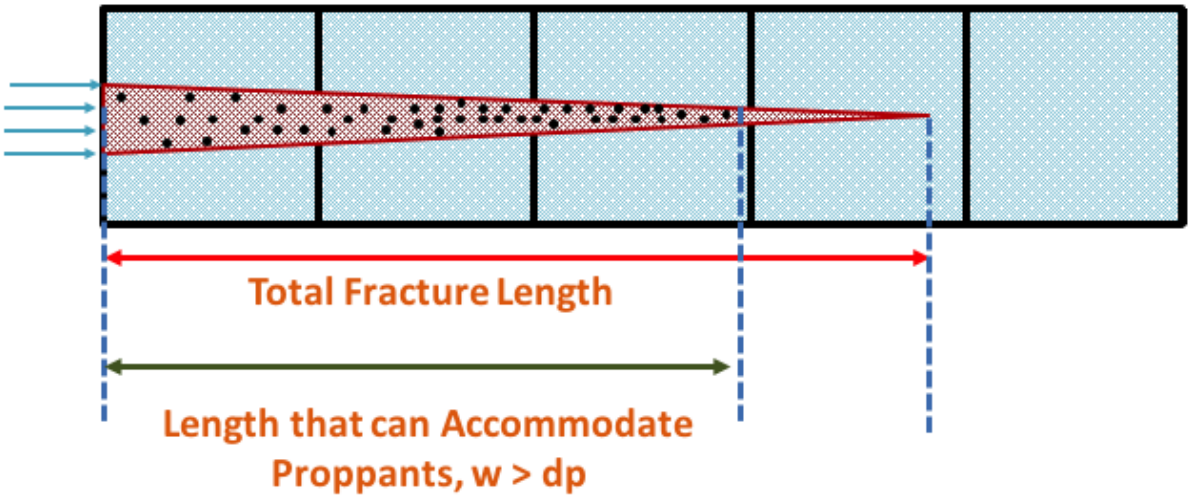

Figure 6.1: Fracture Width Determines Entry

6.2.2 Mesh Design and Adaptive Re-meshing of Different Modules

Fluid flow and geomechanics modules are incorporated the hydraulic fracture simulator. Although the two modules can have different meshing strategies, the same mesh was used for both to prevent the necessity of mappings between the two modules. However, proppant simulator grids are designed to be much finer than the hydraulic fracture simulator to explicitly model the fracture. Therefore, the fracture grid that may contain proppants should be merged into the bigger reservoir grid. We use the term "subgrids" to refer to the proppant simulator grids, since they are much smaller than the reservoir and geomechanics grids. Figure 6.2 is a schematic of the mesh design of the simulators. In all the simulations of this part, based on the input parameters which determine the numerical stability of the model, we divided each reservoir simulator grid into 10 subgrids for proppant transport simulation. The width of the fracture, as mentioned before, is calculated from the geomechanics module. Although the proppant simulator assumes uniform properties along the width of the fracture and does not solve mass balance along the width, a gradual width reduction towards the tip of the fracture is considered in calculating fracture permeability according to the cubic law. Fracture width in each subgrid is calculated by linear interpolation between the widths coming from geomechanics module.

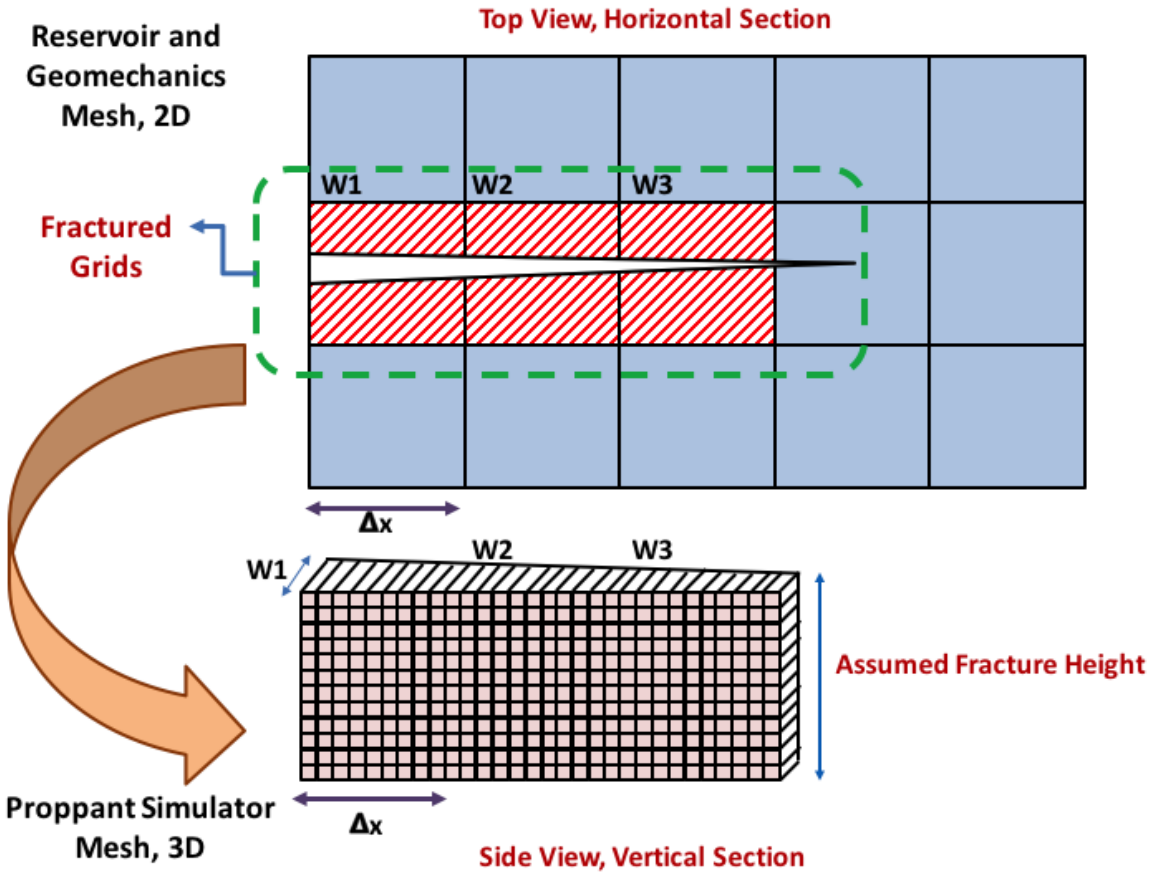

Figure 6.2: Mesh Design for Different Modules

As the fracture propagates, its length and width will change while the height is assumed to be constant. At the start of each time step, the mesh of the proppant simulator is adaptively changed to include newly fractured grids. However, the dimension of the grids is kept the same during the entire simulation time. This approach provides two advantages. First, the stable time step of proppant simulator (based on CFL condition) will change only due to change of velocity and not change of fracture length. Second, there is no need to interpolate the result of previous time step from the old mesh to the new time step with new mesh. Figure 6.3 below shows how the adaptive re-meshing technique has been implemented in our model.

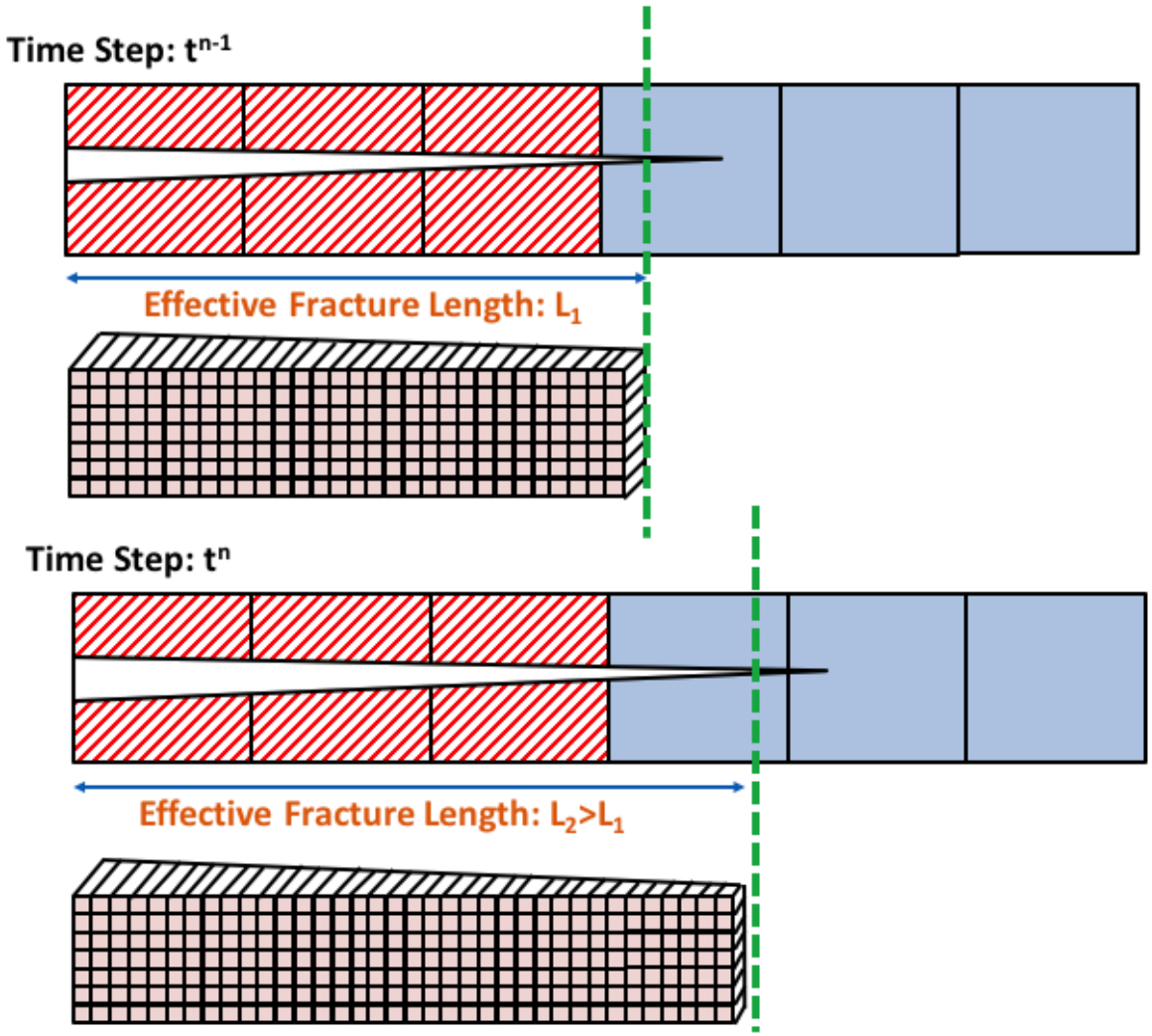

Figure 6.3: Fracture Propagation and Adaptive Re-meshing

In addition to interpolating width between larger geomechanics grids and proppant subgrids, the pore pressures should also be linearly interpolated between larger reservoir grids and proppant subgrids. Figure 6.4 is a schematics of interpolation process.

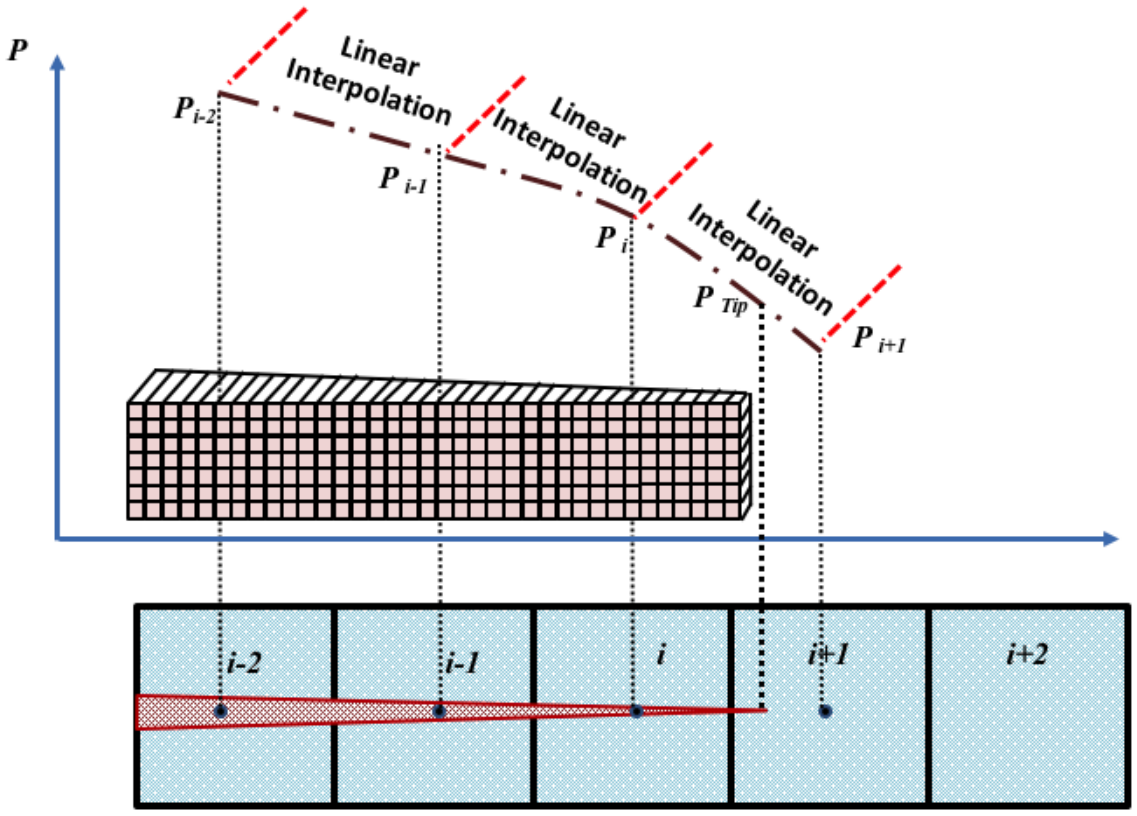

Figure 6.4: Linear Interpolation of Pressure at the Fracture Tip

It should be noted although the length and height of the subgrids are kept constant, the width of them might change during each time step. Consequently, the volume of each subgrid is not constant during the simulation. Obviously, proppant concentration is inversely proportional to the volume of the subgrids:

$$c = \frac{V_p}{V_{subgrids}} \tag{6.1}$$

where V_p denotes proppant volume. As it can be seen from above equation, any change in the volume of the subgrids will change the concentration. Therefore, before each time step, the concentration of previous time step should be adjusted to account for the change of subgrids volume. The old volume of each subgrid is assumed to be:

$$V_{subgrid}^{Old} = dx.dy.w^{Old} \tag{6.2}$$

while the new volume of the subgrid is:

$$V_{subgrid}^{Old} = dx.dy.w^{New} \tag{6.3}$$

Hence, the adjusted proppant concentration would be:

$$c^{new} = \frac{V_p}{V_{subgrid}^{New}} = c^{Old} \times \frac{V_{subgrid}^{Old}}{V_{subgrid}^{New}} = c^{Old} \times \frac{w^{Old}}{w^{New}} \tag{6.4}$$

6.2.3 Averaging Mobility

As the concentration of proppants increases, the viscosity of the slurry is also increased. On the other hand, the width of the fracture and consequently, the permeability, along its length will be different. Therefore, the ratio of permeability to viscosity or mobility of the slurry will be variable during the simulation.

The mobility that is needed in the reservoir simulator should be obtained by averaging. Before running the simulators, we ensure that each reservoir grid block contains a certain number of proppant subgrids (for example, in every and each reservoir gridblocks, there exists 10 subgrids). For each subgrid, after running the proppant simulator, the proppant concentration and the dimensions of the subgrid are known. If the permeability and viscosity of subgrids is assumed to be k_1, k_2, …, k_n, and μ_1, μ_2, …, μ_n respectively, with n being the total number of subgrids in a reservoir gridblock, considering Fig. 6.5, the total pressure drop along all subgrids will be:

$$\Delta p_t = \sum_{i=1}^{n} \Delta p_i \tag{6.5}$$

Substituting Darcy's equation for the pressure drop in Eq. 6.5:

$$\frac{q_t \Delta X}{dy w_{avg}} \left(\frac{\mu}{k}\right)_{fr} = \frac{q_1 dx}{dy} \left(\frac{\mu}{wk}\right)_1 + \frac{q_2 dx}{dy} \left(\frac{\mu}{wk}\right)_2 + \cdots + \frac{q_n dx}{dy} \left(\frac{\mu}{wk}\right)_n \tag{6.6}$$

where ΔX is the length of the coarse reservoir grids:

$$\Delta X = \sum_{i=1}^{n} \Delta x_i \tag{6.7}$$

and w_{avg} is the average width of first and last subgrids:

$$w_{avg} = \frac{w_i + w_{i+1}}{2} \tag{6.8}$$

However, flow rate passing through each subgrid would be equal:

$$q_t = q_1 = \cdots = q_n \tag{6.9}$$

Therefore,

$$\frac{\Delta X}{w_{avg}}\left(\frac{\mu}{k}\right)_{fr} = dx\left[\left(\frac{\mu}{wk}\right)_1 + \left(\frac{\mu}{wk}\right)_2 + \cdots + \left(\frac{\mu}{wk}\right)_n\right] \tag{6.10}$$

or

$$\left(\frac{\mu}{k}\right)_{fr} = \frac{w_{avg}dx}{\Delta X}\left[\left(\frac{\mu}{wk}\right)_1 + \left(\frac{\mu}{wk}\right)_2 + \cdots + \left(\frac{\mu}{wk}\right)_n\right] \tag{6.11}$$

Since permeability of each subgrid is related to the width according to cubic law, we finally obtain:

$$\left(\frac{k}{\mu}\right)_{fr} = \frac{\Delta X}{w_{avg}dx}\left[\frac{1}{\sum_{i=1}^{n}\left(\frac{12\mu}{w^3}\right)_i}\right] \tag{6.12}$$

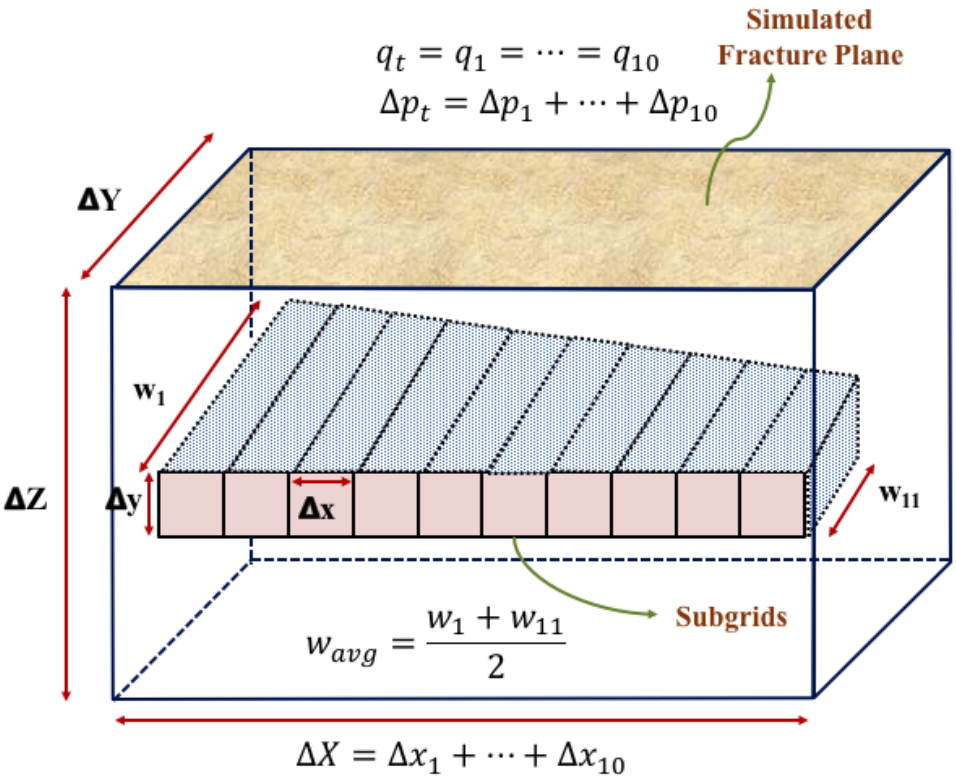

Figure 6.5: Averaging Mobility of Fracture Subgrids

Now that the average mobility of the subgrids is found, a parallel averaging should be used between matrix and fracture mobilities. According to Fig. 6.6 the total flow rate passing through reservoir grid is the sum of flow rates through matrix and fracture:

$$q_t = q_m + q_f \tag{6.13}$$

Using Darcy's law in Eq. 6.13:

$$(\frac{k}{\mu})_{avg} \frac{\Delta Y \Delta Z \Delta p_t}{\Delta X} = (\frac{k}{\mu})_{fr} \frac{w_{avg} \Delta Z \Delta p_{fr}}{\Delta X} + (\frac{k}{\mu})_m \frac{(\Delta Y - w_{avg}) \Delta Z \Delta p_m}{\Delta X} \tag{6.14}$$

But the pressure drops would be the same across the fracture and matrix:

$$\Delta p_t = \Delta p_f = \Delta p_m \tag{6.15}$$

Finally, the average mobility of the grids containing proppants will be:

$$(\frac{k}{\mu})_{avg} = \frac{1}{\Delta Y} [(\frac{k}{\mu})_{fr} w_{avg} + (\frac{k}{\mu})_m (\Delta Y - w_{avg})] \tag{6.16}$$

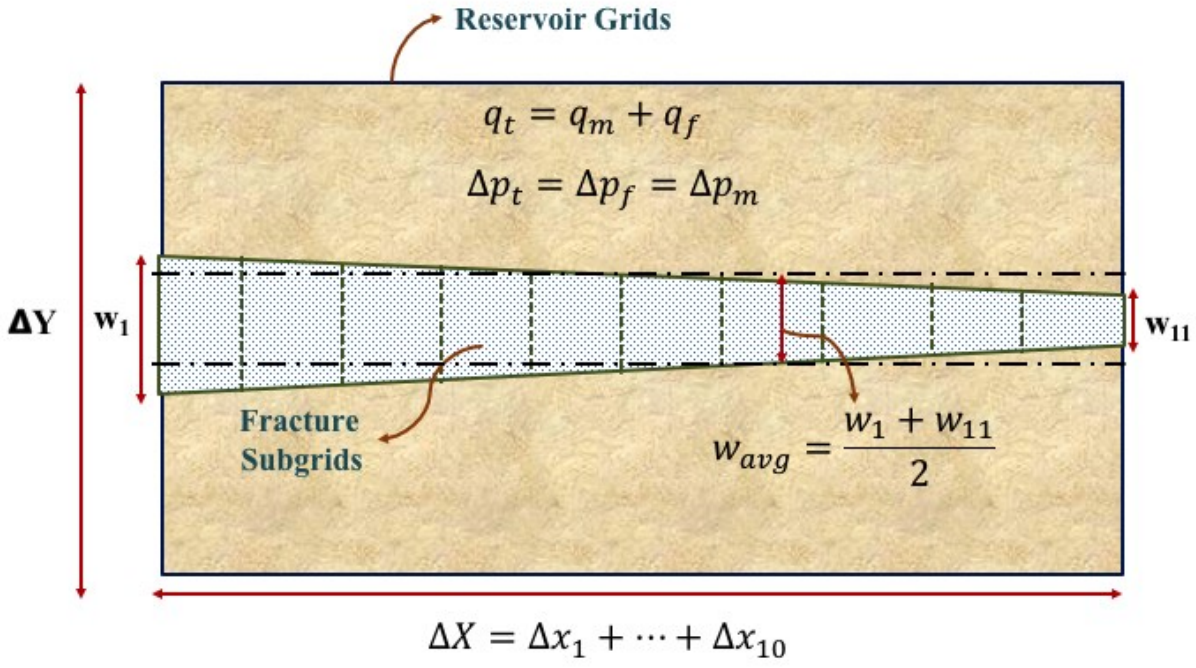

Figure 6.6: Averaging Mobility of Reservoir Grids

If the fracture partially penetrates a grid, the procedure of finding total mobility will be the same, with another series averaging between the portion of grid that is fractures and the portion that is

not fractured. Injection of proppants may cause a significant increase in the viscosity of slurry which in turn decreases the slurry mobility to very low values. Our formulation accounts for the change of width and proppant concentration on a subgrid scale.

6.2.4 Closure

When the mobility of the injection fluid is decreased due to presence of proppant particles, a large pressure drop might occur inside the fracture. Consequently, the length and width of the fracture will change. As shown in Fig. 6.7, two outcomes should be expected to occur:

1. If no proppant exists in some portions of the fracture, it may completely close to zero width. Therefore, the fracture length will be shortened.
2. On the other hand, portions of the fracture that contain proppant will not completely close to zero width since the proppants prevent the fracture from closing. However, the width of the fracture will be reduced to "propped fracture width". At this state, the fracture width cannot decrease any further.

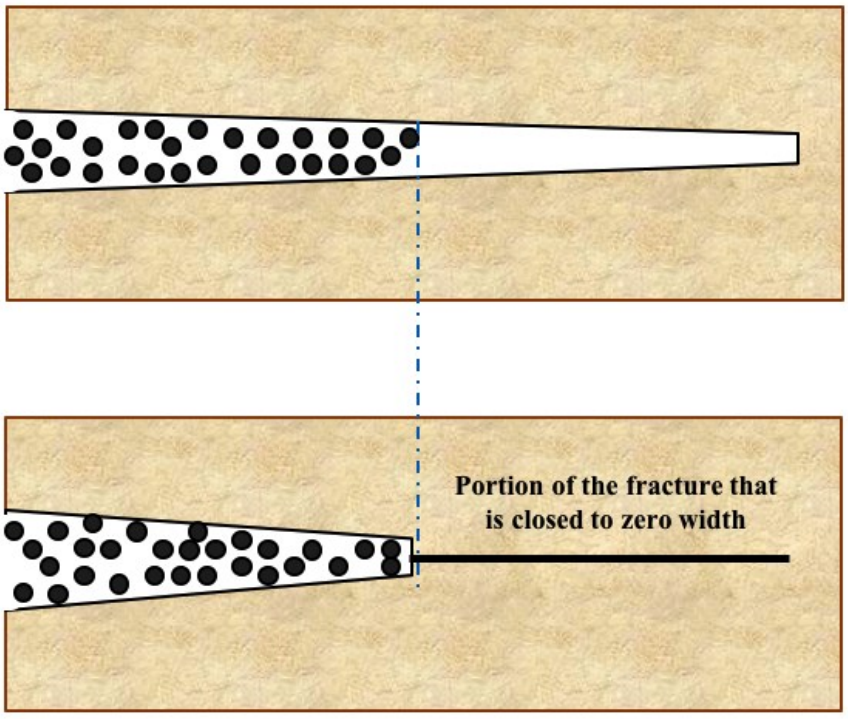

Figure 6.7: Fracture Closure When No Proppant Exists

The first case can be easily implemented in the numerical code, since an adaptive re-meshing technique along with a moving BC has been utilized in our code. However, the amount of

fracture closure on proppants and resulting width reduction in the second scenario should be calculated.

The reduction of fracture width will modify proppant concentration, while the volume of the proppants inside subgrids will be constant. Before fracture width reduction happens, volume of proppants in subgrids will be:

$$V_{p1} = c_1 dxdyw_1 \tag{6.17}$$

We assume that after fracture closes on proppants, the concentration in the subgrid will reach saturation concentration. Hence, the proppant volume can be obtained from:

$$V_{p2} = c_{sat} dxdyw_{propped} \tag{6.18}$$

where $w_{propped}$ is fracture propped width. Since the volume of proppant will not change during closure,

$$V_{p1} = V_{p2} \tag{6.19}$$

or

$$w_{propped} = \frac{c_1 w_1}{c_{sat}} \tag{6.20}$$

This calculation process is shown schematically in Fig. 6.8.

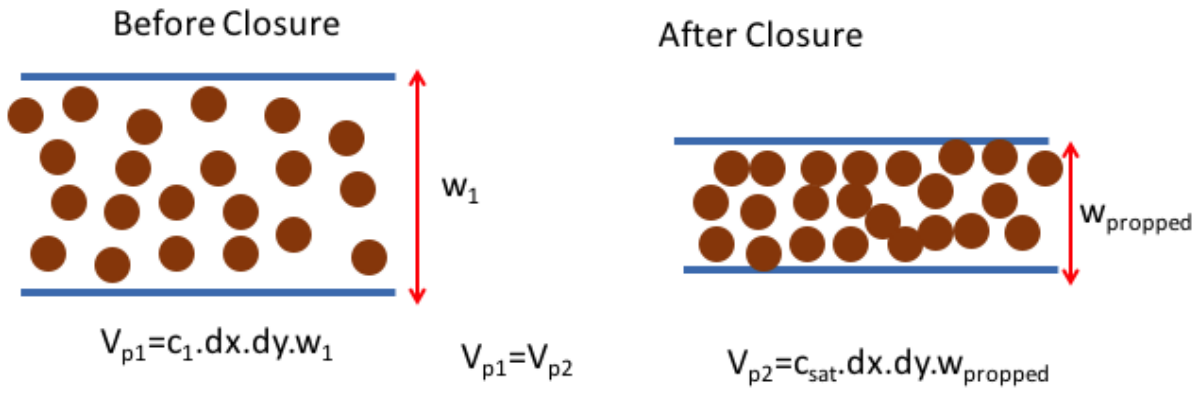

Figure 6.8: Fracture Closure on Proppants

The value of propped width is calculated for all the subgrids at the beginning of each time step. It determines the maximum reduction of y-displacement in the geomechanics module. When the total y-displacement in two adjacent geomechanics nodes reach the critical y-displacement

(propped width) the nodes are fixed in the y-direction which assures that no more y-displacement happens. There is, however, one issue with this approach that needs to be resolved. If due to the injection of slurry, the fracture reopens, the previously fixed nodes should be freed. This can be done by looking at the pore pressures inside the grids. For every gridcell, the pore pressure and corresponding fracture width is saved like a table in the numerical code. The propped width will also correspond to a certain pore pressure. We call this pore pressure, "critical pore pressure". As soon as the pore pressure of the grid reaches the critical pore pressure, two nodes of that grid will be freed.

There are other methods of simulating fracture closure in which the stiffness matrix is changed to ensure nodal y-displacement is a constant number ($w_{propped}/2$). The approach is called penalty approach (Chandrupatla and Belegunda, 1991; Ji, 2008). Penalty approach could not be implemented in our work since we are using commercial software FLAC2D and only a method that does not require a change of the global stiffness matrix could be utilized.

6.2.5 Saturation Concentration and Proppant Pack Permeability

As it was explained in Chapter 2, there is a maximum concentration of proppants that can fill up fracture. This maximum concentration is an empirical parameter and depends on density of packing. In the simulations of this chapter, it was assumed that the maximum proppant packing concentration is 0.6 which corresponds to a dense pack.

Before the proppant concentration reaches its maximum value, the permeability of the fracture is calculated from cubic law. However, this law does not apply to a stationary pack of particles. If the concentration in any element reaches the maximum value, it is assumed that it behaves like a porous medium with a permeability coming from Kozeny-Carman equation (Rajani, 1988):

$$k = \frac{(1-c)^3 {d_p}^2}{180c^2} \tag{6.21}$$

the coefficient 1/180 was suggested by Carman (1939) for uniform spherical particles.

6.3 Verification of Finite Conductivity Fracture

When proppants are injected inside the fracture, the mobility of the slurry reduces since viscosity is increasing. The effect of mobility decrease on pressure profile would be similar if permeability

decreases. In other words, it can be said that conductivity of the fracture will not be infinite any longer.

To verify the average mobility calculations explained in the previous section, the results of our numerical model is compared with analytical solutions of Cinco-Lay et al. (1978), and numerical work of Barker (1978), for static fractures. Cinco-Lay et al. model contains a vertical fracture with finite conductivity at the center of an isotropic, horizontal, infinite, circular drainage area. They assumed the cylindrical reservoir slab was bounded by impermeable strata. As shown in Fig. 6.9 a finite conductivity fracture intersects the wellbore and a slightly compressible fluid is injected inside the wellbore. Barker (1978) in a numerical work simulated an explicit fracture in a finite acting square reservoir with the same abovementioned assumptions. In both studies, the results were presented in terms of dimensionless pressure and dimensionless time defined in Eq. 6.22 and 6.23:

$$t_{Df} = \frac{kt}{\mu c \phi x_f^2} \tag{6.22}$$

$$p_{wD} = \frac{2\pi kh}{q\mu B}(p_{wf} - p_{init}) \tag{6.23}$$

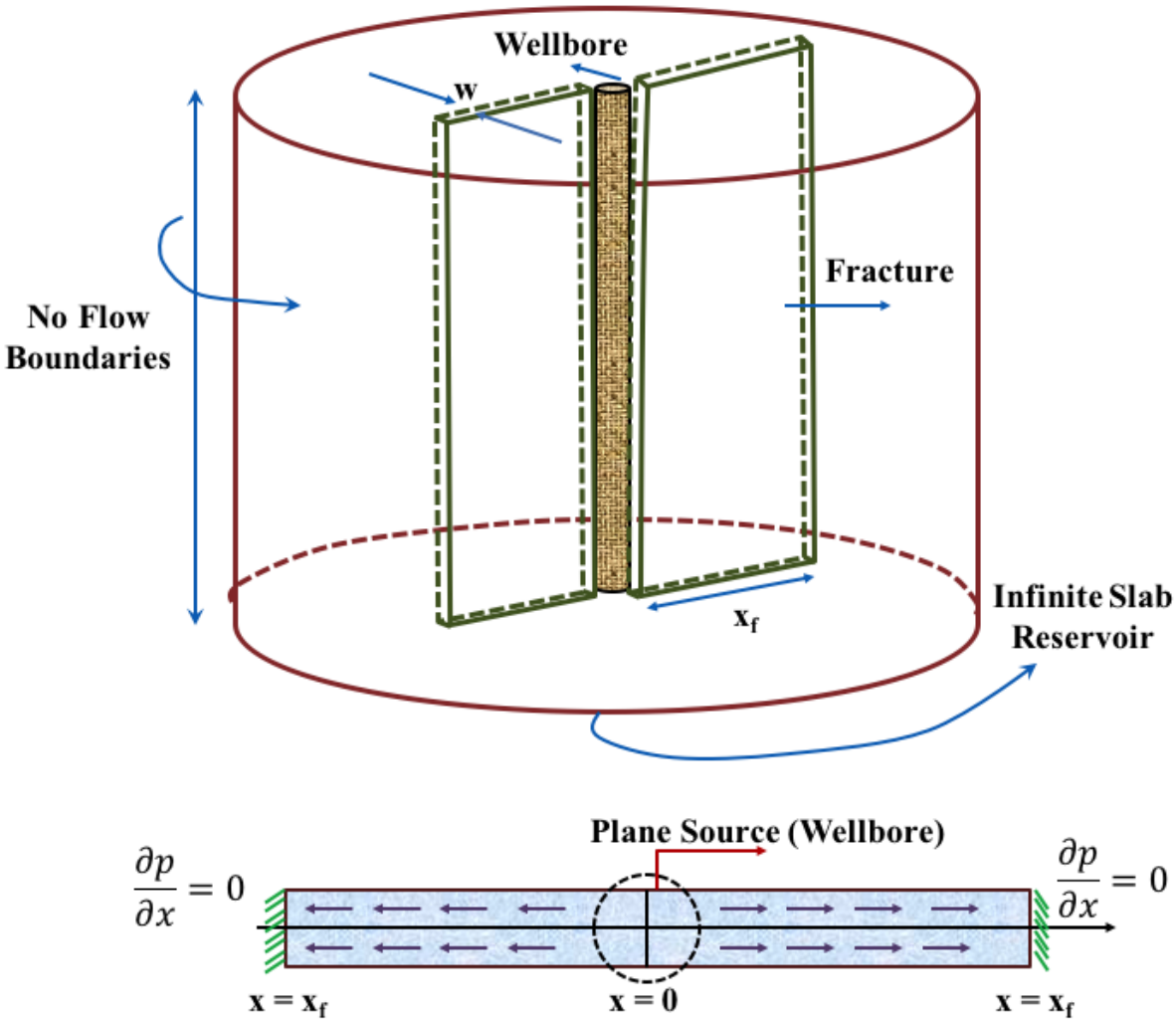

Figure 6.9: Geometry of the Verification Model

It should be noted that the two reference results from literature deviates at larger times since Cinco-Lay et al. (1978) assumed an infinite acting reservoir. Figure 6.10 shows a comparison between the analytical work of Cinco-Lay et al. (1978) and numerical work of Barker (1978) for a full penetrating fracture with 0.2π conductivity.

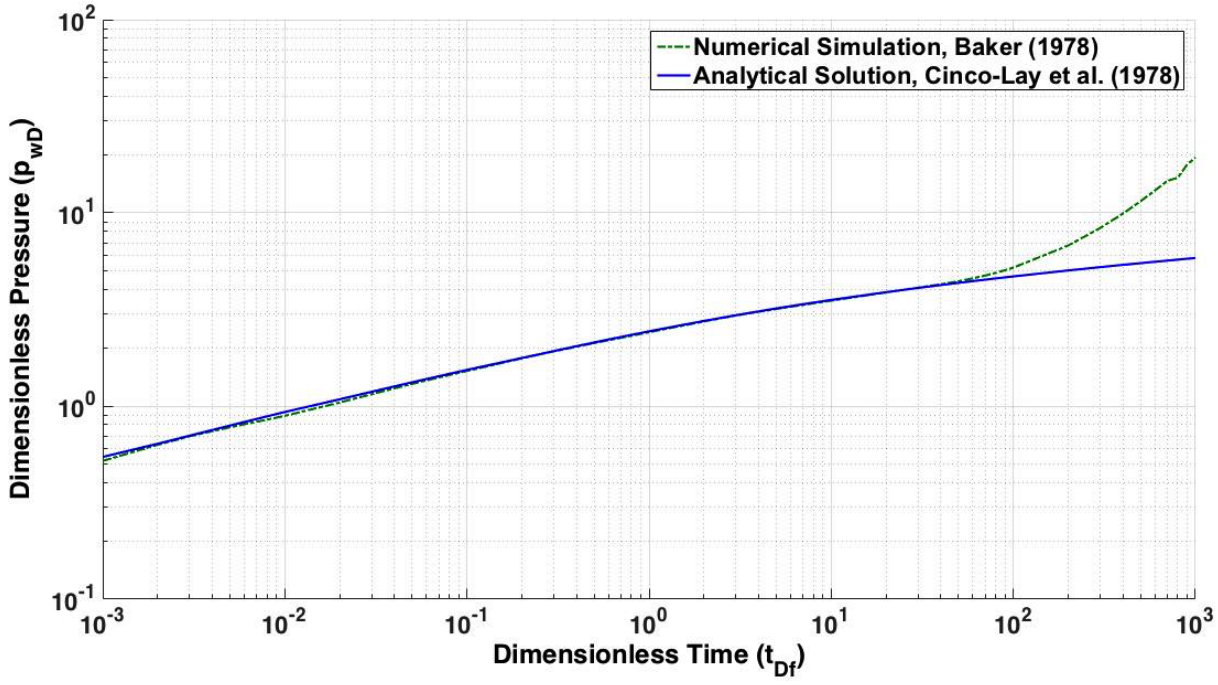

Figure 6.10: Analytical Solution of Cinco-Lay et al. (1978) vs. Numerical Simulation of Barker (1978) for a Full Penetrating Fracture with 0.2π Conductivity

To verify our averaging scheme explained in Section 6.2.3, we built a 2D model with input parameters of Table 6.1. We assumed the half length of the fracture is 150 m and its width is constant at 0.001 m with a proppant concentration of 0.5. Assuming the maximum packing concentration is 0.66, this amount of concentration gives a slurry viscosity of 107.5 cp according to Barree equation (1994) mentioned in Chapter 2, Table 2.7. Each reservoir grid is divided into 10 subgrids for all the simulations. According to Eq. 6.16 the average mobility of the slurry becomes 9.3×10^{-9} m^2/Pa.Sec. This is equivalent of having a fracture conductivity of 0.2π.

Table 6.1: Input Parameters for Finite Conductivity Fracture Simulation

Parameter	**Value**
Porosity	0.25
Permeability	0.9869×10^{-13} m^2 (0.1 Da)
Fluid Viscosity	1 cp (0.001 Pa.Sec)
Fluid Compressibility	1e-10 Pa^{-1}
Injection Flow Rate	8×10^{-5} m^3/Sec
Reservoir Dimensions (Drainage Area)	300 m by 300 m (90000 m^2)
Initial Reservoir Pore Pressure	5 MPa
Fracture Conductivity	0.2π
Fracture Half Length	150 m
Reservoir Grid Size	Variable
Fracture Subgrid Size	0.1 of Reservoir Grid Size
Fracture Width	0.001 m
Slurry Viscosity	107.5 cp (0.1075 Pa.Sec)

Figure 6.11 is a comparison between our result and Cinco-Lay et al. (1978) analytical and Barker (1978) numerical results. A good match is observed except for the early time. According to the mesh sensitivity shown in Fig. 6.11, accurate modeling of early transient flow requires a very fine grid, comparable to wellbore radius, near the wellbore to capture wellbore boundaries.

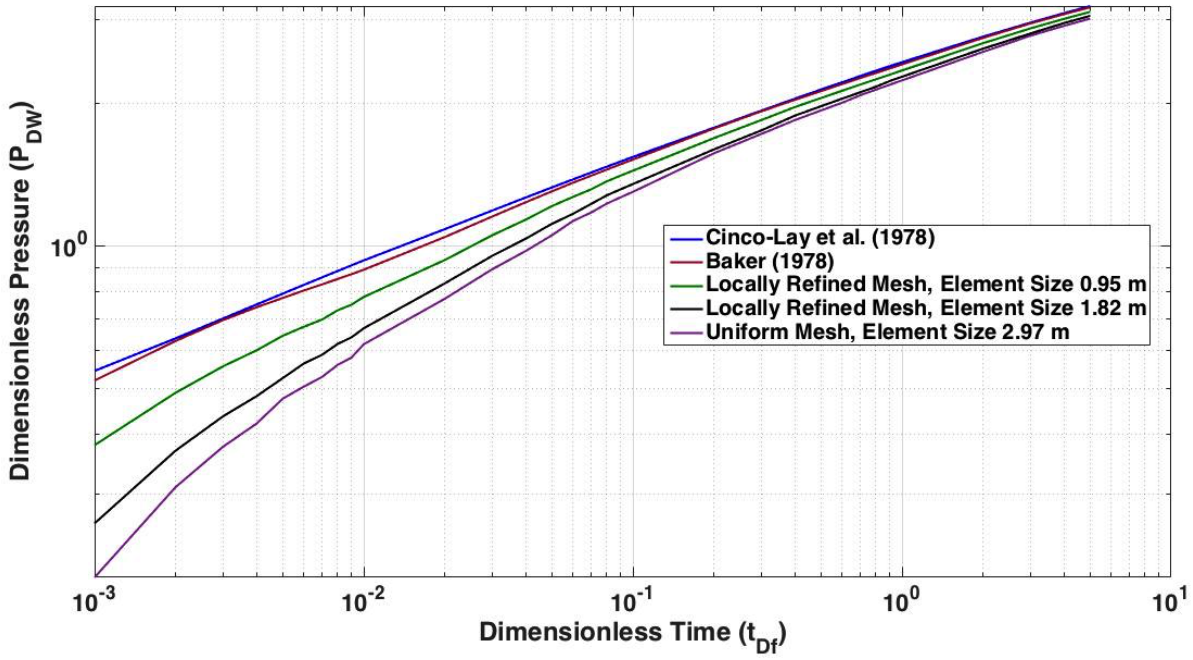

Figure 6.11: Comparison of Current Numerical Results with Analytical and Numerical Works in the Literature

6.4 Numerical Algorithm of Coupling the Three Modules

In our simulations, we are utilizing three modules, namely, fluid flow, geomechanics and proppant simulators. The coupling between the fluid flow and geomechanics has been previously explained in Chapter 5. The result was a new stress-dependent hydraulic fracture simulator, in which, an in-house finite difference fluid flow simulator is coupled to the finite difference code FLAC2D. Following the definition of Settari and Mourits (1994), such a treatment is called a partially coupled simulation. The coupling between the modules relies on the stress state computations inside the reservoir induced by injection and the increase in pore pressure. In the next step, the calculated strains and displacements in the geomechanical module are used to modify reservoir permeability for fluid flow simulation. The partial coupling has the advantage of being flexible and computationally cost effective compared to the fully coupled based solver. In this section, we describe the coupling of our stress dependent reservoir simulator, geomechanical simulator, and proppant transport simulator in detail.

In the linkage that we implemented, any existing sophisticated modeling tool for each component can be used. The linkage has been termed partially decoupled or partially coupled approach,

since there is a separate module for stress and fluid flow that solves the equations separately in each time increment.

The critical aspect in partially decoupled modeling is the fracture in the reservoir model. Our numerical tool consists of three computational modules. The geomechanics module gives the stresses and also fracture geometry based on the smeared approach. The reservoir module solves the fluid flow equations in the reservoir and includes fracture by assigning a high permeability to the grids that contain the fracture. Finally, the proppant module simulates the proppant transport until all the proppant become immobile when the concentration reaches the saturation concentration and the fracture is filled up with proppants. Figure 6.12 is a schematic of the coupling process.

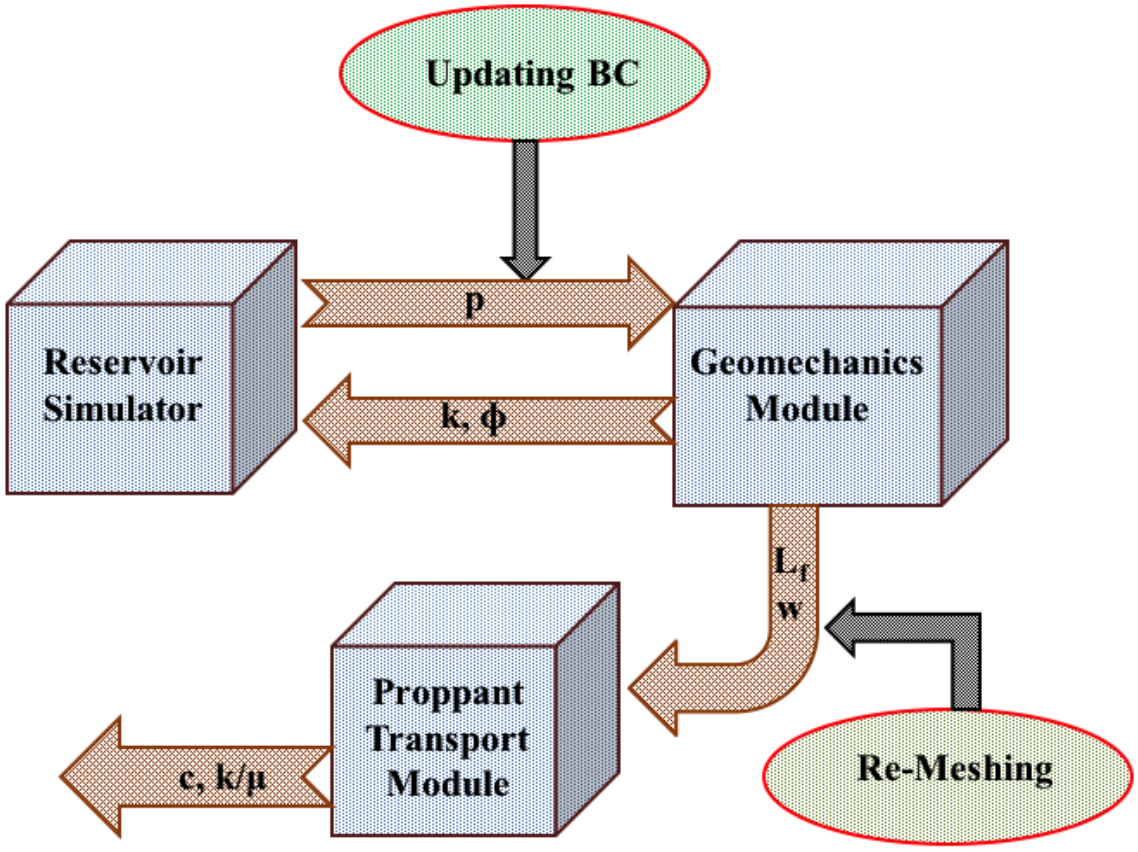

Figure 6.12: Information Transfer between the Modules

The proppant simulator solves the hyperbolic partial differential equations described in Chapter 3. The grids for proppant simulator are generated dynamically based on fracture growth in the geomechanics module. If a fixed number of gridblocks is assigned to the entire fracture in all the time steps, the sizes of the cells become bigger as the simulation progresses and this reduces the

accuracy significantly. Therefore, we assigned a constant size to the elements in all the time steps. In this way, as the computations proceed, the number of gridblocks becomes larger and no stability problems occur. In addition, since the position of the gridblocks is the same for all the time steps, no interpolation is required. If the length of the fracture in the current time step was L_f^n and the assumed length of the proppant cells is Δx_p, then the number of gridblocks that are added to the simulation model will be:

$$N_{new\ Elements} = \frac{L_f^n - L_f^{n-1}}{dx} \tag{6.24}$$

Since structured mesh is employed to discretize our moving boundary problem there is no need to check smoothness of the mesh or regularity of the elements. The incremental addition of new elements effectively prevents the element size from becoming too large.

As shown in Fig. 6.13, there are two iteration loops in the coupled algorithms. The first iteration loop is between fluid flow and geomechanics simulators and provide fracture dimension. The second iteration loop is between proppant transport simulator and HF package (fluid flow and geomechanics) and obtains proppant concentration distribution and mobility.

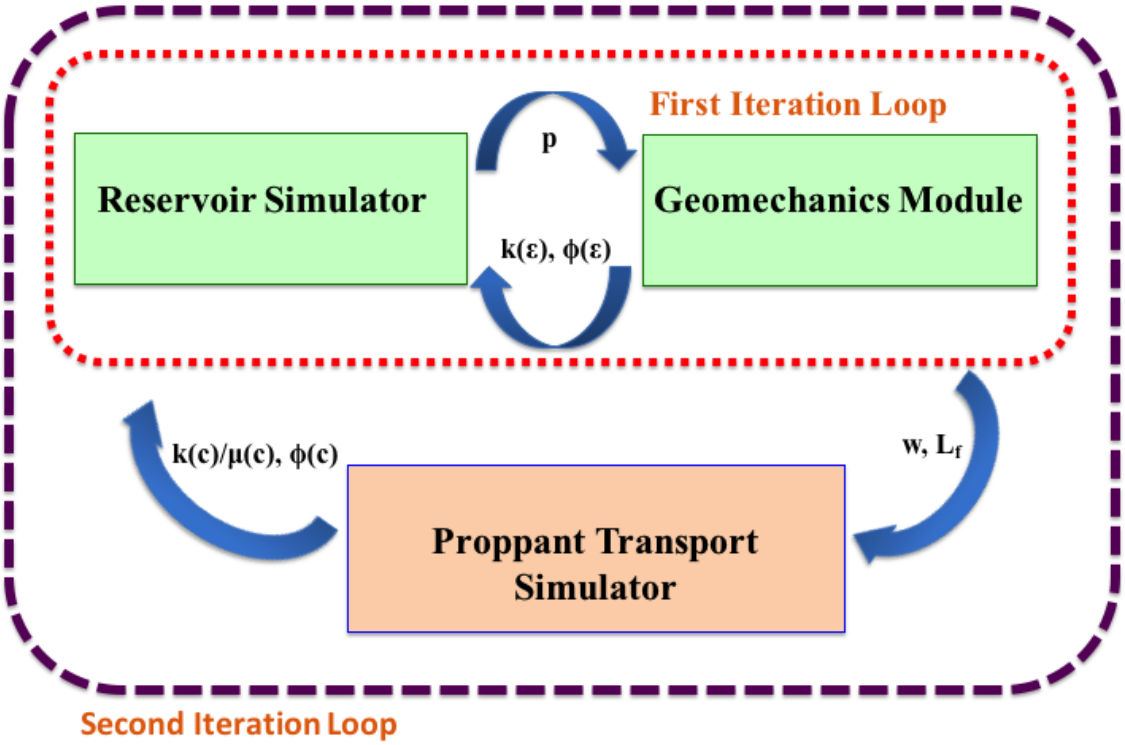

Figure 6.13: Iteration Loops in Numerical Linkage

The primary result of the proppant simulator is the distribution of proppant concentration in the fracture, which can be translated into the independent grid of reservoir simulator by reducing the fractured gridblock mobility.

Because permeability of the gridblock which contains the fracture has a strong dependency on the displacements in geomechanics module, the proppant calculations must be done in small time steps after proppant injection starts. The stable time step of explicit reservoir simulator is different than the same in proppant simulator and is usually larger (Eq. C-5). However, both of these stable times are very small. Therefore, the hydraulic fracture module is run for several time steps at constant concentration and the result is transferred to proppant module. Next, the proppant transport simulator is run for several time steps at constant fracture dimensions until the total time reaches to that of reservoir simulator. Figure 6.14 is the numerical algorithm of the linked modules.

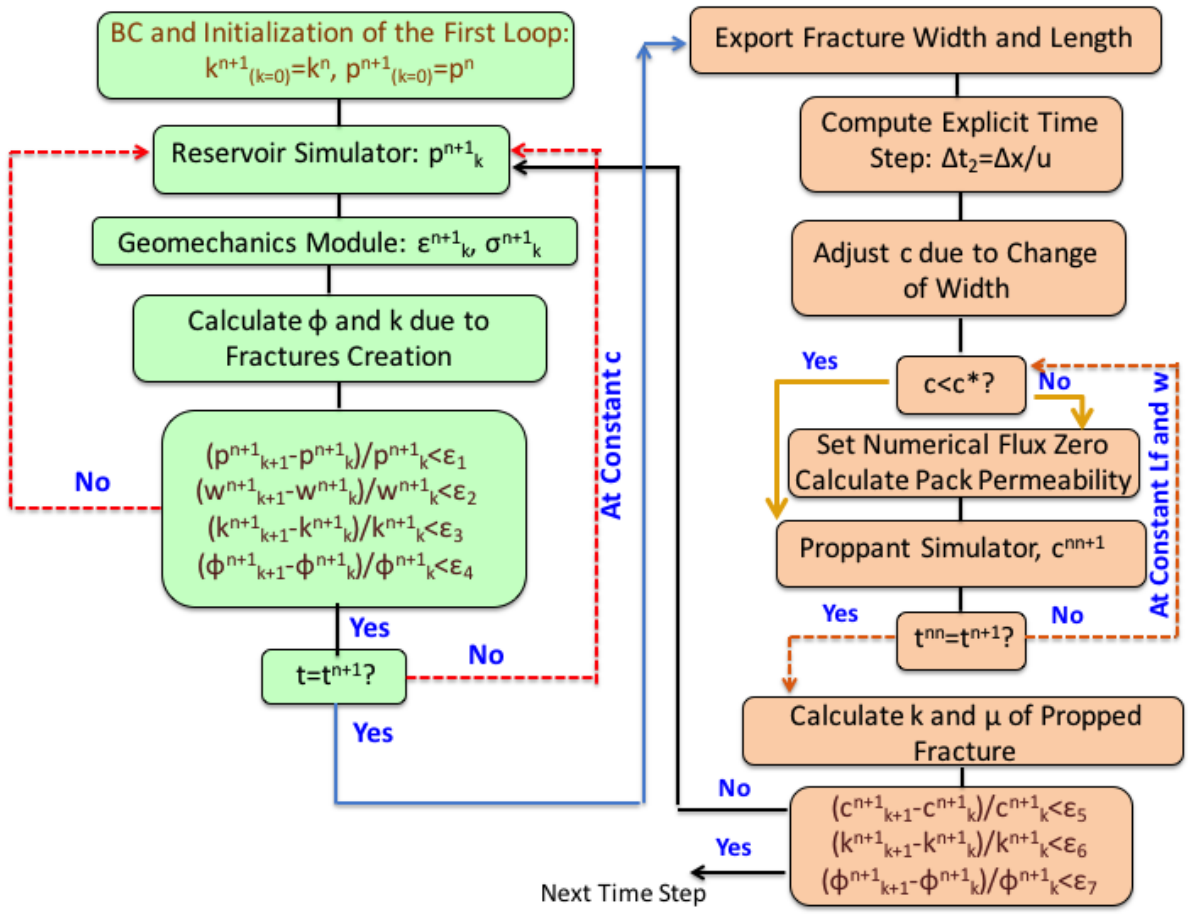

Figure 6.14: Numerical Algorithm of Linking Three Modules

The implemented system has several advantages over the fully coupled models:

1. Since fracture and reservoir use different grids, better resolution of the fracturing process can be obtained. Any mesh sensitivity analysis with the reservoir model can be performed without the need to regenerate the fracture description.
2. The proppant simulator can be coupled with any fracture simulator, either smeared or explicit, numerical or analytical. This greatly increases the versatility of the approach and its range of applications.
3. Due to the smeared approach, the computational efficiency is greatly improved and the memory requirement, especially for the fracturing simulation is greatly reduced.
4. Since the leak off and fracture growth happen naturally in smeared approach, the numerical problems of simulating them in the fracture is removed.
5. The proppant simulator requires very small time steps for stability purposes. Decoupling it from the reservoir and geomechanics allow small time steps be assigned to the proppant simulator, while bigger time steps assigned to the reservoir simulator. The proppant module is run for several time steps until it catches up to the other simulators in time. Due to this severe time step limitation, decoupling is inevitable.

6.5 Numerical Simulations

Several numerical examples are carried out in this section to investigate the effects of proppant injection on hydraulic fracture shape and propagation. Since there are many parameters that can influence the results, it is more informative to specify a base case with reference parameters and then in a sensitivity analysis change one parameter at a time. The same hydraulic fracture model that was simulated in Chapter 5 is used for proppant injection. The fracture is allowed to propagate during 2000 seconds of pad injection. At this time, a proppant laden slurry is introduced and injection continues until the whole fracture is packed with proppants. The boundary conditions and input parameters of the reservoir and geomechanics simulators is previously described in Fig. 5.16 and Table 5.2. The additional proppant related parameters and boundary conditions of proppant simulator is described here in Fig. 6.15 and Table 6.2.

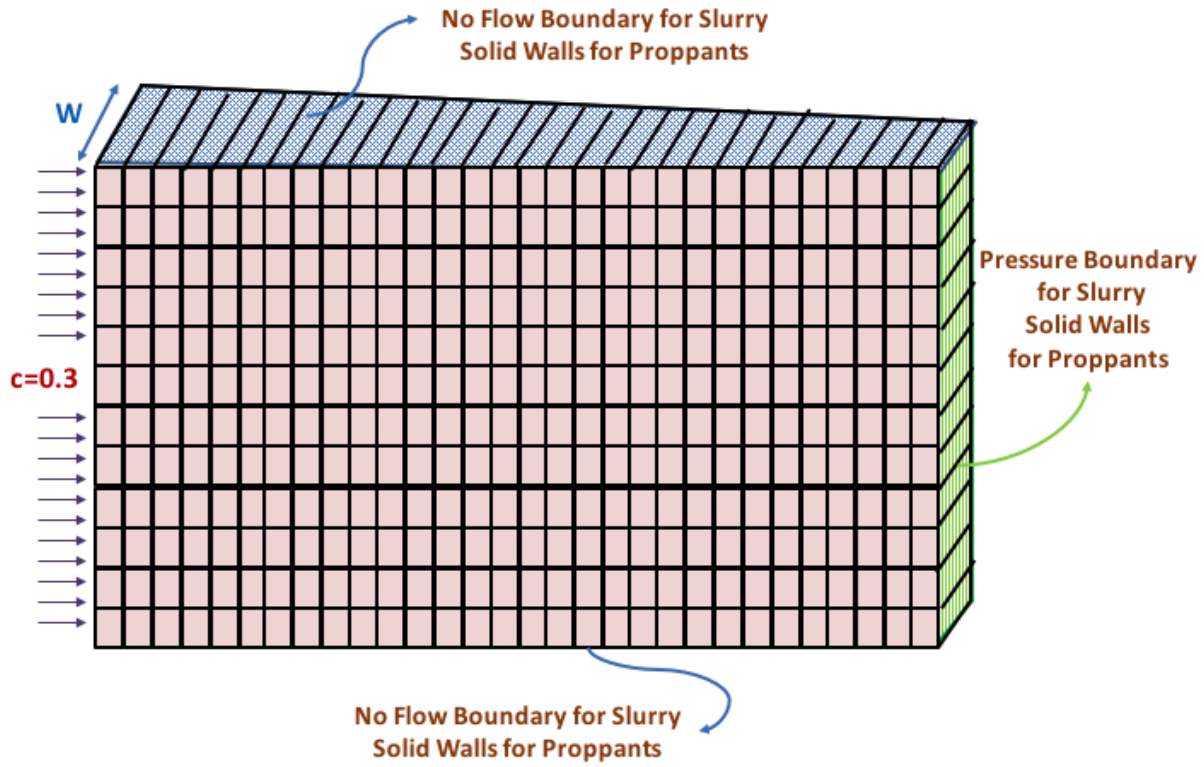

Figure 6.15: Moving Boundary Condition of Proppant Transport Simulator

It is assumed that at top and bottom of the reservoir section, two barriers exist and they block any flow going outside the reservoir. It should also be noted that the proppant transport simulator needs two sets of boundary conditions as slurry and proppant mass balances are solved separately in this module. As the location of the fracture tip changes due to fracture extension or shrinkage, the boundary condition specified at right hand side of the model also moves accordingly.

Table 6.2: Input Parameters for Proppant Module

Parameter	**Value**
Model Dimensions	Varies According to Fracture Proppagation
Injecting Fluid Initial Viscosity	0.001 Pa.Sec.
Proppant Diameter	0.006 m
Proppant Density	2600 kg/m^3
Saturation Concentration	0.6
Slurry Viscosity Exponent	1.82
Slurry Injection Start Time	2000 Seconds

Figure 6.16 shows fracture length, fracture width and proppant front advance during injection time. As proppants are introduced at 2000 second time, the fracture length reduces which means fracture partially closes due to increase viscosity of the slurry. Since there are no proppants present in the grids near the tip of the fracture to prevent its closure, the length of the fracture shortens. However, after injection is continued the length start to increase again. After some time, this propagation is stopped again because mobility of injecting fluid is decreased significantly. If the closure algorithm explained earlier in this chapter was not implemented, the length of the fracture would go to zero. However, the algorithm keeps the track of proppant front advancement and does not let full closure happen. When the proppant front reaches the end of the fracture, no more propagation is observed and the fracture length is stabilized.

The situation for the width of the fracture is very different. Increasing viscosity of the injection fluid causes an increase in the pressure inside the fracture. Consequently, it is expected the width at injection point to increase at a higher rate. This fact is clear in Fig. 6.16 after start of proppant injection. Even when proppant front reaches the end of the fracture, the width unlike length, increases since the concentration and consequently slurry viscosity are still increasing.

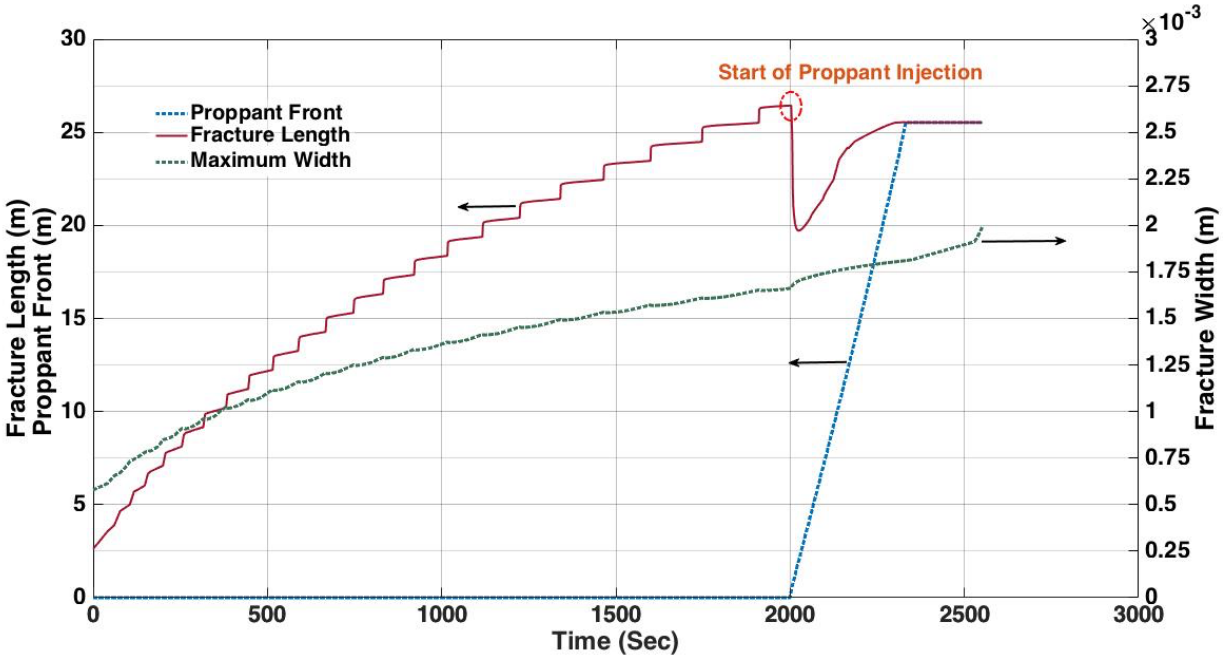

Figure 6.16: Fracture Length, Maximum Width and Proppant Front Advance through Time

Figure 6.17 shows fracture width evolution at different locations along the fracture through time. The first observation is the change in rate of width variation after start of proppant injection. In subgrids closer to the injection point, the rate of width increase is enhanced while in subgrids further away this rate is reduced. As the subgrids become closer to the fracture tip, the width might become zero, which means fracture total closure in this area. However, as it can be seen in Fig. 6.17, some width development occurs after closure which indicates fracture reopening during proppant injection.

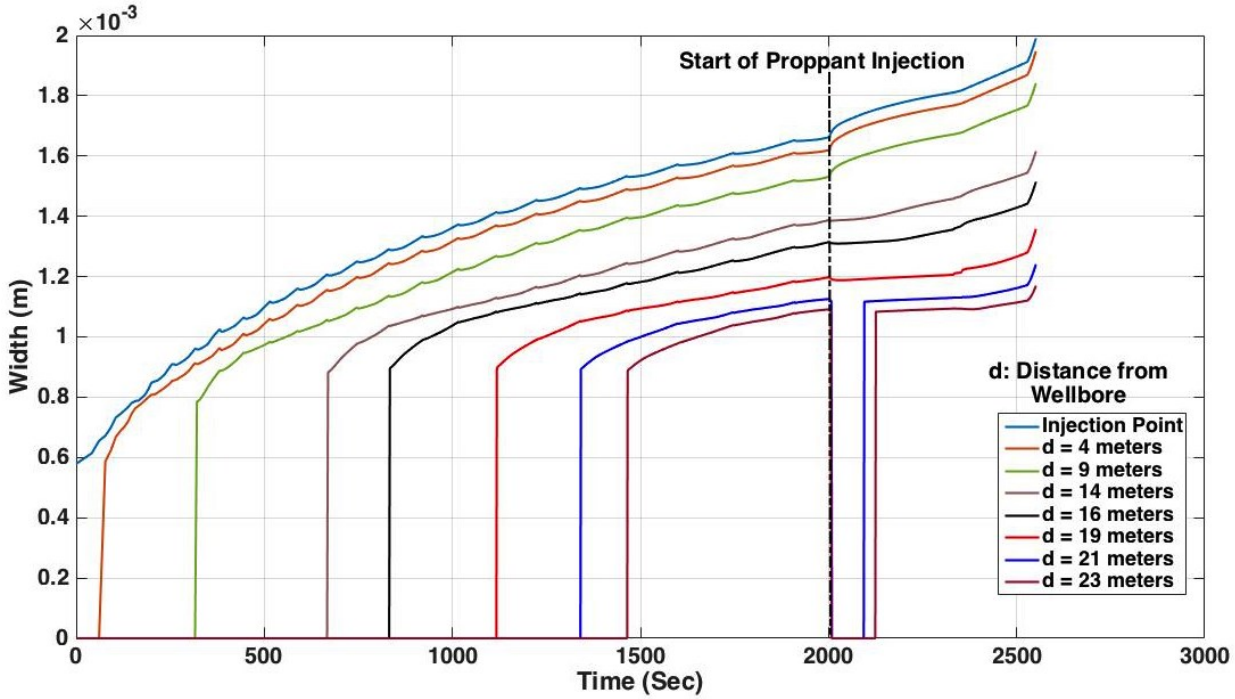

Figure 6.17: Fracture Width Variation through Time

Figure 6.18 and 6.19 show proppant concentration contours at different times during the slurry injection period. Again, the length of the fracture is changing until proppant front reaches the end of the fracture at which further length development or shrinkage stops. A bed of proppants with maximum packing concentration is formed at the bottom of the fracture. The size of this bed determines the efficiency of the frac-packing job. If a large bed is formed, it can block the transport of proppants to the near tip area of fracture and result in premature screenout.

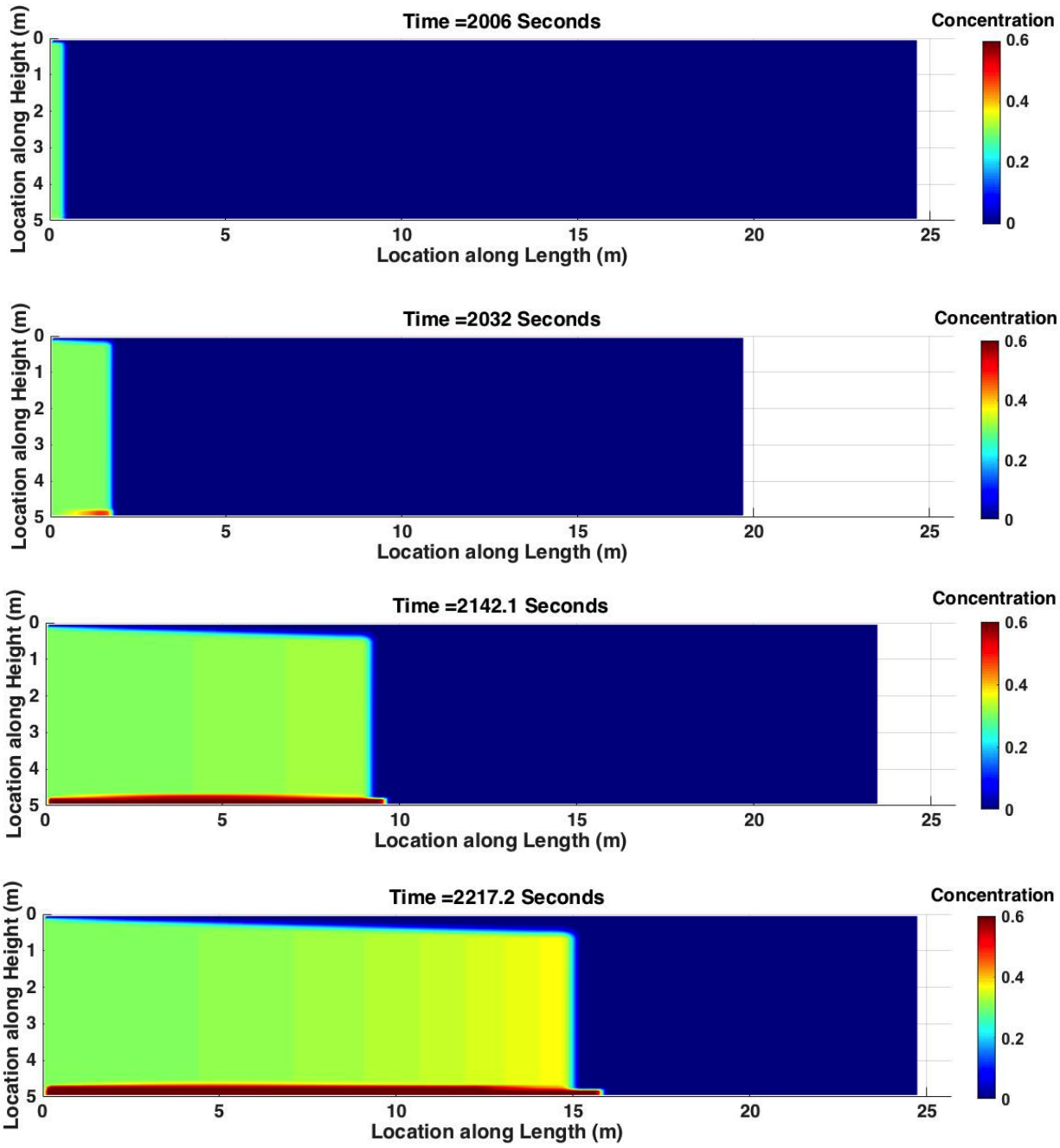

Figure 6.18: Proppant Concentration Distribution at Different Injection Times

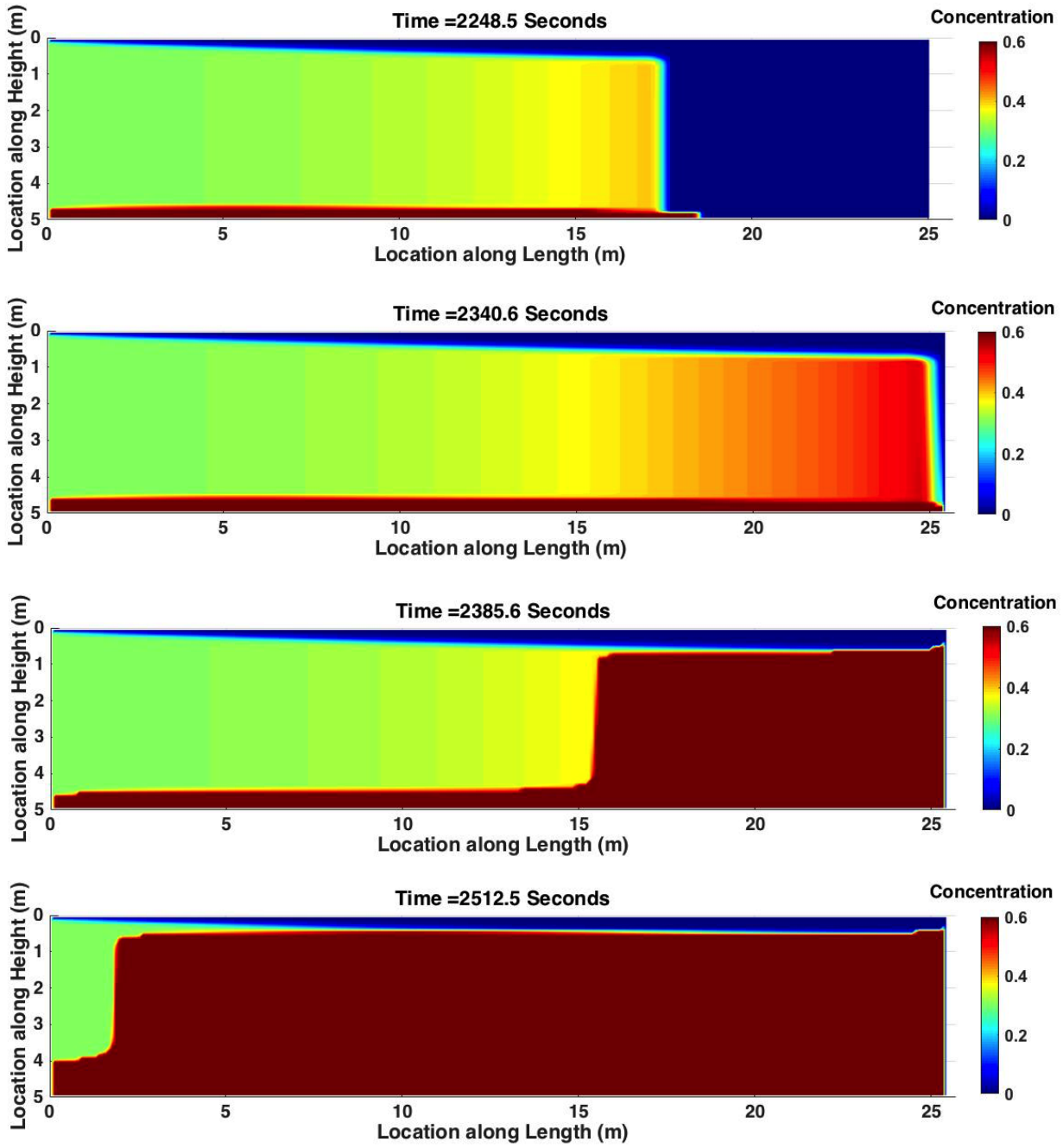

Figure 6.19: Proppant Concentration Distribution at Different Injection Times

At this point it is necessary to check the global proppant mass balance error and use it as a verification to accuracy of the numerical tool. The mass of proppant that is being injected into the fracture can be easily obtained as:

$$m_{injected} = q_{inj} c_{inj} \rho_p t \tag{6.25}$$

where q_{inj} is slurry volumetric flow rate, c_{inj} is proppant injection concentration, ρ_p is proppant density and t is injection time. On the other hand, the amount of proppants inside the fracture can be obtained using:

$$m_{inside} = \sum_{i=1}^{N} c_i V_i \rho_p \tag{6.26}$$

where c is the amount of proppant concentration in each subgrid and V is subgrid volume. The difference between these two parameters serves as a check on mass balance error. This error always exists in numerical simulations. Figure 6.20 shows the mass of proppants injected and inside the fracture and their difference which is called mass balance error percent. Although the error is accumulating through time, its value is very negligible compared to the injected mass of proppant.

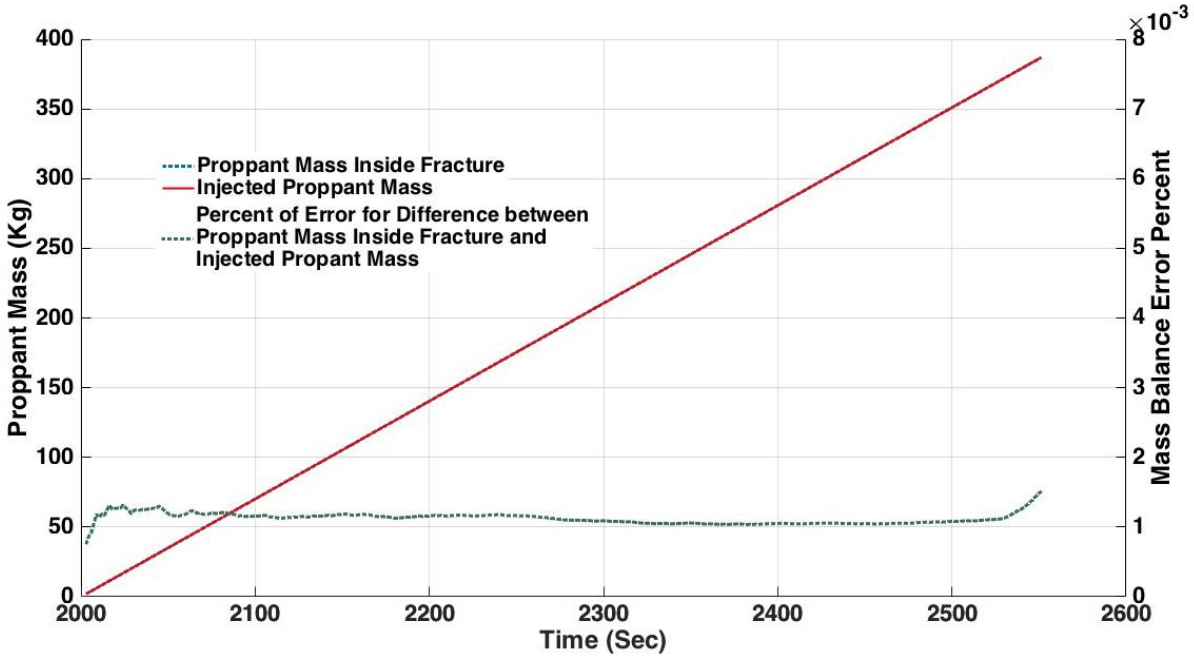

Figure 6.20: Global Mass Balance Check

6.6 Sensitivity Analysis

A sensitivity analysis was conducted to investigate the effect of proppant density, proppant diameter and injection fluid viscosity. In all the simulations, the initial fracture geometry was assumed to be the same as in previous section and similarly the proppant was introduced after

2000 seconds of pad injection. Table 6.3 shows the value of different parameters in each simulation.

Table 6.3: Input Parameters for Sensitivity Analysis Simulations

Simulation Number	Proppant Density (kg/m^3)	Proppant Diameter (m)	Viscosity of Injection Fluid (Pa.Sec)
1-1	1100	0.0006	0.01
1-2	1800		
1-3	2600		
1-4	3900		
2-1	2600	0.0001	0.01
2-2		0.0006	
3-1	2600	0.0006	0.001
3-2			0.01
3-3			0.4
3-4			1

Figure 6.21 shows the proppant concentration distribution at 2194.3 seconds of injection for different proppant densities ranging from 1100 kg/m^3 to 3900 kg/m^3 (the maximum density that can be found in ultra-high strength ceramic proppants). Based on the discussions of Chapter 2 and 3, settling and convection velocities in Stokes region can be expressed as:

Settling Velocity:

$$v_{setlling} = \frac{g(\rho_p - \rho_f)d_p^2}{18\mu} f(c)f(w) \tag{6.27}$$

Convection velocity:

$$v_{convection} = \frac{w^2}{12\mu}\frac{\partial(\rho_{sl} g y)}{\partial y} \tag{6.28}$$

where $f(c)$ is the voidage function, $f(w)$ is wall factor and ρ_{sl} is the slurry density.

According to Eq. 6.27 and 6.28, increasing proppant density increases the settling velocity directly. In addition, proppants with higher densities create a higher density slurry and convection velocity may increase. As a result, a bigger layer of proppant bed is expected to form at the bottom of the fracture. Compared to slot flow simulations of Chapter 4, the effect of density is more pronounced here due to lower viscosity that is assigned to carrying fluid.

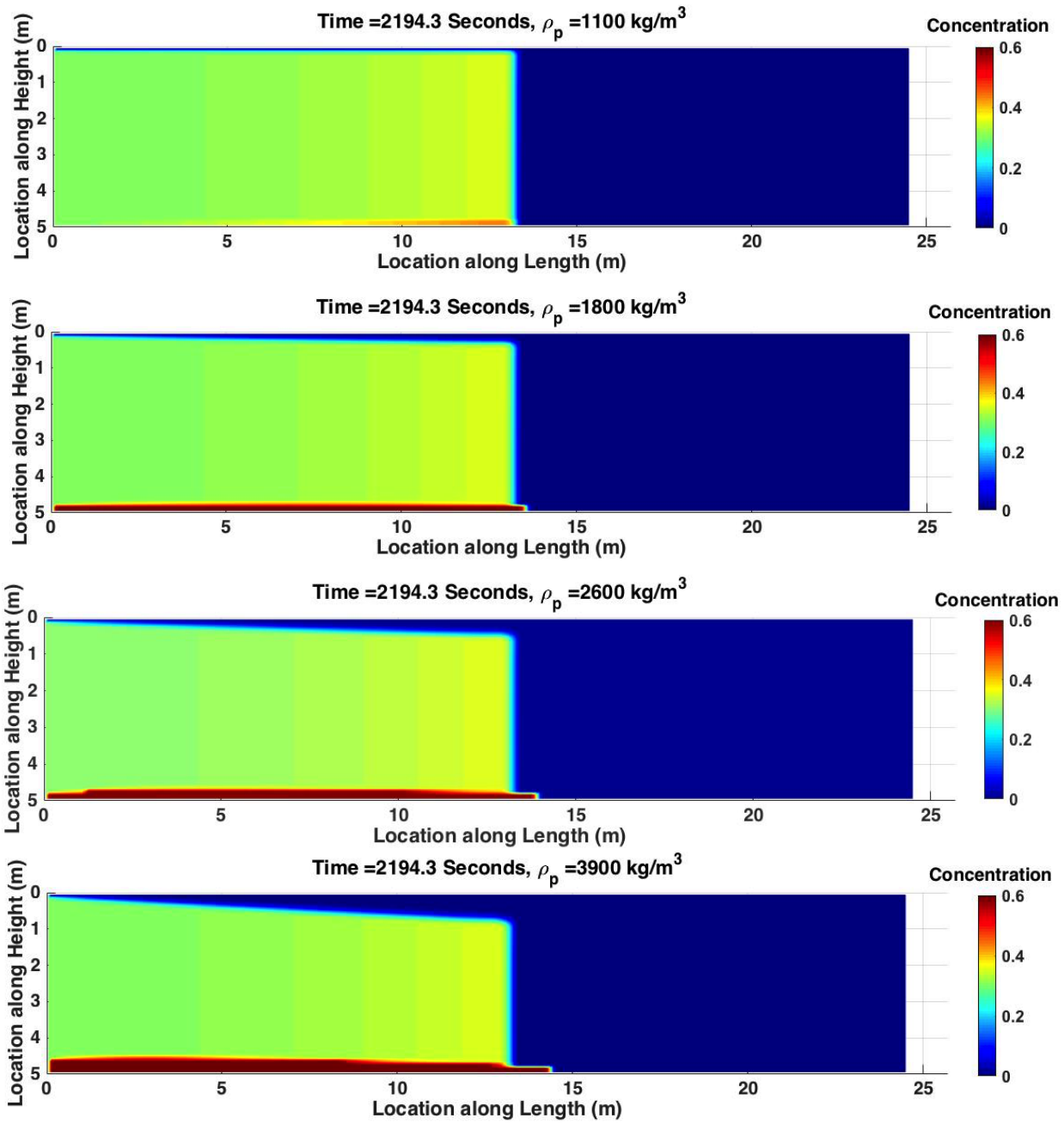

Figure 6.21: Proppant Distribution Concentration for Different Proppant Densities

Although very different proppant distribution is obtained, the fracture geometry in all simulations remain the same as shown in Fig. 6.16. The reason is that the concentration in most part of the fracture has the almost same value of 0.3, except for the proppant bed that is created at the bottom of the fracture. This gives very similar value of viscosity and consequently mobility which is the main fracture geometry controlling parameter. The same fracture propagation behavior was also observed in simulations with varying proppant diameter (Fig. 6.22).

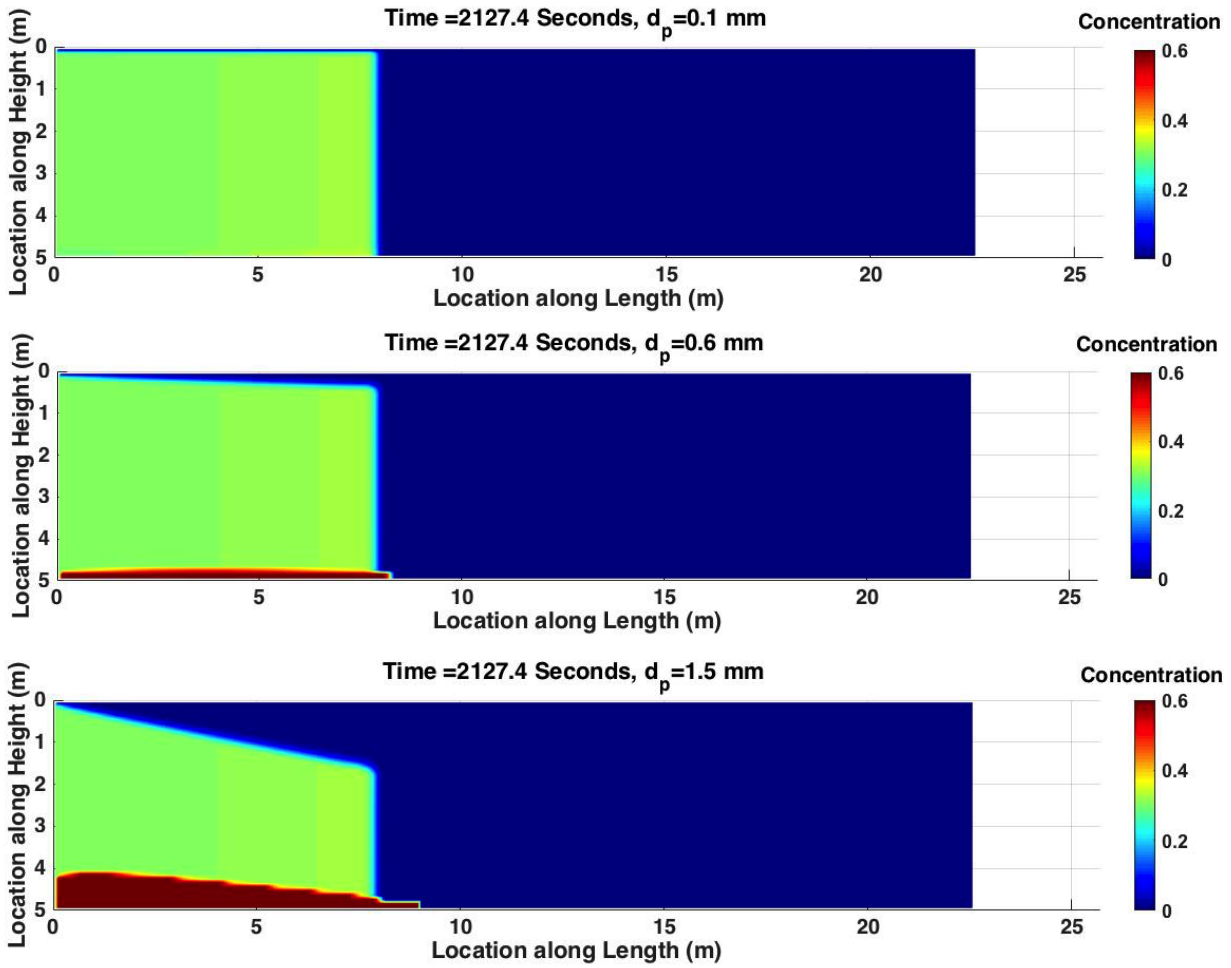

Figure 6.22: Proppant Distribution Concentration for Different Proppant Diameters

According to Eq. 6.28, proppant diameter does not affect convection velocity. This is particularly true when fracture aperture is several orders of magnitude larger than the proppant diameter. However, settling velocity is proportional to proppant diameter to the power of 2. Therefore, increasing proppant diameter will create a bigger bed of proppants compared to the same order increase in density. Although having larger proppants will result in a proppant packed fracture with higher permeability (Eq. 6.21), large proppants may not go into a big portion of fracture due to minimum width for entry requirement.

Based on the results of our simulations, viscosity of the carrying fluid has the strongest effect on the fracture geometry and proppant distribution. Figure 6.23a and 6.23b shows how the length and width of the fracture changes when the carrying fluid viscosity is 400 cp and 1000 cp. In both cases, shortly after proppant injection starts, fracture shortens and widens due to mobility

increase. The final propped length of fracture is larger and its width is narrower when lower viscosity fluid is used.

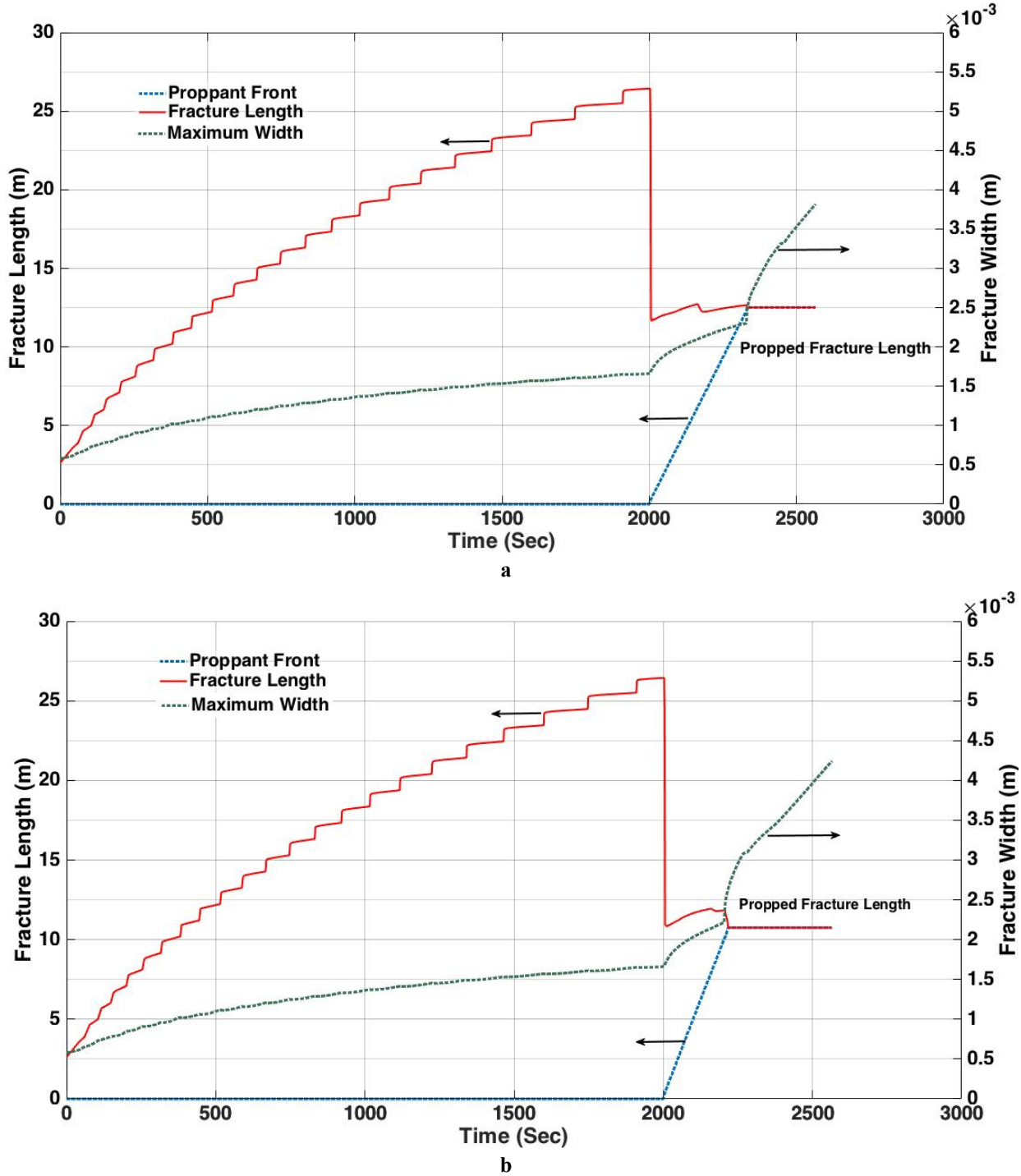

Figure 6.23: Fracture Length, Maximum Width and Proppant Front for Different fluid Viscosities a) 400 cp, b) 1000 cp

Figure 6.24 shows the proppant distribution for the two viscosity cases at 2312.2 and 2411.2 seconds. Viscosity strongly changes both settling and convection, as can be seen in Eq. 6.27 and 6.28. A better proppant placement is obtained by having a higher viscosity fluid. However, at the same time, a shorter fracture is to be expected.

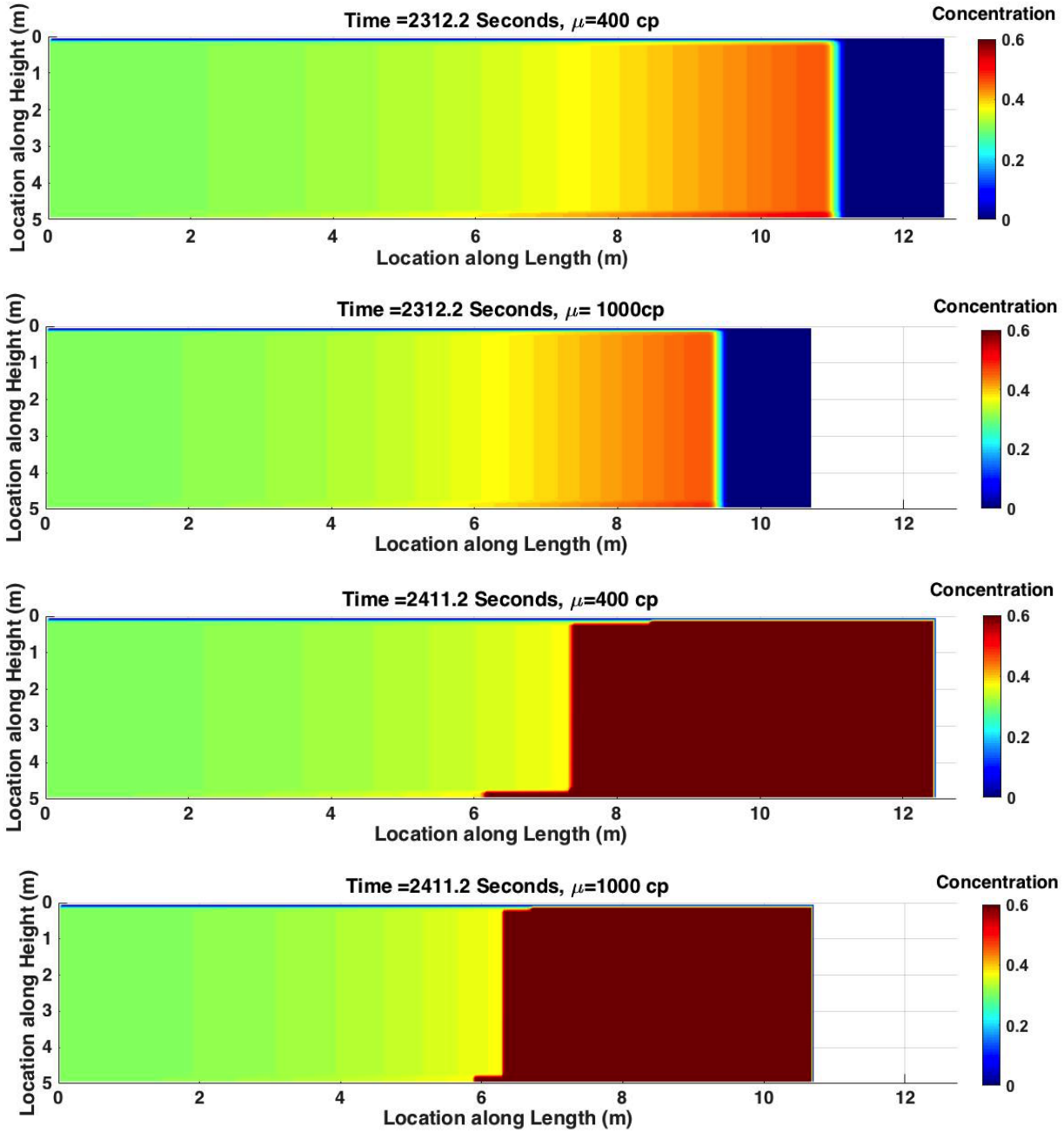

Figure 6.24: Proppant Distribution Concentration for Different Carrying Fluid Viscosities

In another simulation, we decreased the slurry viscosity to 1cp. A perfect example of tip screen out was obtained in this simulation. As it is apparent from Fig. 6.25, small values of viscosity result in longer and narrower fractures. It is interesting to note that the proppant front never reaches the fracture tip. The reason is more clear when we look at the proppant concentration distribution in Fig. 6.26.

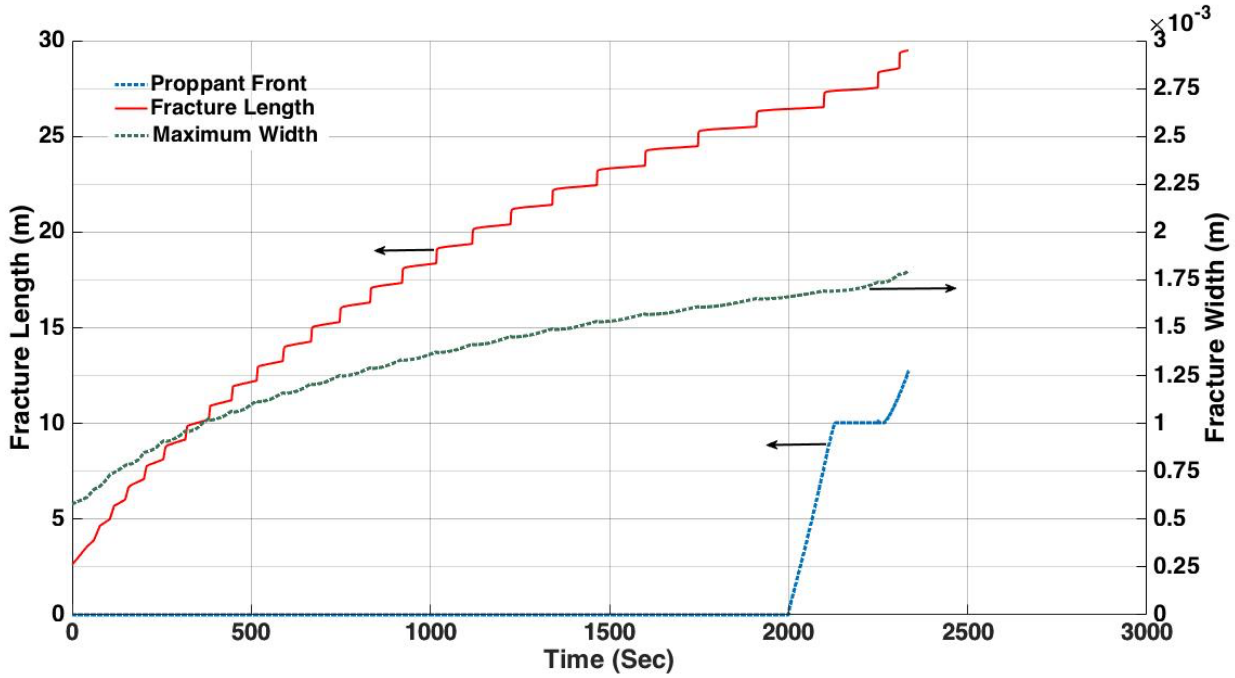

Figure 6.25: Fracture Length and Maximum Width in Low Viscosity Fluid

It can be concluded from Fig. 6.26 that a large bed of settled proppant is created at the bottom that covers a huge portion of the fracture. This is expected to happen as the carrying capacity of the fluid is reduced when viscosity is reduced. However, the size of the bed is so large that it blocks nearly full height of the fracture before proppants reach the tip. In Fig. 6.25 proppant front is depicted in the middle section of the model and it can be seen in Fig. 6.26 that it never reaches the tip of the fracture during the simulated injection time.

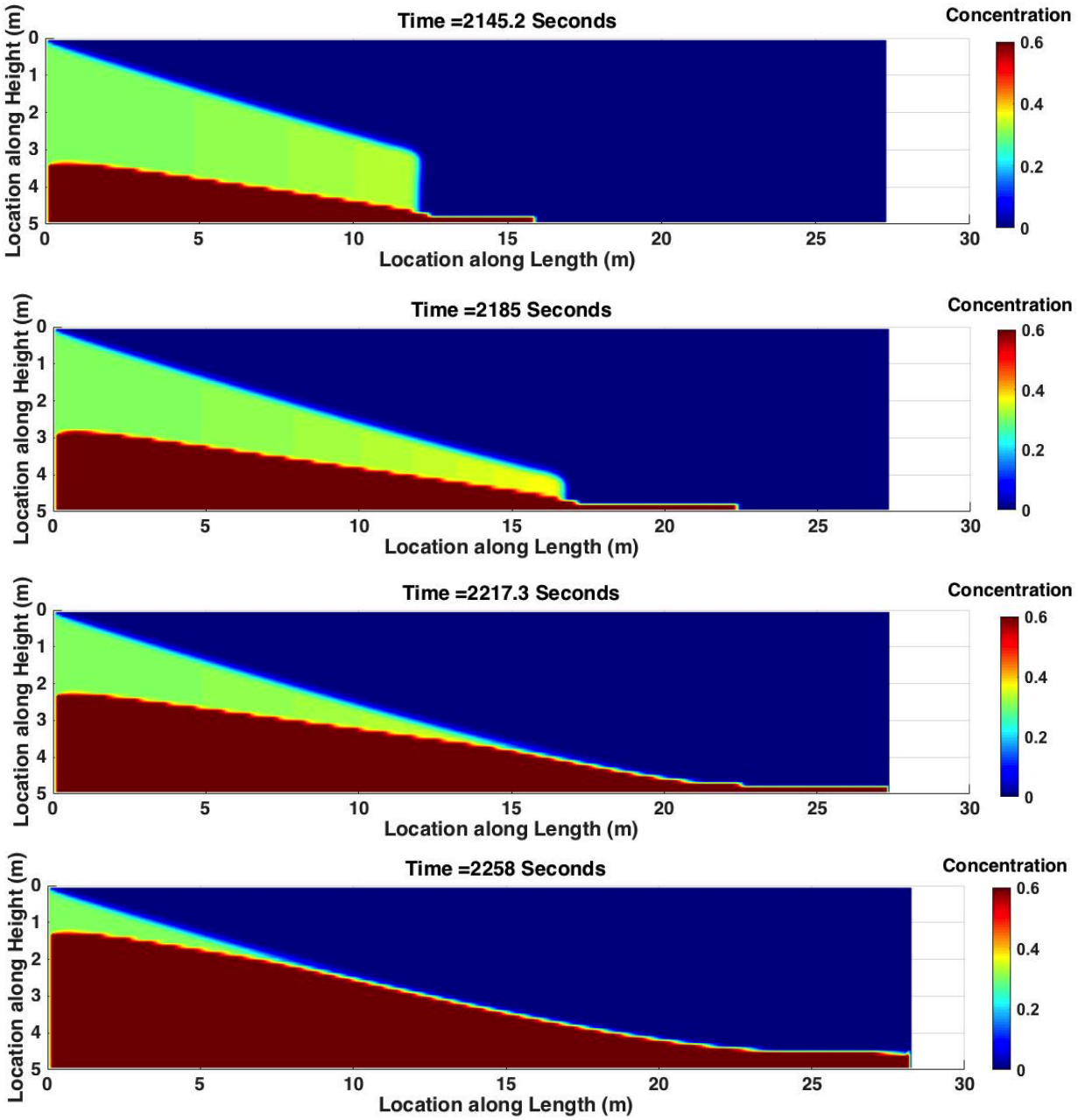

Figure 6.26: Tip Screen-out in Low Viscosity Fluid

6.7 Conclusion

In this chapter, a hydraulic fracture and proppant transport simulator that includes reservoir and geomechanical effects was formulated. The model can consider variable fracture permeability, poroelastic effects, fracture closure on proppants and adaptive mesh design to reflect the physics of proppant transport in a more accurate manner compared to the existing numerical simulators. The fluid flow, mechanical and proppant equations were iteratively coupled in a multi-module

numerical tool with adaptive time stepping and re-meshing. The significance of our coupling development is its flexibility in integrating any commercial fracture, fluid flow or geomechanics simulator in an efficient manner.

We developed a framework that allows the simulator to seamlessly capture proppant settling, fracture closure on proppants, fracture width variation, proppant accumulation into a packed bed between fracture walls and tip screen-out.

A series of sensitivity analysis was performed to confirm the simulation results are plausible and also to investigate the effect of different controlling parameters on proppant distribution inside hydraulic fractures. Our sensitivity analysis shows the effect of proppant density, proppant diameter and fluid viscosity on hydraulic fracture behavior. Viscosity is by far the most important parameter in this regard, that can significantly alter fracture geometry and proppant placement.

Chapter 7: Conclusions and Recommendations for Future Work

In this research, a numerical tool to simulate proppant transport inside propagating hydraulic fractures has been developed. Based on the results from simulated examples, the model indeed produces reasonable shape of fracture and of proppant concentration distribution inside the fracture. Unfortunately, other than fixed shape slots or analytical hydraulic fractures, there are no experimental or numerical works in proppant transport area to compare our results. However, since the model is consistent with the actual physical condition of hydraulic fracture and proppant transport phenomenon, and since the model considers geomechanics and reservoir simulation interactions, it is believed that accurate results can be expected from the model. This chapter summarizes the key points that can be concluded from this research.

7.1 Conclusions

The primary objective of this research was to improve the design of hydraulic fracture and proppant transport operation using our developed multi-module simulator. The main tasks achieved can be broken down as follows:

1. A proppant transport simulator was developed using appropriate mathematical solution techniques. Most popular mathematical solution approaches were tested to see the capability of them in capturing proppant front and distribution.
2. A hydraulic fracture model following smeared approach was developed that couples a reservoir simulator and a commercial geomechanics simulator and captures the initiation and propagation of a 2D planar fracture. The model was verified and validated earlier in our research group.
3. We developed the first linkage between a proppant transport simulator and a fully numerical hydraulic fracture model in a partially decoupled manner. It is assumed that the fluid is Newtonian and incompressible and the system is isothermal. Several examples were shown that illustrate the power and usefulness of the model.

We performed sensitivity analysis for both slots and actual propagating hydraulic fractures and provided design recommendations for different type of proppants and injection fluids., in lieu of a costly field trial and error approach. Through the analysis, we identified the fluid and proppant properties that are crucial in the design of the operation.

The following conclusions are made based on the results presented in this dissertation:

- The modular coupling removes the necessity of having very fine grids due to the fracture existence. In other words, only the fracture itself needs to have fine grids.
- The challenging task of finding numerical solution to first-order hyperbolic transport PDE is twofold: the traditional FD methods are either inaccurate or oscillatory. Flux or slope limiters resolve both issues but are first-order accurate near the shocks. More recent ENO or WENO methods additionally provide high order accuracy everywhere in the model.
- The main disadvantage of flux limiters and ENO or WENO schemes is their complexity in multi-dimensions. Notably, using Godunov splitting approach, this complexity is eliminated and the schemes can be coded conveniently.
- Inertia, fracture walls and presence of other particles have an effect on the settling velocity of the particles. There exists extensive data on relation between Galileo number (coming from physical properties of fluid and proppant) and Reynolds number from which settling velocity can be obtained in all flow regimes. Fracture walls significantly reduce settling velocity of particles due to extra drag force they exert on particles. Proppant concentration has a similar effect to walls. However, after concentration reaches a certain level, the packed fracture behaves like a porous medium.
- Advanced numerical techniques and state of the art in solid transport experiments were combined to develop an efficient numerical tool. Effects of injection rate, proppant density and diameter and injection fluid viscosity was investigated. Viscosity of injection fluid shows a strong impact on the concentration distribution (by changing settlement and convection) and shape of the fracture. Increased flow rate causes the fracture to fill up faster and reduces both convection and settlements. Proppant density and diameter have a moderate effect on settlement only.
- The Buoyancy number proves to be an important factor in determining the shape of concentration plume. Very different design parameters, if provide similar Buoyancy number, are expected to result in similar distribution of proppants.

- The existence of the proppants changes the mobility of the fluid since the viscosity of carrying fluid is enhanced. Comparing to the case without proppants, an increase in the net pressure and consequently fracture width is obtained. The higher the concentration, the higher the slurry viscosity, net pressure and fracture width. The length of the fracture, on the other hand, shortens due to the higher pressure losses inside the fracture.

The major original contribution, of our research is the development of a model that incorporates numerical fracture simulation and a proppant transport model. The important feature of the model includes the following:

1. Numerical modeling of the hydraulic fracture
2. Capturing plastic deformations in the reservoir and updating the porosity and permeability in the flow model in relation to the deformations
3. Modeling of proppant injection, by several important phenomena such as Stokes velocity corrections for inertia, wall and concentration effects, retardation factor, and fracture closure, etc. While each of these phenomena had been investigated separately, they had not been collectively incorporated in a proppant transport model.
4. Applying an accurate form of finite volume method that has been proposed specifically for hyperbolic (transport) partial differential equations. Further, we utilized different techniques to reduce the expected long run-time of the model. Local mesh refinement, dimensional splitting and sparse method of solving matrix equations were employed to optimize the running time of the model.

The closest numerical model to our model consists of an analytical hydraulic fracture model from PKN, KGD, P3D or PL3D models combined with a proppant transport model which did not include several important phenomena in proppant transport. Further, these models neglect plastic deformations of the medium, and neglect the effect of sand deformation on its porosity and permeability.

We did not apply the model to or validate the model against a real field case due to the lack of data. However, we verified the model in different ways against analytical models, published simulations, and commercial software and did a sensitivity analysis using a synthetic model to

investigate the sensitivity of the results to multiple parameters such as flow rate, fracturing fluid rheology and proppant properties on proppant transport.

7.2 Recommendations for future work

The technique of modular coupling that we utilized in our numerical simulation is very well accepted in the literature. Consequently, the limitation of the modeling will remain mainly in the limitations of the physics of each module. Progress towards models that include all the important physics will require a large research effort. However, the idea of modular coupling appears promising for the inclusion of these physics and resolving current limitations.

The following issues seem to make the presented model more effective for practical analysis and design use:

- Probably the main limitation of our model lies in the fact that it is restricted to planar (vertical or horizontal) fractures. The ultimate approach is the development of an arbitrary 3D fracture model under dynamic in-situ conditions in the reservoir. Obviously, a more realistic model should numerically simulate fracture height extension. Another important extension of the model can be development of the ability to simulate more than one fracture in the reservoir.
- Our proppant module is using FVM to simulate transport of the proppant. Although in this research we only dealt with planar fractures, FVM is capable of simulating transport in rotating fractures as well.
- Majority of the fracturing fluids are non-Newtonian. As mentioned in Chapter 2, the most important parameter describing proppant movement in fracture is its settling velocity, which is a function of the rheological behaviour of the fluid. Non-Newtonian fluids present a series of characteristics including plasticity, yield stress and time-dependent behavior. In contrast to the extensive literature on settling in Newtonian media, much less work has been carried out on the free settling in non-Newtonian fluids. In non-Newtonian fluids, settling velocity change due to inertia, wall effect and proppant concentration follow complex correlations. The viscosity evolution of slurry will also be more complex. On the numerical aspect, the following form of cubic law applies to non-Newtonian fluids:

$$q_x = -\frac{n}{2n+1} K^{\frac{1}{n}} \frac{w^{\frac{2n+1}{n}}}{2^{\frac{n+1}{n}}} \left[\left(\frac{dp}{dx}\right)^2 + \left(\frac{dp}{dy}\right)^2\right]^{\frac{1-n}{2n}} \frac{dp}{dx} \tag{7.1}$$

Such a complex relation between pressure and flow rate make the system of equations non-linear and accordingly the running time of the simulation will become much longer.

- We assumed that proppant particles are perfectly spherical and are of uniform size. Settling velocity of non-spherical particles has not been the focus of majority of experimental works. There are some experiments on settling of cylinders, cubes spheroids or discs in the literature. However, naturally occurring sands are different from other non-spherical particles such as discs, cubes, spheroids, and cylinders, because of their highly irregular shapes and sizes. The drag force acting on the particles during settling highly depends on the shape of the particles. Surface irregularities lead to increased drag force and thus reducing the settling velocity compared to that of spherical particles.

On the other hand, although proppants are made to have a narrow grain size distribution, they are not perfectly of the same size. Clearly, different sizes of the proppants particles make the settling phenomena even more complex as each particle exhibits different settling velocity. The experiments in the literature are very limited and mostly consider settling of binary mixtures.

Bibliography

Abraham, F. F. (1970). Functional dependence of drag coefficient of a sphere on Reynolds number. Physics of Fluids,13(8), 2194. doi:10.1063/1.1693218

Achenbach, E. (1974). The effects of surface roughness and tunnel blockage on the flow past spheres. Journal of Fluid Mechanics,65(01), 113. doi:10.1017/s0022112074001285

Adachi, J., Siebrits, E., Peirce, A., & Desroches, J. (2007). Computer simulation of hydraulic fractures. International Journal of Rock Mechanics and Mining Sciences,44(5), 739-757. doi: 10.1016/j.ijrmms.2006.11.006

Al-Quraishi, A., & Christiansen, R. (1999). Dimensionless groups for interpreting proppant transport in hydraulic fractures. Proceedings of Middle East Oil Show and Conference. doi:10.2523/53262-ms

Al-Salim, Q., & Geldart, D. (1969). A new method for the calculation of large numbers of terminal velocities. Powder Technology,3(1), 251-253. doi:10.1016/0032-5910(69)80085-9

Allen, H. S. (1900). L. The motion of a sphere in a viscous fluid. The London, Edinburgh, and Dublin Philosophical Magazine and Journal of Science, 50(306), 519-534.

Almedeij, J. (2008). Drag coefficient of flow around a sphere: Matching asymptotically the wide trend. Powder Technology,186(3), 218-223. doi: 10.1016/j.powtec.2007.12.006

Arsenijević, Z., Grbavčić, Ž, Garić-Grulović, R., & Bošković-Vragolović, N. (2010). Wall effects on the velocities of a single sphere settling in a stagnant and counter-current fluid and rising in a co-current fluid. Powder Technology, 203(2), 237-242. doi: 10.1016/ j.powtec.2010.05.013

Ataíde, C. H., Pereira, F. A., & Barrozo, M. A. (1999). Wall effects on the terminal velocity of spherical particles in Newtonian and non-Newtonian fluids. Brazilian Journal of Chemical Engineering,16(4), 387-394. doi:10.1590/s0104-66321999000400007

Aziz, K., & Settari, A. (1979). Petroleum reservoir simulation. Chapman & Hall.

Babcock, R. E., Prokop, C. L., & Kehle, R. O. (1967, January). Distribution of propping agent in vertical fractures. In Drilling and Production Practice. American Petroleum Institute.

Baker, F. (1913). CLXXX.—The viscosity of cellulose nitrate solutions. Journal of the Chemical Society, Transactions, 103, 1653-1675. doi:10.1039/ct9130301653

Balaramakrishna, P. V., & Chhabra, R. P. (1992). Sedimentation of a sphere along the axis of a long square duet filled with non-newtonian liquids. The Canadian Journal of Chemical Engineering,70(4), 803-807. doi:10.1002/cjce.5450700427

Bale, A., Owren, K., & Smith, M. B. (1994). Propped fracturing as a tool for sand control and reservoir management. SPE Production & Facilities,9(01), 19-28. doi:10.2118/24992-pa

Ballesteros, R., Riba, J., & Couderc, J. (1982). Dissolution of non spherical particles in solid-liquid fluidization. Chemical Engineering Science,37(11), 1639-1644. doi:10.1016/0009-2509(82)80034-1

Barker, B. J., & Ramey, H. J. (1978). Transient flow to finite conductivity vertical fractures. SPE Annual Fall Technical Conference and Exhibition. doi:10.2118/7489-ms

Barnea, E., & Mednick, R. (1978). A generalized approach to the fluid dynamics of particulate systems part III: general correlation for the pressure drop through fixed beds of spherical particles. The Chemical Engineering Journal,15(3), 215-227. doi:10.1016/0300-9467(78)80006-9

Barnea, E., & Mizrahi, J. (1973). A generalized approach to the fluid dynamics of particulate systems. The Chemical Engineering Journal,5(2), 171-189. doi:10.1016/0300-9467(73)80008-5

Barree, R., & Conway, M. (1994). Experimental and numerical modeling of convective proppant transport. SPE Annual Technical Conference and Exhibition. doi:10.2118/28564-ms

Barree, R., & Conway, M. (1995). Experimental and numerical modeling of convective proppant transport (includes associated papers 31036 and 31068). Journal of Petroleum Technology,47(03), 216-222. doi:10.2118/28564-pa

Batchelor, G. K. (1972). Sedimentation in a dilute dispersion of spheres. Journal of Fluid Mechanics,52(02), 245. doi:10.1017/s0022112072001399

Batchelor, G. K. (1977). The effect of Brownian motion on the bulk stress in a suspension of spherical particles. Journal of Fluid Mechanics,83(01), 97. doi:10.1017/s0022112077001062

Beam, R. M., & Warming, R. (1978). An implicit factored scheme for the compressible Navier-Stokes equations. AIAA journal, 16(4), 393-402.

Behr, A., Mtchedlishvili, G., Friedel, T., & Haefner, F. K. (2006). Consideration of damaged zone in a tight gas reservoir model with a hydraulically fractured well. SPE Production & Operations,21(02), 206-211. doi:10.2118/82298-pa

Bird, R., Stewart, W., and Lightfoot, E. (1976). Transport phenomena. John Wiley and sons.

Blot, M., & Medlin, W. (1985). Theory of Sand Transport in Thin Fluids. SPE Annual Technical Conference and Exhibition. doi:10.2118/14468-ms

Bolster, D., Hershberger, R. E., & Donnelly, R. J. (2011). Dynamic similarity, the dimensionless science. Physics Today,64(9), 42-47. doi:10.1063/pt.3.1258

Boris, J. P., & Book, D. L. (1973). Flux-corrected transport. I. SHASTA, a fluid transport algorithm that works. Journal of Computational Physics,11(1), 38-69. doi:10.1016/0021-9991(73)90147-2

Bowen, W., & Sharif, A. O. (1994). Transport through Microfiltration Membranes—Particle Hydrodynamics and Flux Reduction. Journal of Colloid and Interface Science,168(2), 414-421. doi:10.1006/jcis.1994.1437

Brady, J. F. (1993). The rheological behavior of concentrated colloidal dispersions. The Journal of Chemical Physics,99(1), 567-581. doi:10.1063/1.465782

Brannon, H., Wood, W., & Wheeler, R. (2005). The quest for improved proppant placement: investigation of the effects of proppant slurry component properties on transport. Proceedings of SPE Annual Technical Conference and Exhibition. doi:10.2523/95675-ms

Brannon, H. D., Wood, W. D., & Wheeler, R. S. (2006, January). Large scale laboratory investigation of the effects of proppant and fracturing fluid properties on transport. In SPE International Symposium and Exhibition on Formation Damage Control. Society of Petroleum Engineers.

Brannon, H. D., Kendrick, D. E., Luckey, E., & Stipetich, A. (2009). Multistage fracturing of horizontal shale gas wells using >90% foam provides improved production. SPE Eastern Regional Meeting. doi:10.2118/124767-ms

Brauer, H., & Mewes, D. (1972). Strömungswiderstand sowie stationärer und instationärer Stoff- und Wärmeübergang an Kugeln. Chemie Ingenieur Technik, 44(13), 865-868.

Brinkman, H. (1947). A calculation of the viscosity and the sedimentation constant for solutions of large chain molecules taking into account the hampered flow of the solvent through these molecules. Physica,13(8), 447-448. doi:10.1016/0031-8914(47)90030-x

Brouwers, H. J. (2010). Viscosity of a concentrated suspension of rigid mono-sized particles. Physical Review E,81(5). doi:10.1103/physreve.81.051402

Brouwers, H. J. (2011). Packing fraction of geometric random packings of discretely sized particles. Physical Review E,84(4). doi:10.1103/physreve.84.042301

Brown, P. P., & Lawler, D. F. (2003). Sphere drag and settling velocity revisited. Journal of Environmental Engineering,129(3), 222-231. doi: 10.1061/(asce)0733-9372(2003)129:3(222)

Burstein, S. Z., & Mirin, A. A. (1970). Third order difference methods for hyperbolic equations. Journal of Computational Physics,5(3), 547-571. doi:10.1016/0021-9991(70)90080-x

Cai, W., & Shu, C. (1993). Uniform high-order spectral methods for one- and two-dimensional euler equations. Journal of Computational Physics,104(2), 427-443. doi:10.1006/jcph.1993.1041

Carman, P. C. (1939). Permeability of saturated sands, soils and clays. The Journal of Agricultural Science, 29(02), 262-273.

Ceylan, K., Altunbaş, A., & Kelbaliyev, G. (2001). A new model for estimation of drag force in the flow of Newtonian fluids around rigid or deformable particles. Powder Technology, 119(2), 250-256.

Chandrupatla, T., & Belegundu, A. Introduction to finite elements in engineering. 1991.

Charles, W., Bob, B., Mike, E., & Tom, L. (2004). Improved horizontal well stimulations in the Bakken formation, Williston Basin, Montana. Proceedings of SPE Annual Technical Conference and Exhibition. doi:10.2523/90697-ms

Chen, C. (2006). High order shock capturing schemes for hyperbolic conservation laws and the application in open channel flows. Kentucky: University of Kentucky. Ph.D. Dissertation

Cheng, N. (2009). Comparison of formulas for drag coefficient and settling velocity of spherical particles. Powder Technology,189(3), 395-398. doi: 10.1016/j.powtec.2008.07.006

Chester, W., Breach, D. R., & Proudman, I. (1969). On the flow past a sphere at low Reynolds number. Journal of Fluid Mechanics,37(04), 751-760. doi:10.1017/s0022112069000851

Chhabra, R., Uhlherr, P., & Boger, D. (1980). The influence of fluid elasticity on the drag coefficient for creeping flow around a sphere. Journal of Non-Newtonian Fluid Mechanics,6(3-4), 187-199. doi:10.1016/0377-0257(80)80002-4

Chhabra, R. P., Unnikrishnan, A., & Nair, V. R. (1992). Hindered settling in non-newtonian power law liquids. The Canadian Journal of Chemical Engineering, 70(4), 716-720.

Chhabra, R., & Kee, D. D. (1993). Transport processes in bubbles, drops and particles. Drying Technology,11(1), 263-264. doi:10.1080/07373939308916817

Chhabra, R. (1995). Wall effects on free-settling velocity of non-spherical particles in viscous media in cylindrical tubes. Powder Technology,85(1), 83-90. doi:10.1016/0032-5910(95)03012-x

Chhabra, R., Uhlherr, P., & Richardson, J. (1996). Some further observations on the hindered settling velocity of spheres in the inertial flow regime. Chemical Engineering Science,51(19), 4531-4532. doi:10.1016/0009-2509(96)00285-0

Chhabra, R., Agarwal, S., & Chaudhary, K. (2003). A note on wall effect on the terminal falling velocity of a sphere in quiescent Newtonian media in cylindrical tubes. Powder Technology,129(1-3), 53-58. doi:10.1016/s0032-5910(02)00164-x

Chin, L., Raghavan, R., & Thomas, L. (1998). Fully-coupled geomechanics and fluid-flow analysis of wells with stress-dependent permeability. Proceedings of SPE International Oil and Gas Conference and Exhibition in China. doi:10.2523/48857-ms

Chin, L., & Thomas, L. (1999). Fully coupled analysis of improved oil recovery by reservoir compaction. SPE Annual Technical Conference and Exhibition. doi:10.2118/56753-ms

Chong, J. S., Christiansen, E. B., & Baer, A. D. (1971). Rheology of concentrated suspensions. Journal of applied polymer science, 15(8), 2007-2021.

Christofi, S. (1995). The study of building blocks for ENO schemes (Doctoral dissertation, Ph. D. thesis, Division of Applied Mathematics, Brown University).

Cinco, L., Samaniego, V., & Dominguez, A. (1978). Transient pressure behavior for a well with a finite-conductivity vertical fracture. Society of Petroleum Engineers Journal, 18(04), 253-264.

Cipolla, C. (2009). Modeling production and evaluating fracture performance in unconventional gas reservoirs. Journal of Petroleum Technology,61(9). doi:10.2118/118536-ms

Clark, P. E., Harkin, M. W., Wahl, H. A., & Sievert, J. A. (1977, January). Design of a large vertical prop transport model. SPE Annual Fall Technical Conference and Exhibition. Society of Petroleum Engineers.

Clark, P., & Quadir, J. (1981). Prop transport in hydraulic fractures: a critical review of particle settling velocity equations. Proceedings of SPE/DOE Low Permeability Gas Reservoirs Symposium. doi:10.2523/9866-ms

Clark, P. E., & Zhu, Q. (1996). Convective transport of propping agents during hydraulic fracturing. SPE Eastern Regional Meeting. doi:10.2118/37358-ms

Cleary, M., & Amaury, F. (1992). Proppant convection and encapsulation in hydraulic fracturing: practical implications of computer and laboratory simulations. Proceedings of SPE Annual Technical Conference and Exhibition. doi:10.2523/24825-ms

Cleary, M. P., & Fonseca Jr, A. (1992, January). Proppant convection and encapsulation in hydraulic fracturing: practical implications of computer and laboratory simulations. SPE Annual Technical Conference and Exhibition. Society of Petroleum Engineers.

Clift, R. (1978). Bubbles. Drops and Particles.

Clifton, R., & Wang, J. (1988). Multiple Fluids, Proppant transport, and thermal effects in three-dimensional simulation of hydraulic fracturing. Proceedings of SPE Annual Technical Conference and Exhibition. doi:10.2523/18198-ms

Colella, P. (1985). A direct Eulerian MUSCL scheme for gas dynamics. SIAM Journal on Scientific and Statistical Computing,6(1), 104-117. doi:10.1137/0906009

Concha, F., & Almendra, E. (1979). Settling velocities of particulate systems, 1. Settling velocities of individual spherical particles. International Journal of Mineral Processing,5(4), 349-367. doi:10.1016/0301-7516(79)90044-9

Concha, F., & Almendra, E. (1979). Settling velocities of particulate systems, 2. Settling velocities of suspensions of spherical particles. International Journal of Mineral Processing,6(1), 31-41. doi:10.1016/0301-7516(79)90030-9

Concha, F., & Barrientos, A. (1982). Settling velocities of particulate systems, 3. Power series expansion for the drag coefficient of a sphere and prediction of the settling velocity. International Journal of Mineral Processing,9(2), 167-172. doi:10.1016/0301-7516(82)90025-4

Coussy, O. (1995). Mechanics of porous continua. Chichester: Wiley.

Coutanceau, M. (1972). Sur l'étude éperimentale de l'écoulement engendré par une sphère qui se déplace dans l'axe d'un cylindre au-delà du régime de Stokes. CR Acad. Sci. A, 274, 853-856.

Crafton, J. W. (2008). Modeling flowback behavior or flowback equals "slowback". SPE Shale Gas Production Conference. doi:10.2118/119894-ms

Dabak, T., & Yucel, O. (1986). Shear viscosity behavior of highly concentrated suspensions at low and high shear-rates. Rheologica Acta,25(5), 527-533. doi:10.1007/bf01774404

Dalla Valle, J. M. (1948). Micromeritics, Pitman. London, UK.

Daneshy, A. (1978). Numerical solution of sand transport in hydraulic fracturing. Journal of Petroleum Technology,30(01), 132-140. doi:10.2118/5636-pa

Davis, S. F. (1992). An interface tracking method for hyperbolic systems of conservation laws. Applied Numerical Mathematics,10(6), 447-472. doi:10.1016/s0168-9274(06)80001-2

Dowdle, W. L., & Hyde, P. V. (1977). Well test analysis of hydraulically fractured gas wells. SPE Deep Drilling and Production Symposium. doi:10.2118/6437-ms

Du, C. M., & Li, J. (2011). Generalization of dual porosity system representation and reservoir simulation of hydraulic fracturing stimulated shale gas reservoirs. SPE Asia Pacific Oil and Gas Conference and Exhibition. doi:10.2118/145752-ms

Duduković, A. P., & Končar-Djurdjević, S. K. (1981). The effect of tube walls on drag coefficients of coaxially placed objects. AIChE Journal,27(5), 837-840. doi:10.1002/aic.690270519

Dullien, F. (1975). Single phase flow through porous media and pore structure. The Chemical Engineering Journal,10(1), 1-34. doi:10.1016/0300-9467(75)88013-0

Dyke, M. V. (1970). Extension of Goldsteins series for the Oseen drag of a sphere. Journal of Fluid Mechanics,44(02), 365. doi:10.1017/s0022112070001878

Economides, M. J., & Nolte, K. G. (2000). Reservoir stimulation. Chichester, England: Wiley.

Ehrl, E., & Schueler, S. (2000). Simulation of a Tight Gas Reservoir with Horizontal Multifractured Wells. SPE European Petroleum Conference. doi:10.2118/65108-ms

Eilers, H. (1941). The viscosity of the emulsion of highly viscous substances as function of concentration. Kolloid-Zeitschrift, 97(3), 313-321.

Einstein, A. (1906). A new determination of molecular dimensions. Ann. Phys, 19(2), 289-306.

El-Kaissy, M. M., & Homsy, G. M. (1973). A theoretical study of pressure drop and transport in packed beds at intermediate Reynolds numbers. Industrial & Engineering Chemistry Fundamentals,12(1), 82-90. doi:10.1021/i160045a014

Ellis, R. (1998). An overview of frac packs: a technical revolution (evolution) process. Journal of Petroleum Technology,50(1). doi:10.2118/39232-ms

Eskin, D., & Miller, M. J. (2008). A model of non-Newtonian slurry flow in a fracture. Powder Technology,182(2), 313-322. doi: 10.1016/j.powtec.2007.06.027

Eskin, D. (2009). Modeling non-Newtonian slurry convection in a vertical fracture. Chemical Engineering Science,64(7), 1591-1599. doi: 10.1016/j.ces.2008.12.019

Fair, G. M., Geyer, J. C., & Morris, J. C. (1954). Water supply and waste water disposal. In Water supply and waste water disposal. John Wiley.

Faisal, A., Dominic, A., Raj, B., & Issaka, M. (2004). Pressure transient analysis of horizontal wells in a fractured reservoir; gridding between art and science. Proceedings of SPE Asia Pacific Conference on Integrated Modelling for Asset Management. doi:10.2523/87013-ms

Farr, R. S., & Groot, R. D. (2009). Close packing density of polydisperse hard spheres. The Journal of Chemical Physics,131(24), 244104. doi:10.1063/1.3276799

Fatemi, E., Jerome, J., & Osher, S. (1991). Solution of the hydrodynamic device model using high-order nonoscillatory shock capturing algorithms. IEEE Transactions on Computer-Aided Design of Integrated Circuits and Systems,10(2), 232-244. doi:10.1109/43.68410

Faxén, H. (1923). Die Bewegung einer starren Kugel längs der Achse eines mit zäher Flüssigkeit gefüllten Rohres.

Felice, R. D. (1995). Hydrodynamics of liquid fluidisation. Chemical Engineering Science,50(8), 1213-1245. doi:10.1016/0009-2509(95)98838-6

Felice, R. D. (1996). A relationship for the wall effect on the settling velocity of a sphere at any flow regime. International Journal of Multiphase Flow,22(3), 527-533. doi:10.1016/0301-9322(96)00004-3

Fennema, R. J., & Chaudhry, M. H. (1987). Simulation of one-dimensional dam-break flows. Journal of Hydraulic Research,25(1), 41-51. doi:10.1080/00221688709499287

Fennema, R. J., & Chaudhry, M. H. (1990). Explicit methods for 2-D transient free surface flows. Journal of Hydraulic Engineering, 116(8), 1013-1034.

Fidleris, V., & Whitmore, R. L. (1961). Experimental determination of the wall effect for spheres falling axially in cylindrical vessels. British Journal of Applied Physics,12(9), 490-494. doi:10.1088/0508-3443/12/9/311

Finol, A., & Ali, S. F. (1975). Numerical simulation of oil production with simultaneous ground subsidence. Society of Petroleum Engineers Journal,15(05), 411-424. doi:10.2118/4847-pa

Fisher, M., Heinze, J., Harris, C., Davidson, B., Wright, C., & Dunn, K. (2004). Optimizing horizontal completion techniques in the barnett shale using microseismic fracture mapping. SPE Annual Technical Conference and Exhibition. doi:10.2118/90051-ms

Flemmer, R., & Banks, C. (1986). On the drag coefficient of a sphere. Powder Technology,48(3), 217-221. doi:10.1016/0032-5910(86)80044-4

Foscolo, P., Gibilaro, L., & Waldram, S. (1983). A unified model for particulate expansion of fluidised beds and flow in fixed porous media. Chemical Engineering Science,38(8), 1251-1260. doi:10.1016/0009-2509(83)80045-1

Fouda, A., & Capes, C. (1976). Calculation of large numbers of terminal velocities or equivalent particle diameters using polynomial equations fitted to the Heywood tables. Powder Technology,13(2), 291-293. doi:10.1016/0032-5910(76)85016-4

Francis, A. W. (1933). Wall effect in falling ball method for viscosity. Physics,4(11), 403-406. doi:10.1063/1.1745151

Frankel, N., & Acrivos, A. (1967). On the viscosity of a concentrated suspension of solid spheres. Chemical Engineering Science,22(6), 847-853. doi:10.1016/0009-2509(67)80149-0

Friehauf, K. E., & Sharma, M. M. (2008). A new compositional model for hydraulic fracturing with energized fluids. SPE Annual Technical Conference and Exhibition. doi:10.2118/115750-ms

Friehauf, K. (2009). Simulation and design of energized hydraulic fractures. University of Texas at Austin, Ph.D. Thesis.

Friehauf, K. E., Sharma, M. M., & Sullivan, R. B. (2009). Application of a new compositional model for hydraulic fracturing with energized fluids: a south Texas case study. SPE Hydraulic Fracturing Technology Conference. doi:10.2118/119265-ms

Gadde, P. B., Liu, Y., Norman, J., Bonnecaze, R., & Sharma, M. M. (2004). Modeling proppant settling in water-fracs. SPE Annual Technical Conference and Exhibition. doi:10.2118/89875-ms

Ganguly, U. P. (1980). Direct method for the prediction of expanded bed height in liquid-solid fluidization. The Canadian Journal of Chemical Engineering,58(5), 559-563. doi:10.1002/cjce.5450580502

Garon, A., Lin, C., & Dunayevsky, V. (1988). Simulation of thermally induced waterflood fracturing in prudhoe bay. Proceedings of SPE California Regional Meeting. doi:10.2523/17417-ms

Garside, J., & Al-Dibouni, M. R. (1977). Velocity-voidage relationships for fluidization and sedimentation in solid-liquid systems. Industrial & Engineering Chemistry Process Design and Development,16(2), 206-214. doi:10.1021/i260062a008

Geertsma, J., & Klerk, F. D. (1969). A rapid method of predicting width and extent of hydraulically induced fractures. Journal of Petroleum Technology,21(12), 1571-1581. doi:10.2118/2458-pa

Gelperin, N. I., Ainshtein, V. G., & Toskubaev, I. N. (1972). Heat exchange between finned tubes and a fluidized bed of granular material. Chemistry and Technology of Fuels and Oils,8(9), 697-699. doi:10.1007/bf00717975

Ghalambor, A., Ali, S. A., & Norman, W. D. (2009). Frac packing handbook. SPE Textbook.

Gidaspow, D. (1994). Multiphase flow and fluidization: continuum and kinetic theory descriptions. Boston, Mass.: Boston, Mass.: Academic press; Harcourt.

Goldstein, S. (1929). The steady flow of viscous fluid past a fixed spherical obstacle at small Reynolds numbers. Proceedings of the Royal Society A: Mathematical, Physical and Engineering Sciences,123(791), 225-235. doi:10.1098/rspa.1929.0067

Govier, G. W., Aziz, K., & Schowalter, W. R. (1973). The flow of complex mixtures in pipes. Journal of Applied Mechanics,40(2), 404. doi:10.1115/1.3422996

Grieser, W. V., Shelley, R. F., & Soliman, M. Y. (2009). Predicting production outcome from multi-stage, horizontal Barnett completions. SPE Production and Operations Symposium. doi:10.2118/120271-ms

Gringarten, A. C., Ramey, H. J., & Raghavan, R. (1974). Unsteady-state pressure distributions created by a well with a single infinite-conductivity vertical fracture. Society of Petroleum Engineers Journal,14(04), 347-360. doi:10.2118/4051-pa

Guth, E., & Simha, R. (1936). Investigations of viscosity of suspensions and solutions: part 3. The viscosity of spherical suspensions.

Gutierrez, M., & Makurat, A. (1997). Coupled HTM modelling of cold water injection in fractured hydrocarbon reservoirs. International Journal of Rock Mechanics and Mining Sciences & Geomechanics Abstracts,34(3-4), 429-429. doi:10.1016/s0148-9062(97)00033-8

Haberman, W. L., & Sayre, R. M. (1958). David Taylor model basin report No. 1143. US Navy Department, Washington DC.

Hagoort, J., Weatherill, B. D., & Settari, A. (1980). Modeling the Propagation of Waterflood-Induced Hydraulic Fractures. Society of Petroleum Engineers Journal,20(04), 293-303. doi:10.2118/7412-pa

Haider, A., & Levenspiel, O. (1989). Drag coefficient and terminal velocity of spherical and nonspherical particles. Powder Technology,58(1), 63-70. doi:10.1016/0032-5910(89)80008-7

Hammond, P. (1995). Settling and slumping in a Newtonian slurry, and implications for proppant placement during hydraulic fracturing of gas wells. Chemical Engineering Science,50(20), 3247-3260. doi:10.1016/0009-2509(95)00152-u

Hannah, R., Park, E., Porter, D., & Black, J. (1994). Combination fracturing/gravel-packing completion technique on the Amberjack, Mississippi Canyon 109 field. SPE Production & Facilities,9(04), 262-266. doi:10.2118/26562-pa

Happel, J. (1957). Viscosity of suspensions of uniform spheres. Journal of Applied Physics,28(11), 1288-1292. doi:10.1063/1.1722635

Happel, J. (1958). Viscous flow in multiparticle systems: Slow motion of fluids relative to beds of spherical particles. AIChE Journal,4(2), 197-201. doi:10.1002/aic.690040214

Happel, J. (1965). H., Brenner. Low Reynolds number hydrodynamics, Prentice-Hall, Englewood Cliffs, NJ, 133.

Happel, J., & Brenner, H. (1973). Low Reynolds number hydrodynamics, Noordhoff Int. Publishing, Leyden, Netherland, 235.

Happel, J., & Bart, E. (1974). The settling of a sphere along the axis of a long square duct at low Reynolds number. Applied Scientific Research,29(1), 241-258. doi:10.1007/bf00384149

Harten, A., Engquist, B., Osher, S., & Chakravarthy, S. R. (1987). Uniformly high order accurate essentially non-oscillatory schemes, III. Upwind and High-Resolution Schemes,218-290. doi:10.1007/978-3-642-60543-7_12

Hatschek, E. (1913). The general theory of viscosity of two-phase systems. Transactions of the Faraday Society,9, 80. doi:10.1039/tf9130900080

Hawksley, P. G. W. (1951). The effect of concentration on the settling of suspensions and flow through porous media. Some aspects of fluid flow, 144.

Heffer, K., Koutsabeloulis, N., & Wong, S. (1994). Coupled geomechanical, thermal and fluid flow modelling as an aid to improving waterflood sweep efficiency. Rock Mechanics in Petroleum Engineering. doi:10.2118/28082-ms

Hesketh, R., Etchells, A., & Russell, T. (1991). Bubble breakage in pipeline flow. Chemical Engineering Science,46(1), 1-9. doi:10.1016/0009-2509(91)80110-k

Hess, K., & Philippoff, W. (1935). Über die Konzentrations-Abhängigkeit der Zähigkeit bei Cellulose-estern. Berichte der deutschen chemischen Gesellschaft (A and B Series), 68(4), 688-699.

Higdon, J. J., & Muldowney, G. P. (1995). Resistance functions for spherical particles, droplets and bubbles in cylindrical tubes. Journal of Fluid Mechanics,298(-1), 193. doi:10.1017/s0022112095003272

Hirata, A., & Bulos, F. B. (1990). Predicting bed voidage in solid-liquid fluidization. Journal Of Chemical Engineering Of Japan,23(5), 599-604. doi:10.1252/jcej.23.599

Hoek, V. D., Matsuura, T., M., D., & Gheissary, G. (1996). Simulation of produced water re-injection under fracturing conditions. Proceedings of European Petroleum Conference. doi:10.2523/36846-ms

Holditch, S. A. (1979). Factors affecting water blocking and gas flow from hydraulically fractured gas wells. Journal of Petroleum Technology,31(12), 1515-1524. doi:10.2118/7561-pa

Horri, B. A., Ranganathan, P., Selomulya, C., & Wang, H. (2011). A new empirical viscosity model for ceramic suspensions. Chemical Engineering Science,66(12), 2798-2806. doi: 10.1016/j.ces.2011.03.040

Howard, G. C., & Fast, C. (1970). Hydraulic fracturing. Dallas, Texas: Millet the Printer. Packed

Hunter, R. (1938). Fluid Mechanics for Hydraulic Engineers.

Hustedt, B., Qiu, Y., Zwarts, D., & Hoek, P. J. (2005). Modeling water-injection induced fractures in reservoir simulation. SPE Annual Technical Conference and Exhibition. doi:10.2118/95726-ms

Ihme, F., Schmidtt. H, & Brauer, H. (1972). Theoretical studies on mass transfer at and flow past spheres. Chemie Ingenieur Technik, 44(5), 306.

Ishii, M., & Zuber, N. (1979). Drag coefficient and relative velocity in bubbly, droplet or particulate flows. AIChE Journal,25(5), 843-855. doi:10.1002/aic.690250513

Iske, A., & Sonar, T. (1996). On the structure of function spaces in optimal recovery of point functionals for ENO-schemes by radial basis functions. Numerische Mathematik,74(2), 177-201. doi:10.1007/s002110050213

Iwaoka, M., & Ishii, T. (1979). Experimental wall correction factors of single solid spheres in circular cylinders. Journal of Chemical Engineering of Japan,12(3), 239-242. doi:10.1252/jcej.12.239

Jameson, A., Schmidt, W., & Turkel, E. (1981). Numerical solution of the Euler equations by finite volume methods using Runge Kutta time stepping schemes. 14th Fluid and Plasma Dynamics Conference. doi:10.2514/6.1981-1259

Jean, R., Tang, W., & Fan, L. (1989). The sedimentation-dispersion model for slurry bubble columns. AIChE Journal,35(4), 662-665. doi:10.1002/aic.690350418

Ji, L., Settari, A. T., Sullivan, R., & Orr, D. (2004). Methods for modeling dynamic fractures in coupled reservoir and geomechanics simulation. SPE Annual Technical Conference and Exhibition. doi:10.2118/90874-ms

Ji, L., Settari, A., & Sullivan, R. B. (2006). A new approach to hydraulic fracturing modeling - fully coupled with geomechanical and reservoir simulation. SPE Europec/EAGE Annual Conference and Exhibition. doi:10.2118/99428-ms

Ji, L. (2008). Modeling hydraulic fracturing fully coupled with reservoir and geomechanical simulation. ProQuest.

Jiang, G., & Shu, C. (1996). Efficient implementation of weighted eno schemes. Journal of Computational Physics,126(1), 202-228. doi:10.1006/jcph.1996.0130

Joseph, G. G., Zenit, R., Hunt, M. L., & Rosenwinkel, A. M. (2001). Particle–wall collisions in a viscous fluid. Journal of Fluid Mechanics,433, 329-346. doi:10.1017/s0022112001003470

Jottrand, R. (1952). An experimental study of the mechanism of fluidization. J. Appl. Chem, 2, S17-S26.

Kansal, A. R., Torquato, S., & Stillinger, F. H. (2002). Computer generation of dense polydisperse sphere packings. The Journal of Chemical Physics,117(18), 8212-8218. doi:10.1063/1.1511510

Kehlenbeck, R., & Felice, R. D. (1999). Empirical relationships for the terminal settling velocity of spheres in cylindrical columns. Chemical Engineering & Technology,22(4), 303-308. doi:10.1002/(sici)1521-4125(199904)22:4<303:aid-ceat303>3.0.co;2-8

Kern, L. R., Perkins, T. K., & Wyant, R. E. (1959). The mechanics of sand movement in fracturing. Journal of Petroleum Technology, 11(07), 55-57.

Khan, A., & Richardson, J. (1987). The resistance to motion of a solid sphere in a fluid. Chemical Engineering Communications,62(1), 135-150. doi:10.1080/00986448708912056

Khan, A., & Richardson, J. (1990). Pressure gradient and friction factor for sedimentation and fluidisation of uniform spheres in liquids. Chemical Engineering Science,45(1), 255-265. doi:10.1016/0009-2509(90)87097-c

Kmieć, A. (1976). Some remarks on the Richardson-Zaki equation. The Chemical Engineering Journal,11(3), 237-238. doi:10.1016/0300-9467(76)80046-9

Konoplyov, V., & Zazovsky, A. (1991). Numerical simulation of oil displacement in pattern floods with fractured wells. SPE Annual Technical Conference and Exhibition. doi:10.2118/22933-ms

Koos, E. (2009). Rheological measurements in liquid-solid flows (Doctoral dissertation, California Institute of Technology).

Krieger, I. M., & Dougherty, T. J. (1959). A mechanism for non-Newtonian flow in suspensions of rigid spheres. Transactions of the Society of Rheology,3(1), 137-152. doi:10.1122/1.548848

Krigbaum, W. R., & Flory, P. J. (1953). Molecular weight dependence of the intrinsic viscosity of polymer solutions. II. Journal of Polymer Science,11(1), 37-51. doi:10.1002/pol.1953.120110103

Kunitz, M. (1926). An empirical formula for the relation between viscosity of solution and volume of solute. The Journal of General Physiology,9(6), 715-725. doi:10.1085/jgp.9.6.715

Kurten, B. (1966). Pleistocene bears of North America.

Ladenburg, R. (1907). Über den einfluß von wänden auf die bewegung einer kugel in einer reibenden flüssigkeit. Annalen der Physik,328(8), 447-458. doi:10.1002/andp.19073280806

Lali, A., Khare, A., Joshi, J., & Nigam, K. (1989). Behaviour of solid particles in viscous non-newtonian solutions: Settling velocity, wall effects and bed expansion in solid-liquid fluidized beds. Powder Technology,57(1), 39-50. doi:10.1016/0032-5910(89)80102-0

Lapple, C. E., & Shepherd, C. B. (1940). Calculation of particle trajectories. Industrial & Engineering Chemistry,32(5), 605-617. doi:10.1021/ie50365a007

Lapple, C.E., 1951. Fluid and particle mechanics. University of Delaware Publ., Newark, Del., 284 pp.

Latto, B., Round, G. F., & Anzenavs, R. (1973). Drag coefficients and pressure drops for hydrodynamically suspended spheres in a vertical tube with and without polymer addition. The Canadian Journal of Chemical Engineering,51(5), 536-541. doi:10.1002/cjce.5450510502

Lavrov A. and Laux H. (2007) DEM modeling of particle restitution coefficient vs Stokes number: The role of lubrication force. In: Proceedings of the International Conference on Multiphase Flow (ICMF 2007), Leipzig, Germany, July 9-13, 2007, paper S2_Thu_C_54.

Lavrov, A. (2011). Models for proppant transport and deposition in hydraulic fracture simulation, A Review of the State of the Art. Trondheim, Norway: SINTEF Petroleum Research.

Lax, P. D. (1954). Weak solutions of nonlinear hyperbolic equations and their numerical computation. Communications on pure and applied mathematics, 7(1), 159-193.

Lax, P., & Wendroff, B. (1960). Systems of conservation laws. Communications on Pure and Applied mathematics, 13(2), 217-237.

Lebel, J. P. (2002). Dynamic fracture modelling approach for cold lake cyclic steam stimulation. SPE International Thermal Operations and Heavy Oil Symposium and International Horizontal Well Technology Conference. doi:10.2118/79010-ms

Leclair, B. P., & Hamielec, A. E. (1968). Viscous flow through particle assemblages at intermediate reynolds numbers. Steady-State Solutions for Flow through Assemblages of Spheres. Industrial & Engineering Chemistry Fundamentals,7(4), 542-549. doi:10.1021/i160028a003

Leer, B. V. (1977). Towards the ultimate conservative difference scheme. IV. A new approach to numerical convection. Journal of Computational Physics,23(3), 276-299. doi:10.1016/0021-9991(77)90095-x

Leighton, D., & Acrivos, A. (1987). Measurement of shear-induced self-diffusion in concentrated suspensions of spheres. Journal of Fluid Mechanics,177(-1), 109. doi:10.1017/s0022112087000880

Letan, R. (1974). On vertical dispersed two-phase flow. Chemical Engineering Science,29(2), 621-624. doi:10.1016/0009-2509(74)80073-4

Leveque, R. J. (2004). Finite volume methods for hyperbolic problems. Cambridge: Cambridge University Press.

LeVeque, R. J. (2011). Finite volume methods for hyperbolic problems. Cambridge: Cambridge University Press.

Lewis, J. A., & Carrier, G. F. (1949). Some remarks on the flat plate boundary layer. Quarterly of Applied Mathematics,7(2), 228-234. doi:10.1090/qam/34160

Lewis, W. K., Gilliland, E. R., & Bauer, W. C. (1949). Characteristics of fluidized particles. Industrial & Engineering Chemistry, 41(6), 1104-1117.

Lewis, E. W., & Bowerman, E. W. (1952). Fluidization of solid particles in liquids. Chemical Engineering Progress, 48(12), 603-610.

Li, Y., Wang, S., Zhao, J., Jiyao, Z., Wang, X., & Gao, R. (2011). Numerical simulation research on proppant transport in hydraulic fracture. 2011 International Conference on Computational and Information Sciences. doi:10.1109/iccis.2011.189

Liao, S. (2002). An analytic approximation of the drag coefficient for the viscous flow past a sphere. International Journal of Non-Linear Mechanics,37(1), 1-18. doi:10.1016/s0020-7462(00)00092-5

Liu, X. D., Osher, S., & Chan, T. (1994). Weighted essentially non-oscillatory schemes. Journal of computational physics, 115(1), 200-212.

Liu, Y., & Sharma, M. (2005). Effect of fracture width and fluid rheology on proppant settling and retardation: an experimental study. SPE Annual Technical Conference and Exhibition. doi:10.2118/96208-ms

Liu, Y. (2006). Settling and hydrodynamic retardation of proppants in hydraulic fractures. University of Texas at Austin, Ph.D. Thesis.

Liu, Y., Gadde, P. B., & Sharma, M. M. (2006). Proppant placement using reverse-hybrid fracs. SPE Gas Technology Symposium. doi:10.2118/99580-ms

Liu, Y., Gadde, P. B., & Sharma, M. M. (2007). Proppant placement using reverse-hybrid fracs. SPE Production & Operations,22(03), 348-356. doi:10.2118/99580-pa

Loeffler, A. L., & Ruth, B. F. (1959). Particulate fluidization and sedimentation of spheres. AIChE Journal,5(3), 310-314. doi:10.1002/aic.690050312

Longuemare, P., Detienne, J., Lemonnier, P., Bouteca, M., & Onaisi, A. (2001). Numerical modeling of fracture propagation induced by water injection/re-injection. SPE European Formation Damage Conference. doi:10.2118/68974-ms

Lorenz, J. (1999). Stress-sensitive reservoirs. Journal of Petroleum Technology,51(1). doi:10.2118/50977-ms

Machač, I., & Lecjaks, Z. (1995). Wall effect for a sphere falling through a non-Newtonian fluid in a rectangular duct. Chemical Engineering Science,50(1), 143-148. doi:10.1016/0009-2509(94)00211-9

Madhav, G., & Chhabra, R. (1994). Settling velocities of non-spherical particles in non-Newtonian polymer solutions. Powder Technology,78(1), 77-83. doi:10.1016/0032-5910(93)02761-x

Maron, S., & Pierce, P. (1956). Application of ree-eyring generalized flow theory to suspensions of spherical particles. Journal of Colloid Science,11(1), 80-95. doi:10.1016/0021-9797(56)90012-1

McGauhey, P. H. (1956). Theory of sedimentation. Journal (American Water Works Association), 48(4), 437-448.

McNown, J. S., Lee, H. M., McPherson, M., & Engez, S. M. (1948). Influence of boundary proximity on the drag of spheres. In Proc. 7th Int. Congress Appl. Mech (Vol. 2, No. Part 1).

Mendoza, C. I., & Santamaría-Holek, I. (2009). The rheology of hard sphere suspensions at arbitrary volume fractions: An improved differential viscosity model. The Journal of Chemical Physics,130(4), 044904. doi:10.1063/1.3063120

Merle, H., Kentie, C., Opstal, G. V., & Schneider, G. (1976). The Bachaquero Study - A Composite Analysis of the Behavior of a Compaction Drive/Solution Gas Drive Reservoir. Journal of Petroleum Technology,28(09), 1107-1115. doi:10.2118/5529-pa

Mewis, J., & Wagner, N. J. (2011). Colloidal suspension rheology. Cambridge: Cambridge University Press.

Mikhailov, M., & Freire, A. S. (2013). The drag coefficient of a sphere: An approximation using Shanks transform. Powder Technology,237, 432-435. doi:10.1016/j.powtec.2012.12.033

Miranda, C. G., Soliman, M. Y., Settari, A., & Krampol, R. (2010). Linking reservoir simulators with fracture simulators. SPE Eastern Regional Meeting. doi:10.2118/137752-ms

Miyamura, A., Iwasaki, S., & Ishii, T. (1981). Experimental wall correction factors of single solid spheres in triangular and square cylinders, and parallel plates. International Journal of Multiphase Flow,7(1), 41-46. doi:10.1016/0301-9322(81)90013-6

Mobbs, A., & Hammond, P. (2001). Computer simulations of proppant transport in a hydraulic fracture. SPE Production & Facilities,16(02), 112-121. doi:10.2118/69212-pa

Mooney, M. (1951). The viscosity of a concentrated suspension of spherical particles. Journal of Colloid Science,6(2), 162-170. doi:10.1016/0095-8522(51)90036-0

Morrison, F. A. (2013). Data correlation for drag coefficient for sphere. Department of Chemical Engineering, Michigan Technological University, Houghton, MI.

Morsi, S. A., & Alexander, A. J. (1972). An investigation of particle trajectories in two-phase flow systems. Journal of Fluid Mechanics,55(02), 193. doi:10.1017/s0022112072001806

Munroe, H. S. (1889). The english versus the continental system of jigging: is close sizing advantageous?

Newton, I. 1687 Principia. Lib. II, Prop. XXXIX, Theor. XXXI.

Nghiem, L., Forsyth, P., & Behie, A. (1984). A fully implicit hydraulic fracture model. Journal of Petroleum Technology,36(07), 1191-1198. doi:10.2118/10506-pa

Nicodemo, L., & Nicolais, L. (1974). Viscosity of concentrated fiber suspensions. The Chemical Engineering Journal,8(2), 155-156. doi:10.1016/0300-9467(74)85018-5

Nolte, K. (1988). Fluid flow considerations in hydraulic fracturing. Proceedings of SPE Eastern Regional Meeting. doi:10.2523/18537-ms

Nordgren, R. (1972). Propagation of a vertical hydraulic fracture. Society of Petroleum Engineers Journal,12(04), 306-314. doi:10.2118/3009-pa

Nott, P. R., & Brady, J. F. (1994). Pressure-driven flow of suspensions: simulation and theory. Journal of Fluid Mechanics,275(-1), 157. doi:10.1017/s0022112094002326

Novotny, E. (1977). Proppant transport. Proceedings of SPE Annual Fall Technical Conference and Exhibition. doi:10.2523/6813-ms

Oliver, D. R., & Ward, S. G. (1953). Relationship between Relative Viscosity and Volume Concentration of Stable Suspensions of Spherical Particles. Nature,171(4348), 396-397. doi:10.1038/171396b0

Oliver, D. (1961). The sedimentation of suspensions of closely-sized spherical particles. Chemical Engineering Science,15(3-4), 230-242. doi:10.1016/0009-2509(61)85026-4

Oseen, C. W. (1910). Stokes' formula and a related theorem in hydrodynamics. Arkiv. Mat. Astron. Fysik, 6, 20.

Osher, S., & Shu, C. W. (1991). High-order essentially nonoscillatory schemes for Hamilton–Jacobi equations. SIAM Journal on numerical analysis, 28(4), 907-922.

Ouyang, S. (1994). Propagation of hydraulically induced fractures with proppant transport. University of Texas at Austin. Ph.D. Dissertation.

Paine, P., & Scherr, P. (1975). Drag coefficients for the movement of rigid spheres through liquid-filled cylindrical pores. Biophysical Journal,15(10), 1087-1091. doi:10.1016/s0006-3495(75)85884-x

Patwardhan, V. S., & Tien, C. (1985). Sedimentation and fluidization in solid-liquid systems: A simple approach. AIChE Journal,31(1), 146-149. doi:10.1002/aic.690310117

Patwardhan, V., & Tien, C. (1985). Sedimentation and liquid fluidization of solid particles of different sizes and densities. Chemical Engineering Science,40(7), 1051-1060. doi:10.1016/0009-2509(85)85062-4

Pearson, J. (1994). On suspension transport in a fracture: framework for a global model. Journal of Non-Newtonian Fluid Mechanics,54, 503-513. doi:10.1016/0377-0257(94)80039-1

Peter, V., & Economides, M. J. (2001). Hydraulic fracture mechanics. Chichester: John Wiley & Sons.

PetroWiki. (n.d.). Retrieved June 02, 2017, from http://petrowiki.org/PetroWiki

Phan, S., Russel, W. B., Zhu, J., & Chaikin, P. M. (1998). Effects of polydispersity on hard sphere crystals. The Journal of Chemical Physics,108(23), 9789-9795. doi:10.1063/1.476453

Pletcher, R. H., Tannehill, J. C., and Ander, D. (1997). Computational fluid mechanics and heat transfer. Washington, DC: Taylor and Francis.

Prandtl, L., & Tietjens, O. (1931). Hydro-und aeromechanik: nach vorlesungen von L. Prandtl. J. Springer.

Proudman, I., & Pearson, J. R. (1957). Expansions at small Reynolds numbers for the flow past a sphere and a circular cylinder. Journal of Fluid Mechanics,2(03), 237. doi:10.1017/s0022112057000105

Pruppacher, H. R., Clair, B. P., & Hamielec, A. E. (1970). Some relations between drag and flow pattern of viscous flow past a sphere and a cylinder at low and intermediate Reynolds numbers. Journal of Fluid Mechanics,44(04), 781. doi:10.1017/s0022112070002148

Quemada, D., & Berli, C. (2002). Energy of interaction in colloids and its implications in rheological modeling. Advances in Colloid and Interface Science,98(1), 51-85. doi:10.1016/s0001-8686(01)00093-8

Rajani, B. B. (1988). A simple model for describing variation of permeability with porosity for unconsolidated sands. In Situ;(United States), 12(3).

Ramamurthy, K., & Subbaraju, K. (1973). Bed expansion characteristics of annular liquid-fluidized beds. Industrial & Engineering Chemistry Process Design and Development,12(2), 184-189. doi:10.1021/i260046a010

Rattia, A. J., & Ali, S. F. (1981). Effect of formation compaction on steam injection response. SPE Annual Technical Conference and Exhibition. doi:10.2118/10323-ms

Riba, J. P., & Couderc, J. P. (1977). Expansion de couches fluidisées par des liquides. The Canadian Journal of Chemical Engineering,55(2), 118-121. doi:10.1002/cjce.5450550202

Ribeiro, L., & Sharma, M. M. (2012). A new three-dimensional, compositional, model for hydraulic fracturing with energized fluids. SPE Annual Technical Conference and Exhibition. doi:10.2118/159812-ms

Ribeiro, L. H. (2013). Development of a Three-Dimensional Compositional Hydraulic Fracturing Simulator for Energized Fluids. The University of Texas at Austin. Ph.D. Dissertation.

Richardson, J., & Zaki, W. (1954). The sedimentation of a suspension of uniform spheres under conditions of viscous flow. Chemical Engineering Science,3(2), 65-73. doi:10.1016/0009-2509(54)85015-9

Richardson, J., & Jerónimo, M. D. (1979). Velocity-voidage relations for sedimentation and fluidisation. Chemical Engineering Science,34(12), 1419-1422. doi:10.1016/0009-2509(79)85167-2

Rijn, L. C. (1984). Sediment transport, part II: suspended load transport. Journal of Hydraulic Engineering,110(11), 1613-1641. doi:10.1061/(asce)0733-9429(1984)110:11(1613)

Robinson, C. D. (1926). Some factors influencing sedimentation. Industrial & Engineering Chemistry,18(8), 869-871. doi:10.1021/ie50200a036

Roe, P. L. (1985). Some contributions to the modelling of discontinuous flows. In Large-scale computations in fluid mechanics (pp. 163-193).

Rogerson, A. M., & Meiburg, E. (1990). A numerical study of the convergence properties of ENO schemes. Journal of Scientific Computing,5(2), 151-167. doi:10.1007/bf01065582

Roodhart, L., Fokker, P., Davies, D., Jacob, S., & Wong, G. (1994). Frac-and-pack stimulation: application, design, and field experience. Journal of Petroleum Technology,46(03). doi:10.2118/26563-pa

Roscoe, R. (1952). The viscosity of suspensions of rigid spheres. British Journal of Applied Physics,3(8), 267-269. doi:10.1088/0508-3443/3/8/306

Rowe, P. (1987). A convenient empirical equation for estimation of the Richardson-Zaki exponent. Chemical Engineering Science,42(11), 2795-2796. doi:10.1016/0009-2509(87)87035-5

Rusanov, V. (1970). On difference schemes of third order accuracy for nonlinear hyperbolic systems. Journal of Computational Physics,5(3), 507-516. doi:10.1016/0021-9991(70)90077-x

Rutgers, I. R. (1962). Relative viscosity and concentration. Rheologica Acta,2(4), 305-348. doi:10.1007/bf01976051

Schiller, L. (1932). Fallversuche mit kugeln und scheiben. Handbuch der Experimentalphysik, 4, 339-398.

Schiller, L., & Naumann, A. (1933). Fundamental calculations in gravitational processing. Zeitschrift Des Vereines Deutscher Ingenieure, 77, 318-320.

Schlichting, H., & Kestin, J. (1979). Boundary- layer theory. New York: McGraw-Hill.

Schols, R. S., & Visser, W. (1974, January). Proppant bank buildup in a vertical fracture without fluid loss. In SPE European Spring Meeting. Society of Petroleum Engineers.

Settari, A. (1980). Simulation of hydraulic fracturing processes. Society of Petroleum Engineers Journal,20(06), 487-500. doi:10.2118/7693-pa

Settari, A. (1988). Quantitative analysis of factors influencing vertical and lateral fracture growth. SPE Production Engineering,3(03), 310-322. doi:10.2118/13862-pa

Settari, A., Kry, P., & Yee, C. (1989). Coupling of fluid flow and soil behaviour to model injection into uncemented oil sands. Journal of Canadian Petroleum Technology,28(01). doi:10.2118/89-01-08

Settari, A., Puchyr, P., & Bachman, R. (1990). Partially decoupled modeling of hydraulic fracturing processes. SPE Production Engineering,5(01), 37-44. doi:10.2118/16031-pa

Settari, A., & Mourits, F. M. (1994). Coupling of geomechanics and reservoir simulation models. Computer Methods and Advances in Geomechanics, 3, 2151-2158.

Settari, A., Bachman, R., Hovem, K., & Paulsen, S. (1996). Productivity of fractured gas condensate wells - a case study of the Smorbukk field. SPE Reservoir Engineering,11(04), 236-244. doi:10.2118/35604-pa

Settari, A., & Mourits, F. (1998). A coupled reservoir and geomechanical simulation system. SPE Journal,3(03), 219-226. doi:10.2118/50939-pa

Settari, A., Warren, G., Jacquemont, J., Bieniawski, P., & Dussaud, M. (1999). Brine disposal into a tight stress-sensitive formation at fracturing conditions: design and field experience. SPE Reservoir Evaluation & Engineering,2(02), 186-195. doi:10.2118/56001-pa

Settari, A., & Walters, D. (1999). Advances in coupled geomechanical and reservoir modeling with applications to reservoir compaction. Proceedings of SPE Reservoir Simulation Symposium. doi:10.2523/51927-ms

Settari, A., & Walters, D. A. (2001). Advances in coupled geomechanical and reservoir modeling with applications to reservoir compaction. SPE Journal,6(03), 334-342. doi:10.2118/74142-pa

Settari, A. (2002). Reservoir compaction. Journal of Petroleum Technology,54(8). doi:10.2118/76805-ms

Shah, S. (1993). Rheological characterization of hydraulic fracturing slurries. SPE Production & Facilities,8(02), 123-130. doi:10.2118/22839-pa

Shaoul, J. R., Behr, A., & Mtchedlishvili, G. (2007). Developing a tool for 3d reservoir simulation of hydraulically fractured wells. SPE Reservoir Evaluation & Engineering,10(01), 50-59. doi:10.2118/108321-pa

Shapiro, A. P., & Probstein, R. F. (1992). Random packings of spheres and fluidity limits of monodisperse and bidisperse suspensions. Physical Review Letters,68(9), 1422-1425. doi:10.1103/physrevlett.68.1422

Sharma, M. M., & Gadde, P. B. (2005). The impact of proppant retardation on propped fracture lengths. SPE Annual Technical Conference and Exhibition. doi:10.2118/97106-ms

Shokir, E. M., & Al-Quraishi, A. (2007). Experimental and numerical investigation of proppant placement in hydraulic fractures. Proceedings of Latin American & Caribbean Petroleum Engineering Conference. doi:10.2523/107927-ms

Shu, C. W., & Osher, S. (1989). Efficient implementation of essentially non-oscillatory shock-capturing schemes, II. Journal of Computational Physics, 83(1), 32-78.

Shu, C. (1990). Numerical experiments on the accuracy of ENO and modified ENO schemes. Hampton, VA: Institute for Computer Applications in Science and Engineering, NASA Langley Research Center.

Simha, R. (1952). A treatment of the viscosity of concentrated suspensions. Journal of Applied Physics,23(9), 1020-1024. doi:10.1063/1.1702338

Slot, R. (1984). Terminal velocity formula for objects in a viscous fluid. Journal of Hydraulic Research,22(4), 235-243. doi:10.1080/00221688409499381

Song, D., Gupta, R. K., & Chhabra, R. P. (2009). Wall effects on a sphere falling in quiescent power law fluids in cylindrical tubes. Industrial & Engineering Chemistry Research,48(12), 5845-5856. doi:10.1021/ie900176y

Staben, M. E., Zinchenko, A. Z., & Davis, R. H. (2003). Motion of a particle between two parallel plane walls in Low-Reynolds-number Poiseuille flow. Physics of Fluids,15(6), 1711. doi:10.1063/1.1568341

Steinour, H. H. (1944). Rate of sedimentation. non-flocculated suspensions of uniform spheres. Industrial & Engineering Chemistry,36(7), 618-624. doi:10.1021/ie50415a005

Steinour, H. H., (1944 b), Rate of sedimentation—suspensions of uniform-size angular particles. Ind. Engng Chem. 36, 840-847.

Stokes, G. (1850). On the effect of the internal friction of fluids on the motion of pendulums. Cambridge Philosophical Society, 9(02), 8-106.

Sutterby, J. L. (1973). falling sphere viscometry. I. wall and inertial corrections to Stokes law in long tubes. Transactions of the Society of Rheology,17(4), 559-573. doi:10.1122/1.549308

Swamee, P. K., & Ojha, C. S. (1991). Drag coefficient and fall velocity of nonspherical particles. Journal of Hydraulic Engineering,117(5), 660-667. doi:10.1061/(asce)0733-9429(1991)117:5(660)

Taghipoor, S., Nouri, A., & Chan, D. (2013). Numerical modelling of hydraulic fracturing in weakly consolidated sandstones using smeared fracture approach. Canadian Energy Technology and Innovation, 1(2), 31-41.

Taghipoor, S., Roostaei, M., Nouri, A., & Chan, D. (2014). A numerical investigation of the hydraulic fracturing mechanism in oil sands. SPE Heavy Oil Conference-Canada. doi:10.2118/170132-ms

Tanaka, N., Makino, K., & Iinoya, K. (1970). Theoretical analysis of dust cleaning operarion in multi-compartment bag filter. Chemical engineering,37(7). doi:10.1252/kakoronbunshu1953.37.718

Terfous, A., Hazzab, A., & Ghenaim, A. (2013). Predicting the drag coefficient and settling velocity of spherical particles. Powder Technology,239, 12-20. doi: 10.1016/j.powtec.2013.01.052

Thomas, D. G. (1965). Transport characteristics of suspension: VIII. A note on the viscosity of Newtonian suspensions of uniform spherical particles. Journal of Colloid Science,20(3), 267-277. doi:10.1016/0095-8522(65)90016-4

Torobin, L. B., & Gauvin, W. H. (1959). Fundamental aspects of solids-gas flow: Part I: Introductory concepts and idealised sphere motion in viscous regime. The Canadian Journal of Chemical Engineering,37(4), 129-141. doi:10.1002/cjce.5450370401

Torquato, S., Truskett, T. M., & Debenedetti, P. G. (2000). Is random close packing of spheres well defined? Physical Review Letters,84(10), 2064-2067. doi:10.1103/physrevlett.84.2064

Turian, R. M., Yuan, T., & Mauri, G. (1971). Pressure drop correlation for pipeline flow of solid-liquid suspensions. AIChE Journal,17(4), 809-817. doi:10.1002/aic.690170409

Turton, R., & Levenspiel, O. (1986). A short note on the drag correlation for spheres. Powder Technology,47(1), 83-86. doi:10.1016/0032-5910(86)80012-2

Turton, R., & Clark, N. (1987). An explicit relationship to predict spherical particle terminal velocity. Powder Technology,53(2), 127-129. doi:10.1016/0032-5910(87)85007-6

Unwin, A., & Hammond, P. (1995). Computer simulations of proppant transport in a hydraulic fracture. Proceedings of SPE Western Regional Meeting. doi:10.2523/29649-ms

Vairogs, J., Hearn, C., Dareing, D. W., & Rhoades, V. (1971). Effect of rock stress on gas production from low-permeability reservoirs. Journal of Petroleum Technology,23(09), 1161-1167. doi:10.2118/3001-pa

Vand, V. (1948). Viscosity of solutions and suspensions. ii. experimental determination of the viscosity–concentration function of spherical suspensions. The Journal of Physical and Colloid Chemistry,52(2), 300-314. doi:10.1021/j150458a002

Vlajinac, M., & Covert, E. E. (1972). Sting-free measurements of sphere drag in laminar flow. Journal of Fluid Mechanics,54(03), 385. doi:10.1017/s0022112072000746

Wadell, H. (1934). The coefficient of resistance as a function of Reynolds number for solids of various shapes. Journal of the Franklin Institute,217(4), 459-490. doi:10.1016/s0016-0032(34)90508-1

Warming, R., Kutler, P., & Lomax, H. (1973). Second- and third-order non-centered difference schemes for nonlinear hyperbolic equations. AIAA Journal,11(2), 189-196. doi:10.2514/3.50449

Warming, R., & Hyett, B. (1974). The modified equation approach to the stability and accuracy analysis of finite-difference methods. Journal of Computational Physics,14(2), 159-179. doi:10.1016/0021-9991(74)90011-4

Weill, L., & Latil, M. (1992). Modeling hydraulic fracture in finite difference reservoir simulator. ECMOR III - 3rd European Conference on the Mathematics of Oil Recovery. doi:10.3997/2214-4609.201411092

Weissberg, S., Simha, R., & Rothman, S. (1951). Viscosity of dilute and moderately concentrated polymer solutions. Journal of Research of the National Bureau of Standards,47(4), 298. doi:10.6028/jres.047.038

Wen, C. Y., & Yu, Y. H. (1966). A generalized method for predicting the minimum fluidization velocity. AIChE Journal,12(3), 610-612. doi:10.1002/aic.690120343

Wen, C. Y., & Fan, L. S. (1974). A comparison of recent axial dispersion correlations in liquid-solid fluidized beds. The Canadian Journal of Chemical Engineering,52(5), 673-675. doi:10.1002/cjce.5450520523

Weng, X., & Klein, H. (1998). Numerical simulation of proppant accumulation at fracture wall due to fluid leak-off. Proceedings of SPE Rocky Mountain Regional/Low-Permeability Reservoirs Symposium. doi:10.2523/40061-ms

Wesseling, P. (2009). Principles of computational fluid dynamics (Vol. 29). Springer Science & Business Media.

Wham, R. M., Basaran, O. A., & Byers, C. H. (1996). Wall effects on flow past solid spheres at finite reynolds number†. Industrial & Engineering Chemistry Research,35(3), 864-874. doi:10.1021/ie950354c

Wieselsberger, C. (1922). Further information on the laws of fluid resistance.

Yang, H., Fan, M., Liu, A., & Dong, L. (2015). General formulas for drag coefficient and settling velocity of sphere based on theoretical law. International Journal of Mining Science and Technology,25(2), 219-223. doi:10.1016/j.ijmst.2015.02.009

Zigrang, D. J., & Sylvester, N. D. (1981). An explicit equation for particle settling velocities in solid-liquid systems. AIChE Journal,27(6), 1043-1044. doi:10.1002/aic.690270629

Zimmerman, R., Kumar, S., & Bodvarsson, G. (1991). Lubrication theory analysis of the permeability of rough-walled fractures. International Journal of Rock Mechanics and Mining Sciences & Geomechanics Abstracts,28(4), 325-331. doi:10.1016/0148-9062(91)90597-f

Appendix A: Solution to the Momentum Equation for Drag Force on a Single Particle Falling in an Infinite Medium

The general 1D momentum equation of the particles can be written as (Wallis, 1969):

$$\rho_p \left(\frac{\partial v}{\partial t} + v\frac{\partial v}{\partial z}\right) = b + f - \frac{\partial p}{\partial z} \tag{A-1}$$

where b represents any body force, p is the pressure, f accounts for surface forces on the particles, ρ_p is the particle density and v is velocity. In uniform, steady state condition, velocity does not change with space and time, and the left hand side vanishes. Therefore, the only body force in the system will be gravitational forces. The surface forces will include hydrodynamic drag plus direct contact force (this latter force would be zero for suspended particles) and p will be fluid pressure. All the terms in above equation represent force per unit volume. Multiplying all the terms by the volume of a single particle and applying the abovementioned considerations, the steady-state force balance equation for a single particle becomes:

$$-V_p\rho_p g + F_D - V_p\frac{dp}{dz} = 0 \tag{A-2}$$

where Vp is the volume of a single particle and F_D is the hydrodynamic drag force. The pressure gradient term for a suspension of particles under equilibrium will be:

$$\frac{dp}{dz} = -g\rho_f \tag{A-3}$$

Substituting this in the momentum equation, we obtain:

$$F_D = \frac{\pi d_p^3}{6}(\rho_p - \rho_f)g \tag{A-4}$$

The resistance force per unit projected area in a plane perpendicular to the direction of motion for a sphere falling at its terminal velocity is:

$$f = \frac{\pi\frac{d_p^3}{6}(\rho_p - \rho_f)g}{\pi\frac{d_p^2}{4}} = \frac{2}{3}d_p g(\rho_p - \rho_f) \tag{A-5}$$

This equation means that for a particle moving with steady terminal velocity, the drag force balances the difference between the weight and buoyancy. Therefore:

$$C_D = \frac{f}{\frac{1}{2}\rho u^2} = \frac{4}{3}\frac{d_p g\left(\rho_p - \rho_f\right)}{u^2 \rho_f} \tag{A-6}$$

Appendix B: General Notes on Advection, Diffusion and Partial Differential Equations

Partial differential equations describe a wide range of physical phenomena. These equations can be classified into different groups, and each group has certain mathematical method for finding the solution. In this chapter, we will show that the transport of proppant is described by a first-order hyperbolic partial differential equation. In general, mathematical form, the transport equation can be written as:

$$\frac{\partial q}{\partial t}+\frac{\partial (Aq)}{\partial x}=0 \tag{B-1}$$

or

$$\frac{\partial q}{\partial t}+\frac{\partial f}{\partial x}=0 \tag{B-2}$$

where f is a function of conserved quantity q. This type of hyperbolic equation describes wave (information) propagation or transport in the *x* direction with velocity A.

For this PDE to be hyperbolic, the matrix A must satisfy certain properties. This PDE is classified as hyperbolic if matrix A is diagonalizable with real eigenvalues. Second-order partial differential equations are classified in a different way. A linear second-order PDE in two dimensions has the following general form:

$$A(x,y)\frac{\partial^2 q}{\partial x^2}+B(x,y)\frac{\partial^2 y}{\partial x \partial y}+C(x,y)\frac{\partial^2 q}{\partial y^2}=D(q,\frac{\partial q}{\partial x},\frac{\partial q}{\partial y},x,y) \tag{B-3}$$

This PDE is said to be:

$$\begin{cases} Parabolic\ if\ B^2-4AC=0 \\ Hyperbolic\ if\ B^2-4AC>0 \\ Elliptic\ if\ B^2-4AC<0 \end{cases}$$

It should be noted that although proppant transport PDE is first-order hyperbolic, slurry transport PDE is elliptic. Therefore, from here on we only focus on first-order hyperbolic and seccond order elliptic type of PDEs.

Eq. B-1 is the general form of advection equation. Linear advection equation, which is a simplified form of Eq. B-1, can be stated as:

$$\frac{\partial q}{\partial t} + A\frac{\partial (q)}{\partial x} = 0 \tag{B-4}$$

which means matrix A (velocity in transport application) is uniform or it can be said that the conserved quantity has no effect on the velocity. By taking a closer look at the first-order linear hyperbolic PDEs, a general solution to such equation can be found as:

$$q = f(x - At) \tag{B-5}$$

The proof is easy. If we define:

$$x - At = s \tag{B-6}$$

Then by chain rule:

$$\frac{\partial q}{\partial t} = \frac{\partial f}{\partial s}\frac{\partial s}{\partial t} = -A\frac{\partial f}{\partial s} \tag{B-7}$$

and

$$\frac{\partial q}{\partial x} = \frac{\partial f}{\partial s}\frac{\partial s}{\partial x} = \frac{\partial f}{\partial s} \tag{B-8}$$

Now substituting into Eq. B-4, we obtain:

$$\frac{\partial q}{\partial t} + A\frac{\partial (q)}{\partial x} = -A\frac{\partial f}{\partial s} + \frac{\partial f}{\partial s} = 0 \tag{B-9}$$

Now, this solution has an intuitive meaning. It means that the solution to a purely advective PDE is simply a shift of initial conditions. In other words, any given initial condition is simply translated forward or backward, depending on the sign of the velocity, with velocity A through the model, without any change in its initial profile (Fig. B-1).

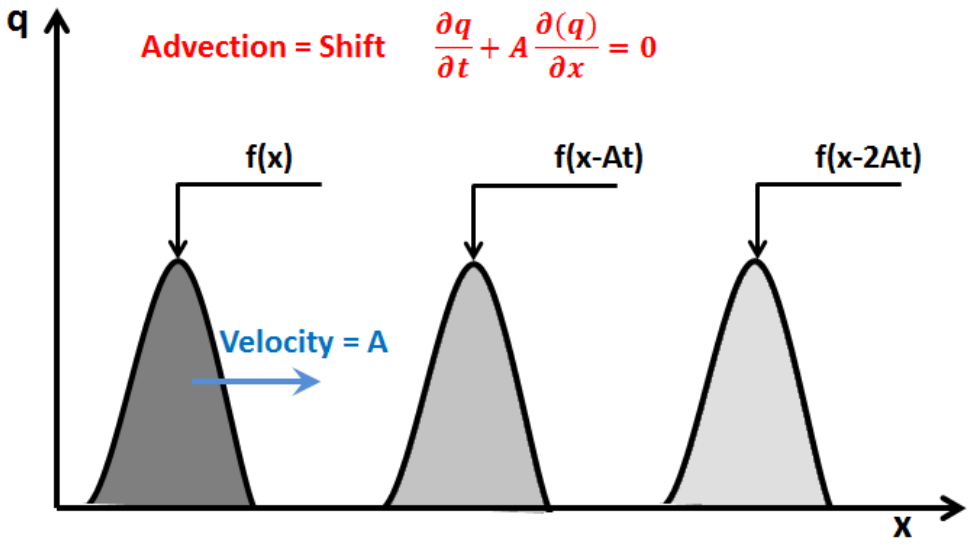

Figure B-1: Purely Advection Equation Translating Initial Condition with No Smearing

The other consequence of such a solution is that q is constant along any path in x-t space which satisfies:

$$x - At = cte \tag{B-10}$$

These paths or rays are called characteristics of the equation and this method of finding the solution is called method of characteristics.

Realistically, the proppant transport falls into a different category of hyperbolic PDEs since the velocity field is not uniform at every location inside the fracture. In this case, the hyperbolic PDE is called non-autonomous PDE:

$$\frac{\partial q}{\partial t} + \frac{\partial (A(x,t)q)}{\partial x} = 0 \tag{B-11}$$

Since the velocity is non-uniform, the characteristic curves are not straight lines and the solution is not constant along the curves anymore.

Another important phenomenon that should be described here is diffusion. We need to define diffusion mathematically to be able to explain the inadequacy of finite difference schemes in later sections. Without going into the details of the proof, using Fick's law of diffusion which states that the net flux is proportional to the gradient of q, the parabolic PDE that describes diffusion will be:

$$\frac{\partial q}{\partial t} = D\frac{\partial^2 q}{\partial x^2} \tag{B-12}$$

where D is known as diffusivity coefficient. The solution to the pure diffusion equation is the smearing or damping of the initial condition, without any movement or shift. Fig. B-2 shows schematically how the solution changes with time by solving a pure diffusion equation.

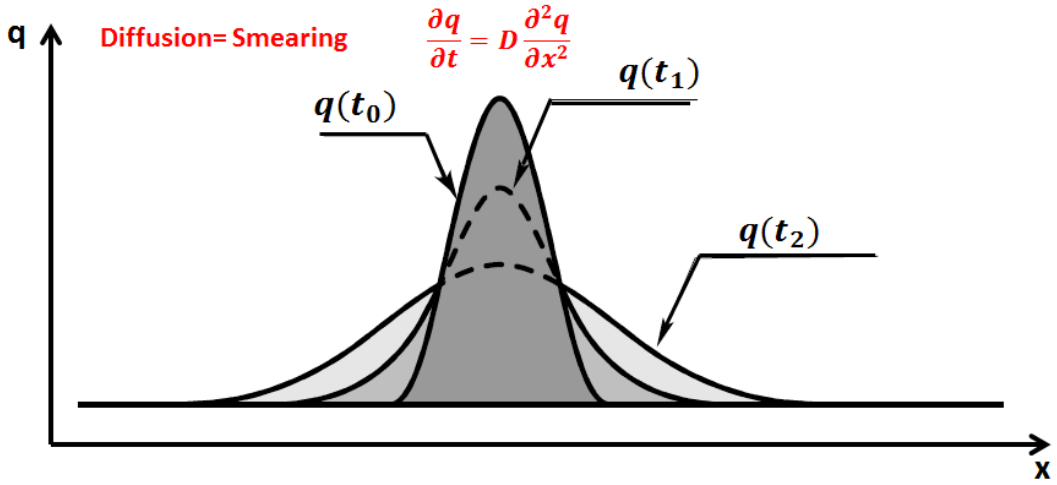

Figure B-2: Pure Diffusion Equation Only Smears the Initial Condition with No Shift

In a more general case, the transport equation can involve advection and diffusion simultaneously. The parabolic PDE of this type can be written as:

$$\frac{\partial q}{\partial t} + \frac{\partial (A(x,t)q)}{\partial x} = D\frac{\partial^2 q}{\partial x^2} \tag{B-13}$$

It is obvious that the solution to this type of problem will shift and smear the initial condition at the same time. We will discuss the negligible diffusion in proppant transport problem in the following sections. An important conclusion that can be drawn from above discussion is that any PDE that contains first-order space derivative will advect and shift the initial condition, while the presence of second-order space derivatives ensures diffusion and smearing of the initial condition. From this discussion and with the help of modified partial differential equations, we will show why usual finite difference schemes smear the solution and therefore are inadequate for pure advection problem of proppant transport.

Appendix C: A Short Note on Courant-Friedrichs-Lewy Stability Condition

The domain of dependence of hyperbolic partial differential equations should be defined before explaining the CFL condition. The solution to scalar hyperbolic PDE, as explained in Chapter 3, is q^0(X-At) which means the solution depends only on a single point at (X, T). For system of m hyperbolic PDEs the solution depends on m particular points x-A^p. In other words, for hyperbolic PDEs, the data at other points at t^n has no influence on the value of q at t^{n+1}.

$$\mathcal{D}(X,T) = \{X - A^p t : p = 1, 2, \dots, m\} \tag{C-1}$$

This set is called domain of dependence. This concept is shown in Fig. C-1. This bounded domain of dependence is a consequence of finite speed travel of information in a hyperbolic equation.

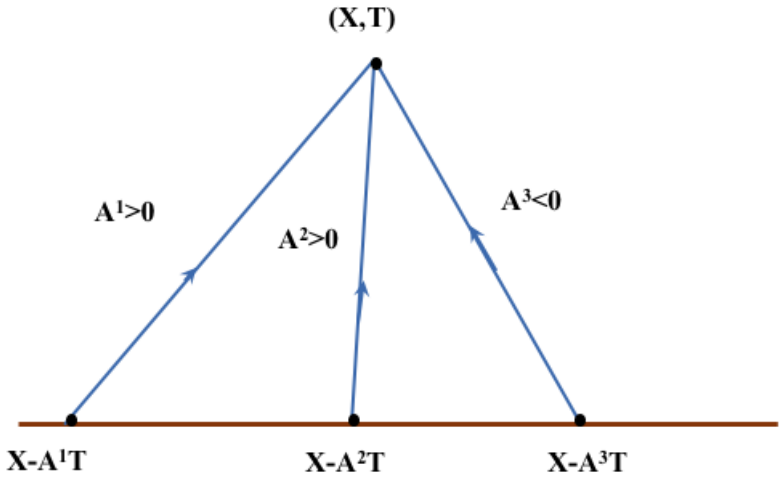

Figure C-1: Domain of Dependence of a System of Hyperbolic Equations

The CFL condition is a necessary condition that is satisfied by any stable and FVM or FDM. Stability here means that the method converges to the solution of PDE as the grid is refined.

If numerical flux function is defined as:

$$\mathcal{F}^n_{i-\frac{1}{2}} = \mathcal{F}(Q^n_{i-1}, Q^n_i) \tag{C-2}$$

a three-point stencil numerical method is obtained:

$$Q_i^{n+1} = Q_i^n - \frac{\Delta t}{\Delta x}[\mathcal{F}(Q_i^n, Q_{i+1}^n) - \mathcal{F}(Q_{i-1}^n, Q_i^n)] \tag{C-3}$$

Three-point stencil means that the value of Q_i^{n+1} depends on three points Q_{i-1}^n, Q_i^n and Q_{i+1}^n at the previous time step. If such a method is applied to the advection equation $q_t + Aq_x = 0$, the

exact solution translates a distance of AΔt over one time step. If AΔt ≤ Δx the information propagates less than one grid cell in each time step. As shown in Fig. C-2, in this case it would be logical that the numerical flux be defined in terms of two adjacent Q values. On the other hand, if AΔt > Δx the current value of Q_i^{n+1} clearly depends on the value of Q_{i-2}^{n} which is not used in definition of numerical flux. In this case the method would be unstable no matter how the flux is defined in terms of Q_i^n and Q_{i-1}^n.

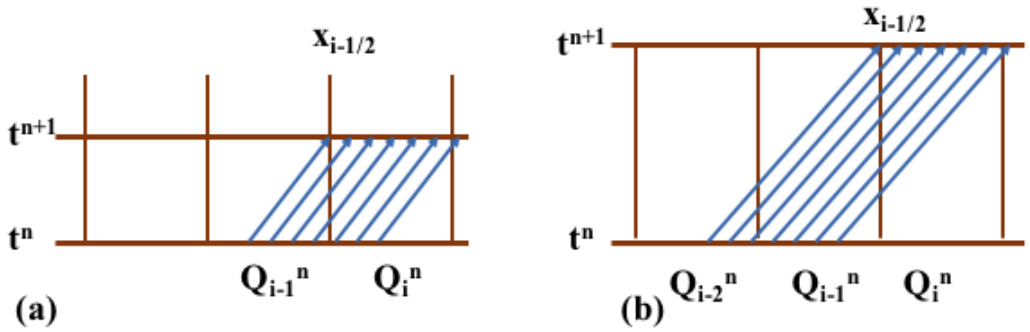

Figure C-2: a) For small time step, flux depends on neighboring cells, b) For larger time steps, flux depends on values further away

The numerical domain of dependence can be defined in the same way as the set of points that initial data can affect. As shown in Fig. C-3 the value of Q_i^2 depends on Q_{i-1}^1, Q_i^1, Q_{i+1}^1 and hence on Q_{i-2}^0, …, Q_{i+2}^0. This means that only initial data at interval $X - 2\Delta X^{coarse} \le x \le X + 2\Delta X^{coarse}$ can affect the numerical solution. Refining the grid by a factor of 2 ($\Delta X^{fine} = \Delta X^{coarse}/2$) means that the numerical approximation depends on $X - 4\Delta X^{fine} \le x \le X + 4\Delta X^{fine}$, which is the same interval as before. Generally, continuous grid refinement with ratio $r = \Delta t/\Delta x$ results in a domain of dependence of $X - T/r \le x \le X + T/r$ for a point at (X,T).

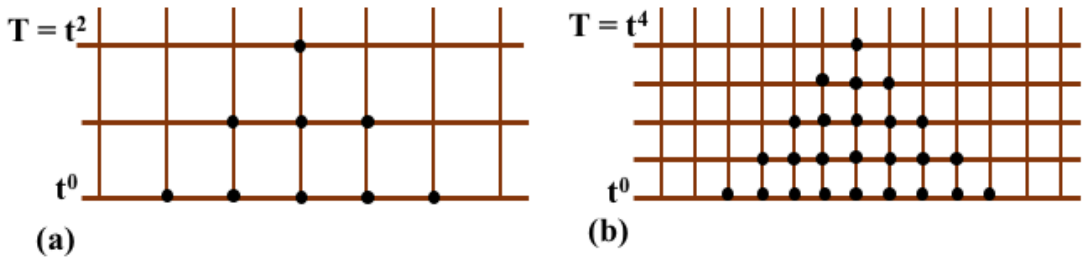

Figure C-3: Numerical Domain of Dependence of a) Coarse and b) fine Mesh

The CFL condition will be satisfied if the numerical method domain of dependence contains the domain of dependence of the true solution:

$$X - \frac{T}{r} \leq X - AT \leq X + \frac{T}{r} \tag{C-4}$$

which means:

$$\upsilon = \left|\frac{A\Delta t}{\Delta x}\right| \leq 1 \tag{C-5}$$

The ratio ν is called the CFL number or Courant number. A change in the initial condition q^0 at X-AT, while changing true solution, will not change the numerical solution if CFL condition is not satisfied. It should also be noted that if a numerical method had a wider stencil, CFL condition would be more lenient. For example, for a centered five point stencil, $\nu \leq 2$.